SPACE PHYSICS LABORATORY

Scientific Accomplishments 2010-2011

VIKRAM SARABHAI SPACE CENTRE
Thiruvananthapuram-695022, India

Space Physics Laboratory

Scientific Accomplishments 2010-2011

VIKRAM SARABHAI SPACE CENTRE

Thiruvananthapuram - 695 022

Compiled By

Suresh Raju, Mukunda Gogoi, Siddarth Shankar Das

From the Director

Inventorying on the 'eve' of the 28th meeting of the Scientific Advisory Committee, it is gratifying to note that, **SPL has not only lived up to the expectation, but also has made giant strides forward** in the areas of atmospheric, space, and planetary sciences; occupying its rightful position amongst the top laboratories. While the ongoing activities have strengthened, the recent and new initiatives are blossoming. New **emerging concepts** have also raised **new questions** that are of current interest at international levels. In terms of **peer-reviewed scientific publications** in impact factor journals, SPL has **broken all its previous records**. SPL scientists continue to receive awards and honours.

The successful launch of the **YOUTHSAT**, ISRO's small satellite dedicated for science, in April 2011, has been a landmark achievement for **SPL** in general, and the **ITMP Branch** in particular. The data from the two **SPL-initiated payloads, RaBIT and LiVHySI**, are regularly being collected and deposited at the Payload Operation Centre at SPL and also at the ISSDC. Good quality **Tomograms** are being generated from the RaBIT data, some of which have revealed, **for the first time**, features such as the spatial map of **Traveling Ionospheric Disturbances, and Topside Ionization Layers (F3)**, which have hitherto remained unexplored from the ground-based radars; thereby providing a unique opportunity for the aeronomy science community.

In the area of **aerosols and climate impact** under **ARFI** (Aerosol Radiative Forcing over India), and RAWEX (Regional Aerosol Warming Experiment), under **I-GBP, the first-ever in situ measurements** of **aerosol BC** using high-altitude balloon borne instrumentation has resulted in the **discovery of the impact of aerosol absorption on the atmospheric stability and environmental lapse rate**. It provided the **first observational evidence** of strong elevated layers of BC in the middle and upper troposphere, the warming of the atmosphere caused by absorption of radiation within these layers resulting in a **large reduction** in the environmental **lapse rate** and a **near-isothermal region** around these layers. The consequent increase in atmospheric stability raises new questions such as 'do BC layers **build their own homes up in the atmosphere**'?

New results continue to emerge in the area of **Planetary and cometary** research. The generation, **for the first time,** of a **spatial map of deflected solar wind protons by the magnetic anomaly regions on the far side of the moon**, opens up new avenues for investigation of plasma processes in the lunar ambience. **Modeling studies of cometary emissions** (Cameron band) have revealed possibilities of **re-writing** some of the current beliefs and understanding, as well as methods to infer on species abundances based on these emissions.

Leading from the front, SPL was instrumental in making extensive exploration and **bringing out new and multi-disciplinary scientific results** from the "**Sooryagrahan-2010**" campaign. A **two-day national workshop**, **NaWRoSE**, was organized by SPL to deliberate the results and the compilation was brought out within an year of the campaign. The experiment also put forward certain **novel concepts to explain the atmospheric processes during eclipse**, which manifested **in strong CEJ, inhibition of equatorial fountain, post eclipse enhancement in the stratospheric ozone, short-period gravity waves propagating through the entire neutral atmosphere and dumping their energy in the**

MLT region, weakening of atmospheric boundary layer dynamics and perturbations to the vertical structure of aerosols. The new concepts put forth have raised the need for more experiments. **About 20 peer reviewed papers** appeared in international journals; again a **first time achievement** in the country.

Making significant progress in the recently initiated, multi-departmental activity on **Polar Research**, SPL is poised to make **year-round** observation of **Arctic aerosols**, **for the first time in the country**, **under the ARFI project** of I-GBP, while the results on characterization of Antarctic aerosols are yielding deeper insights. **ARFI** also achieved **year-round aerosol characterization from Hanle**, the results are in the pipeline.

Spatial distributions of trace gases (O_3, NOx and CO) over the BoB during winter season were examined under the aegis of **Atmospheric Chemistry** using **W-ICARB** data. These were compared **with satellite data and model simulations**. The **microwave radiometer** is being used extensively to examine the evolution of **convective systems**.

In the area of **clouds and modeling**, the quantification of a **pool of inhibited cloudiness** in the south-eastern Arabian Sea, and offering an explanation through a **mini-circulation embedded on the monsoon system** was an outstanding contribution to the science of Indian monsoon. Synthesizing observations and climate models, the **modeling group** has brought out the **first observational evidence** of the strong role played by the **Arabian Sea warm pool on the monsoon rainfall** along the west coast of India. The group also provided regular weather forecasts for the GSLV and PSLV launches from SHAR.

The **Atmospheric Dynamics Branch** has carried out extensive studies focusing mainly on **(i) Convection, turbulence and gravity waves (ii) Stratopshere - Troposphere Exchanges (iii) Planetary Wave Interactions and (iv) processes in the MLT region using instruments (radars, lidars), models and satellite data**, providing deeper insights into the wave- mean-flow interactions, dynamical coupling between various atmospheric regions, and the exchange of energy and momentum.

The discipline of **ionosphere thermosphere and magnetosphere physics** has focused on investigating the unique scenario created by the **annular eclipse** and has brought out **stupendous results**. These include **the novel explanation based on a moving neutral-wind dynamo for the eclipse time CEJ, double pre-reversal enhancement** and **reverse fountain** effects during annular eclipse, the large changes in the E- and F - region ionization and thermospheric effects. Investigations of the impact of **geomagnetic disturbances on the ESF occurrence, on equatorial anomaly through a disturbance dynamo and on thermospheric processes** were the major studies carried out.

SPL is the implementing institution for **ARFI, RAWEX, ICARB** (integrated campaign for Aerosols, gases and Radiation Budget), and Atmospheric Boundary Layer Network and Characterization (**ABLN&C**) projects of ISRO - GBP at national level. A systematic **data archival centre** is being developed to archive the valuable and exhaustive data generated over the decades across the country and link it to the **ISRO Geoportal**.

The Atmospheric Technology Division supports the entire experimental activities of SPL. Its major activities include the development of **ChACE-2 payload** for **Chandrayaan-2 mission**, development of the prototype of **MENCA payload for Mars 2013 mission, ENWi payload for rocket experiments** and development of a **FPGA based C & DA and processing system for the HF radar**. For the ARFI-NET, **a stand-alone, micro-controller based control and data acquisition system** has been developed for the MWR, **thereby eliminating once for all the impediments** on the dependence on PC and its continuously changing operating systems and architectures. The development of wireless and GSM based data transfer system, and Internet based network links are amongst the developments aiming at seamless network activity and data warehousing. ATD is also responsible for maintaining the **Youthsat Payload Operation Centre and interfacing with ISSDC**.

Publications in peer-reviewed, **impact factor** journals of repute are the ultimate benchmarks of the scientific accomplishments of any science laboratory. In this discipline, SPL has broken all its earlier records, with **71** publications during the current year. Scientists from SPL have received **Awards and Honours at National level**.

Interactions, collaboration and exchange programs are the key elements in the progress of a laboratory. SPL performed remarkably in these areas during the reporting year. **Prof. J. P. St. Maurice**, University of Saskatchewan, Canada was in SPL under the ADREF scheme for a period of three months, and worked on equatorial aeronomy problems; Ms **Audrey Schaufelberger**, Physikalisches Institute, University of Bern, Switzerland, was awarded Indo-Swiss Joint Research Programme Fellowship to work in SPL for two months on Planetary Science area. Ms **M. B. Dhanya of SPL** was awarded Indo-Swiss Joint Research Programme Fellowship to work for one month at Sweden on SARA data and Ms **K M Ambili**, visited University of Saskatchewan for three months to work with ionospheric modeling. SPL continued its extensive collaborations with other departments and institutions and continued to contribute to programs, such as the **CTCZ and the CAIPEEX of MoES, and the Polar Research program of the National Centre for Antarctic and Ocean Research, as well as the National Carbonaceous Aerosol Program (NCAP) of the MoEF**.

In the field of human resources and capacity building, SPL carefully nurtures a very **strong and vibrant research fellowship program** in-house, as well as contributes to the societal needs by guiding the project work of B Tech, M Tech, M Sc and M Phil students and support the curriculum requirement of IIST.

If the past has been glorious, the future looks exciting and challenging. Ascertaining its strong presence in the planetary and space explorations, SPL's payload **CHACE-2 has been approved onboard the orbiter of Chandrayaan–2. Two of our experiments, MENCA (Martian Exospheric Neutral Composition Analyser), and ROX (Radio Occultation experiment for Martian ionosphere and atmosphere)** have been short-listed for the forthcoming 2013-Mars mission. **New satellite and rocket experiments are proposed, while the ground based experimental facilities are poised for** major facelift. SPL also has worked out major experimental plans for the 12th FYP.

I have great pleasure in presenting this report of SPL's accomplishments during 2010-11.

August 22, 2011

K. Krishnamoorthy

AWARDS AND HONOURS

Dr. K. Krishnamoorthy

K. R. Ramanathan Award for the outstanding contribution in the field of Earth and Atmospheric Sciences, from Indian National Science Academy

Dr. Anil Bhardwaj

Indo-Swedish International Collaborative Research Grant by the Swedish Research Council, SIDA, Sweden

Dr. Vijayakumar S. Nair

Young Scientist Medal Award from Indian National Science Academy

Dr. C. Vineeth

Young Associate, Indian Academy of Sciences

VISITS : SCIENTISTS FROM OTHER INSTITUTIONS

Prof. W. M. Boerner

Director, UIC-ECE, Communications, Sensing & Navigation, Chicago, USA,

Dr. Sarika Kulkarni

Center for Global and Regional Environmental Research, University of Iowa, USA

Dr. Christopher D. Elvidge

National Oceanic and Atmospheric Administration (NOAA), National Geophysical Data Center (NGDC) in Boulder, Colorado, USA

Dr. V. Ramanathan

Scripps Institution of Oceanography, University of California, San Diego, USA

Prof. J. P. St. Maurice

Institute of Space and Atmospheric Studies, University of Saskatchewan, CANADA

Prof. P. V. Joseph

Department of Atmospheric Sciences, Cochin University of Science and Technology, Cochin, INDIA

Dr. B. V. Krishnamurthy

SRM University, Chennai, INDIA

Dr. M. Rajeevan

National Atmospheric Research Laboratory, Gadanki, INDIA

INTERNATIONAL EXCHANGE OF SCIENTISTS

Prof. J. P. St. Maurice

Institute of Space and Atmospheric Studies, University of Saskatchewan, CANADA was awarded ISRO's ADREF visiting Scientist Fellowship

Audrey Schaufelberger

Physikalisches Institute of University of Bern, Switzerland, was awarded Indo-Swiss Joint Research Programme Fellowship 2010

M. B. Dhanya

Space Physics Laboratory, VSSC, was awarded Indo-Swiss Joint Research Programme Fellowship 2010

K. M. Ambili

Space Physics Laboratory, VSSC, was awarded I.S.A.S. Research Fellowship, University of Saskatchewan, CANADA

JOURNAL PUBLICATIONS

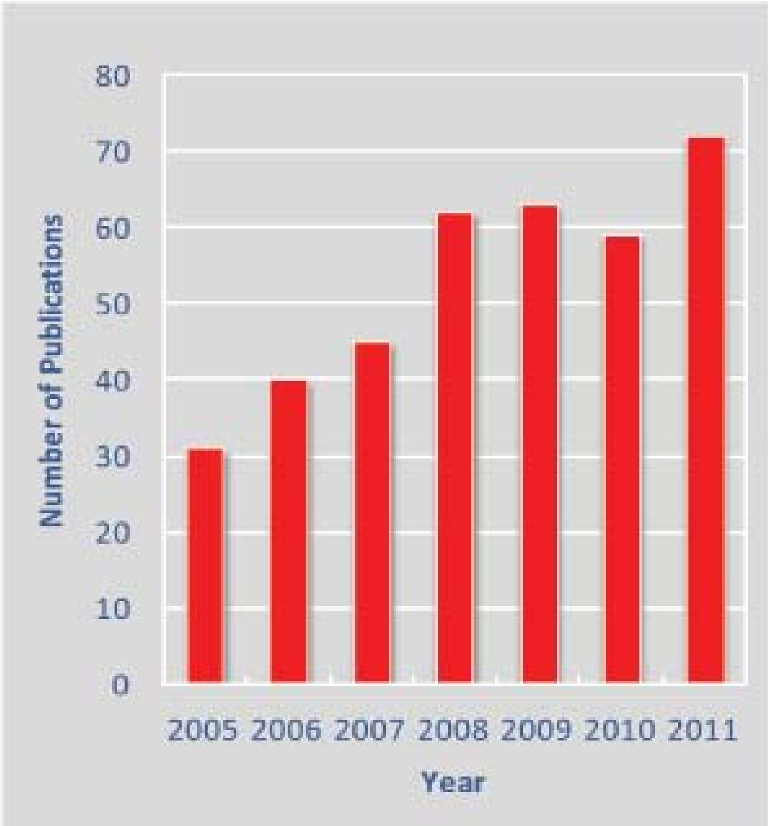

PROCEEDING PUBLICATIONS

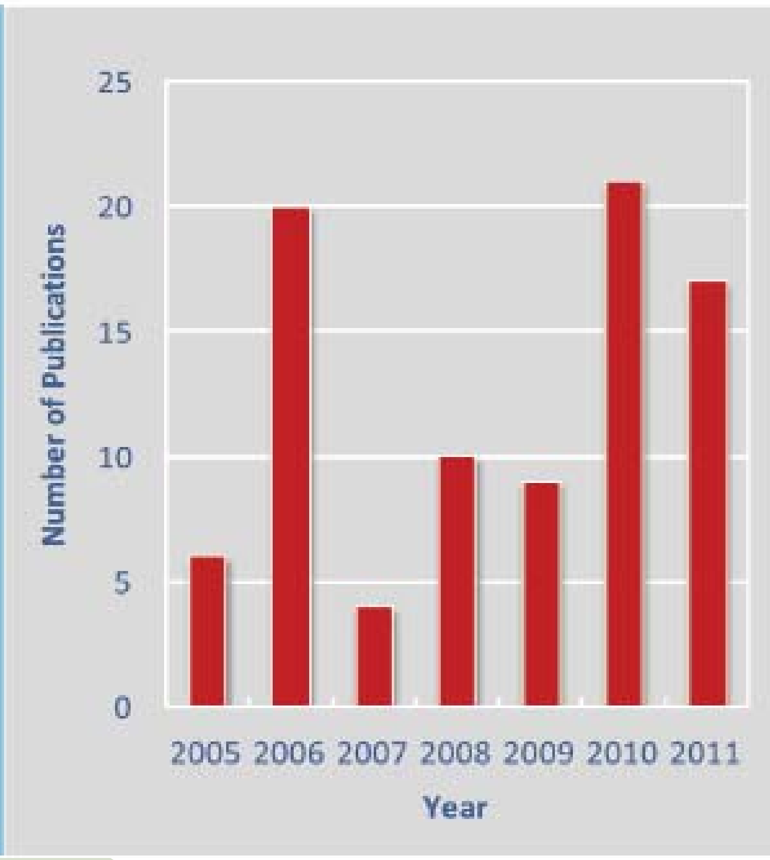

ACADEMIC ACTIVITIES

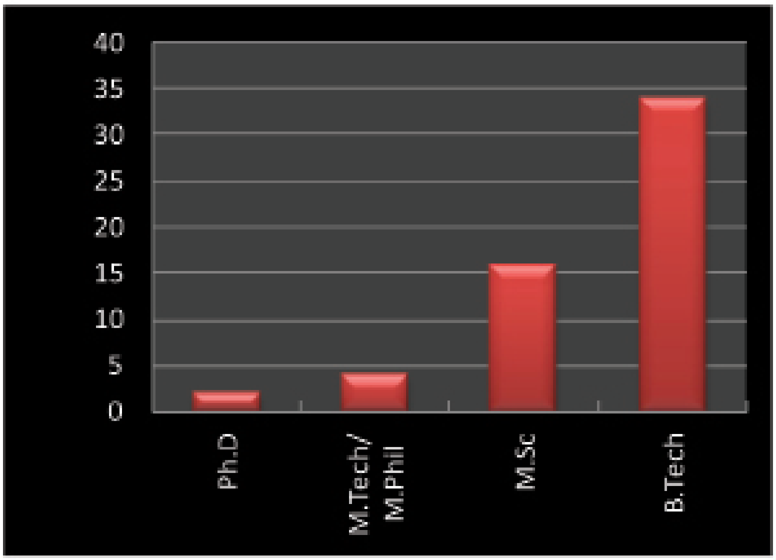

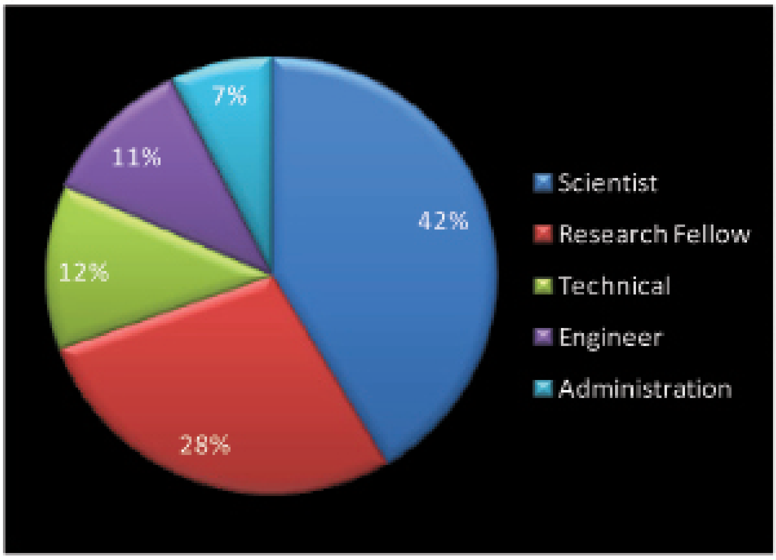

HUMAN RESOURCES

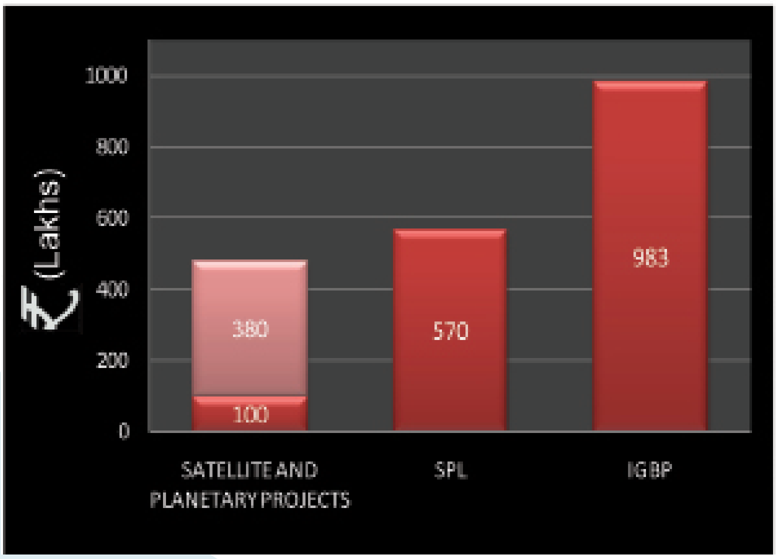

BUDGET 2010-11

Contents

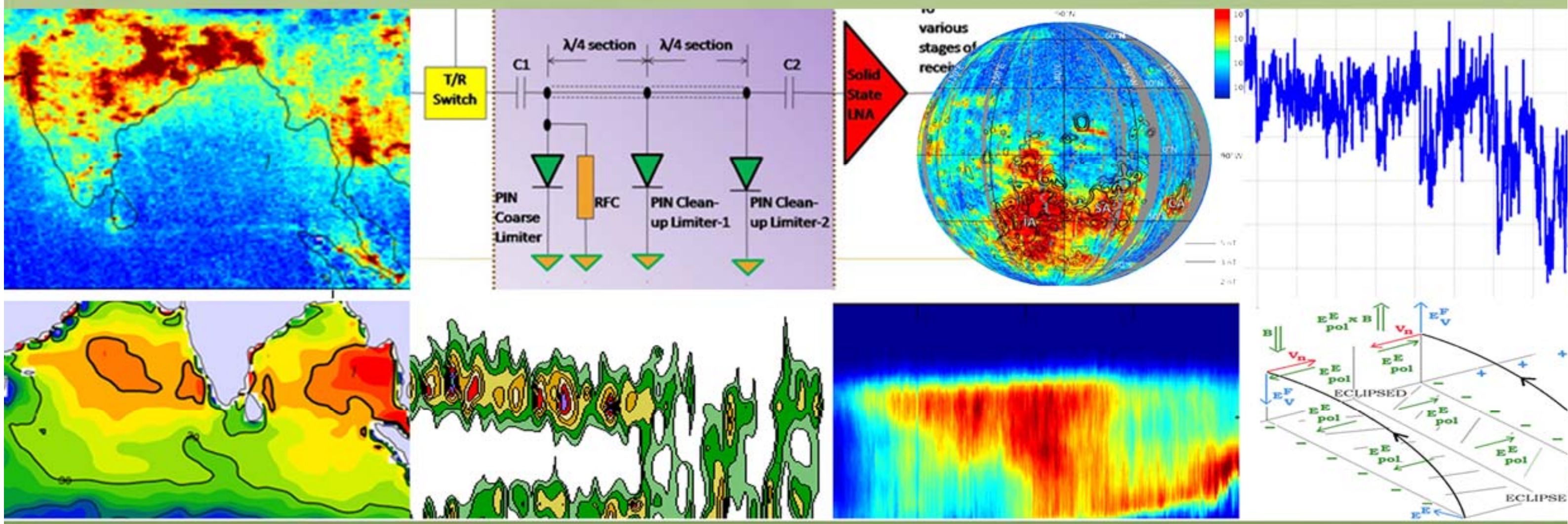

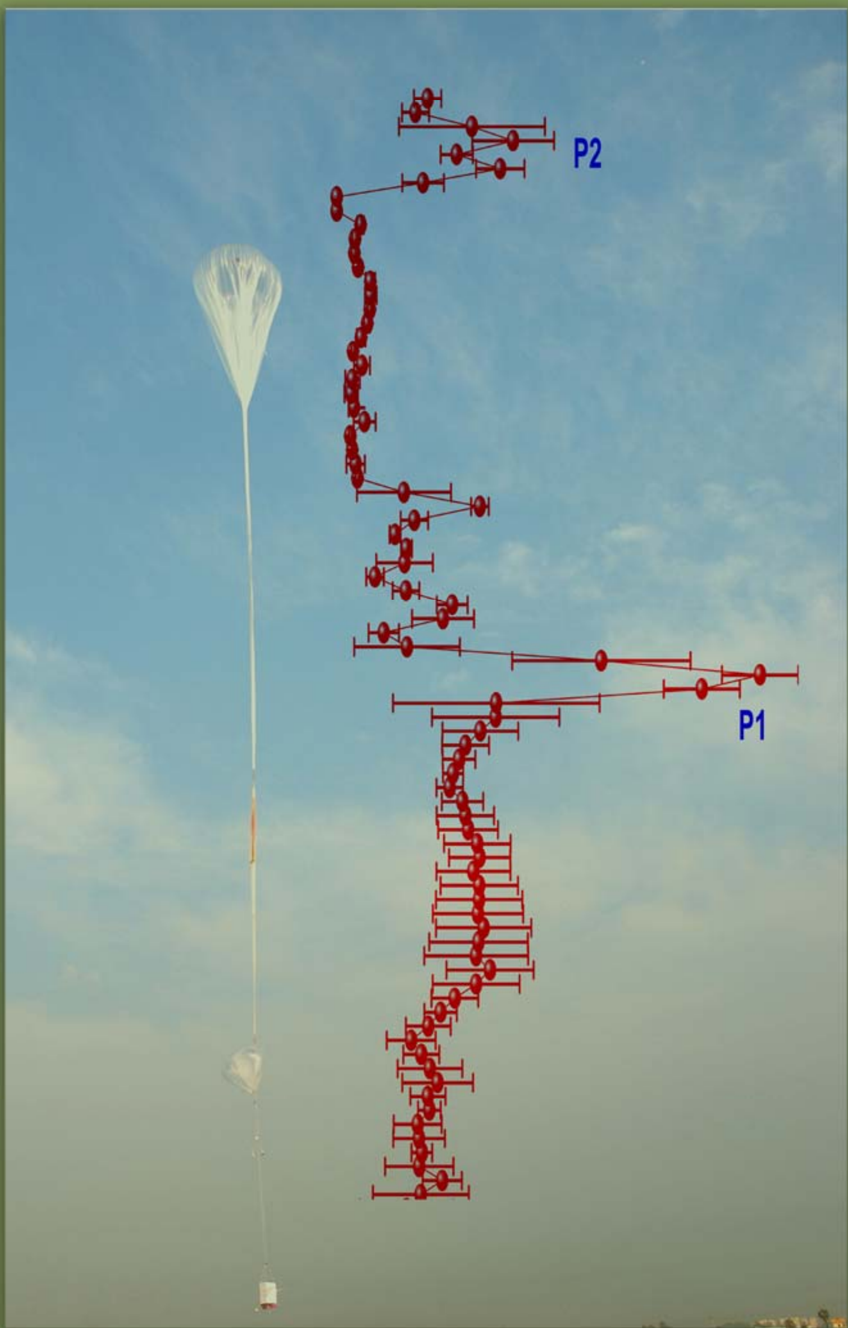

Space Physics Laboratory, Phone: +91 471 256 3663, Fax: +91 471 270 6535

ATMOSPHERIC AEROSOLS CHEMISTRY CLOUDS RADIATION

Science Faculty

Prabha R Nair
* Rajeev K
Suresh Raju C
#Prashant Hegde
Manoj Kumar Mishra
+Uma K N
Girach Imran Asatar

Visiting Scientist

Parameswaran K

Technical Team

Pradeep Kumar P
Anumod PG

Research Associates/Fellows

Meenu S
Liji Mary David
Anish Kumar M Nair
Tinu Antony
Aryasree S
Renju R

**Presently Head BLPAM*
#On deputation to Japan
+New appointment

The radiation balance of the earth-atmosphere system is the result of the interactions of solar/terrestrial radiation with aerosols, trace gases, and clouds. The interactions among these components, their spatial and temporal heterogeneities added with tropospheric chemistry and water vapour make the quantitative assessment of radiative impacts complex. Activities of AACCR Branch focus on the physio-chemical characterisation of aerosols, production, distribution and transport of trace gases, vertical and horizontal distribution and the morphological features of clouds and their dynamics using a variety of state-of-the- art techniques including Lidar, Satellites, Microwave Radiometer, GPS, in-situ Samplers and sophisticated on-line Gas Analysers and and modelling efforts.

1. CLOUDS

A 'pool of inhibited cloudiness' over the Bay of Bengal during the Asian summer monsoon

Spatial and vertical distributions of clouds derived from multi-year spaceborne observations have shown the persistence of a 'pool of inhibited cloudiness' covering an area of >10^6 km^2 between 3-13°N and 77-90°E over the Bay of Bengal (BoB) during the Asian summer monsoon season (ASM). Zonal and meridional cross sections of the altitude distribution of clouds derived from CloudSat data during 2006-2009 (Fig.1) reveal a vault-like structure at the 'pool' with little cloudiness below ~ 7 km. The frequency of occurrence of clouds (F_{ALT}) below ~ 7 km is generally < 10% at the centre of the 'pool', and is markedly lower than that over the surrounding regions (F_{ALT} ~ 25-35%) where deep convective clouds extend up to ~ 13 km. This suggests the absence of convection in the 'pool' region. However, F_{ALT} increases considerably above ~ 7 km and its spatial gradient almost vanishes in the altitude band of ~ 10-13 km where F_{ALT} is > 40% over a vast region, making this 'pool' inconspicuous in the regional distribution of semitransparent cirrus clouds observed using CALIPSO and KALPANA-1. The 'pool' is most prominent during July-August. Most of the high-altitude clouds observed over the 'pool' region appear to be the cirrus clouds generated by westward spreading of outflows from the deep convective systems situated over the eastern BoB. Seasonal mean precipitation rate over the 'pool' is < 3 mm day^{-1} while that over the surrounding regions is mostly in the range of 6-14 mm day^{-1}.

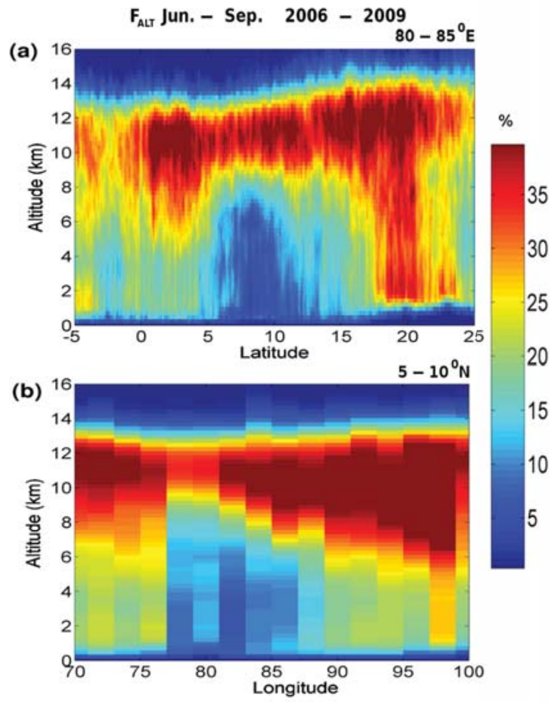

Figure 1: Four-year (2006-2009) average seasonal mean latitude-altitude cross section of the frequency of occurrence of clouds (F_{ALT}, expressed in percentage) during ASM along 80-85°E (a); (b) same as (a) but for the longitude-altitude cross section averaged along 5-10°N

Observational evidence for an embedded mini-circulation and genesis of the 'pool'

Genesis of the 'pool of inhibited cloudiness' is examined by combining the observed features of cloudiness with long-term (1996-2009) observations of surface wind divergence (scatterometer observations), sea surface temperature (SST), and reanalysis data on atmospheric circulation. Seasonal (June-September) mean spatial distribution of SST (Fig.2) shows a cold tongue originating off the southern tip of India and extending up to the south central BoB, which arises from the ocean upwelling caused by the prevailingh surface wind and its eastward spreading. However, the locations of minima in SST and cloudiness are quite different. Furthermore, SST is > 28.4°C at most parts of the 'pool', which is sufficiently high for the development of convection and clouds. These observations suggest that the genesis of the 'pool' cannot be mainly attributed to the weak reduction in SST

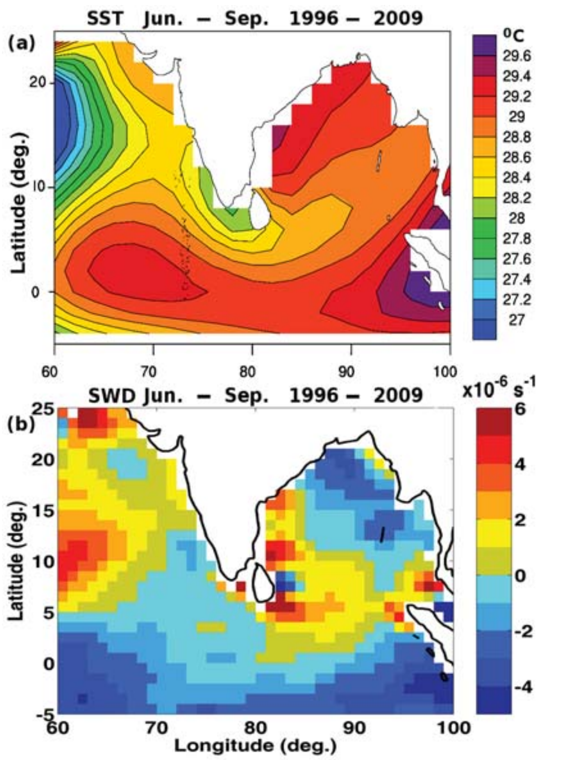

Figure 2: Long-term (1996-2009) seasonal mean patterns of (a) SST and (b) surface wind divergence (s^{-1}) during ASM

associated with the cold tongue. Long-term seasonal mean scatterometer observations show divergence of surface wind at the 'pool' and convergence at its surroundings (Fig.2). Together with the spatial and vertical distribution of clouds, these observations, for the first time, provide direct observational evidence for the existence of a regional scale mini-circulation extending between the surface and >7 km over and around the pool region, which is embedded in the large-scale summer monsoon circulation. Even though the SST at the south BoB during ASM is sufficiently high to trigger convection, the subsidence associated with the mini-circulation inhibits it, resulting in the 'pool'. This mini-circulation appears to be the result of the dynamical response of the atmosphere to the substantial spatial gradient of latent heating by large-scale cloudiness and precipitation at the vast and geographically fixed convective zones surrounding the 'pool'. This is seen in Fig.3 which depicts the multi-year mean (2006-2009) vertical profiles of latent heat released by precipitating clouds (estimated from the TRMM-Precipitation radar data) at the centre of the pool and its surroundings. Between 3-11 km, the latent heat at the centre of the 'pool' is very small (< 0.03 K hr^{-1}) while that at the surrounding regions is 2 to 4 times larger. It is proposed that the subsidence at the 'pool' might contribute to the maintenance of convection at the pool boundaries and be an important, but hitherto overlooked, component of ASM.

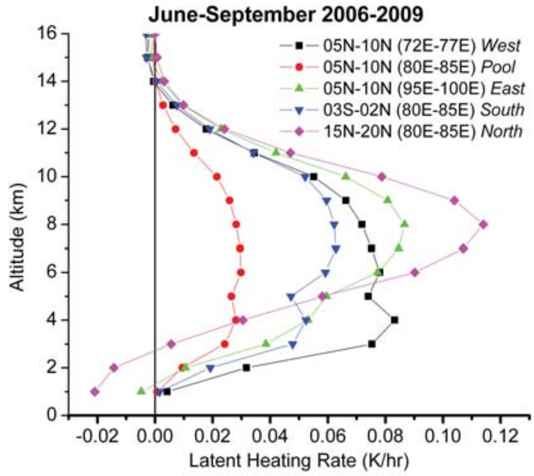

Figure 3: Multi-year (2006-2009) seasonal mean vertical profiles of latent heating rate of the atmosphere (K hr^{-1}) due to precipitating clouds at the centre of the 'pool' and its surroundings during ASM

Three-Dimensional distribution of clouds over the Indian region

Detailed analysis of the vertical distribution of optically thick clouds over the Indian region were carried out based on multi-year (2006-2009) observations using the polar sun-synchronous satellite, CloudSat. Together with the earlier analyses (reported during the previous years) of the long-term mean spatial distribution of total cloud occurrence (NOAA-AVHRR, 1996-2009) and vertical distribution of semi-transparent cirrus (CALIPSO, 2006-2009), this study provides for the first time the 3-dimensional distribution of clouds over the Indian region and its characteristics.

Figure 4 shows the latitude-altitude cross sections of the frequency of occurrence of clouds (F_C, averaged along the longitude bands of 65-75°E (the Arabian Sea sector), 77-87°E (Indian landmass sector), 85-95°E [the Bay of Bengal (BoB) sector] and 95-105°E (the East Indian Ocean sector) during winter (DJF). The ITCZ manifests in it as a zone of intense convective clouds extending between 0.5 to ~ 14 km altitudes. Cloudiness and latitudinal width of this band increases from the Arabian Sea to the East Indian Ocean sector with its centre shifting from ~ 8°S in the Arabian Sea sector to ~ 3°S in the East Indian Ocean. Though the cloudiness in the upper troposphere is largest over the East Indian Ocean, the northward and southward spreading of cloudiness (thick cirrus associated with the outflows) is largest over the western sectors and least over the East Indian Ocean (where the convection is strongest). Figure 5 shows the longitude-altitude cross sections of F_C, averaged along the latitude bands of 15-25°N (descending branch of Hadley cell), 5-10°N (intermediate region between the descending

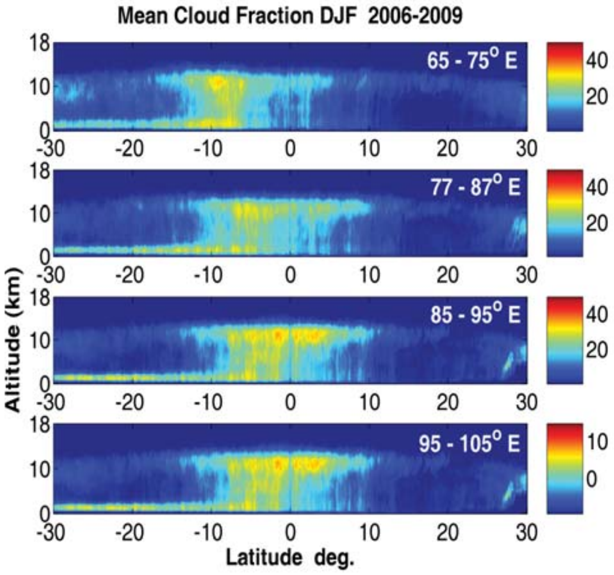

Figure 4: Multi-year (2006-2009) mean latitude-altitude cross sections of F_C, averaged along the longitude bands of 65-75°E (the Arabian Sea sector), 77-87°E (Indian landmass), 85-95°E (the BoB sectoe) and 95-105°E (the East Indian Ocean sector) during winter (DJF)

and ascending branches of Hadley cell), and 10-5°S (ITCZ) during winter. Cloudiness over the descending branch of Hadley cell is very small (< 10% over most of the regions) and is mainly comprised of cirrus clouds. In contrast, cloudiness over most parts of the ITCZ is mainly comprised of low- and high-altitude clouds. The prominence of deep convective clouds in the ITCZ is highest over the East Indian Ocean, which is the ascending limb of Walker circulation.

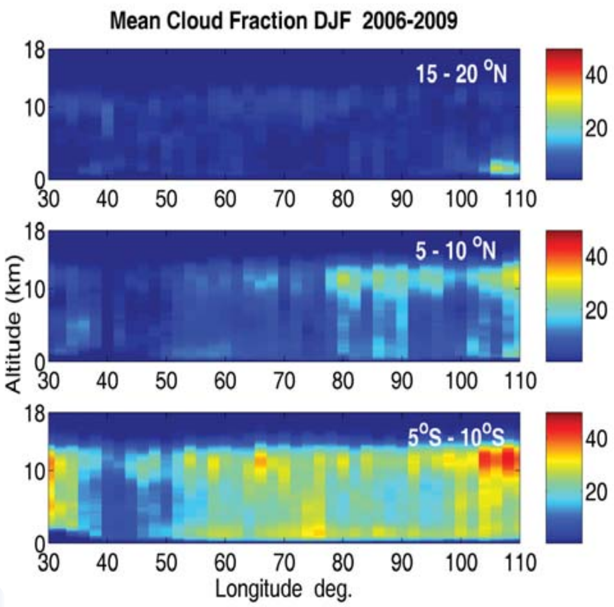

Figure 5: Multi-year (2006-2009) mean longitude-altitude cross sections of F_C, averaged along the latitude bands of 15-25°N (descending branch of Hadley cell), 5-10°N (intermediate region between the descending and ascending branches of Hadley cell), and 10-5°S (ITCZ) during winter

Upper altitude of maximum cloudiness is also highest in this region, indicating deeper penetration of convection. Remarkably, the longitude band of 40-50°E has considerably less cloudiness over the ITCZ and to its north and is associated with the descending limb of Walker circulation.

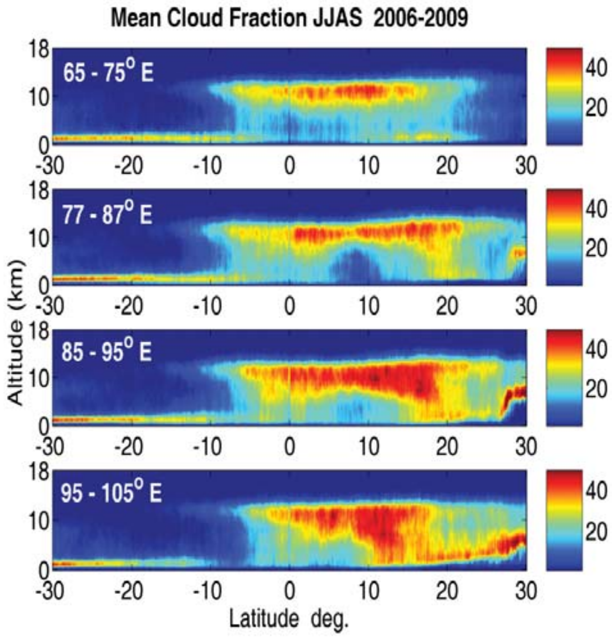

Figure 6: Same as Fig.4, but for the summer monsoon season

Meridional and zonal cross sections of the altitude distribution of F_C averaged during the summer monsoon season, shown in Figs. 6 and 7, respectively, reveal large enhancement in cloudiness and its vertical extent from the Arabian Sea to the BoB sector. Shallow summer monsoon current is clearly manifested in the Arabian Sea sector where cloudiness in the latitude region of 8-20°N shows two distinct bands: one below 4 km and the other above 8 km, with considerably less cloudiness in between. However, cloudiness over a broad latitude band of 5°S-25°N in the Arabian Sea sector is dominated by high altitude clouds which mostly occur between 8-13 km (presumably optically thick cirrus). In contrast, except for the vault-like 'pool of inhibited clouds, the deep convective clouds dominate over the BoB, east Indian Ocean and Indian sectors, especially due north of 10°N. The upper altitude of maximum convection increases from the south to north by about 1.5 km, and the penetration of deep convection is highest over the BoB sector and quite significant over the equatorial trough region just south of the equator. Over the Indian and BoB sectors, a band of weak cloudiness is observed around 25-28°N, which is sandwiched between the regions of intense convection at the southern parts and the Himalayan region.

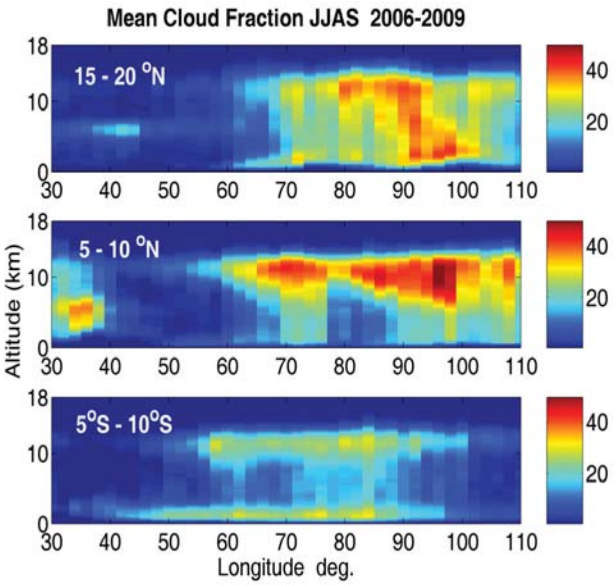

Figure 7: Same as Fig.5, but for the summer monsoon season

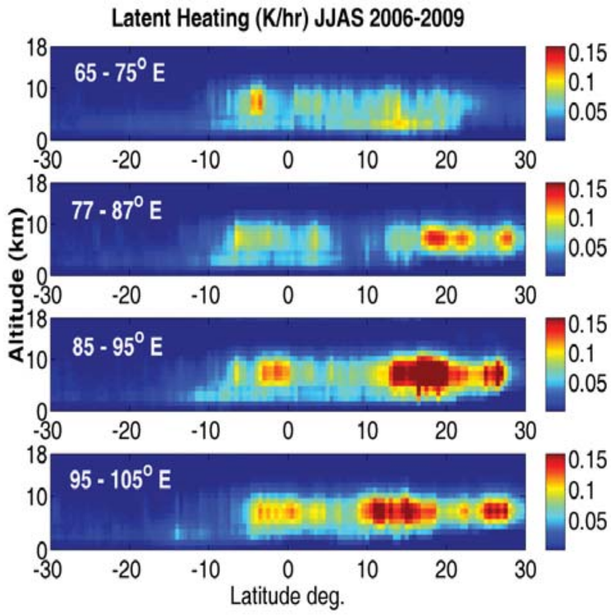

Figure 8: Multi-year (2006 - 2009) mean latitude-altitude cross sections of latent heat rate in the atmosphere (K hr^{-1}) by precipitating clouds, averaged along the longitude bands of 65-75°E (the Arabian Sea sector), 77-87°E (Indian landmass), 85-95°E (the BoB sector) and 95-105°E (the East Indian Ocean sector) during the summer monsoon season

Latent heating of the atmosphere by precipitating clouds

Latent heat released by precipitating clouds play a pivotal role in modulating the atmospheric stability and circulation. Three-dimensional variations of latent heat released into the atmosphere by precipitating clouds are investigated using the TRMM-Precipitating Radar data during 2006-2009. Together with the 3-dimensional distribution of clouds and their radiative impact, these observations provide closure for the changes in atmospheric energetics caused by clouds. Fig.8 shows the mean latitude-altitude cross sections of the latent heating rate (K hr^{-1}) averaged over the Arabian Sea sector, Indian landmass, the BoB sector and East Indian Ocean sector during the summer monsoon season of 2006-2009. Except over the north Arabian Sea, the latent heating maximizes between 5-10 km altitudes. Regionally the latent heating is largest over the BoB sector in the latitude band of 12-20°N, where its seasonal mean value exceeds 0.14 K hr^{-1}. This large latent heating will further enhance atmospheric deep convection, and might be an important factor in making the BoB the most intense deep convective region, globally. Further, the large spatial gradient of atmospheric latent heat, especially in the meridional direction, might feedback positively in driving the meridional circulation over the BoB during the summer monsoon season. Over the Arabian Sea, the latent heat liberated in the atmosphere is mostly in the lower altitudes (< 4 km), which further reinforces the shallow convection over this region during summer monsoon season.

2. TRACE GASES

Trace gases in the atmosphere have key roles to play in climate, atmospheric chemistry and air pollution. With the view to assess their roles in the geosphere-biosphere system, regular measurements of key trace gases namely ozone (O_3), nitrogen oxides (NOx), sulphur dioxide (SO_2) and carbon monoxide (CO)- mostly anthropogenic- are being carried out at SPL. Further to the temporal characteristics of ozone and NOx reported last year, those of CO are examined. In addition to this, the spatial characteristics of these trace gases over Bay of Bengal (BoB) and their seasonal changes were also examined by synthesising the cruise-based measurements conducted under ICARB with satellite data. As a new initiative, modelling studies using photochemical box model has been undertaken and preliminary results brought out.

Carbon monoxide (CO) at Thumba: Diurnal and Seasonal variations

Carbon Monoxide (CO), emitted during incomplete combustion of carbon-containing materials, is a major pollutant in the atmosphere having adverse effects on animals and plants. It is used as a tracer to study the transport of regional pollutants from industrial activities and large-scale biomass burning. CO has an indirect radiative forcing effect by elevating concentrations of methane and tropospheric ozone through chemical reactions with hydroxyl radical (OH). It is

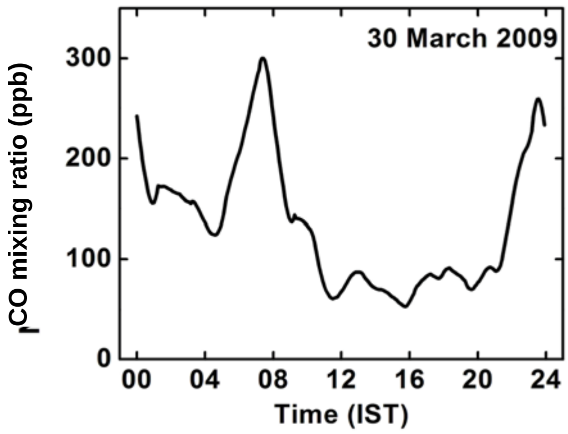

Figure 9: Typical Diurnal variation of CO at Thumba

considered as the single most important sink for OH accounting for about 40% of its loss. In view of the above, regular measurements of near-surface CO was initiated at SPL since February 2009, as part of the AT-CTM project of IGBP.

The typical diurnal variation of the mixing ratio CO (Fig.9) shows a day time low (with values as low as 50 ppb) and night time high (reaching values as high as 300 ppb). A sharp peak, seen in the morning around ~0700 IST is attributed to the fumigation effect. The diurnal pattern is closely modulated by the changes in Sea Breeze/Land Breeze activity and boundary layer dynamics.

The month to month variation of mean concentration of CO, O_3 and NO_x for the period Feb-2009 to Nov-2010 in Fig.10 reveals high CO concentration (around 200-225 ppb) during winter (December, January and February) and low (around 100-125 ppb) during monsoon (June, July, August and September) months. Even the day to day variability is higher during the winter. The variations are closely associated with synoptic airflow patterns. The north easterlies during winter bring in high levels of CO over to this coastal site from inland. On the other hand, during monsoon, the westerlies (from ocean) advect relatively prestine marine airmass. In addition, the shallow boundary layer during winter favours increased confinement of species near the surface. Near-surface NO_2 also shows similar seasonal pattern. On the other hand, surface ozone exhibits high in winter as well as in summer which can be attributed to increased photochemistry.

Tropospheric column O_3, NO_2 and CO over Thumba using satellite data

Tropospheric ozone is estimated from satellite data by subtracting stratospheric O_3 from the total following the 'residual method'. Currently the total ozone data of Ozone Monitoring Instrument (OMI) and stratospheric ozone data of Microwave Limb Sounder (MLS) onboard EOS-AURA provide global coverage in ozone measurements. OMI has a pixel size of 13 x 24 km^2 at nadir and a swath of 2600 km. The monthly averaged tropospheric column ozone (TCO) from MLS is available at 1° x 1.25° (latitude x longitude) resolution (ftp://jwocky.gsfc.nasa.gov/pub/ccd/data_monthly_new). The precision uncertainty for derived gridded ozone is 5 DU (7 ppbv) with a mean offset of 2 DU (OMI/MLS). Total ozone with a resolution of 0.25° x 0.25° is available from the website http://toms. gsfc.nasa.gov/pub/omi/ data/ Level3e/ozone. OMI also gives the tropospheric column NO_2 which is available daily with a resolution of 0.25° x 0.25° (level 3, gridded) from the website (http://avdc.nasa.gov/) and it is underestimated by 15-30%. Satellite-based surface CO obtained from MOPITT is also used in this study. Level-3 MOPITT data of surface CO have been obtained from the website https://wist.echo.nasa.gov/api/ and/or http://eosweb.larc.nasa.gov/.

Figure 11 shows the month-to month variation of mean tropospheric O_3, NO_2 and CO as estimated from

Figure 10: Monthly variation of near-surface O_3, NO_2, CO over Thiruvananthapuram during 2009-2010

Figure 11: Seasonal variation of Tropospheric O_3, NO_2, CO over Thumba

satellite data. All the three species show similar features such as high during winter months (December-January-February) and low during summer monsoon months (July-September).

Relation between Near-Surface, Tropospheric and Total Ozone

Figure 12 gives the monthly variation of tropospheric O_3 and near surface O_3 along with total O_3 from Nov 2007 to Nov 2009. Total ozone increases from the annual minimum in winter to reach the peak in May and remain so till October. This annual variation is the result of the combined effects of photochemistry and vertical transport processes characteristic of tropics.

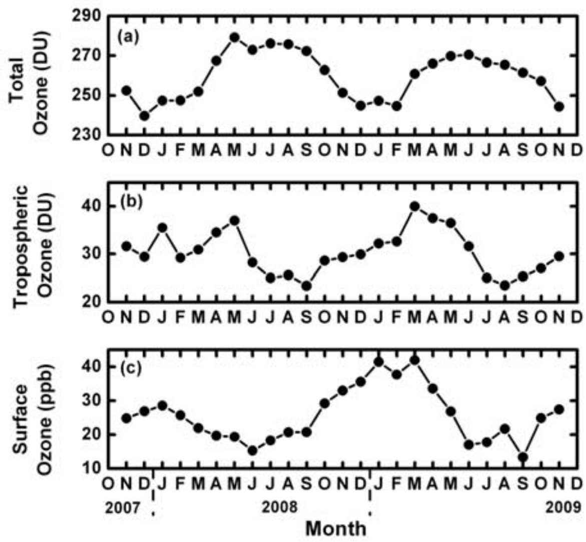

Figure 12: Annual variation of (a) total ozone, (b) tropospheric ozone and (c) surface ozone respectively

On the other hand, tropospheric ozone shows low values during June-September and starts increasing from winter to peak by May. Surface ozone also behaves more or less similar to that of tropospheric ozone, but with the winter peak being more pronounced than May. The strong convections prevailing over tropics during summer and the strong vertical winds in upper troposphere and lower stratosphere (UTLS) region during April to September are partly responsible for the reduction in surface/tropospheric ozone during this period. The lifting of surface ozone would also lead to increase in tropospheric ozone during March to May. Similarly, October till March is the period of weak updrafts or strong downdrafts in the UTLS region and this is the period of overall increase in tropospheric ozone and surface ozone. Fig.13 shows that the percentage contribution of tropospheric ozone to columnar ozone varies in the range 10-15% over a year with the minimum observed during June-September period.

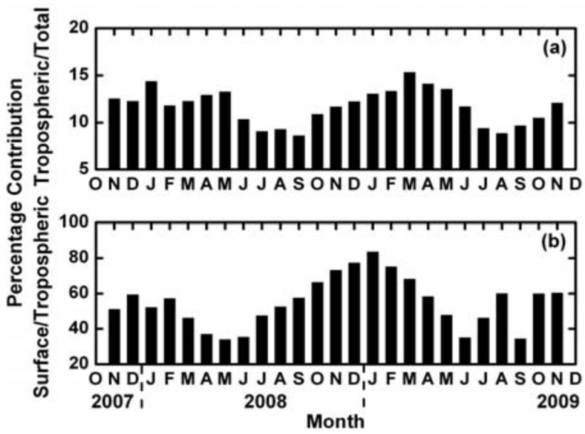

Figure 13: Percentage contribution of tropospheric ozone to total ozone (a) and surface ozone to tropospheric ozone (b)

Seasonal changes in Ozone over BoB: premonsoon and winter

Surrounded by land on three sides and being the region of outflow from IGP, BoB exhibits ample spatial distributions for trace atmospheric species. ICARB campaigns (ICARB and W-ICARB) have provided an opportunity to understand these and the transport pathways. Data collected during the premonsoon period, March 18–April 12, 2006 (ICARB) and during winter period (WICARB) December 27, 2008- January 30 (winter) 2009 were examined in this context. Figs.14a and b show the mean flow patterns during these two seasons. The March-May months represent the transitional period of the synoptic flow with a

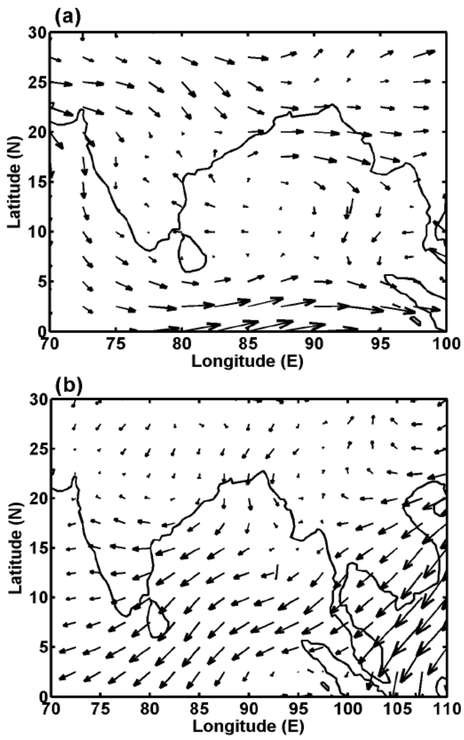

Figure 14: The mean airflow pattern for (a) ICARB and (b) WICARB over the BoB

weak outflow from northern landmass (IGP) to Head BoB and the mixing of airmass from the southern oceanic regions. During winter, the wind was northerly/ northeasterly over the head BoB and easterly/north easterly over the southern regions.

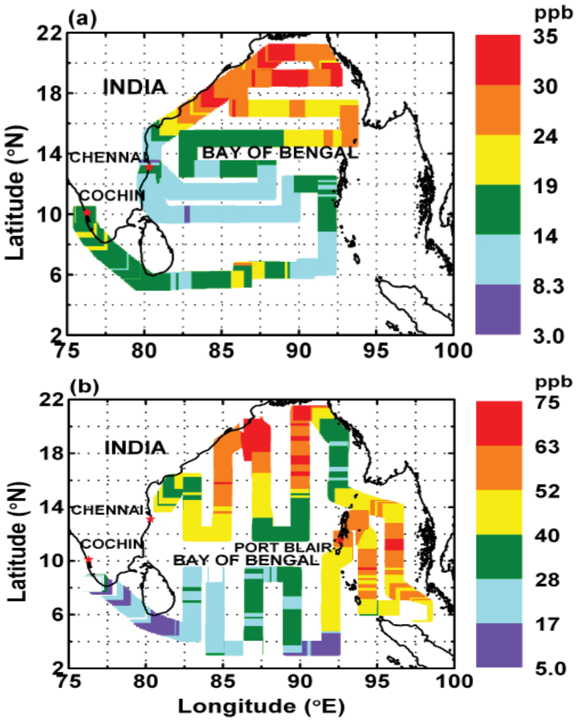

Figure 15: The spatial variation of surface ozone during (a) ICARB and (b) WICARB along the cruise track

Figures 15a and b show the spatial variation of surface ozone along the cruise track as observed during the premonsoon and winter periods, respectively. There is an overall increase in ozone from pre monsoon (27 ± 3 ppb) to winter (61 ± 7). Irrespective of the season, high mixing ratio existed over the head BoB. There is also a wide region of high ozone in the southeast BoB. Over mid-BoB, the mixing ratio was very low being (13 ± 3 ppb) in pre-monsoon and moderate (36 ± 8 ppb) in winter. Coming to the southern part, where the premonsoon values remained about the same, in winter, the values were lowest (24 ± 7 ppb).

During the premonsoon months, the airmass back trajectories (Fig.16a) favour advection from the northwestern and central regions of the Indian subcontinent to the head BoB, while during winter, the trajectories (Fig.16b) passed through eastern part of Indo Gangetic Plains (IGP) and Bangladesh where strong source regions of pollutants exist. The back trajectories reaching southeast BoB (where high ozone and precursors were observed) originated from East Asian region (Fig.16c). These indicate that airmass pathways are different over different parts of BoB and are seasonally varying. The spatial distribution of ozone was also closely associated with available water vapour content and vertical transport in addition to horizontal advection of ozone and/or its precursors.

Seasonal changes in Tropospheric column O_3 and NO_2 over BoB

In Fig.17a and b are shown the tropospheric O_3 and NO_2 respectively over BoB region, for pre-monsoon and in Figs.17c and d, for winter period. While tropospheric ozone reveals higher concentration during the premonsoon/summer as compared to winter (like in Fig.9), the tropospheric NO_2 over BoB showed higher levels close to the coast, spread over the entire central and southern BoB. The presence of high levels of NO_2 could be due to less active photochemistry and the upper air dynamics. Pollution transport over to ocean from near-by landmass is more prominent during winter.

Diurnal variation of ozone over the marine Environment: Role of water vapour

In general, the diurnal variation of ozone over oceans is caused by (1) photochemical production (2) loss by reactions involving OH radical, the concentration factor depends on the availability of water vapour, and (3) transport mechanisms (vertical and horizontal). Over the land, O_3 shows an increase few hours after sunrise reaching peak values before noon and starts

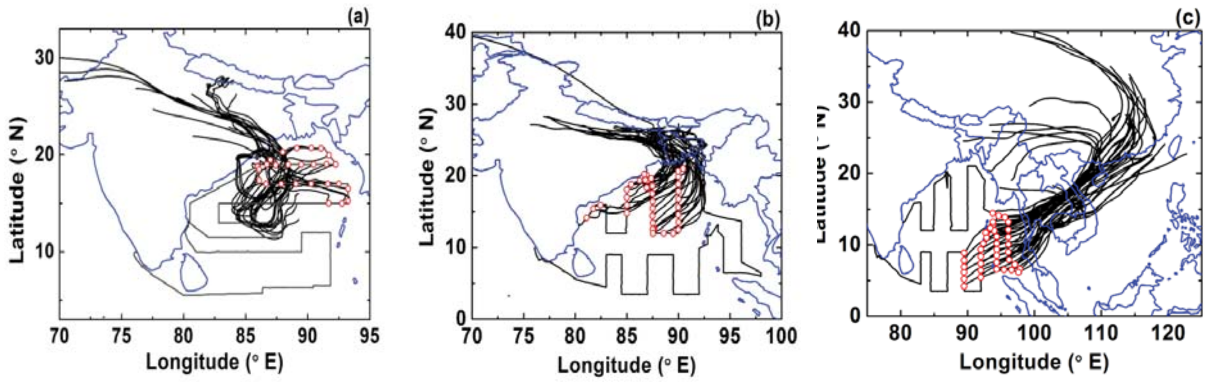

Figure 16: The back trajectories reaching (a) head BoB during ICARB (b) head BoB during WICARB (c) south east BoB during WICARB

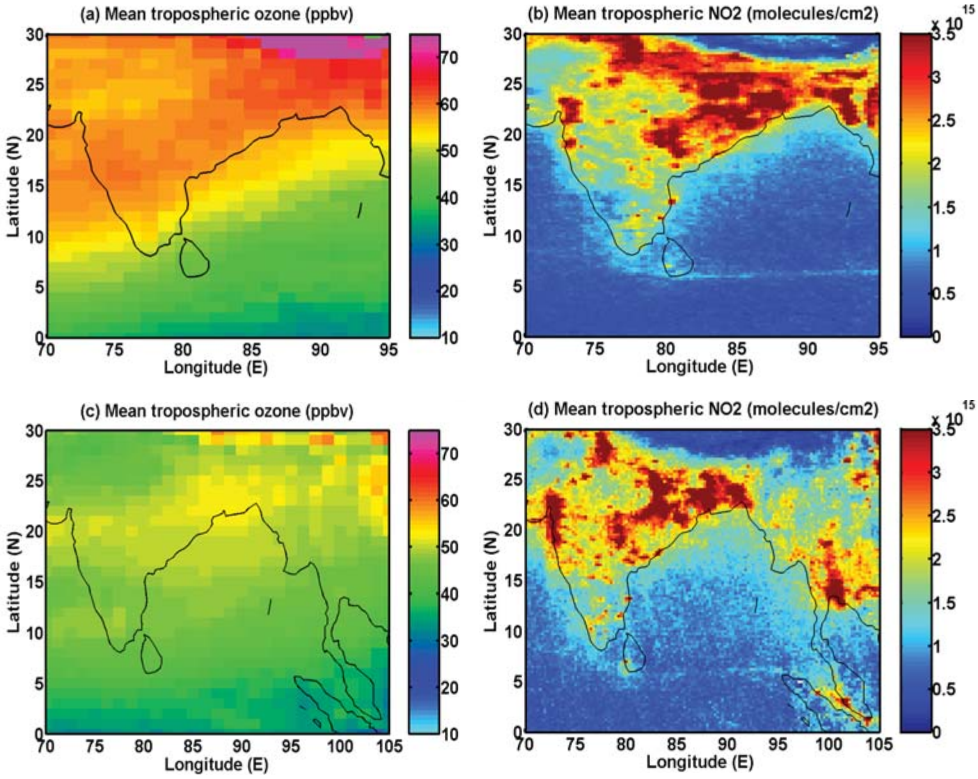

Figure 17: Spatial distribution of (a) tropospheric ozone and (b) tropospheric NO2 during premonsoon (c) tropospheric Ozone (d) tropospheric NO2 during winter

decreasing in the afternoon reaching low values at night governed mostly by photochemistry. But, over the oceanic environments O_3 exhibited two broad types of diurnals (1) noon/afternoon decrease with a nighttime high, and (2) whereas afternoon and nighttime are low. On majority of days, the O_3 mixing ratio showed decrease during noon/afternoon followed by an increase and remaining high till the next day morning hours. No significant increase/decrease in NO_2 is observed associated with changes in O_3. The noontime low can be partly attributed to the vertical mixing and dispersion of O_3 by strong convection. At night, vertical mixing of free tropospheric air with the marine boundary layer lead to the higher O_3 mixing ratio. O_3 destruction by OH radical from water vapour would also be predominant during daytime rather than the photochemical production involving NO_x. It is observed that the noontime decrease in O_3 is always associated with an increase in water vapour. For many days, it was seen that the O_3 mixing ratio that remained high during morning hours decreased during noon/afternoon hours and remained low until the next day morning. On these days also, the afternoon decrease in O_3 was linked with an increase in the water vapour content. Fig.18a-d show typical diurnal variations of O_3 discussed above along with that of water vapour content which indicates an out of phase relation. On these days, there were no indications of active photochemistry as seen from the variation of temperature and NO_2. On the other hand, when the ship was near to the coast, the diurnal pattern of O_3 showed a daytime high and a nighttime low similar to that observed over several urban and inland sites. This increase in O_3 was attributed to the photochemical reactions involving precursors as shown by the positive correlation with temperature. In the tropical atmosphere, moist convective processes form the primary mechanism for the vertical mixing and hence, the equivalent potential temperature (θ_E) is used as a proxy to identify the downdrafts and updrafts. The diurnal variation of θ_E also showed an out of phase relation with O_3 similar to that of water vapour content shown in Fig.18. The evening increase in O_3 is closely

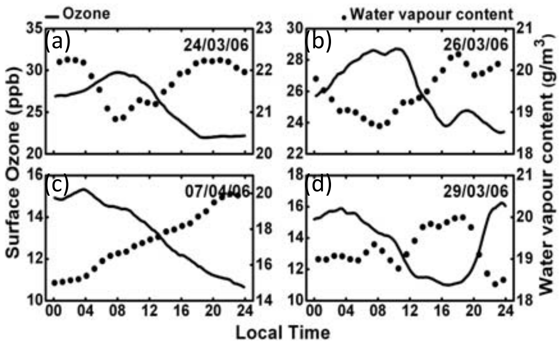

Figure 18: Typical diurnal variations of ozone along with that of water vapour

linked with decrease in θE (about 4-6 K) which continues until the next day morning. The low O_3 mixing ratio observed was associated with high θ_E. In cases where the diurnal variation of O_3 is similar to that of inland sites, θ_E shows a similar pattern indicating that daytime photochemistry dominates over the vertical mixing. This study showed that the water vapour content and equivalent potential temperature played a significant role in governing the diurnal patterns of near-surface O_3 in this marine environment rather than only photochemistry.

Potential Source Contribution Function (PSCF) analysis for CO over BoB

PSCF is the probability function which indicates how potentially a source region contributes to the receptor site. The high values in the spatial distribution of PSCF will pinpoint geographical regions that are likely to produce high concentration values at the receptor site if crossed by a trajectory.

PSCF analysis was carried out to account for the spatial pattern of CO with distinct CO mixing ratio, observed over BoB during WICARB. It was done for three regions namely southeast-BoB where highest CO values were observed, north-BoB with moderate values and for southwest-BoB where lowest CO mixing ratios were observed. 7-day airmass back-trajectories and the measured CO values in these regions formed the base date. Generally, PSCF analysis is done with region representative stationary point measurements. But in this study, since the measurement platform was moving, the analysis was conducted using the satellite measured CO values available on day to day basis for each location. Daily averaged CO mixing ratio for 7days in each region obtained from MOPITT measurements along with 7-day airmass back-trajectories are used in the calculation of PSCF. Fig.19a-c show the contribution from different source regions to north BoB, Southeast BoB and southwest BoB respectively. The contribution to north-BoB is very high from nearby landmass region and from Bangladesh region as seen from Fig.19a. On the other hand, source regions for high CO over southeast-BoB are distributed along the trajectory path (Fig.19) and there is a significant contribution from east-Asian region. PSCF distribution over south-west BoB shows a different picture with the significant contribution from the surrounding grids. Even though, north-BoB and southeast BoB contributed to this region (see the high PSCF grids), the CO mixing ratios are relatively low probably due to the long marine path encountered.

Chemical box model simulation: New Initiative

A chemical box (zero-dimensional) model, NCAR Master Mechanism (NCAR-MM), developed at National Center for Atmospheric Research, was used to study the diurnal variation of near-surface ozone. The model simulates chemical evolution of an air parcel taking into account the detailed gas phase chemistry consisting of ~ 5000 reactions among ~ 2000 species. The estimation of photolysis rate coefficients is done using the Tropospheric Ultraviolet Visible (TUV) radiative transfer model with a 4-stream discrete ordinate radiative transfer solver. Model simulations were done for a typical case of January 18, 2010.

The initial/background concentrations of CH_4, CH_2O, isoprene, C_3H_6 and i-butane were taken as 1.7 ppm, 5, 5, 5 and 4 ppb respectively which represent the typical coastal conditions. While the background values of O_3, NO, NO_2, CO were the nighttime averaged values i.e., 4, 0.3, 4, 150 ppb, the initial values of that were observed values at 0 hours (i.e, 10 ppb for O_3). The crucial diurnal constraints used in the simulation were the observed temperature, humidity, NO, NO_2, and CO. The ABL height taken as 0.2 during night and 2.1 km during day based on the lidar- based measurements. The observed NO_2 diurnal values were used in the simulation giving an offset of 0.98 ppb taking into account the instrumental errors in measurement.

Figure 20 shows the model simulated evolution of O_3 along with observed variation for January 18. The

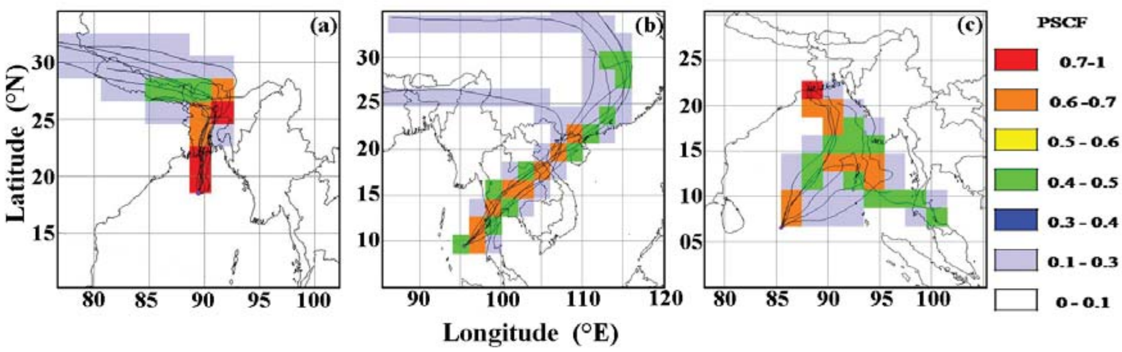

Figure 19: PSCF analysis for (a) north-BoB, (b) southeast-BoB and (c) southwest-BoB. The lines represent the back-trajectories

Figure 20: The observed and model simulated near-surface ozone for 18 January 2010

model has reproduced the main feature very well though daytime values are slightly higher. It is worth mentioning that model does not account for transport and dynamics which play important role in controlling observed variations. Also no additional emissions, no dilution and no heterogeneous processes assumed in the present model simulation. Figures 21a-c show the diurnal patterns simulated using the model (with 2218 reactions) along with observation for three typical cases discussed in section 5. In Fig.21a is also shown the diurnal variation of NO_2 used simulation. While

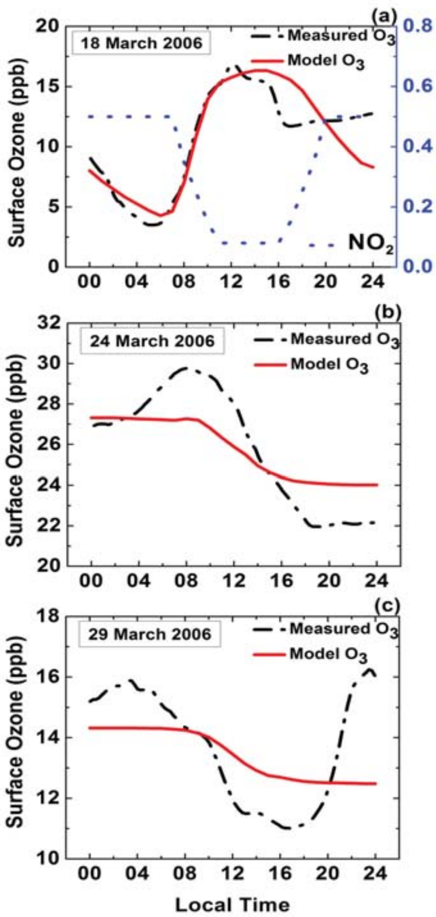

Figure 21: The observed and model simulated ozone for different diurnal patterns over BoB

NO_2 and NO mixing ratios of 0.2ppb and 0.04ppb, respectively were used for initialization on March 24 (airmass was from IGP), 0.02 and 0.01, respectively were used on March 29 (oceanic airmass). In general, the model could reproduce the broad features of the pattern with minor deviations in the mixing ratio levels. In the pattern having morning high and afternoon decrease, the maximum deviation is ~ 2-3 ppb. Figs 21b and c shows that the destruction of ozone occurs during noon/afternoon in the low NO_x environment. However, the evening increase observed on March 29 (Fig.21c) was not reproduced. This can be because the increase is attributed to the free tropospheric transport. It is to be noted that the diurnal amplitudes are also low in these cases (~ 5-8 ppb). Moreover, since the measurements are on a moving platform and not from a fixed location, it represents a region along the track. Hence, model may not be fully capable of reproducing the variations.

ISRO's Environmental Monitoring Satellite Programme (New Activity)

Environmental Monitoring Satellites are planned for the monitoring of green house gases, aerosols and other atmospheric trace gases. Three satellites are planned with this objective. The first mission will be an experimental mission with aim to get information primarily on aerosols and CO_2 gas concentration, the second mission will acquire information on other trace gases through enhanced instrumentation and the third will be a follow on and if necessary an improved version to the second. A document was submitted on the detailed scientific and technical requirements for the measurement of green house gases, other pollutant gases like CO, NO_2, SO_2, and aerosols. As an initial step, it has been decided to put an experimental mission in polar sun-synchronous orbit for the measurements of aerosols and CO_2.

3. MICROWAVE REMOTE SENSING

Measurement of Atmospheric water vapour

Estimation of Columnar water vapour (PWV) from GPS Data

The accuracy of columnar water vapour (PWV) retrievals from GPS measurements is strongly influenced by changes (diurnal/season) in atmosphere temperature. In this context the effect of temperature on PWV estimation over Trivandrum was investigated by comparing the average PWV estimated (i) using the simple linear relation between wet zenith delay and PWV and (ii) the model that accounts for

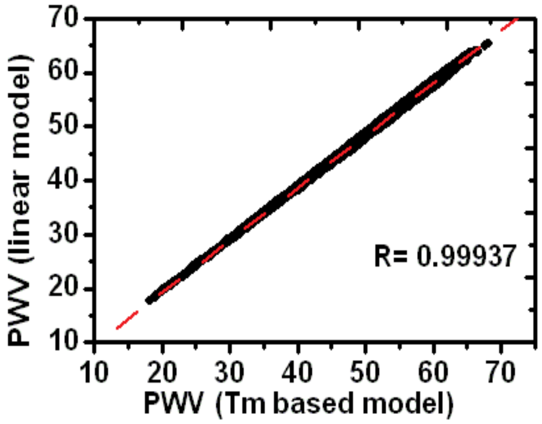

Figure 22: Scatter plot of PWV estimated using the linear model and that from the Tm based model for the period May 2010 to December 2010

temperature through the parameter -effective mean temperature- which accounts for the vertical temperature distribution (Fig.22). While both these estimates agreed well, the PWV from linear relation had a small offset of < ~ 3 mm when the atmosphere water vapour content > 50 mm, indicating that for a tropical station like Trivandrum, simple linear relation which does not need the atmospheric temperature distribution can be used for PWV estimation, for low to moderate PWV.

Water Vapour from Microwave Radiometer Profiler, GPS receiver and Radiosonde: Comparison

Precipitable Water vapour (PWV) has been estimated using the hyperspectral Microwave Radiometer Profiler (MRP) of SPL and the collocated Triple frequency GPS receiver, operational since last year. An inter-comparison between the PWV values (half-hourly averaged) from the GPS and radiometer observations are carried out. As an independent data source in the comparison, the PWV measurement from regular radiosonde ascents of IMD Trivandrum at 0000UTC and 1200 UTC were also included. The PWV derived from GPS and MRP revealed a good agreement, in terms of their temporal variations, but with a constant negative bias of about ~ 4 mm.

Regression analysis between the PWV from MRP versus PWV from GPS (Fig.23a) yielded good agreement with a correlation coefficient of 0.988 with a bias of -4.4 mm, indicating constant underestimation of PWV from GPS with respect to MRP measurements. Regression analysis between the MRP and RS (Fig.23b) was a bit weaker with a correlation coefficient of 0.85 which could be arising partly from the spatial separation (MRP being at a coast and radiosonde at least 6 km inland) and partly due to the further drifting of RS balloon due to wind and to the separation between the MRP and RS sites. The good agreement between

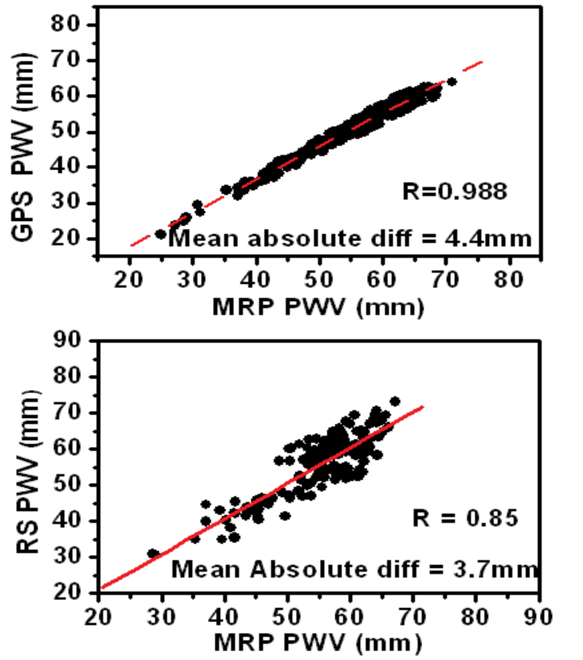

Figure 23: Scatter plot of PWV estimated from (a) MRP and GPS; (b) MRP and RS for the period May to December 2010

the MRP and GPS measured PWV values during the monsoon period indicates the potential of microwave radiometric measurements even during the tropical torrential rain conditions.

Temporal Variation of PWV over Trivandrum

The information about the atmospheric water vapour variation is an important indicator for the onset of monsoon in Kerala. Temporal variation of PWV over Trivandrum for one year period from May 2010 to April 2011, obtained from the MRP observation is shown in Fig.24. The sudden increase in amount of PWV observed in the second half of May (Day No- ~135-150) was associated with wide spread and pro-

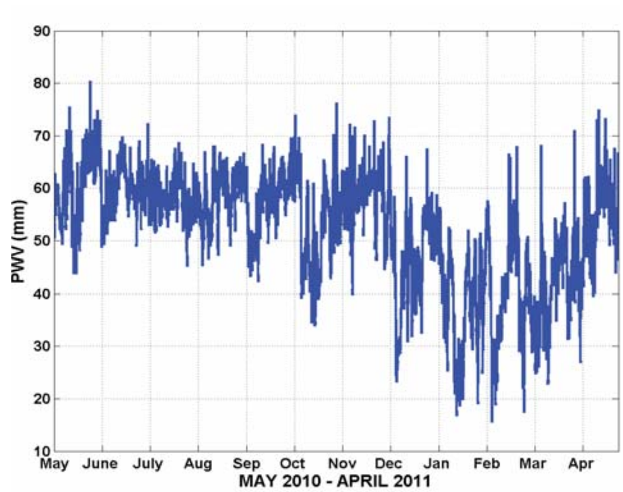

Figure 24: Temporal variation of integrated water vapour content over Trivandrum

longed premonsoon rains at Kerala coast due to the appearance of strong depression in the Arabian Sea. During this period, PWV increased very high above 70 mm. The sudden fall in water vapour by the end of May and the subsequent gradual building up as a part of the onset of monsoon, in the first week of June are well depicted in the figure. The break periods during August and October are characterised with low water vapour below 50 mm. During the active monsoon period the water vapour loading was above 60 mm over Trivandrum. The active period of North-East monsoon in 2010 (2nd week to end of November) is also characterized by high PWV. During the study period, lowest values (< 20 mm) of water vapour is observed in January and February and highest (~ 70 mm) in May.

Diurnal variation of PWV

The diurnal variation of integrated water vapour for one year period of 2010 is analysed on monthly mean basis (Fig.25). Significant diurnal variation is observed only during January to May (when continental air mass prevails) with a peak at ~ 14 UTC (1930 IST). PWV distribution in March-May is typical for tropical atmosphere in summer period with the high water vapour loading that lead to regular convective summer thunder shower in the evening. During the monsoon period, mean value of the total water vapour content was about 52 mm, while in the winter it was about 42 mm.

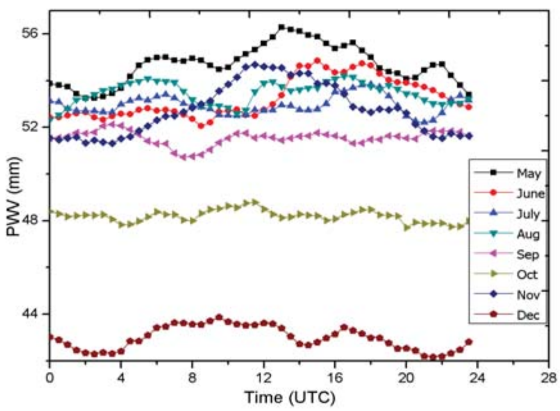

Figure 25: Diurnal distribution of water vapour over Trivandrum on monthly mean basis

3.2. LAND EMISSIVITY

Microwave land surface emissivity: Seasonal & Interannual variability

A-priory information on land surface emissivity is essential for using the satellite microwave radiometry observations for atmospheric studies over the continental region. As a part of the on going studies on the land surface emissivity of the Indian subcontinent in microwave region, the seasonal and inter annual variation of microwave emissivity for different land surface classes are examined quantitatively for a two year period, 2007 and 2008 at 19, 37 and 85GHz using SSM/I data. Forests (evergreen tropical forest, and mixed forest in the valley of Himalaya) and the deserts, (Thar & Taklamakan), are the regions having large spatial and temporal near homogeneity. Monthly mean emissivities of these two classes (Fig. 26a-c at 19, 36 and 85 GHz, respectively) shows very small seasonal and interannual variation at 19 and 36 GHz, significant changes occur at 85GHz. The forest regions have higher emissivity (of annual mean ~ 0.97221 and 0.943 respectively for evergreen forest and the mixed forest, than that of desert regions, ~ 0.864 and 0.858, respectively, for Thar and Taklamakan deserts). However, at 85 GHz, the mixed forest

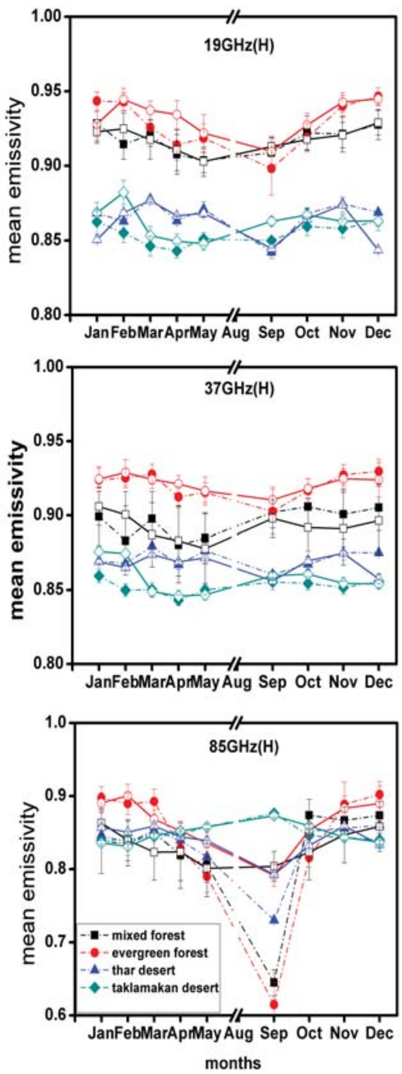

Figure 26 (a-c): Seasonal and interannual variation of emissivity of Desert and Forest at 19, 37 and 85 GHz, respectively (doted line with filled marks indicates 2007 & continuous line indicates 2008)

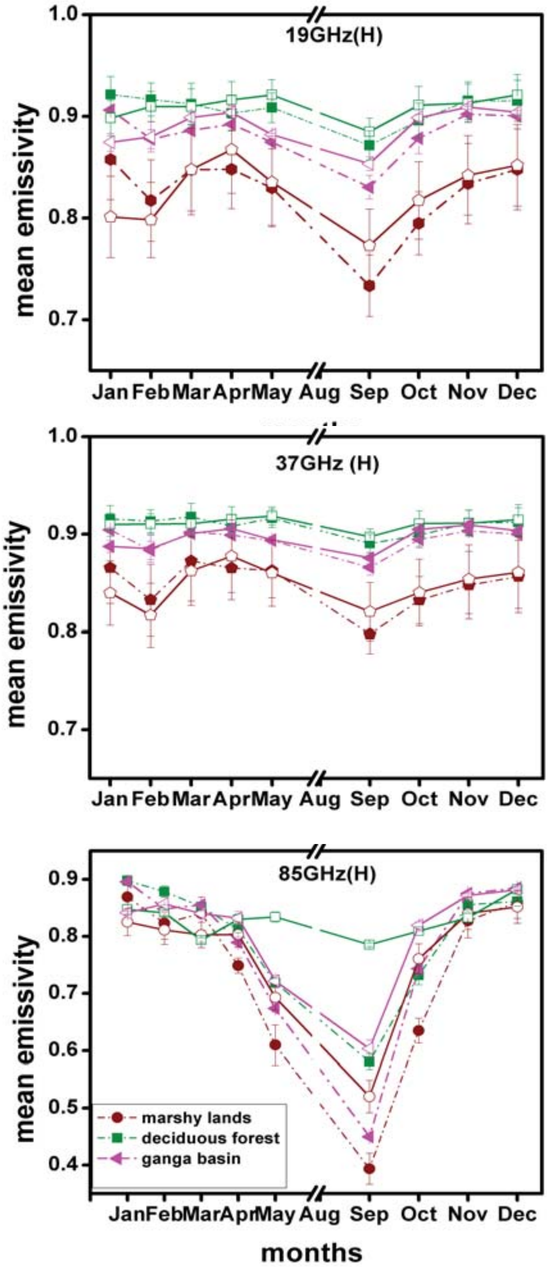

Figure 27 (a-c): Seasonal and interannual variation of emissivity of Ganga basin, deciduous forest, marsh land at 19, 37 and 85 GHz, respectively. (doted line with filled marks indicates 2007 & continuous line indicates 2008)

and Thar desert show significant decrease in emissivity during monsoon

The emissivity variations of other land surface classes, like marsh land, cultivated land in Ganga basin, and arid region with dry deciduous forest, have significant seasonal changes in surface properties at 19, 36 and 85 GHz frequencies (Fig.27a-c, respectively). The large standard deviations (vertical lines) indicate significant day to day variation. The most significant seasonal changes observed in September and October, with a reduction in emissivity due to the enhancement of land wetness. The larger reduction in emissivity in the year 2007 (Fig.27a & 27b) is attributed to the multiple concurrent floods that affected India, Nepal, Bhutan, Pakistan and Bangladesh during July-August. Flooding in Pakistan began with the landfall of Cyclone 03B. The plight of the traditional flood plains of the Ganges-Brahmaputra-Meghna river deltas and their tributaries were prominent.

New Initiative: Vertical profiling of soil temperature at Thumba

The diurnal evolution of soil moisture and temperature are the important parameters for boundary layer, land-atmosphere interaction and radiation studies. A new experimental study has been initiated to measure the vertical profiles of the soil parameters at Thumba by installing soil temperature (platinum resistance) and moisture at varying depths. Fig.28 shows the time series of diurnal evolution of temperature at different depths in a sandy soil medium. The soil temperature shows clear diurnal variation at all the depths with decreasing amplitude and inversion in temperature during cooling down period of evening to late night. The effect of clouds and rain days (eg: Dec 29.) and the summer showers (eg: Dec 31) can significantly modify the soil temperature in the surface upto ~3 cm. The heavy thunder shower on Dec 31 evening after

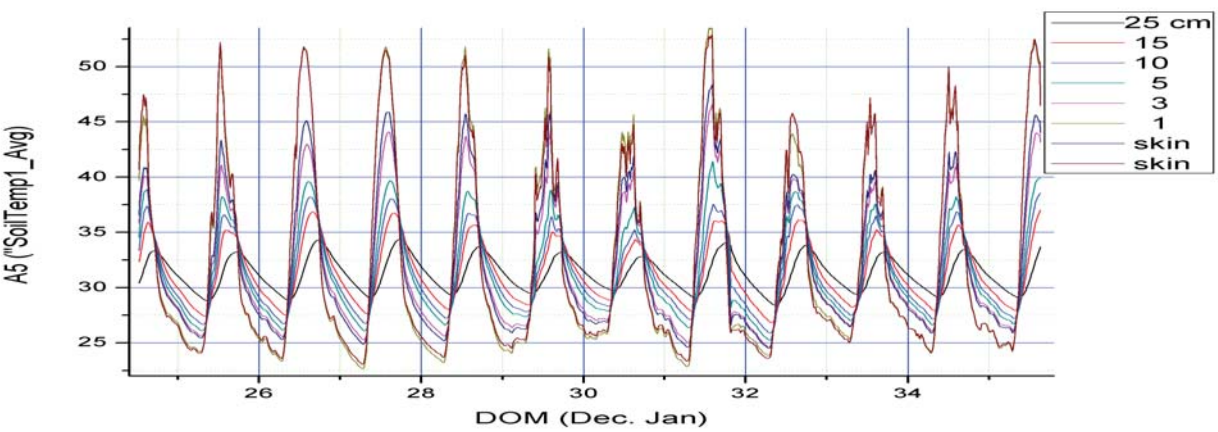

Figure 28: Diurnal evolution of soil temperature at Thumba

the bright sunny day caused a fall in soil temperature again and gradual increase in soil temperature during the subsequent days are seen in figure.

4. RADIATION

Limb darkening of solar disc observed during the annular solar eclipse

Spectral variation of the direct solar spectral irradiance at the Earth's surface at ~ 13:05 IST during the eclipse (15th January) and the control day (16th January 2010) are shown in Fig.29. Timing of this observation is just before the second contact of the eclipse. Bottom panel of Fig.29 shows the percentage decrease in spectral irradiance at ~ 13:05 IST on the eclipse day with reference to the control day. Strikingly, the reduction of solar spectral irradiance during the eclipse event has a significant spectral dependence, with the percentage reduction in solar spectral irradiance decreasing from ~ 91% at 350 nm to ~ 84% at the shortwave IR band. However, the geometrical masking of a uniform solar disk is expected to produce a uniform spectral variation. The observed spectral dependence of the reduction in solar irradiance during the eclipse is associated with the limb darkening effect and can be explained as follows: During the annular eclipse period, the radiation reaching the Earth is from the edges of the solar disk while it is from the complete disc during normal times. In Fig.29, the relative variation in spectral irradiance is obtained by comparing the spectral irradiance obtained from edges of the disc (annular eclipse) with that obtained from the full

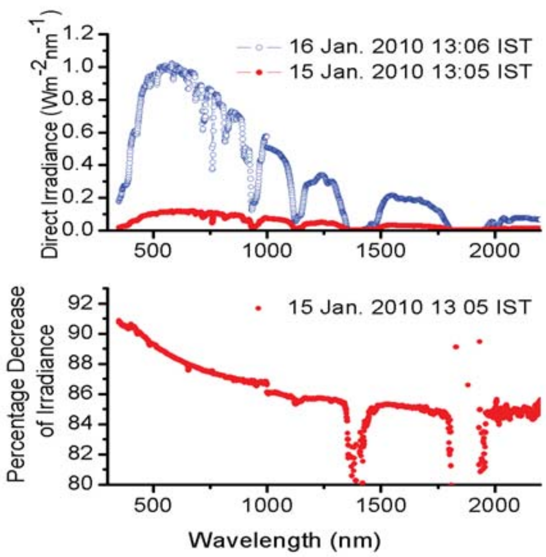

Figure 29: Ground reaching direct solar irradiance spectra just before the second contact of the annular eclipse of 15 January 2010 and its comparison with that on 16 January (top panel). Percentage reduction of direct irradiance on the eclipse day is given in the bottom panel

disc during a control day. Note that the radiation observed at Earth from the centre of the solar disc passes through a relatively shorter optical path within the Sun, compared to that from the edge of the disk. Thus, the probability that the irradiance from a slightly interior region of the photosphere would be coming out of the solar disk is larger at the centre compared to the edges. If the photosphere of the Sun exhibit an altitude variation in temperature with the interior having larger temperature (which is actually the case), the irradiance emanating from the disk will show a spectral variation with the spectra shifting to the shorter wavelength band in the centre compared to the edges of the disk. Thus, a comparison of the spectral irradiance from the edges of the disk (annular solar eclipse) will show larger reduction at shorter wavelengths when compared with the irradiance from the total solar disk. This finding is important from the perspective of atmospheric remote sensing through scanning the solar disk (e.g., solar occultation) and, to our knowledge, is the first ever estimate of the actual spectral dependence in the variation of solar irradiance from the solar disk observed from a ground-based system.

5. AEROSOLS

Seasonal and interannual variations of vertical distribution of aerosols over Trivandrum

In continuation of the observations and analysis of the vertical distribution of aerosol properties using Micropulse Lidar (MPL) reported in the previous years, the seasonal and interannual variations of the mean backscatter coefficient (β_a) and volume depolarization ratio (VDR) at different altitudes over Trivandrum are extended to the period of 2008-2010, and are depicted in Fig.30. In general, β_a in the lower troposphere is least during the September-October period and the largest during the pre-monsoon season. In contrast, the value of β_a in the middle troposphere is substantially small during September-February compared to that in March-May and July-August. The annual variation is highly prominent in VDR which shows that the non-sphericity of aerosols peaks during the pre-monsoon and summer monsoon seasons in the altitude region of 1-5 km. The annual variation of VDR below 1 km altitude is less pronounced and very low values of VDR occur over the entire troposphere during the winter period. Annual cycle of the monthly mean values of integrated backscatter coefficient (IBC) and VDR at different altitude slabs of thickness 1 km shows a peak-to-trough ratio varying in the range of 5-10 in the 2-5 km altitude region. Phase of the annual cycle is remarkably consistent throughout the observation

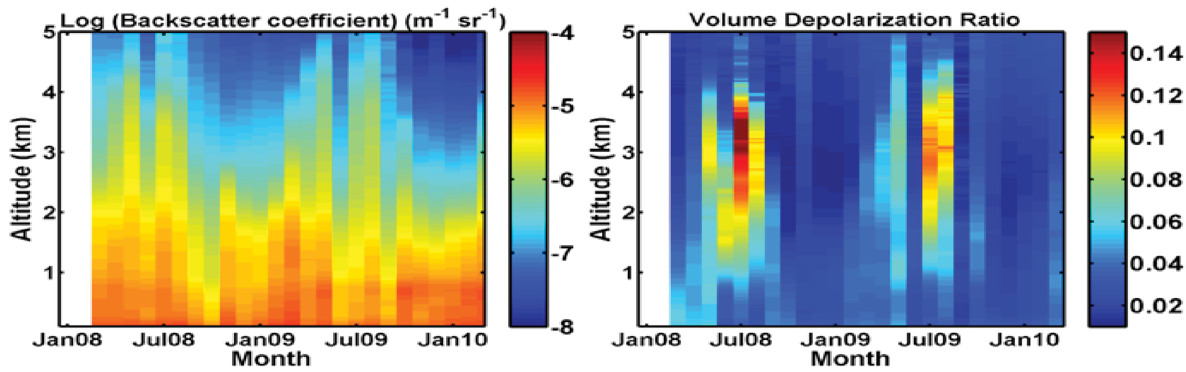

Figure 30: Altitude-time cross sections of the monthly mean values of log (β_a) and VDR during 2008-2010

period. In the altitude region below 2 km, the peak-to-trough ratio of the annual variation of IBC varies in the range of 2-4, while its phase varies by ~ 1 month during the above observation period. Though significant inter-annual variations occur in the annual cycle of IBC below 2 km, the annual cycle of VDR is highly systematic and repeats with comparable amplitudes. Peak values of VDR are observed in the 0-1 and 1-2 km altitude bands during the pre-monsoon and summer monsoon seasons respectively.

Comparison of MPL observations with CALIPSO data

The spaceborne lidar, CALIPSO, provides a unique opportunity to investigate the altitude structure of aerosols (backscatter coefficient and depolarization) on a global scale. We have compared the altitude profiles of β_a and VDR obtained from CALIPSO with those obtained from SPL-MPL, though this task is hindered by the highly infrequent availability of collocated satellite data. This study is based on CALIPSO data on 14 January 2009 (at 13:30 IST) over a region very close to Trivandrum within the grid 8.25-8.61°N in latitude and 76.65-76.73°E in longitude. The MPL data averaged for 40 minutes (centered at 13:30 IST) is inverted to derive the altitude profiles of β_a and VDR. Fig.31a shows the altitude profile of β_a obtained from these two measurements and Fig.31b shows the same for VDR. The altitude resolution of MPL is 30 m, while that of CALIPSO is 120 m. The backscatter coefficient profiles derived from MPL and CALIPSO are in good agreement in the lower atmosphere between 1-2 km, up to which the aerosol amount is significant. The decrease in backscatter coefficient shown by CALIPSO is almost reproduced in the MPL-derived β_a as well. However, the kink at ~ 2.5 km observed in CALIPSO profile is not observed in the MPL profile. Below 1 km, the profiles start deviating with decrease in altitude, which is significant below 0.5 km. These differences could be due to the fairly large spatial averaging across the latitude for estimating β_a from CALIPSO as well as the inherent variations in mixing height. Backscatter coefficient values were not available above 3 km from CALIPSO due to the large decrease in the aerosol concentration and hence the SNR. The altitude profile of VDR estimated from CALIPSO and MPL also show good agreement within the respective uncertainty limits. Two small peaks, one near the surface and another around 3 km are reproduced in both.

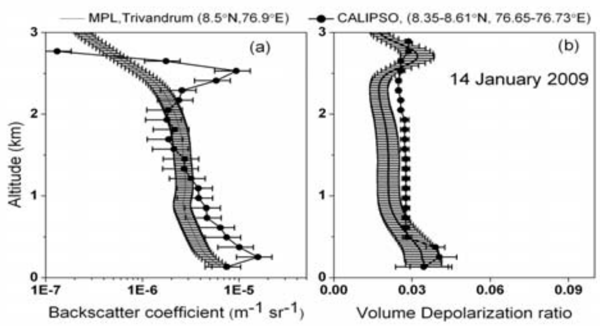

Figure 31: Comparison of the altitude profiles of (a) backscatter coefficient and (b) VDR estimated from MPL at Trivandrum and that obtained from CALIPSO over the region close to Trivandrum on 14 January 2009. The horizontal bars represent the respective standard errors

Integrated picture of the altitude distribution of aerosols over the Indian region and surrounding oceans derived from CALIPSO

The seasonal mean spatial distribution of aerosols over the Arabian Sea, BoB, Indian subcontinent and the Indian Ocean are derived from the CALIPSO observations of β_a and VDR during 2006-2009. Importance of such a study stems from the large uncertainties in the satellite derived AOD over continental regions and the insensitivity of CALIPSO-derived ba and VDR to the surface reflectance. Fig.32 shows the latitude variations of CALIPSO-derived integrated aerosol backscatter coefficient (IAB) in the altitude range of 0-6 km over three longitude sectors viz. the

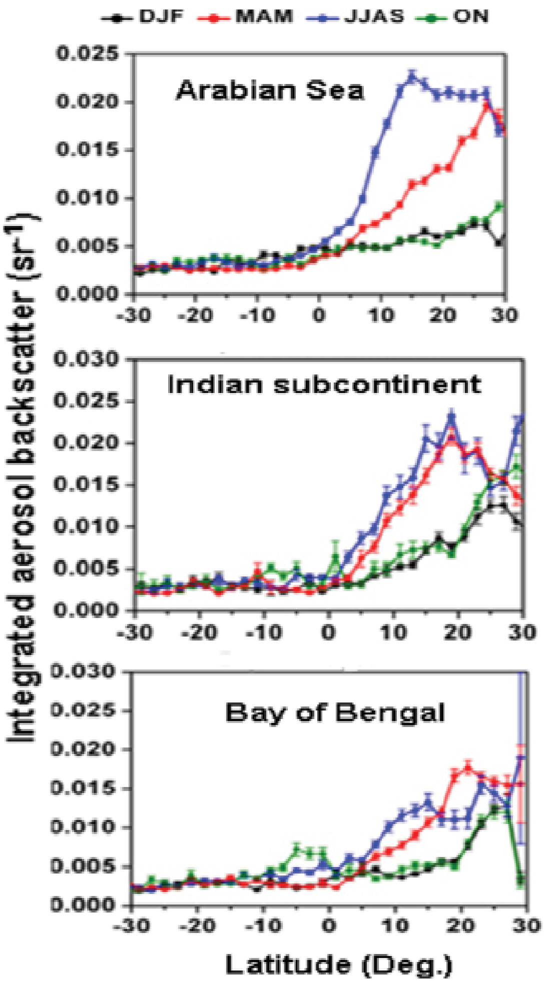

Figure 32: Latitude variations of the CALIPSO-derived integrated aerosol backscatter (IAB) averaged over the Arabian Sea sector (45-75°E), the Indian sector (75-85°E) and the BoB sector (85-100°E) during winter, pre-monsoon, summer monsoon, and post-monsoon seasons

Arabian Sea sector (45-75°E), the Indian sector (75-85°E) and the Bay of Bengal sector (85-100°E) during the winter, pre-monsoon, summer monsoon, and post-monsoon seasons. This is an indicator of the total aerosol loading in the atmosphere. Latitude variations of IAB are largest over the Arabian Sea sector between 0-15°N where IAB varies by a factor of 4. In contrast, the latitude variation of IAB over the Arabian Sea is a minimum during the winter and post-monsoon seasons when the increase is by a factor of ~ 2 from 10°S to 10°N. The latitude variation of IAB over the Bay of Bengal sector also is large during the summer monsoon and pre-monsoon seasons compared to winter and post-monsoon. However, the latitude variations of IAB over the land (north of 15°N) in the BoB longitude sector differ significantly and are more pronounced at the north of ~ 26°N during the pre-monsoon and summer monsoon seasons. The latitude variation at north of 20°N strongly depends on the geographical region as well as the season. Over the Arabian Sea, this gradient is highest during the pre-monsoon and summer monsoon period. Fig.33 shows the longitude variations of IAB averaged over the latitude band of 10-25°N during the four different seasons. On average, IAB decreases from the Arabian region to the central Arabian Sea before showing another significant increase over the east Arabian Sea coast between 70 to 77°E. As expected, the value of IAB is largest and its spatial variation is least over the Arabian Sea during summer monsoon season. During all seasons, the mean values of IAB consistently decrease from about 78 to 98°E.

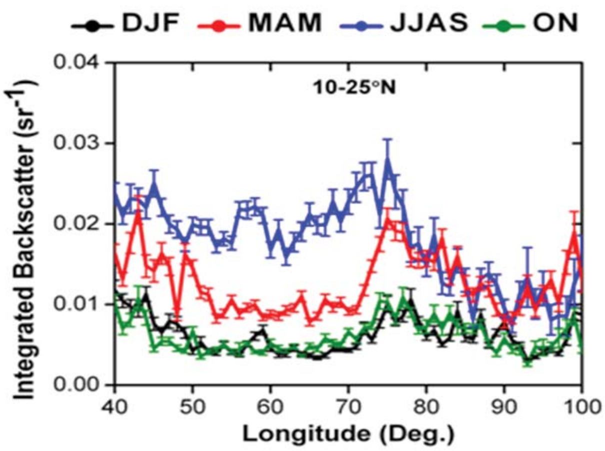

Figure 33: Longitude variations of the CALIPSO-derived IAB averaged in the latitude band of 10-25°N during the winter, pre-monsoon, summer monsoon, and post-monsoon seasons

Studies on organic aerosols - new initiative

Chemically, aerosols can be organic or inorganic in nature. Significant efforts have been taken to quantify the inorganic species. Chemical speciation of carbonaceous aerosols is important in quantifying OC/BC ratios and the aerosol SSA. Such studies are scarce over Indian region. Based on the studies conducted over Indian region it is estimated that organic aerosols contribute > 30% of the total aerosol mass load. In view of the importance of the information over the Indian region, a collaborative research work is undertaken with the Institute of Low Temperature Science, Hokkaido University, Japan. One scientist from SPL is currently working under JSPS (Japan Society of Promotion of Science) fellowship, on the analysis of organic species in aerosol samples from Nainital (a region expected to be rich in organic aerosols) to get expertise in this technique.

Collaborative programme with CUSAT

As part of the DST approved project titled 'an evaluation of public health impact of ambient air pollution in Cochin', a collaborative programme is going on with Department of Atmospheric Sciences, CUSAT. Under this project a High Volume Sampler is operated at selected locations in and around Cochin, a developing urban industrial centre. This work is expected to provide a basic framework for calculating the benefits of policy-related changes in air quality.

Aerosol sampling was carried out at four different locations which include coastal commercial/polluted environment, rural, commercial and highly polluted industrial areas. The mass concentration of aerosols at these four locations were examined. Large increase in mass loading were observed from rural site to commercial to the highly polluted site (~ 164 to ~ 496 µg m^{-3}) and all these values are significantly higher than the typical values for Trivandrum (mean ~ 55 µg m^{-3}). Studies on chemical composition are in progress.

6. FUTURE PROPOSAL FOR PLANETARY MISSION

With a view to participating in ISRO's future planetary mission in the area relevant to AACCR, a few future proposals have been made to explore the Martian environment. These includes

(1) Microwave Sounding of Martian Atmosphere and Terrain (MISMAT)

(2) LIDAR for the observation of Martian dust and clouds

These experiments, though could not be ready for 2013 Mars mission, the development work on these would be taken up with a view to realising the model in the coming year so that the payload work would be realised for the possible mission in 2016 & 2018 with higher payload constitution.

PUBLICATIONS IN REFEREED JOURNAL

1. Mishra, M. K., K. Rajeev, B.V. Thampi, K. Parameswaran, A.K.M. Nair, Lidar observations of the dust layer in the lower troposphere over the southwest coast of Peninsular India during the Asian Summer Monsoon, J. Atmos. Sol. Terr. Phys., 72, 1251–1259, 2010.

2. Girach Imran Asatar and Prabha R Nair, Spatial distribution of near-surface CO over Bay of Bengal during winter: role of transport, J. Atmos. Sol. Terr. Phys., 72 (2010) 1241–1250, doi:10.1016/j.jastp.2010.07.025, 2010

3. Liji Mary David and Prabha R. Nair, Diurnal and seasonal variability of surface ozone and NOx at a tropical coastal site: Association with mesoscale and synoptic meteorological conditions, J. Geophys. Res., doi:10.1029/2010JD015076, 2011

4. Susan K George, Prabha R Nair, K. Parameswaran and Salu Jacob, Wintertime chemical composition of aerosols at a rural location in the Indo-GangeticPlains, J. Atmos. Sol. Terr. Phys., doi:10.1016/j.jastp.2011.04.005, 2011

5. Prabha R Nair, Liji Mary David, Girach Imran Asatar and Susan George K, Ozone In The Marine Boundary Layer Of Bay Of Bengal During Post-Winter Period: Spatial Pattern And Role Of Meteorology, Atmos. Environment, doi:10.1016/j.atmosenv.2011.05.040, 2011

6. Meenu, S., K. Rajeev, K. Parameswaran, Regional and vertical distribution of semitransparent cirrus clouds over the tropical Indian region derived from CALIPSO data, J. Atmos. Sol. Terr. Phys., doi:10.1016/j.jastp.2011.06.007,2011.

7. Nair, A. K. M., K. Rajeev, S. Sijikumar, S. Meenu, Observations of a persistent 'pool of inhibited cloudiness' and its genesis over the Bay of Bengal associated with Asian summer monsoon, Annales Geophysicae, doi:10.5194/angeo-29-1-2011, 2011.

8. Ram, K., M. M. Sarin, and P. Hegde, 2010, Long-term record of aerosol optical properties and chemical composition from a high-altitude site (Manora Peak) in Central Himalaya, Atmos. Chem. Phys. 10, 11791-11803.

PUBLICATIONS IN REFEREED PROCEEDINGS

1. Mishra, M. K., K. Rajeev, A. K. M Nair, B. V. Thampi, K. Krishnamoorthy and K. Paramewaran, Impact of noon-time annular Solar Eclipse on the vertical distribution of aerosols and mixing height over Thumba, Proc. Of National Workshop: Results on Solar Eclipse, Trivandrum, 27-28 Jan. 2011, pages 134-137.

2. Rajeev, K., K. Krishnamoorthy, M. Mohan, P. R. Nair, S. S. Babu, D.B. Subrahamanyam, N. V. P. K. Kumar, V. Sreekanth, M. K. Mishra, A. G. Imran, M. M. Gogoi, M.Santosh, S. K. Kompalli, S. Sijikumar, K.V.S. Namboodiri, R. K. Manchanda, "Impact of the annular Solar Eclipse of 15 January 2010 on the boundary layer structure and distribution of aerosols and trace gases over Thumba", Proc. of National Workshop: Results on Solar Eclipse, Trivandrum, 27-28 Jan. 2011, pages 22-40.

3. Girach Imran A., Prabha R. Nair, Liji Mary David and Prashanth Hegde, The impact of solar eclipse of 15 January 2010 on near-surface ozone at Thiruvananthpuram, Proc. Of National Workshop: Results on Solar Eclipse, Trivandrum, 27-28 Jan. 2011

SYMPOSIUM PRESENTATIONS

1. Girach Imran Asatar, Prabha R Nair and Liji Mary David, Spatial Variation of Ozone, Carbon Monoxide and Nitrogen Dioxide Over Bay of Bengal During Winter, AOGS Conference, Hyderabad, July 5-9, 2010.

2. Liji Mary David and Prabha R. Nair,Association of synoptic circulation on the seasonal variability of near-surface ozone and NOx at a tropical coastal site, AOGS Conference, Hyderabad, July 5-9, 2010.

3. Prabha R. Nair, Susan George, K Parameswaran and Salu Jacob, Composition of Aerosols over Indian Land-mass and Adjoining Oceans: Source Characteristics and Evolution of Chemical Models, AOGS Conference, Hyderabad, July 5-9, 2010.

4. Suresh Raju C., Tinu Antony , Korak Saha, and K. Krishna Moorthy Characterisation of Different Land surface classes using Microwave Land emissivity over the Indian Subcontinent for Microwave Remote Sensing of Atmosphere over the Land, AOGS 2010 (July 5-9), Hyderabad , India

5. Korak Saha, Suresh Raju C., Anupama. G., and K. Parameswaran, Latitudinal variation of atmosphere oscillations in the GPS measurements over the Asian continental region, AOGS 2010, (July 5-9), Hyderabad, India.

6. Girach Imran Asatar, Prabha R Nair, S Siji kumar and Aryasree, Trace gases at coastal station and over marine environment: Close association with meteorology, WRF workshop, Hyderabad.

7. Girach Imran A., Prabha R. Nair, Liji Mary David and Prashanth Hegde, The impact of solar eclipse of 15 January 2010 on near-surface ozone at Thiruvananthpuram, National Workshop on solar eclipse results, Thiruvananthapuram

8. Nair, A K M., S. Sijikumar, S. Meenu, K. Rajeev, K. Parameswaran, A 'Pool of Reduced Cloudiness' over the South Bay of Bengal During the Asian Summer Monsoon Season: Characteristics and Genesis, AOGS2010, Hyderabad, July 2010

9. Mishra. M. K., B. V. Thampi, A K M. Nair, K. Rajeev, K. Parameswaran, Seasonal Variations in the Altitude Distribution of Aerosols and Characteristics of the Elevated Layers over Trivandrum (8.5ºN, 77ºE), AOGS2010, Hyderabad, July 2010.

DEPUTATION

Prashant Hegde, Hokkaido University, Japan

INVITED TALKS

Prabha R Nair, Composition of Aerosols over Indian Landmass and Adjoining Oceans: Source Characteristics and Evolution of Chemical Models, AOGS Conference, Hyderabad, July 5-9, 2010.

Rajeev, K., Clouds, Dynamics and Atmospheric Impacts, National Workshop on Advances in Science of Climate Change and Indian Monsoon, Indian Institute of Tropical Meteorology, 31 Aug.-01 Sept. 2010.

Rajeev, K., Recent trends in Radiation budget and Climate Change research, Department of Physics, University of Kerala, 30 May 2011.

Suresh Raju C, Microwave Radiometry for profiling Mars Atmosphere, Brainstorming on Space and Climate, PRL, Ahmedabad, April 27-28, 2011.

Prashant Hegde, Water soluble dicarboxylic acids and related compounds in southwestern Himalayan aerosols, Hokkaido University, Japan 17-01-2011

Prashant Hegde, Seasonal variation in aerosol organic composition over the Central Himalayas, Hokkaido University, Japan 20-05-2011

CONFERENCES/WORKSHOPS ATTENDED

Manoj K Mishra, Prabha R Nair, Girach Imran Asatar, Liji Mary David, Anish Kumar M Nair, AOGS, Hyderabad, July 5-9, 2010.

K. Rajeev, Manoj K Mishra, Prabha R Nair, Girach Imran Asatar, S. Meenu, Liji Mary David, Anish Kumar M Nair, Aryasree, S, National Workshop: Results on Solar Eclipse, VSSC, Trivandrum, 27-28, January 2011

K. Rajeev, Suresh Raju C: Brainstorming meeting on future Mars Mission of ISRO, Physical Research Laboratory, Ahmedabad, March 24-25, 2011.

Girach Imran Asatar, WRF Workshop, Hyderabad

Girach Imran Asatar, AT-CTM Review meeting, Hyderabad, January 24-25, 2011.

Ph. D. AWARDED

S. Meenu, Studies on the Regional Distribution of Clouds over the Indian Region (30°S-30°N; 40°E-105°E) and its Association with the Atmospheric Dynamical Features using Remote Sensing Data, Kerala University, March 2011.

Ph. D. THESIS SUBMITTED

Bijoy V Thampi, Studies on the Altitude Structure of Atmospheric Aerosols over Tropics, Kerala University, October 2010.

PROJECT WORKS

M.Sc: 1

M. Tech: 3

BOUNDARY LAYER PHYSICS AND ATMOSPHERIC MODELLING

Science Faculty

#Mannil Mohan
*Rajeev K
Bala Subrahamanyam D
Kiran Kumar N V P
Sijikumar S
Sandhya K Nair
Santosh M

Technical Team

Pradeepkumar P
Lali P T

Research Associates & Fellows

+Marina Aloysius
Prijith S S
Anurose T J
Neethu Purushothaman

#Superannuated on 31 May 2011
**From June 2011*
+Relieved from duties on 22 March 2011

The Boundary Layer Physics and Atmospheric Modelling (BLPAM) Branch focuses on two aspects: (i) theoretical and experimental studies of the structure and properties of the Atmospheric Boundary Layer (ABL), and (ii) high- resolution mesoscale and global atmospheric modelling. Main objective of the former is to improve the understanding and parameterization of the boundary layer processes including energy/mass exchanges between the Earth's surface and the atmosphere, turbulence, surface roughness and hydrological processes under different geographical and meteorological conditions. This branch is also responsible for establishing the network of ground stations under the Atmospheric Boundary Layer Network and Characterization (ABLN&C) project of ISRO-GBP, implemented through SPL. Primary objectives of the modelling activities are: (a) understand the mesoscale processes using high-resolution regional models, improve the ABL parameterizations and data assimilation, and (b) carry out sensitivity studies to assess the impact of various climate parameters and anthropogenic activities using global/regional climate models.

1. ROLE OF THE ARABIAN SEA WARM POOL ON THE PRECIPITATION CHARACTERISTICS DURING CONTRASTING MONSOON ONSET PERIODS OF 2009-2010

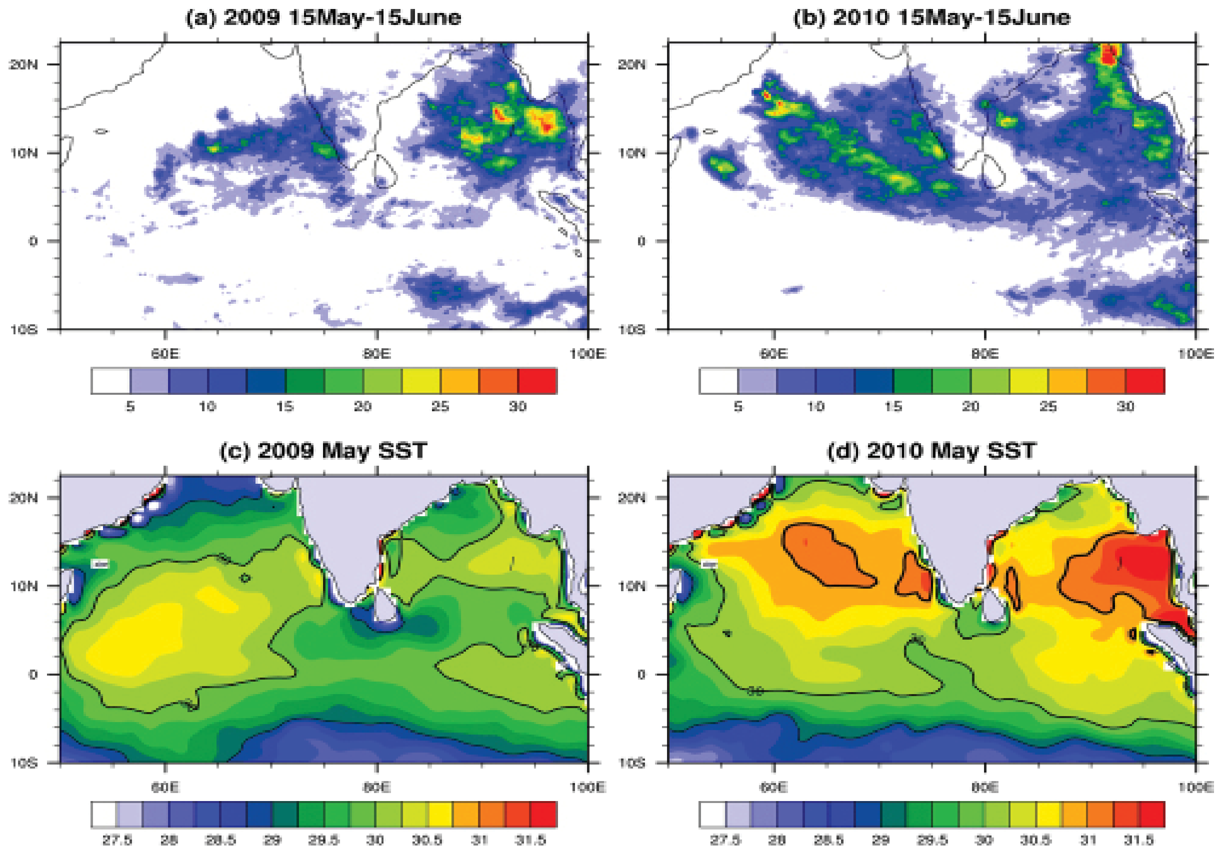

Figure 1: Average precipitation (mm d^{-1}) during 15 May - 15 June observed using TRMM for 2009 and 2010 (a, b). Observed SST (°C) in May for these years (c, d)

Regional distribution of precipitation during the on-set phase of the Indian summer monsoon (15 May-15 June) showed distinct patterns in the years 2009 and 2010 with the latter having considerably larger precipitation over southeast Arabian Sea (AS) and the west coast of Peninsular India (Fig.1a-b). During these years, considerable changes are also observed in the location and regional extent of the warm pool in the AS, where the sea surface temperature (SST) exceeds 29°C in May. In 2009, the warm pool core was located at the equatorial region whereas in 2010 it spreads to a wider region of the AS with a positive SST anomaly of 0.5 to 1°C (Fig.1c-d). Utilising these differences in the regional distribution of precipitation during the monsoon onset phase and the AS warm pool, the studies conducted during the previous year on the impact of changes in the characteristics of the AS warm pool on Indian summer monsoon were extended. The monsoon onset periods of 2009 and 2010 provided the natural variability to carry out sensitivity experiments with Weather Research and Forecasting (WRF) model to decipher the influence of AS warm pool on the precipitation characteristics during monsoon onset.

Nevertheless, SST not being the only factor that controlled the variability observed during these two monsoon onsets, in order to isolate the role of SST, variabilities caused by the other large-scale boundary forcings have to be suppressed. To minimise the interannual variability in large-scale boundary forcings, 11-year (2000 to 2010) averaged data were used as initial and lateral boundary conditions for model simulations. A control simulation (CTRL) using WRF has been carried out with initial and lateral boundary conditions including SST obtained from the 11-year average ERA-Interim data. Sensitivity simulations are also done using these 11-year average boundary conditions but with different SST boundary conditions. Two sets of sensitivity experiments are carried out. In the first set (referred hereafter as Full09

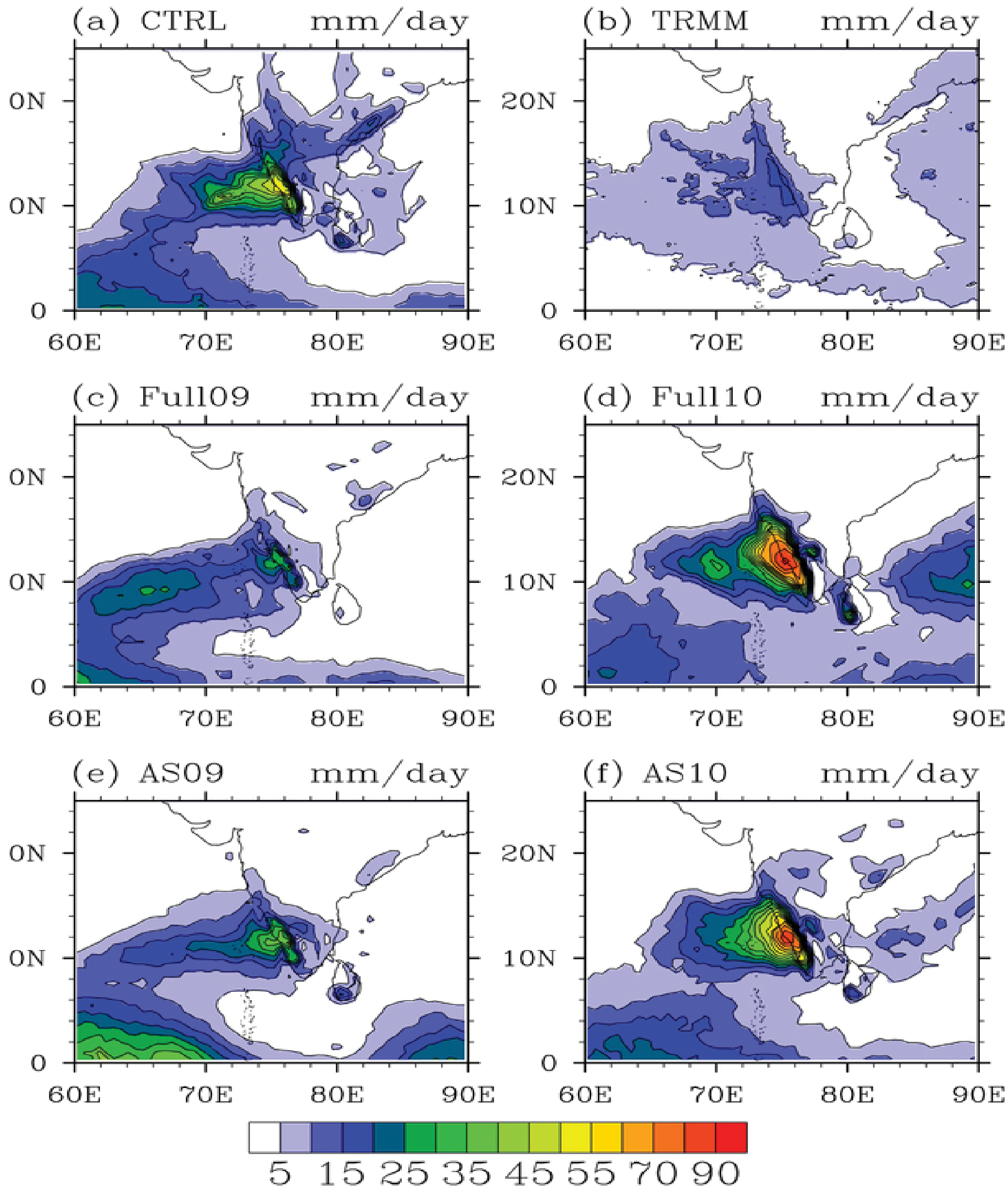

Figure 2: Simulated precipitation (mm d^{-1}) averaged from 15 May to 15 June (a) CTRL, (b) 11 year (2000-2010) climatology from TRMM, (c) Full09, (d) Full10, (e) AS09 and (f) AS10

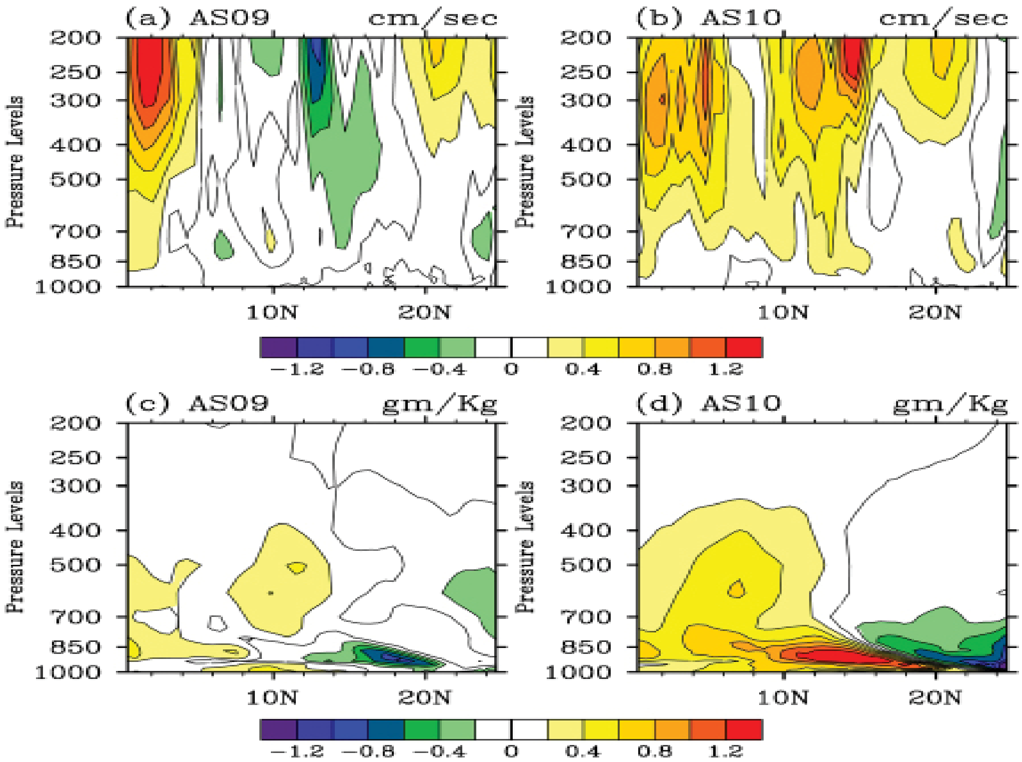

Figure 3: Latitude-altitude cross-sections of the vertical velocity anomalies (cm s^{-1}) averaged in the longitude band of 60-80E for AS09 and AS10 runs with respect to CTRL experiment (a,b). (c,d) same as (a,b) but for specific humidity (g kg^{-1})

and Full10), observed SSTs of 2009 and 2010 were used over the whole ocean domain instead of the 11 year average SST. In order to discern the role of the AS warm pool on the monsoon onset, simulations are performed (referred hereafter as AS09 and AS10) with observed SSTs of 2009 and 2010 in the AS and climatological SSTs elsewhere.

Fig.2a shows the simulated average precipitation during 15 May-15 June for the CTRL simulation, which shows maximum precipitation over the equatorial region and the southwest coast of Peninsular India. The observed climatology (11-year average of TRMM data) of the regional distribution of precipitation for the same period is shown in Fig. 2b for comparison. In the sensitivity experiments, the Full09 simulation shows considerably reduced precipitation (by less than 10 mm day^{-1}) over the southwest coast of Peninsular India compared to CTRL simulations (Fig.2c). In contrast, the Full10 simulation shows an enhancement of precipitation (by more than 15 mm d^{-1}) over the above region (Fig.2d). Spatial distribution of these features over the AS and west coast of the Peninsular India are similar to that of observed during the corresponding periods of 2009 and 2010 (Fig.1a & b). The precipitation patterns corresponding to the AS09 and AS10 simulations are shown in Fig.2d & e. With the AS SST forcing alone the model is able to simulate the distinct behaviour of precipitation observed during the monsoon onset period of 2009 and 2010, clearly indicating the domination of the AS warm pool in regulating the precipitation during the monsoon onset. These simulations show an anomalous large-scale descent of lower tropospheric airmass over the central and northern AS in 2009 while warmer SSTs in the AS favour large scale ascent during 2010 (Fig.3a & b). These are combined with rather sharp contrast in the humidity transport and accumulation of moisture in the southeast AS (Fig.3c & d). The strong intrusion of dry air from the north AS effectively connects the moist air mass from the south, causing a net accumulation of moisture and positive anomalies in precipitation over the southwest part of Peninsular India in 2010. However, during 2009, the dry air from north mixes rather easily over the AS, which suppress the convection. Thus, with observations and numerical simulations, this study clearly demonstrates that location and amplitude of the AS SST do have a dominant effect on the precipitation characteristics during the Indian summer monsoon onset period.

2. SHORT-RANGE WEATHER PREDICTIONS IN SUPPORT OF GSLV-F06 AND PSLV-C16 LAUNCHES

As a part the Weather Forecasting Expert Team of ISRO, SPL is identified for providing short-range weather predictions with the aid of High-resolution Regional Model (HRM). With a goal of providing the best possible information in the terms of Launch Commit Criteria, SPL took part in GSLV-F06 (25 December 2010) and PSLV-C16 (20 April 2011) missions by catering +48 hrs simulated fields to the team members for consolidation of the forecast. HRM simulated fields were useful in consolidation of the forecast and its dissemination to the launch team.

3. CHARACTERIZATION OF THE COASTAL ATMOSPHERIC BOUNDARY LAYER OVER THUMBA

Coastal Atmospheric Boundary Layer (CABL) characteristics are distinctly different from those of inland ABL due to presence of mesoscale sea breeze circulation. With a view to characterizing the general features of CABL based on long-term measurements, vertical profiles of meteorological parameters obtained from balloon-borne (Pisharoty) GPS sonde for a period of 27 months (from September 2008 to November 2010) have been analyzed and observed clear seasonal variability in the thickness of three different sub-layers of the CABL, namely, mixed layer, turbulent flow, and sea breeze flow.

Delineation of Mixed Layer, Turbulent Flow and Sea Breeze Flow

Altitude profiles of virtual potential temperature (θ_V) and its vertical gradient ($d\theta_V/dz$), bulk Richardson number (Ri_B) and sea breeze component (SBC) of wind for the afternoon period on 11th December 2009 are shown in Fig.4a-c. The level of the maximum vertical gradient in θ_V is generally indicative of a transition from a convectively less stable region below to a more stable region above. In the lower altitudes, the magnitudes of θ_V remain nearly steady due to convective heating and turbulent mixing constituting the mixed layer (Fig.4a). The top of this mixed layer is marked at an altitude of about 450 m, where $d\theta_V/dz$ exceeds 3.0 K km^{-1}, and this altitude corresponds to the mixed layer height (MLH). In Fig.4b, Ri_B remains negative in the lower atmosphere and at an altitude between 400 – 500 m, becomes positive and exceeds 0.25 indicating laminar flow conditions. This altitude corresponds to the turbulent flow depth (TFD). Positive values of SBC below 700 m altitude indicate the presence of sea breeze flow in this layer, whereas in the higher altitudes (> 700 m) the SBC becomes negative, indicating reversal of the flow (land breeze) aloft (Fig.4c) and this altitude is the sea breeze cell thickness (SBCT).

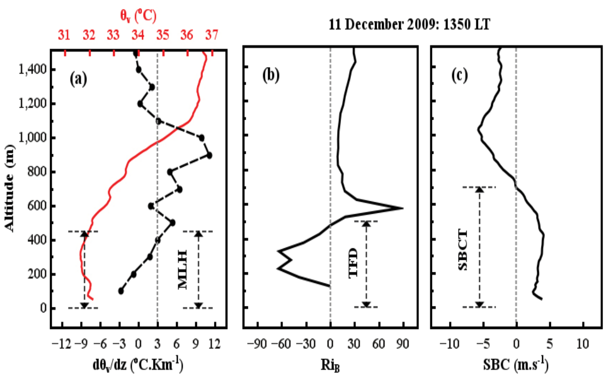

Figure 4: Vertical Profiles of (a) virtual potential temperature (θ_V) and ($d\theta_V/dz$), (b) bulk Richardson number (Ri_B), and (c) sea breeze component (SBC) depicting three different techniques adopted for determination of mixed layer height (MLH), turbulent flow depth (TFD), and sea breeze cell thickness (SBCT), respectively

Annual Variations

Fig.5 shows the annual variation of MLH, TFD, and SBCT, obtained by averaging daily values in monthly ensemble, irrespective of the year. The vertical bars indicate the ensemble standard deviations. The values of SBCT are generally larger than those of MLH and TFD, indicating a dominant role of the sea-breeze circulation in modulating CABL dynamics. During October to April, SBCT magnitudes are almost two times the magnitudes of MLH and TFD, which is indicative of the formation of TIBL within the sea breeze flow, as generally expected over a coastal station. The MLH values lie in the range of 310 m to 650 m with a mean of 420 m ± 36 m, whereas TFD showed variations in the range of 175 m to 560 m with a mean of about 330 m ± 32 m, which is significantly lower than that of the MLH. This is mainly due to very low values of TFD during summer monsoon and post-monsoon seasons, where the higher winds in the lower atmosphere reduce the thickness of turbulent flow, whereas the thermal convection helps in the rise of mixed layer height. The SBCT varied within the range of 500 m to 960 m with a mean of about ~ 760 m ± 60 m.

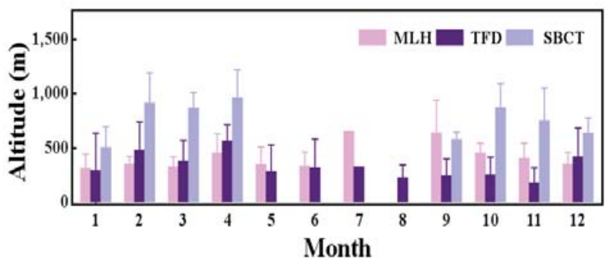

Figure 5: Monthly variations in Mixed Layer Height (MLH), Turbulent Flow Depth (TFD) and Sea Breeze Cell Thickness (SBCT). Vertical bars associated with these parameters indicate the standard deviations for each month

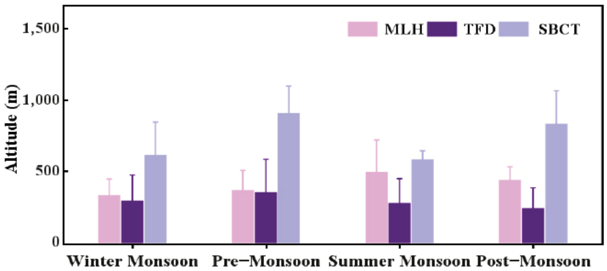

Figure 6: Seasonal variations in Mixed Layer Height (MLH), Turbulent Flow Depth (TFD) and Sea Breeze Cell Thickness (SBCT) shown as histograms. Error Bars associated with these parameters indicate the standard deviations for each season respectively

Fig.6 shows the mean values of MLH, TFD and SBCT during winter (December to February), pre-monsoon (March to May), summer monsoon (June to September) and post-monsoon (October – November). The mean MLH variations are found to be ranging from 300 m to 500 m, with a peak during the summer monsoon, which may also be attributed to convective activities prevailing during this season. The MLH exhibits relatively lower values during winter, presumably due to the lack of intense convection during this season. Seasonal variation of TFD is quite similar to that of the MLH, except for the summer monsoon and post-monsoon seasons. The magnitudes of seasonal mean TFD remain nearly steady throughout the year with a mean of about 330 m, as against large variabilities in the MLH magnitudes. From the estimates of TFD for different seasons, it is seen that larger wind speeds for a given season (such as during the summer monsoon and post-monsoon) often result in lower magnitudes of TFD, in turn indicating the shrinking of turbulent flow in presence of strong winds. The vertical thickness in sea breeze flow shows a large peak at about 900 m in the pre-monsoon and post-monsoon seasons, indicating the increased strength of sea breeze flow. During the Summer Monsoon, the sea breeze flow coincides with the prevailing wind circulation, hence it is difficult to comment on its variability.

4. VERTICAL STRUCTURE OF THE MABL OVER BAY OF BENGAL

Spatial and temporal variabilities in the vertical structure of Marine Atmospheric Boundary Layer (MABL) over the Bay of Bengal (BoB) are investigated through ship-borne measurements pertaining to three stability classes, namely: Nocturnal, Neutral and Unstable conditions. High-resolution vertical profiles of meteorological parameters obtained through balloon-borne Pisharoty sondes onboard the cruise # 254 of ORV Sagar Kanya, during the Winter phase of Integrated Campaign for Aerosols, gases and Radiation Budget (W-ICARB) formed the primary database for the present investigation. The cruise started on 26th of December 2008, from Chennai and called at Cochin on 29th of January 2009. During the field experiment, three Pisharoty Sondes were launched daily, typically at 0030, 0630 and 1330 local time (LT), representing respectively the nocturnal, neutral (transition from stable to unstable conditions) and unstable conditions of the MABL. Overall, 108 sondes were launched during the entire cruise.

Variabilities in TFD, MLH and SHF under different stability conditions

With a view of investigating the daily variations in TFD, MLH and sensible heat flux (SHF) under different stability conditions, the sounding and concurrent SHF measurements (onboard) have been grouped into three different stability regimes based on the time of Pisharoty sonde ascents. Accordingly, there were 27 ascents for the nocturnal case (2200 to 0200 LT); 28 for the neutral case (0600 to 0800 LT) and 34 for unstable case (1200 to 1500 LT). Daily variations of the magnitudes of TFD, MLH and SHF for the entire cruise period are depicted in Fig.7a -c.

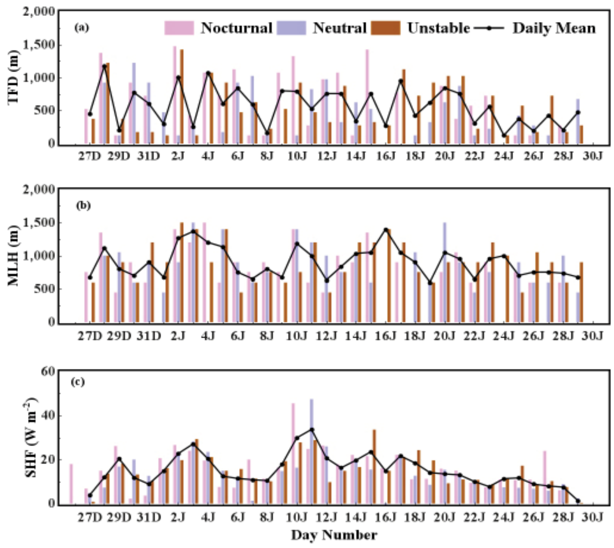

Figure 7. Spatio-temporal variability in (a) TFD (b) MLH and (c) SHF for Nocturnal, Neutral and Unstable classes of the MABL. Daily mean of these parameters are shown through line plus symbol. Day number 1 corresponds to 1st of January 2009

From Fig.7a, it can be noticed that the magnitudes of TFD varied over a wide range of 125 m to 1475 m during the cruise indicating large inhomogeneity in the vertical structure of the MABL, probably caused by the prevailing latitudinal gradients in ambient meteorological parameters. Interestingly, most of the high values of TFD occurred during nocturnal stable condition, while the minimum values occurred during the neutral conditions. On the other hand, the MLH magnitudes did not show such drastic diurnal variations throughout the cruise and its magnitude varied spatially from 450 m to 1500 m with a mean of about 897 m (Fig. 7b). In most of the cases, the MLHs were larger than the corresponding TFDs. With a view of relating the vertical structure of the MABL with surface-layer turbulent fluxes, we show the mean magnitude of SHF for three stability regimes along with its daily mean in Fig.7c. On an average, the magnitudes of SHF varied in the range of 0 to 48 Wm^{-2} with a moderate mean of about 15 Wm^{-2}. During the experiment, the magnitudes of SHF did not show any appreciable differences between the Nocturnal, Neutral and Unstable conditions of the MABL, but varied rather spatially.

In Fig.8, the variations of the daily mean values of MLH and SHF are shown. Barring a few days, the magnitudes of MLH were found to be well associated with that of the SHF. The mean values of TFD, MLH and SHF for three different stability conditions are shown in Fig. 9 along with their standard errors. For all the three classes of stability, MLH does not show any significant diurnal variability, whereas the TFD and SHF attain their peak magnitudes during the Nocturnal stability and become minimum during the Neutral conditions of the MABL. The nocturnal peak in the magnitudes of SHF (16.3 Wm−2, Fig. 9) are attributed to high wind speed and large difference between the SST and air temperature. As per the definition of the mixed layer, water vapour is considered as one of the trace species to determine the extent of mixing prevailing within the MABL and is transported to high altitudes through thermal convection as well as turbulent processes, whereas the vertical extent of TFD is solely dependent on wind and turbulence. It may probably be one of the reasons for random fluctuations in the TFD and for nearly constant magnitudes of MLH over a diurnal scale, as described through three different classes of stability.

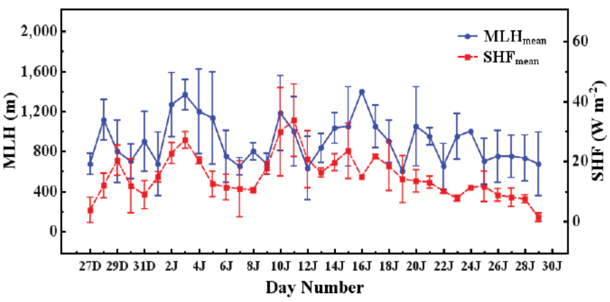

Figure 8: Daily mean of MLH and SHF during W-ICARB field experiment. The vertical bars indicate the daily standard deviations

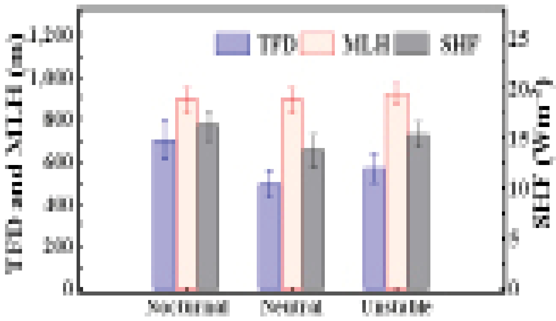

Figure 9: Spatio-temporal mean in TFD, MLH and SHF for Nocturnal, Neutral and Unstable conditions. Vertical bars associated with each variable represent the standard errors

5. IMPACT OF ANNULAR SOLAR ECLIPSE OF 15 JANUARY 2010 ON THE CABL

On 15 January 2010, Thumba witnessed one of the longest known noontime annular solar eclipses spanning a period of about 7 min, centered at 1314 LT. Extensive investigations of the behaviour of the CABL and its vertical structure in response to eclipse were made and the results are given below.

Surface Layer

Surface-layer meteorological observations were made using an automatic weather station equipped with slow response sensors for the measurement of incoming solar irradiance, air temperature, relative humidity, atmospheric pressure, wind speed and wind direction. This was operated in conjunction with a sonic anemometer (fixed at 10 m above mean sea level) for measuring three-axis winds and temperature at high repetition rates (25 Hz).

The diurnal variation of surface-layer meteorological parameters, stability parameter (z/L) and turbulent kinetic energy (TKE) on the eclipse day are compared with the corresponding values of these parameters on other clear sky days, averaged over the month of January 2010 and are shown in Fig.10a-h. On clear-sky days, the maximum insolation ranged between 744 Wm^{-2} to 850 Wm^{-2} with a mean of about 793 Wm^{-2} occurring at 1240 LT. As expected, on 15 January 2010, the irradiance started decreasing from the first contact at 1105 LT (Fig.10a), and at the peak of eclipse the total irradiance has come down to as low as 96 Wm^{-2} between 1310 to 1317 LT. This rate of reduction in irradiance was almost 1.7 times higher than that during the normal evening hours between 1505 to 1705 LT, indicating the rapidity of the event. After the annularity, the irradiance rapidly recovered to about 558 Wm^{-2} at 1505 LT, the pace being about twice that of the sunrise-induced growth rate on the normal days. In response to the above, during the pe-

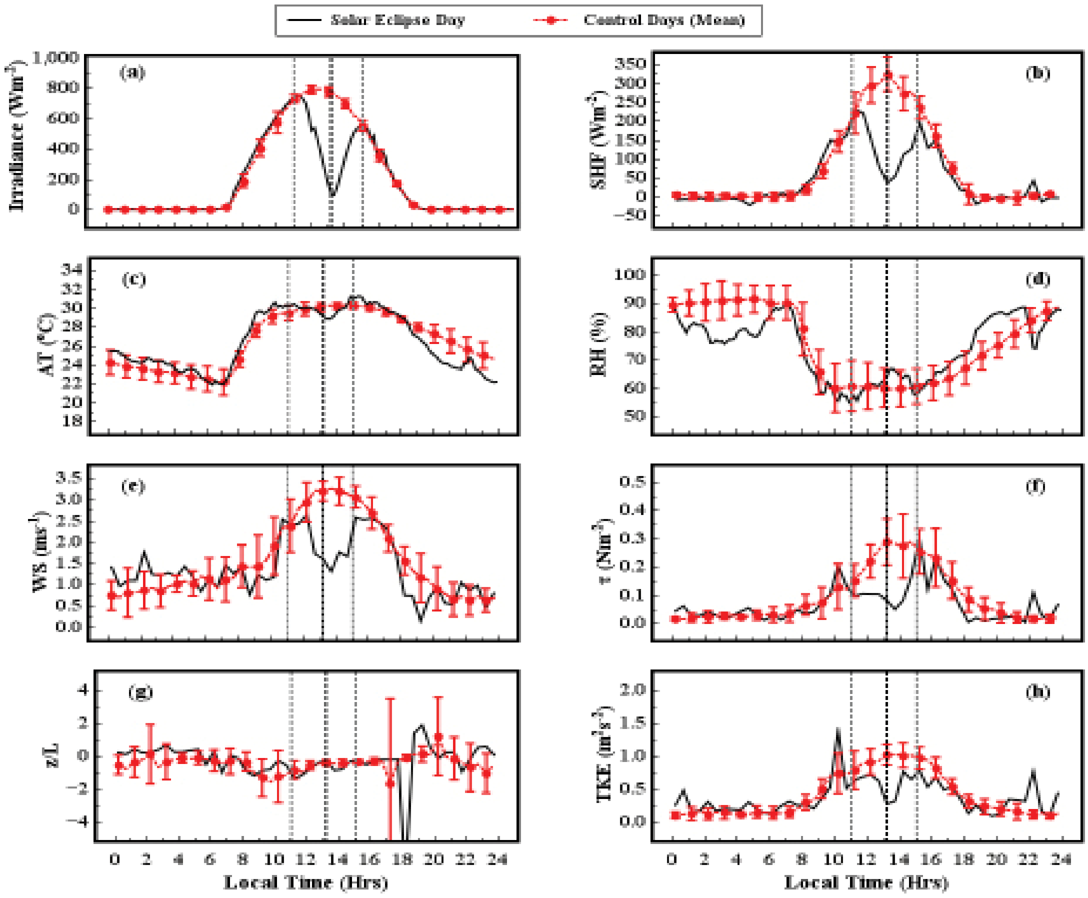

Figure 10: Diurnal variability in atmospheric surface layer parameters on the annular solar eclipse day compared with the mean of control days: (a) incoming solar irradiance (b) sensible heat flux (c) air temperature (d) relative humidity (e) wind speed (f) momentum flux (g) Monin–Obukhov stability parameter and (h) turbulence kinetic energy (TKE)

riod of eclipse, the magnitudes of sensible heat flux and air temperature also showed similar variations (Fig.10). On the mean control day, the sensible heat flux attained its peak magnitude (324 Wm^{-2}) at 1315 LT. At the peak annularity on the eclipse day the value was 36 Wm^{-2}, a decrease by 89% of the mean control day value. Air temperature decreased by ~ 1.2°C during the peak of annularity (Fig.10c). Surface-layer wind speeds in the month of January 2010 ranged between zero to 2.5 ms^{-1} with the diurnal peak in mid-afternoon at about 1400 LT (Fig.10e). On the eclipse day, there was a significant decrease in wind speed (1.3 ms^{-1}) between 1200 to 1600 LT and in the momentum flux. (Fig.10f). During noontime, the magnitudes of momentum flux on the mean control day were about 0.3 Nm^{-2}, but were below 0.1 Nm^{-2} on the eclipse day. Though z/L did not show any appreciable impact of the eclipse, the TKE showed a significant decay at about 1300 LT, indicating weakening in turbulence (Fig.10h).

Sea/Land Breeze Circulation

On most of the control days in the month of January 2010, onset of sea breeze over Thumba was marked by a consistent reversal in magnitudes of SBC from negative to positive values between 1000 and 1030 LT (Fig.11a). These features were almost similar on the eclipse day also with an onset of sea breeze at about 1015 LT. However, subsequent evolution of SBC was quite different. Generally, the SBC peaks at about 1400 LT; however this did not happen on the

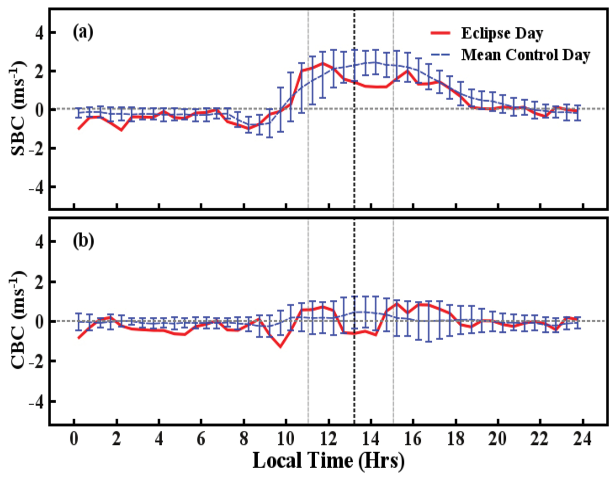

Figure 11: Temporal evolution of (a) sea breeze component (SBC) and (b) coastal breeze component (CBC) on the eclipse day compared with the mean of control days

eclipse day. Moreover the onset of land breeze was advanced by ~ 2 hrs on the eclipse day (at 1900 LT) due to the eclipse induced cooling of the land surface. Magnitudes of coastal breeze component (CBC) did not show any appreciable differences on the eclipse day, remaining closer to zero (Fig.11b).

In order to investigate the eclipse induced impacts on the vertical structure of sea breeze circulation cell over Thumba, a total of eight Pisharoty sonde ascents were conducted on 14 January 2010 (control day) and the eclipse day at 0800, 1030, 1230 and 1430 LT, respectively. Vertical profiles of SBC, CBC and potential temperature corresponding to 0800, 1230 and 1430 LT ascends are depicted in Fig.12. The main observations are summarized below:

• By 1230 LT on both the days, the ABL clearly indicated presence of the sea breeze cell with positive values of SBC in the lower altitudes representing the sea breeze flow and negative values of SBC aloft indicating a compensatory return flow (Fig. 12a-c).

• Thickness of the sea breeze cell on the eclipse day was about 300 m, almost half of that on the control day (Fig.12b), resulting from the weakening of sea breeze intensity on eclipse day.

• By 1430 LT, in the recovery phase of the eclipse, the intensity of sea breeze and the thickness of the sea breeze cell became similar to that on the control day (Fig.12c).

• On both the days, formation of thermal internal boundary layer was eminent; however, the strength of convection on the eclipse day was weaker compared to that of the control day (Fig.12g-i).

Sub-Layers within the ABL

To examine the impact on the sub-layers, the vertical profiles of θ_V, q and T corresponding to 0800, 1230 and 1430 LT for the control day, while the same profiles on the eclipse day are shown in Figs.13 & 14 respectively. The major eclipse induced differences are summarized below:

• By 1230 LT, a shallow ML extended from the surface to about 250 m on the eclipse day, which remained weakly decoupled to the airmass above.

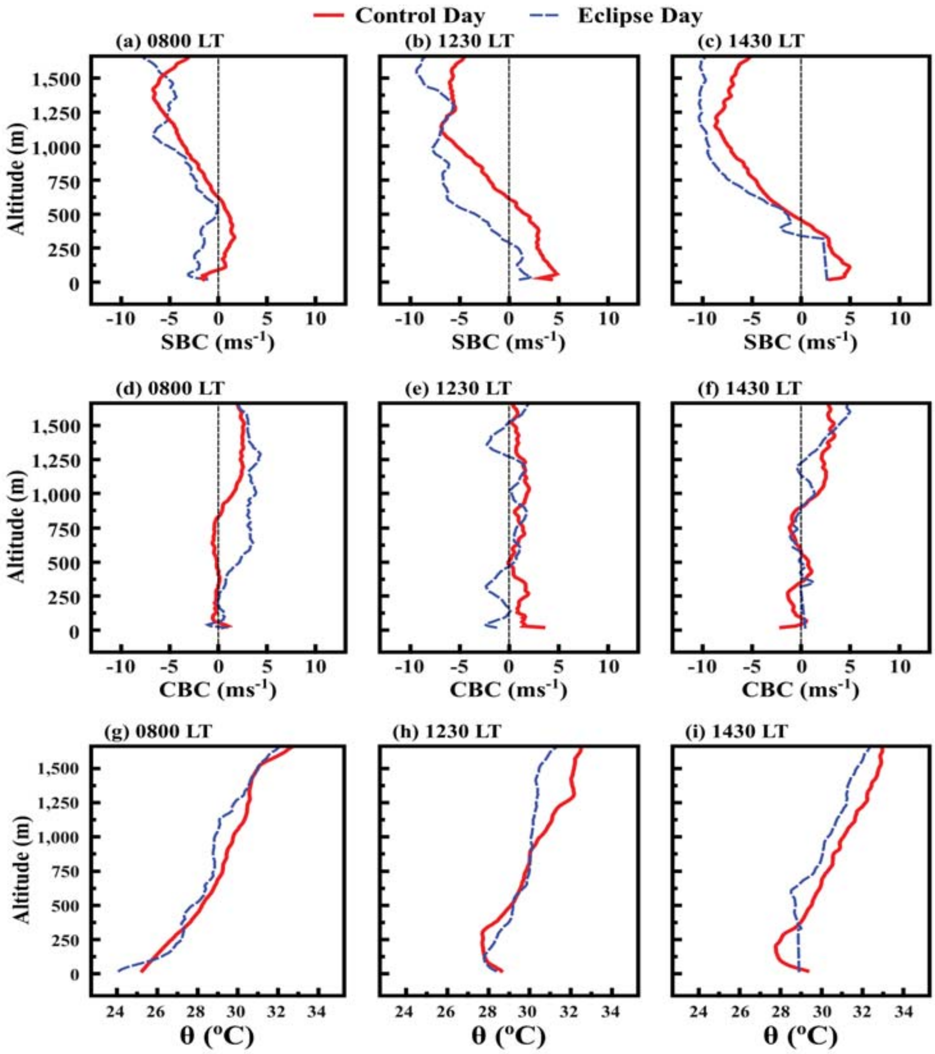

Figure 12: Vertical profiles of sea breeze component (a–c), coastal breeze component (d–f) and potential temperature (g–i) at 0800 LT, 1230LT and 1430 LT, respectively

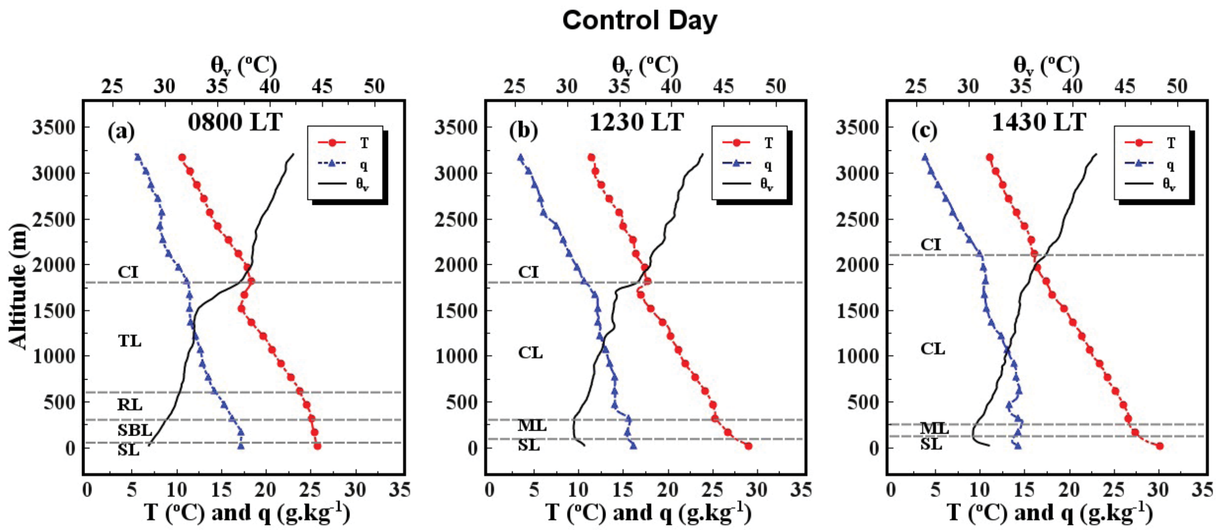

Figure 13: Vertical profiles of virtual potential temperature and ambient air temperature on control day corresponding to (a) 08:00 LT (b) 12:30 LT and (c) 14:30 LT. Abbreviations of different sub-layers within the ABL: SL surface layer; SBL stable boundary layer; RL residual layer; TL transition layer; CI capping inversion; ML mixed layer; CL cloud layer

These features were similar on the control day also. Further aloft, in the altitude range between 700 m and 1.5 km, the formation of a double mixed layer was observed on the eclipse day, which was not seen on the normal days.

• Formation of double mixed layer is attributed to the presence of two distinct airmasses, which gradually diminished by 1430 LT.

Degree of Convection

With a view to explaining the degree of convection, altitude profiles of the difference between saturation equivalent potential temperature and equivalent potential temperature ($\delta\theta = \theta_{ES} - \theta_E$) corresponding to afternoon hours for the control day and the eclipse day are shown in Fig.15. Low and high values of $\delta\theta$ are indicative of intense convection and suppressed convection, respectively. The altitude of maximum convection, indicated by the minimum in $\delta\theta$ increased from 1.5 to 2.0 km between 1230 to 1430 LT, thereby indicating the increase in the strength of convective activities on the control day (Fig.15a). In contrast to this, on the eclipse day, the altitude of maximum convection fell rapidly from 1.5 km to 600 m between 1230 and 1430 LT, suggesting the weakening of thermal convection during the eclipse (Fig.15b).

6. IMPACT OF CONTINENTAL METEOROLOGY AND ATMOSPHERIC CIRCULATION IN THE MODULATION OF AEROSOL OPTICAL DEPTH OVER THE ARABIAN SEA

The aerosol optical depth (AOD) over the oceanic region is mainly influenced by the local production, loss and transport. Variations in any of these components can influence the spatial distribution of AOD. A climatological analysis of AOD derived from NOAA AVHRR and MODIS for a considerably long period

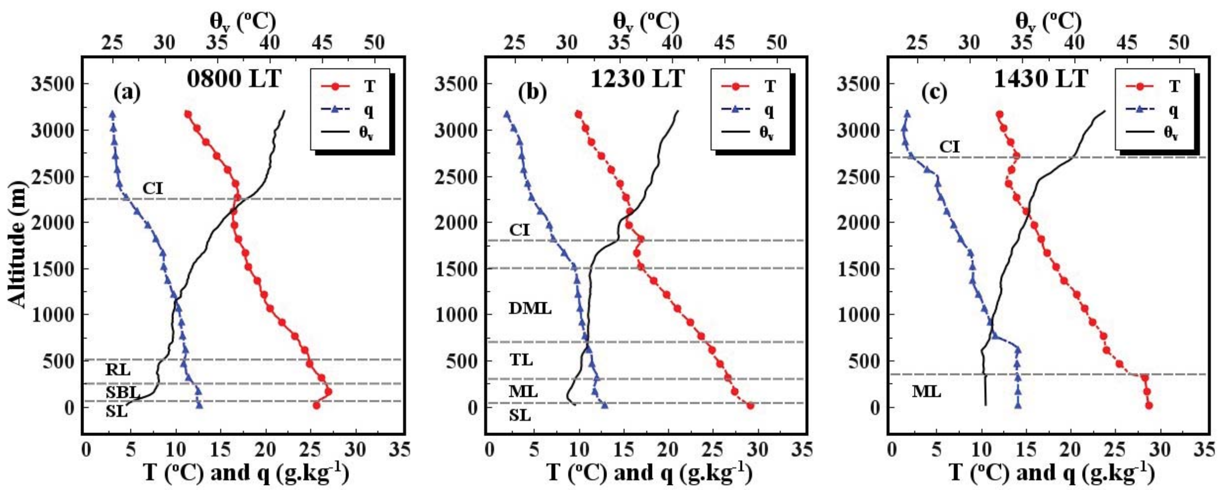

Figure 14: Vertical profiles of virtual potential temperature and ambient air temperature on the eclipse day corresponding to (a) 08:00 LT (b) 12:30 LT and (c) 14:30 LT. DML stands for double mixed layer

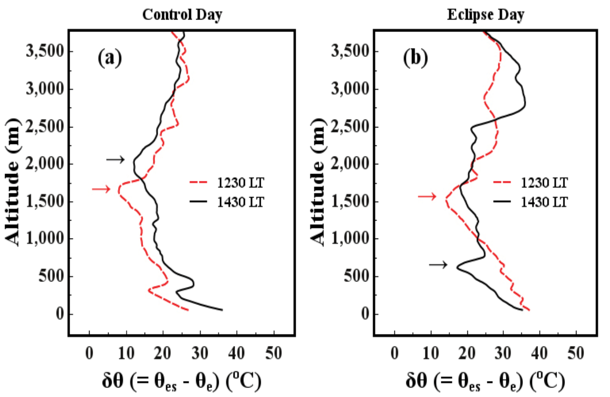

Figure 15: Vertical profiles of difference between θ_{es} and θ_e corresponding to 1230 LT and 1430 LT on (a) control and (b) eclipse days

of 13 years (1996 -2008) showed periodic variations. The prominent annual cycle is clearly observable over the entire Arabian Sea. Over and above this, a biennial modulation is observed in the amplitude of the annual variation in AOD, which is most prominent over Coastal Arabia [15 to 20°N and 58 to 63°E]. Fig.16a shows the time series of AOD over Coastal Arabia during the period 1996-2008. The wavelet spectra of this (Fig.16b) reveals the presence of quasi-biennial oscillation with periodicity of ~ 24 months. It is well known that the largest AOD over the Arabian Sea during summer monsoon season is contributed significantly by the dust aerosols the Peninsular Arabia. The high wind speed associated with the monsoonal circulation also produces significant amount of sea-salt aerosols over the Arabian Sea. The exact mechanisms responsible for the periodic variation in AOD over location are examined using derived AODs and meteorological parameters obtained from NCEP/ NCAR reanalysis, and making use of two quantities (a) aerosol source/sink strength (S) over the Arabian Sea and (b) AOD flux through the western boundary of Arabian Sea. Fig.17 shows the AOD, source strength and lower level flux over the Arabian Sea during the month of July for the period 2000-2010. The ordinate at left shows the variation of AOD flux and that at right gives the variation of AOD and source strength. The source strength is representative of net aerosol production over Coastal Arabia exhibits a near biennial periodicity.

The lower level flux corresponds to the integrated flux from 925 to 700 hPa level through the western boundary of the Arabian Sea. Both source strength and flux show the biennial variations which are in phase with that of AOD during 2000 to 2007. It is important to note here that even though the low level flux consistently reproduces the periodic oscillation upto 2009, AOD over the Arabian Sea failed to capture the same

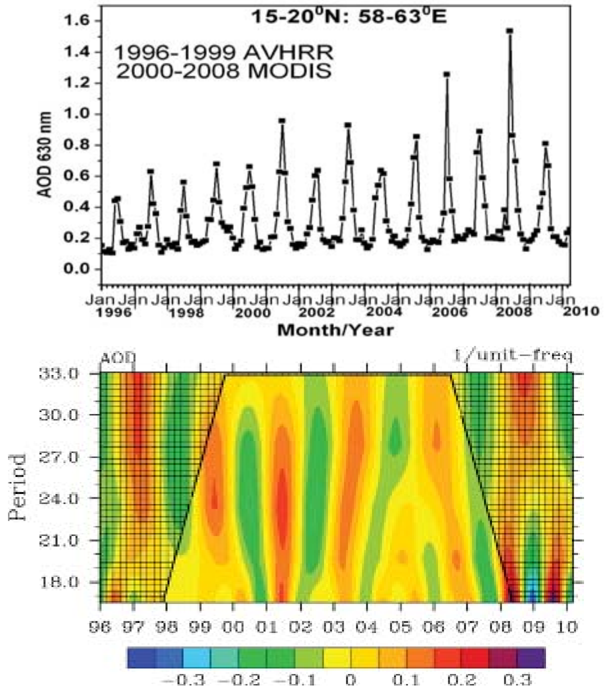

Figure 16: Time series of aerosol optical depth over Coastal Arabia Sea (15 to 20°N and 58 to 63°E) derived from NOAA-AVHRR and MODIS data during 1996 – 2008 (top-panel), Wavelet spectra of the above AOD variations (bottom panel). The mesh indicates the cone of the influence

after 2007. Moreover, the source strength over the Arabian Sea during 2008 and 2009 is out of phase with the low-level flux. The out of phase relation in source strength and flux may be a possible explanation for the absence of biennial oscillation in AOD during 2008 and 2009. This shows that the observed biennial periodicities in AOD are due to the combined effect of biennial oscillations in the abundance of locally produced sea-salt aerosols and advected dust aerosols. The oscillation in AOD is predominant only when both are in the same phase.

7. MIE-SCATTERING CORRECTION FOR THE ESTIMATION OF RAIN RATE FROM MICRO RAIN RADAR

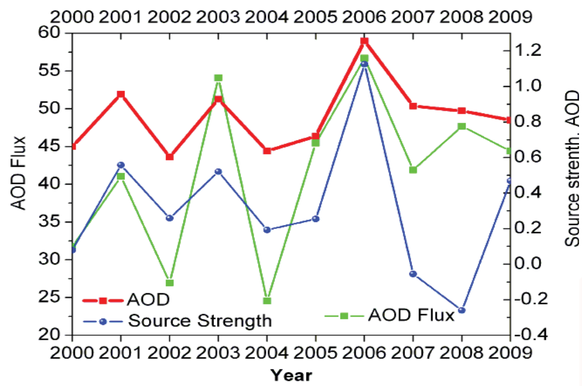

Figure 17: Variations of AOD, source strength and lower level flux (s^{-1})over the Arabian Sea in the month of July during the period of 2000-2010

In continuation of the K-band propagation experiment at SPL, the ability of Micro Rain Radar (MRR) to provide qualitative information on the raindrop size distributions and rainfall intensity was examined in detail. For improving the estimation of rainfall intensity, corrections are applied to the MRR data. Fig.18 shows the systematic underestimation of reflectivity (before correction) by the MRR compared to disdrometer. The accuracy of MRR derived parameters were improved by incorporating the corrections for Mie scattering and radar calibration.

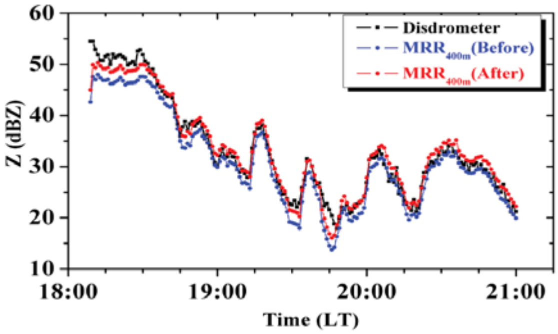

Figure 18: Comparison between the time series of reflectivities estimated from MRR (before (blue); red (after) and disdrometer (black) on 18 October 2006

Mie correction

The scattering characteristics of a spherical particle with a size parameter

$\alpha = \pi D \lambda^{-1}$ (where D is the diameter of the particle and λ is the radar wavelength) less than about 0.1 can be defined by Rayleigh scattering. Since the MRR operates at a wavelength of 12.5 mm, the Rayleigh approximation is applicable only for drop diameters less than about 0.4 mm. For the drop sizes in the range of 0.4 mm to 5 mm, it is necessary to apply the Mie scattering correction. This correction is incorporated by multiplying the Rayleigh approximation with the "Gunn and East correction factor". Such corrections lead to a decrease in the estimates of rain intensities by about 50% during convective events and by 10 to 30% during transition and stratiform rain events.

Calibration

After correcting for the effects of Mie scattering, the calibration of the MRR is performed by adjusting the radar constant. Fig.19a shows histograms of the uncalibrated MRR measured reflectivities at 400 m altitude and that estimated from the disdrometer. Differences between these two reflectivities are depicted in Fig.19b. Values of the reflectivities inferred from disdrometer are very noisy below about 20 dBZ and are not included. Also the values greater than 40 dBZ falls in the convective rain regime and hence are not considered for intercomparison. The distribution of reflectivity differences between MRR and disdrometer implies that the profiler reflectivities need to be increased by ~ 1.5 dB to account for the offset with respect to the disdrometer estimated reflectivities. This offset (1.5 dB) value has been used to adjust the radar constants and to provide the desired calibration of the MRR.

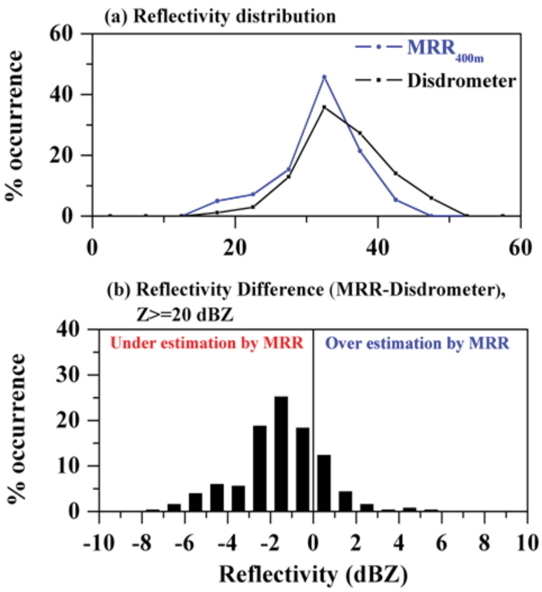

Figure 19: (a) Histograms of reflectivities inferred from MRR and disdrometer for rain event on 18 October 2006. (b) Histogram of the differences in Fig.19a, restricted in the range of 20–40 dBZ

The impact of the corrections is illustrated in Fig.20 by comparing rainfall rates inferred from the MRR and disdrometer. Prior to incorporation of any kind of corrections, the correlation coefficient for rainfall rates inferred from both measurements was about 0.94, which was improved to 0.96 after incorporating the corrections. The slope of the linear regression (after corrections) is close to 1.

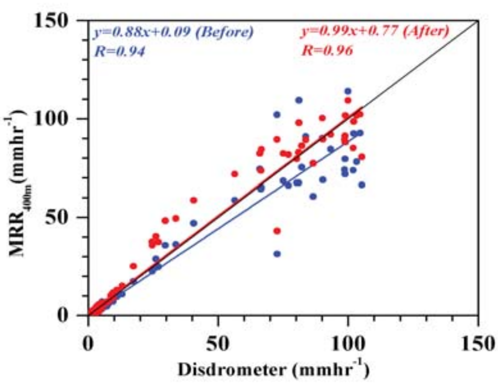

Figure 20: Scatter diagram of MRR and disdrometer for the rain event on 18 October 2006

Under the convective conditions, the reflectivities calculated from the drop size distributions of the MRR were in good agreement with disdrometer observations.

PUBLICATIONS IN REFERRED JOURNALS

1. Vigaud, N., P. Rouchou, V. Fontaine, S. Sijikumar, S. Tyteca, WRF/ARPEGE-CLIMAT simulated climate trends over west Africa, Climate Dynamics, DOI 10.1007/s00382-009-0707-4, 2010.
2. Xavier, P. K., V. O. John, S. A. Buehler, R. S. Ajayamohan, and S. Sijikumar, Variability of Indian summer monsoon in a new upper tropospheric humidity data set, Geophys. Res. Lett., 37, L05705, doi:10.1029/2009GL041861, 2010.
3. Bala Subrahamanyam, D., T. J. Anurose, "Solar eclipse induced impacts on sea/land breeze circulation over Thumba: A case study", J. Atmos. Solar-Terr. Phys., 73, 703 – 708, doi:10.1016/j.jastp.2011.01.002, 2011.
4. Bala Subrahamanyam, D., N.V.P. Kiran Kumar, C.B.S. Dutt, T.J. Anurose, P.K. Kunhikrishnan, Mannil Mohan, "Characterization of air-sea interaction processes over the Bay of Bengal during the winter phase of ICARB field experiment", Atmos. Res., 99, 97 – 111, doi:10.1016/j.atmosres.2010.09.005, 2011.
5. Denny P. Alappattu, P. K. Kunhikrishnan, "Observations of the thermodynamic structure of marine atmospheric boundary layer over Bay of Bengal, Northern Indian Ocean and Arabian Sea during premonsoon period", J. Atmos. Solar-Terr. Phys., 72, 1318 – 1326, doi:10.1016/j.jastp.2010.07.011, 2010.
6. Marina Aloysius, S. Sijikumar, S. S. Prijith, Mannil Mohan, K. Parameswaran, "Role of dynamics in the advection of aerosols over the Arabian Sea along the west coast of peninsular India during pre-monsoon season: A case study based on satellite data and regional climate model", J. Earth Syst. Sci., 120, No. 2, 269 – 279, 2011.
7. Sandhya K. Nair, T. J. Anurose, D. Bala Subrahamanyam, N. V. P. Kiran Kumar, M. Santosh, S. Sijikumar, Mannil Mohan, K. V. S. Namboodiri, "Characterization of the Vertical Structure of Coastal Atmospheric Boundary Layer over Thumba (8.5°N, 76.9°E) during Different Seasons", Advances in Meteorology, Volume 2011, Article ID 390826, 9 pages, doi: 10.1155/2011/390826, 2011.

PUBLICATIONS IN REFEREED PROCEEDINGS

1. Bala Subrahamanyam, D., T. J. Anurose, Radhika Ramachandran, Mannil Mohan, "Short-to-Medium Range Weather Forecasting for Satellite Launches: Utilization of NWP Models in conjunction with the Earth Observing Systems", Bulletin of National Natural Resources Management System, NNRMS(B) - 35, 37 – 49, 2010.
2. Bala Subrahamanyam, D., T. J. Anurose, "Solar Eclipse induced impacts on Sea/Land Breeze Circulation over Thumba: A Case Study", Proceedings of the National Workshop: Results on the Solar Eclipse, NaWRoSE, 154 – 158, 2011.
3. Bala Subrahamanyam, D., T. J. Anurose, Mannil Mohan, M. Santosh, N. V. P. Kiran Kumar, S. Sijikumar, "Impacts of Annular Solar Eclipse of 15 January 2010 on the Atmospheric Boundary Layer Characteristics over Thumba: A Case Study", Proceedings of the National Workshop: Results on the Solar Eclipse, NaWRoSE, 158 – 162, 2011.
4. Kiran Kumar N. V. P, M. Santosh, D. Bala Subrahamanyam, T. J. Anurose, S. S. Prijith, Marina Aloysius, S. Sijikumar, Mannil Mohan, "Response of Atmospheric Surface Layer to Annular Solar Eclipse Event on January 15, 2010", Proceedings of the National Workshop: Results on the Solar Eclipse, NaWRoSE, 162 – 165, 2011.

PRESENTATIONS IN SYMPOSIA/WORKSHOPS/CONFERENCES

International

1. D. Bala Subrahamanyam , T. J. Anurose, Radhika Ramachandran, S. Indira Rani, "Location Specific Weather Predictions for Sriharikota through Numerical Atmospheric Models during PSLV-C11 and PSLV-C12 Launch Campaigns", 7th Annual Meeting of Asia Oceania Geosciences Society, Hyderabad, July 5 - 9, 2010.

2. N. V. P. Kiran Kumar and P. K. Kunhikrishnan, “Vertical Variation of Drop Size Distribution (DSD) parameters at a Tropical Coastal Station Thumba”, Asia Oceania Geosciences Society (AOGS), Hyderabad, July 5-9, 2010.
3. S. S. Prijith, S. Sijikumar, Marina Aloysius and Mannil Mohan, “Inter annual variation of aerosol transport over the Arabian Sea during pre monsoon season”, 7th Annual General Meeting, Asia Oceanic Geosciences (AOGS-2010), Hyderabad, July 5-9, 2010.
4. S. S. Prijith, Marina Aloysius and Mannil Mohan, “Transport of aerosols over the Bay of Bengal during Winter-ICARB”, 7th Annual General Meeting, (AOGS-2010), Hyderabad, July 5-9, 2010.
5. S. Sijikumar, “Impact of Dust Aerosols on Indian Summer Monsoon: A Regional Climate modeling study”. 7th Annual General Meeting, (AOGS-2010), Hyderabad, July 5-9, 2010.
6. N. V. P. Kiran Kumar and P. K. Kunhikrishnan: “Vertical Variation of Drop Size Distribution (DSD) parameters at a Tropical Coastal Station Thumba”, 7th Annual General Meeting, (AOGS-2010), Hyderabad, July 5-9, 2010.

National

1. Sandhya K. Nair and S. Sijikumar, “Impact of Continental meteorology and atmospheric circulation in the modulation of Aerosol Optical Depth over the Arabian Sea”, METOC, Cochin, November 01-02, 2010.
2. M. Santosh, N. V. P. Kiran Kumar, Mannil Mohan and Denny P. Alappattu, “Atmospheric boundary layer characteristics during the Tropical Indian Ocean (TIO) Campaign”, National Conference on Advances in Atmospheric Remote Sensing, Weather Prediction and Climate Change, ARWPCC – 2011, Gadanki, March 10 – 11, 2011.
3. Neethu Purushothaman, N. V. P. Kiran Kumar, Mannil Mohan and P. K. Kunhikrishnan, “Investigation of Solitary wave like phenomenon over Coastal station Thumba”, National Conference on Advances in Atmospheric Remote Sensing, Weather Prediction and Climate Change, ARWPCC – 2011, Gadanki, March 10 – 11, 2011.
4. S. S. Prijith, Marina Aloysius, Mannil Mohan, Naseema Beegum and K. Krishna Moorthy, “Mechanism of aerosol transport over the Bay of Bengal during Winter-ICARB”, National Conference on Advances in Atmospheric Remote Sensing, Weather Prediction and Climate Change, ARWPCC – 2011, Gadanki, March 10 – 11, 2011.
5. S. S. Prijith, Marina Aloysius, Mannil Mohan, Naseema Beegum and K. Krishnamoorthy, “Role of circulation parameters on aerosol transport over the Bay of Bengal during ICARB Winter”, National Conference on Advances in Atmospheric Remote Sensing, Weather Prediction and Climate Change, ARWPCC – 2011, Gadanki, March 10 – 11, 2011.
6. S. S. Prijith, Sandhya K. Nair, Marina Aloysius, Mannil Mohan and K. Parameswaran, “Aerosol Generation and Transport over the Oceans around India: A Study with OCANSAT-2”, Oceansat 2 International AO Science Meet, Ahmedabad, March 23-25, 2011.

INVITED TALKS/LECTURES

D. Bala Subrahamanyam

1. “Atmospheric Impacts and Climate Change”, National Seminar on “Issues of Global Warming and Climate Change”, Christ University Nodal Office, October 08 – 09, 2010, Thiruvananthapuram.

Ph. D. AWARDED

Marina Aloysius, “A Study on Aerosol Transport Dynamics over the Indian Landmass and the Adjoining Oceanic Regions Using Satellite Data”, PhD. awarded in November 2010 under the Faculty of Sciences, Department of Physics, Cochin University of Science and Technology (Guide: Dr. K. Parameswaran/Mannil Mohan, SPL).

DEPUTATIONS TO CONFERENCES/WORKSHOPS/INSTITUTE/SCHOOL

Mannil Mohan, N. V. P. Kiran Kumar, S. Sijikumar, S. S. Prijith, T. J. Anurose, 7th Annual Meeting of Asia Oceania Geosciences Society, Hyderabad, July 5 – 9, 2010.

D. Bala Subrahamanyam, Regional Numerical Weather Prediction and Data Assimilation Training Workshop, Meteorological Training and Conference Centre, Deutscher Wetterdienst, Langen, Germany, July 19 – 30, 2010.

T. J. Anurose, SERC School on "Ocean-Atmosphere Interactions and Global Change" sponsored by the Department of Space and Technology, Organized by the Department of Meteorology and Oceanography, Andhra University, Visakhapatnam, July 14 – August 03, 2010.

Sandhya K. Nair, METOC, Cochin, November 01-02, 2010.

M. Santosh, Neethu Purushothaman, National Conference on Advances in Atmospheric Remote Sensing, Weather Prediction and Climate Change, ARWPCC – 2011, Gadanki, March 10 – 11, 2011.

ACADEMIC PROJECTS

Internship for M. Sc.: 5

Atmospheric Dynamics Branch

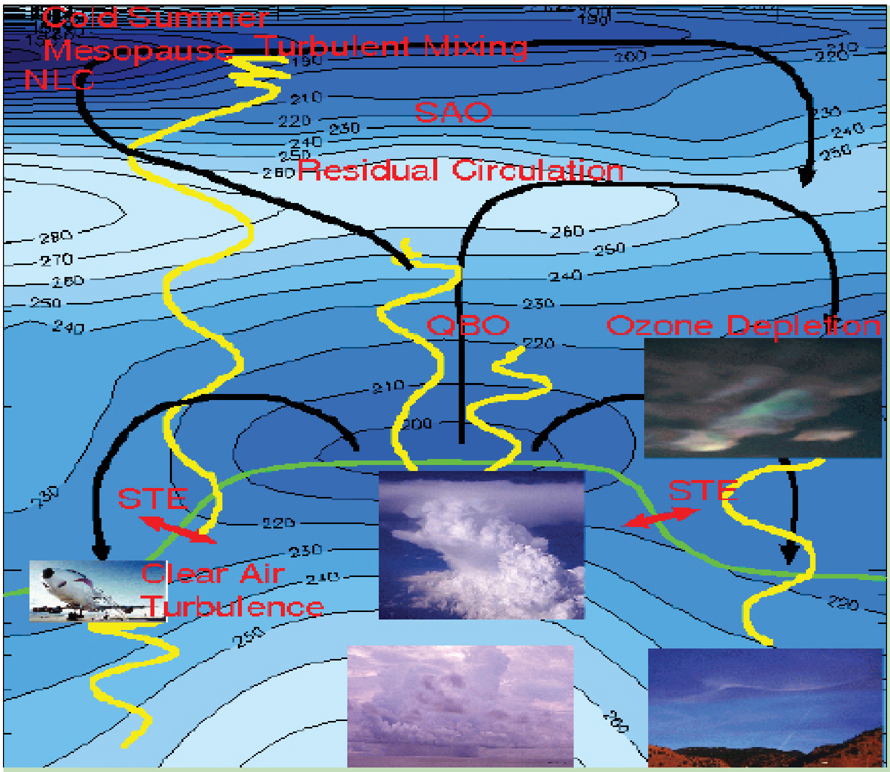

Science Faculty

Geetha Ramkumar
Kishore Kumar K
Sunil Kumar S V
Siddarth Shankar Das
*Uma K N
Subrahmanyam K V

Visiting Scientist

Parameswaran K

Technical Team

Mohankumar S V
Shajahan M
Manikantan Nair
Mohammad Nazeer M

Research Fellows

Veena Suresh Babu
Sherine Rachel John
Asha Babu

Now transfer to AACCR group

Characterization of entire atmospheric motion spectra, ranging from gravity waves to solar cycle, their source mechanisms and the global scale modulations of geophysical parameters is the prime objective of the Atmospheric Dynamics Branch (ADB). Data from ground and space based measurements of geophysical parameters are extensively used to characterize waves, oscillations and their manifestation apart from middle atmospheric dynamics studies, on clouds and climate dynamics including the tropical tropopause layer, troposphere-stratosphere exchange process, mesoscale convective systems, and the long-term variability of middle atmospheric dynamics. Following are the accomplishments of ADB during the year 2010-2011.

1. CONVECTION, TURBULENCE AND GRAVITY WAVE STUDIES

Tropical stratosphere dehydration during Asian Summer Monsoon

Space-time variations of upper troposphere and lower stratosphere (UTLS) water vapor over Asian summer monsoon (ASM) regions are investigated using the six year data from the AURA-MLS in a bid to re-evaluate the role of ASM in dehydrating the tropical stratosphere. Figures 1a and b show the monthly means of water vapor at different pressure levels from MLS over Northern Bay of Bengal (NBoB) and East Equatorial Indian Ocean (EEIO), respectively. It is clearly seen that during June to September, the concentration of water vapor has been consistently high in the UTLS region, caused by the deep convective clouds with a large vertical extent.The plots of daily mean OLR for these two regions, (Fig.2), clearly shows low OLR (< 220 W m^{-2}) during June to September implying deep convection capable of pumping large quantity of water up to and above the tropopause. In the present study, during ASM period ~ 10 ppmv of water vapor is observed in the vicinity of tropopause (VOT), and around 4-8 ppmv is observed in the lower stratosphere. Despite of the water vapor availability at VOT during June to September, the moist air enters lower stratosphere only during August, even over EEIO, where the deep convection prevails throughout the year. In order to investigate this interesting aspect, we have analyzed temperature from MLS in the UTLS regions (Fig.3a and b). It is clearly evident that during the month of August the VOT is warmer compared to other months and study shows that if the tropopause is warmer, moist air enters the stratosphere and hydrate it. However, episodic overshooting of convection and subsequent dehydration of lower stratosphere is not ruled out during ASM. But on the monthly time-scales these episodic

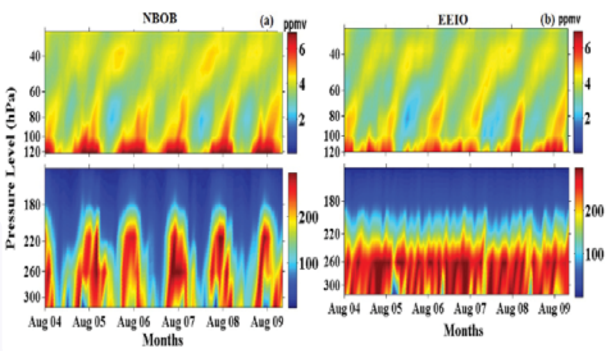

Figure 1: Monthly mean of water vapor at different pressure levels for (a) NBOB, and (b) EEIO

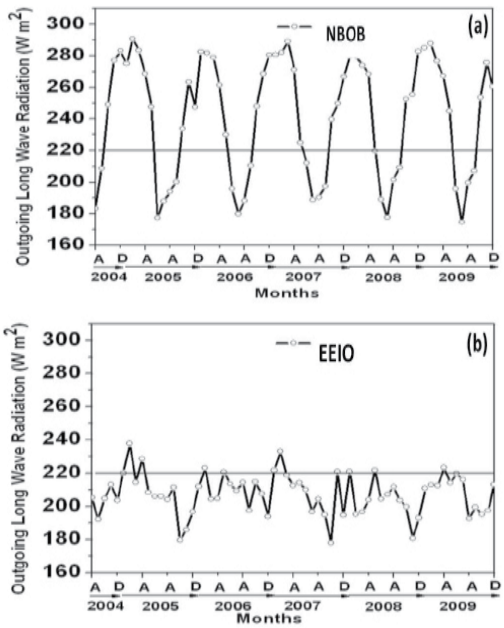

Figure 2: Outgoing long wave radiation (OLR) over (i) NBOB and (ii) EEIO

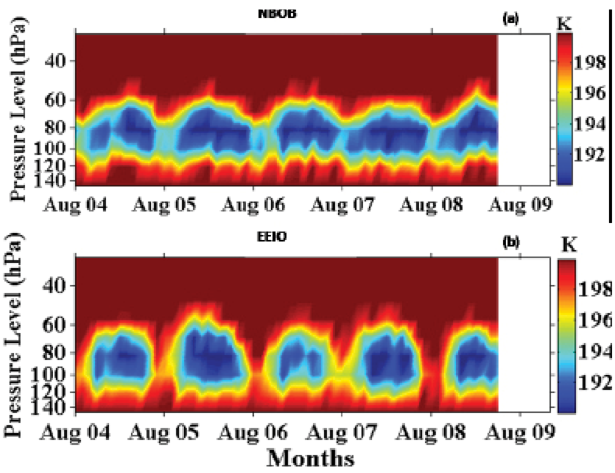

Figure 3: Monthly mean of Temperature at different pressure levels over (a) NBOB and (b) EEIO

intrusions seems to be insignificant as revealed by the Fig.1. The air parcel from the tropical tropopause takes approximately around 10-12 months to reach the mid stratosphere with an ascent rate of 2.8 x 10^{-4} m s^{-1}. The investigations revealed, for the first time, that the ASM region plays an active role in hydrating rather than dehydrating the tropical lower stratosphere.

Mesoscale convective system leading to breaking of Kelvin-Helmholtz instability

Kelvin-Helmholtz instability (KHI) is a dynamical instability produced in a hydrostatically stable layer in the presence of a strong stratified vertical shear in wind flow, and is one of the causative mechanisms for turbulence throughout the atmosphere from Earth's surface to the lower thermosphere. It contributes to vertical mixing of heat, momentum, and constituents, and in extreme cases it poses risks to aircraft navigation. A case study of a mesoscale convective system (MCS) leading to turbulence generated by breaking of KHI in the lower stratosphere (~ 18.5 km) is presented in Fig.4, which shows a successive power burst pattern in the lower stratosphere in the MST radar return signal lasting for ~ 2.5 hr. The thickness of the power burst pattern is about ~ 500 m. Analysis shows the enhancement of stability parameter (N^2, N is the Brunt-Vaisala frequency) in the lower stratosphere, where the power burst pattern is observed, indicating the presence of a statically stable layer. This statically stable layer is overcome by the presence of strong wind shear in its interface to make it dynamically unstable. Further, estimation of Richardson number ($Ri<0.25$) confirmed the favorable conditions for the occurrence of KHI, which broke at 20:15 IST. The time series of vertical velocity at 18.5 km (Fig.5a) shows the presence of strong updrafts and downdrafts of order ± 1 m s^{-1} (± 2 m s^{-1}) in the initial (final) phase of MCS. Figure 5b shows the corresponding wavelet spectra, which indicate the presence of dominant periodicity 15-20 min. This is attributed due to the presence of short-period convectively generated gravity wave (CGW). It is interesting to note the coincidence of breaking of KHI and the enhanced amplitude of CGW. Thus, the strong updrafts and downdrafts of order ± 2 m s^{-1} observed during 20:00-21:30 IST is due to CGW, which is believed to be the main reason behind the breaking of KHI.

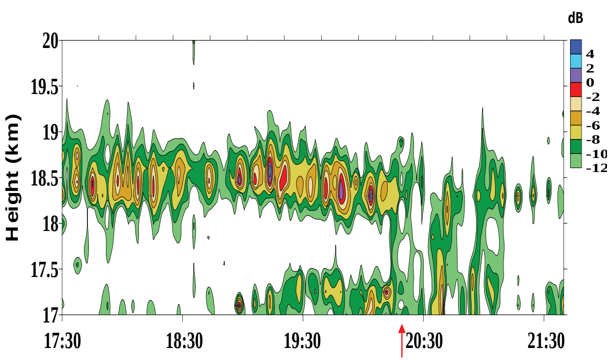

Figure 4: Height-time section of signal-to-noise ratio (SNR) from 17:30 to 21:30 IST on 19 June 2006

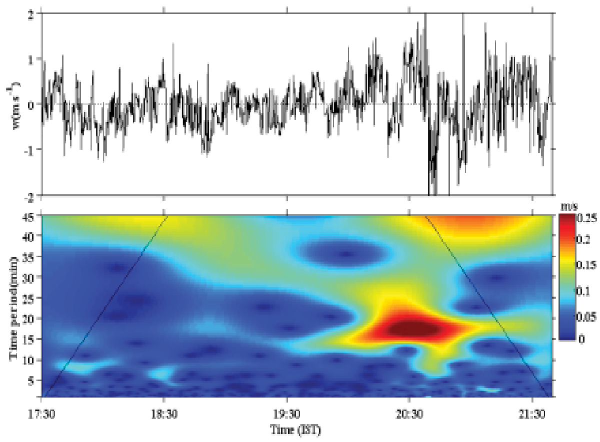

Figure 5: Time series of vertical velocity (a), and (b) wavelet spectra at 18.5 km on 19 June 2006

Turbulence due to shorter-vertical scale gravity waves in the lower stratosphere

Though the role of the layers of temperature gradient in the lower stratosphere in causing multiple specular echoes in VHF radar is known, the exact causative mechanism is not fully understood. These layers are also responsible for aspect-sensitive characteristics of VHF radar, which may also bias the vertical velocity measurements. In order to understand the generative mechanism of these layers, an intensive campaign has been carried out using concurrent operation of VHF radar for 72 hrs with time resolution of ~ 4 min and

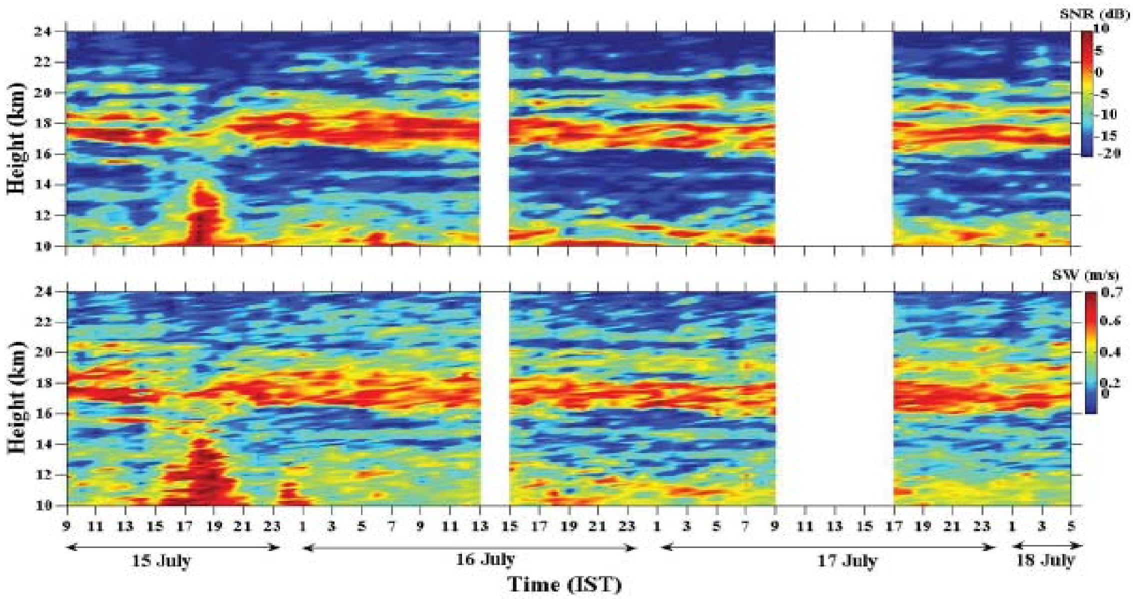

Figure 6: Height-time section of (top) signal-to-noise ratio (SNR) and (bottom) full spectral width (SW) between 15 and 18 July 2008

GPS sondes ascents at 6 hrs interval. Figure 6 shows the height-time section of vertical beam signal-to-noise ratio (SNR) and full power spectral width between 15 and 18 July 2008. Multiple specular echoes in SNR plot are clearly seen in the lower stratosphere. The enhancement in the spectral width corresponding to the specular echoes, indicating the presence of turbulence activity is clearly seen. The corresponding temperature fluctuation profiles are shown in Fig.7. Strong positive and negative temperature gradient is observed in the upper troposphere and lower stratosphere (UTLS) and with amplitude upto ± 5 K. This temperature fluctuation in the UTLS region is attributed to the propagation of gravity wave. The thicknesses of these layers are ~ 500 m and vertical wavelength of the order 2-3 km. Further analysis of wind shows the presence of long-period gravity waves with short vertical wavelengths in the lower stratosphere.

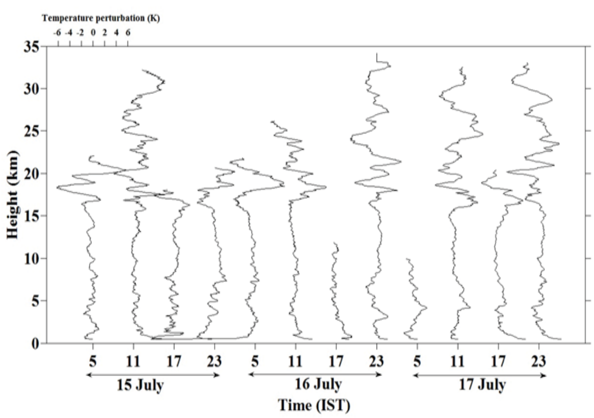

Figure 7: Temperature fluctuation between 15 and 18 July 2008. The temperature profiles are shifted by 7 K

Isotropic VHF radar echoes around tropopause during cyclone/depression

Earlier observations have shown that during clear-sky conditions, the radar backscattered echoes show aspect sensitivity by which the echo strength decreases as a function of zenith angle at a rate of ~ 1dB/degree between 0° to 10° zenith angle and ~ 0.5 dB/degree between 10° to 20° zenith angle in the vicinity of tropopause (VOT). These aspect sensitive characteristics become weak when a depression or cyclone is located close to the radar site. Under such condition, the radar backscattered echoes at zenith and off-zenith depict nearly equal strength. To investigate the probable causative mechanisms, a special multi-beam experiment of MST radar was designed along with GPS sonde flights, which provided high resolution measurements of meteorological parameters during the passage of tropical cyclone 'Nisha' from 24-30 November 2008. The signal-to-noise ratio (SNR) map as a function of zenith angle in (left) east-west and (right) north-south plane when the cyclone Nisha was close to the radar site at 15:30 IST of 27 November 2008 is shown in Fig.8, which shows strong echoes at all zentih angles. Figure 9 shows the height profiles of (a) temperature, (b) stability parameter, (c) square of vertical shear of horizontal wind, and (d) Richardson number at 15:00 IST on the same day. The cold-point tropopause was at 17 km (black arrow), which is ~ 1 km above the mean tropopsue height(~16.2 km) at this latitude. The red arrow indicates height at which the non-aspect sensitive echo layer was observed. Thus, it is found that

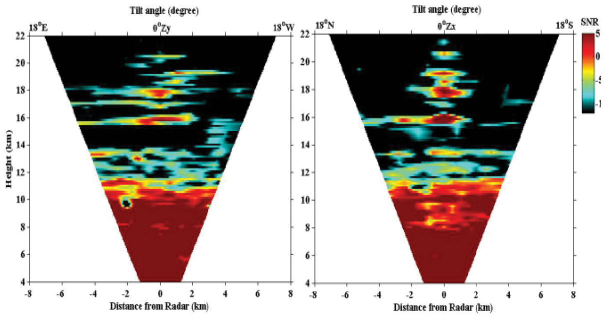

Figure 8: Intensity map of signal-to-noise ratio (SNR) as a function of zenith angle in (left) east-west and (right) north-south plane at 15:30 IST of 27 November 2008

while the aspect sensitive characteristics of tropopause during cyclone remain the same as that of normal weather conditions, the non-aspect sensitive layer structures form beneath the tropopause (~1.5 to 2 km below) during depression. The observed layer structures show a strong temperature inversion of about ~2 K. Enhancement in the stability parameter is also observed in its vicinity with strong wind shear, which overcomes the atmospheric stability. The Richardson number estimated is less than its critical value (Ri < 0.25) to form shear instability. Further, a periodic enhancement in the radar backscattering echoes coupled with enhanced spectral width was manifested during the event. Thus, the present study has shown that it is not the tropopause characteristics manifested by enhanced turbulence but it is the shear instability which occurs ~2 km below the tropopause, which gives rise to strong isotropic echoes.

2. TROPICAL TROPOPAUSE LAYER AND STRATOSPHERE-TROPOSPHERE EXCHANGE

Variability of temperature lapse rate in the Tropopause region over the Indian region

Even though the nature of the annual variations of the tropical tropopause layer (TTL) thickness and the temperature difference between its upper and lower boundaries are similar over the tropics, their magnitudes differ. As such, the temperature gradient within the TTL (and the vertical transport of tropospheric airmass across the TTL) exhibits temporal and spatial variations. In the light of the above, the temperature lapse rate (γ_{TTL}) across the TTL $[-\Delta T_{TTL} / \Delta H_{TTL}]$ for the region from 35°S to 35°N are examined over the Indian longitude sector (70-90°E) using Radio Occultation (RO)-data for the period 2006-2009. Figure 10 shows the annual variations of γ_{TTL} as a function of latitude. In general, γ_{TTL} is quite large in the equatorial region and decreases with increase in latitude beyond ± 15°. The annual variation of γ_{TTL} is small in the equatorial region depicting a winter high and summer low, while at the off-equatorial region of northern hemisphere the annual variations are pronounced with minimum values during Boreal winter and maximum during the ASM (June-September) period.The maximum value of off-equatorial γ_{TTL} is comparable to the minimum value over the equatorial region during the ASM pe-

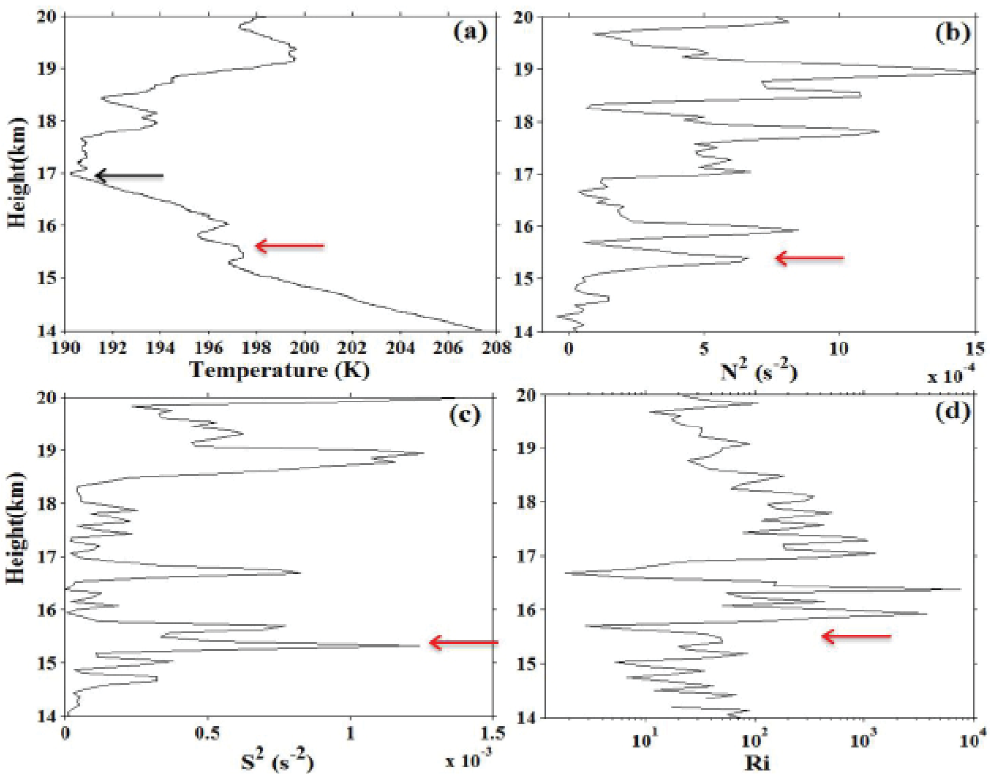

Figure 9: Height profiles of (a) temperature, (b) stability parameter, (c) square of vertical shear of horizontal wind, and (d) Richardson number at 15:30 IST of 27 November 2008

riod. Increase in γ_{TTL} being indicator of a relative increase in the strength of tropospheric convection.The results suggest that the deep convection prevailing in the equatorial region intensifies during the ASM period and spreads towards north engulfing the entire Indian landmass. Over the Southern hemisphere off-equatorial region, annual variations in γ_{TTL} are highly subdued indicating weak convection.

Cloud dynamics and particle microphysics in the Tropopause region

To investigate the "Cloud dynamics and particle microphysics in the UTLS region and its association with Tropical Tropopause Layer" coordinated experiments are being carried out (at SPL, and NARL), since December 2010 as part of the Tropical Tropopause Dynamics (TTD) Experiment under CAWSES-India program. The campaign involves intense observations for three consecutive days in each month using lidars and 3 hr interval GPS-sonde ascents concurrently from Trivandrum and Gadanki, besides MST radar measurements from Gadanki. Satellite (KALPANA / CALIPSO) observations of the regional distribution of tropospheric clouds (effectively the prevailing convection) also would be used.

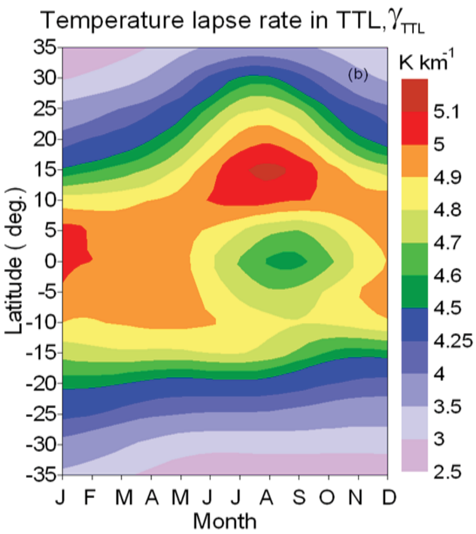

Figure 10: Mean annual variation of γ_{TTL} in different latitude bands from 35°S- 35°N over the Indian longitude sector obtained from RO-data during the period 2006-2009

3. ATMOSPHERIC WAVES/ OSCILLATIONS

Quasi-Biennial Oscillation - An evidence of relation with weather related phenomenon

An investigation on the climatology of the Quasi Biennial Oscillation (QBO) and its influence on monsoon variability and rainfall pattern over Indian regionhas been made making use of the monthly mean winds in the 0-30 km and 30-50 km region over Thumba derived from Radiosonde data (1970-2010), M100 (1970-1993) and RH 200 rocket flights (1980's and 2002-2007). Gaps in the rocketsonde data from June 1974 to April 1975 and 1990-2002 are filled using ECMWF reanalysis data after doing methodical comparison. To examines thevariability of QBO and quantify the same, all the spectral components except in the period range 18-36 months are removed from the deseasoned monthly data by adopting a band pass filtering technique. In the same way for characterizing Semi Annual Oscillation (SAO) variability, we have taken only 6 month periodic components. This trend removed rain fall data is compared with QBO amplitudes.

Figure 11 shows the observed QBO structure from balloon borne data. Alternating easterly and westerly wind regimes with average period of 28 months propagate downward with an average descend rate of 1.1 km month^{-1}. Both period and amplitude is found to vary considerably from cycle to cycle. Maximum amplitude of QBO is observed during 1976-78, 1986-88, 1990-1992, and 2000-2003. During 2000-2003 both amplitude and period of the QBO cycle is found to be extremely large (18 m s^{-1} and ~36 months), compared to all other cycles. Examining these QBO structures from radiosonde data and the SAO structure from rocketsonde data (Fig.12),. it is observed that origin of westerly phase of QBO is associated with decending phase of westerly SAO. SAO is found to exhbit seasonal assmmetry.

The Indian summer monsoon is a giant feedback system involving interactions between land, ocean and atmosphere. In the middle atmosphere different seasons like pre-monsoon, monsoon and post-monsoon are expected to have their signatures in the strength and characteristics of upward propagating waves and their interaction with the mean flow producing QBO. Rainfall data over Indian peninsular region during

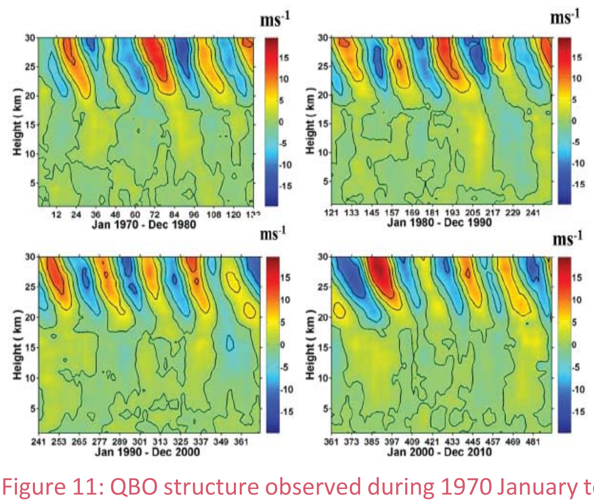

Figure 11: QBO structure observed during 1970 January to 2010 December from Balloon data at Thumba

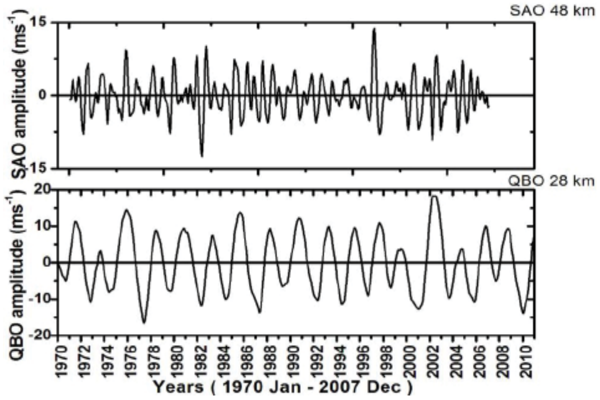

Figure 12: Comparison of observed QBO amplitude at 28 km and SAO amplitude at 48 km

1971-2006 is used for the present study. A comparison of the trend removed rainfall activity with the QBO at 28 km and SAO at 48 km is shown in Fig.13. It is seen that the monsoon seasons associated with maximum easterly phase of QBO have heavy rainfalls while monsoon associated with maximum westerly phases of QBO are associated with drought. A sharp change of QBO phase from westerly to easterly is found to be followed by a heavy rainfall. Maximum amplitude of about 15 m s^{-1} of QBO westerly phase is observed during the year 1977-1978, and 18 m s^{-1} during 2002- 2003 both being severe drought years. Mostly small amplitudes of SAO are indicating of heavy rainfall and large amplitudes of SAO with more durably less rainfall.

Global Signatures of QBO, AO and SAO in Gravity Wave Potential Energy

The global gravity wave activity is studied using the TIMED/SABER measurements of temperature profiles in the 20-100 km height domain. Quasi-biennial oscillation (QBO) in the gravity wave potential energy in the lower stratosphere (20-30 km) and semi-annual oscillation (SAO) in the upper stratosphere (40-60 km) are discernible in the time series of monthly mean gravity wave potential energy over the equatorial region (0-5°N) during 2003-2007, shown in Fig.14. The height-month section of wind measurements made over Thumba (8.5° N, 77° E) during the period 2003-2007 under the MIDAS campaign are superimposed on this. The potential energies resemble the equatorial stratospheric wind pattern, a classic example of wave-mean flow interactions.

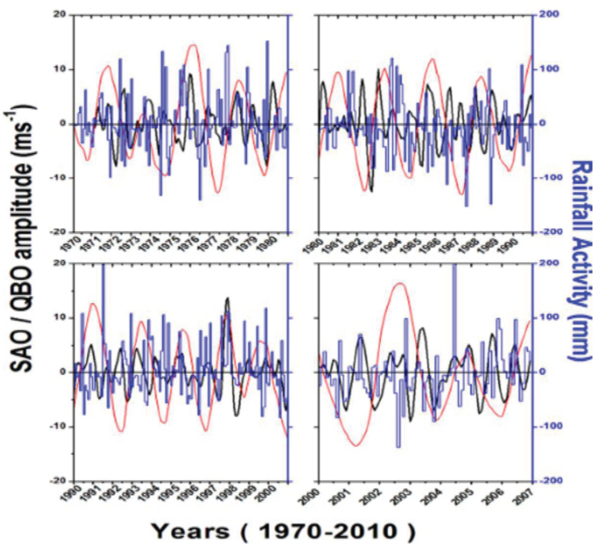

Figure 13: Comparison of observed QBO amplitude at 28 km (red line) and SAO amplitude (black line) at 48 km with trend removed rainfall activity

Extending these analyses to other latitudes and altitudes, the longitudinally averaged time series of monthly mean potential energies are constructed during the years 2003-2007 at 5° latitude intervals

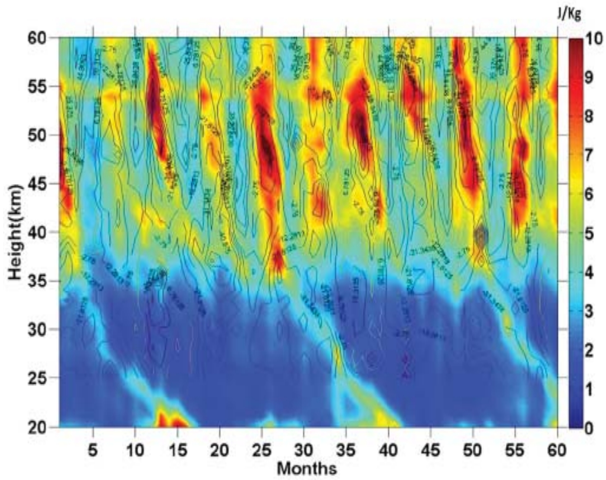

Figure 14: Monthly mean gravity wave potential energy during 2003-2007 in the stratosphere over the equatorial region (0-5°N) and superimposed zonal winds measured over Thumba using rocket flight

between 50°N-50°S region and 1 km altitude bin in the height region 20-100 km. Thus obtained latitude-height-time section of gravity wave potential energy is obtained. To overcome the effect of large difference in the potential energy over different latitudes and altitudes, the potential energy is normalized to the peak value at each latitude and altitude. From the time series, the QBO, AO and SAO amplitudes at each latitude and altitude are extracted through spectral analysis. Results are shown in Fig.15 (a-c). Figure 15a shows that the maximum amplitudes of QBO in GW potential energy is limited to equatorial latitudes and to the height region of 20-30 km, with a north-south asymmetry about the equator.While the amplitudes extend up to 20°N, it is limited to only 10°S. Thus, over the equatorial latitudes the inter-annual variability in gravity wave activity is domi-

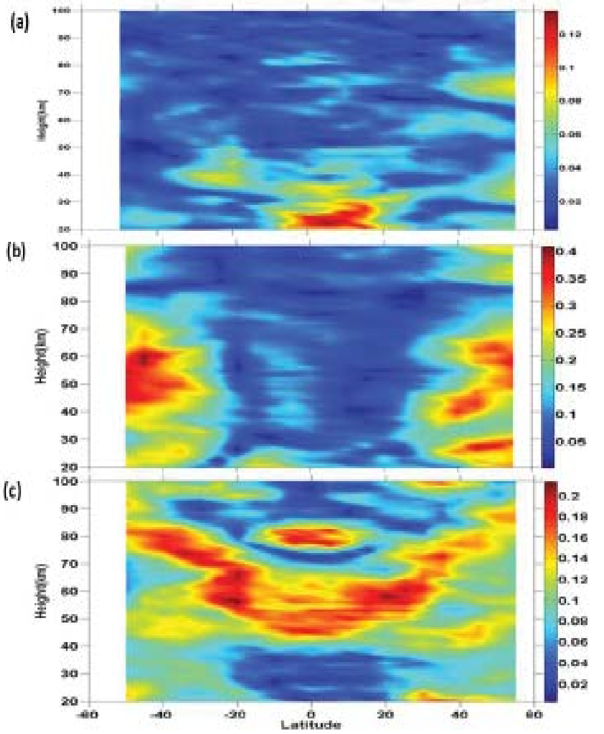

Figure 15: The height-latitude section of the amplitudes of (a) QBO (b) AO and (c) SAO in gravity wave potential energy. The colour scale is in arbitrary units

nated by QBO in the lower stratosphere.Unlike this, it is evident from Fig.15b that the AO is dominant throughout the stratosphere over midlatitudes of both the hemispheres. A secondary peak in AO can be noticed in the MLT region, again over midlatitudes, especially in the Northern hemisphere. However, AO is completely absent over the equatorial latitudes. Finally, the height-latitude section of amplitude of SAO (Fig.15c), quite interestingly shows the variation of amplitudes across the latitudes and altitudes appearing as a necklace. Over the equator, the SAO amplitudes show a broad peak in the upper stratosphere (40-65 km) and another distinct peak in the 75-85 km altitude. The SAO amplitudes are totally absent in the lower stratosphere and lower thermosphere heights. Interestingly the increase in SAO peak altitude with latitude is symmetric about the equator. From 30° to 50° latitude on either side of the equator, the peak SAO altitude gradually increases from 65 to 85 km. The present study, thus, for the first time, reports the height-latitude section of all the three oscillations, QBO, AO and SAO in gravity wave activity.

Dynamics modulating the spatial structure of stratospheric aerosols

Spatio-temporal variabilities in background stratospheric aerosols over the tropics (30ºS to 30ºN) and their association with the dynamical features of stratosphere have been investigated using the zonal averaged, SAGE-II derived aerosol extinction coefficient at 525 nm along with lidar data at 532 nm from Gadanki [13.5ºN, 79.2ºE] during the period 1998-2005, a period relatively free from major volcanic events. In general, a well pronounced increase in aerosol optical depth, τ_p, in the lower stratosphere 18-28 km, has been observed in the spatial distribution of aerosols over the equatorial region compared to the off-equatorial regions. Out of the 8-year period considered here, the period 1998-2002 was volcanically quiescent as far while the period 2003-2005 was mildly disturbed. The temporal variations of zonally averaged, monthly mean τ_p in the latitude region 30°S to 30°N (averaged for every 5°) are examined in Fig. 16. During the former half (very quiet period), the mean τ_p over the equatorial region shows a general enhancement during westerly phase of QBOU (QBO in zonal wind) while over the off-equatorial regions of northern hemisphere it shows an enhancement during the easterly phase of QBOU (Fig 16a). During the westerly phase of QBOU, τ_p decreases sharply with increase in latitude on either side of the equator. During the easterly phase of QBOU, though τ_p decreases with increase in latitude beyond 15ºN, it is fairly uniform in the equatorial region (15ºS to 15°N) with a small 'bite-out' near the equator. During the latter half (mildly disturbed period), the value of τ_p decreases steadily with increase in latitude from the equator on either side, both during the easterly and westerly phase of QBOU (Fig.16b). Moreover, while in the equatorial regions, the values of particulate extinction (α_p) in the altitude region 20 to 27 km are consistently lower during the easterly phase of QBOU than those during the westerly phase, in the off-equatorial region, these values are found to be relatively low during the westerly phase.

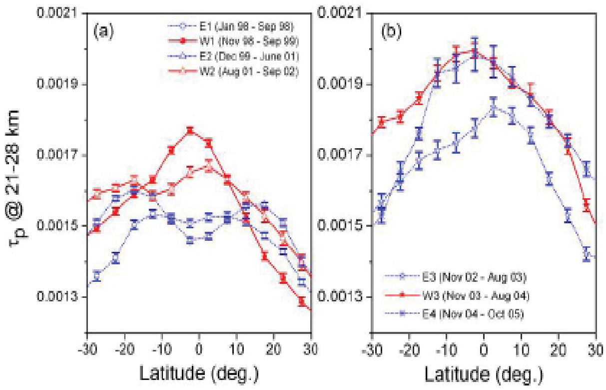

Figure 16: Latitude variation of zonal mean tp in the altitude region 21-28 km from 30°S to 30°N obtained from SAGE-II during the alternate easterly and westerly phases of QBOU during the absolute quiet period (1998-2002) and mildly disturbed period (2003-2005). Vertical bars in each panel show the corresponding standard error

Analysis of the zonally averaged monthly mean τ_p (from SAGE-II) in the altitude region 18-28 km, averaged over the equatorial (0-15°N, 0-15°S) and off-equatorial region (15-30°N and 15-30°S) (Fig. 17a and b), reveal the presence of a strong annual component (~12 months) along with a Quasi-biennial component (with period ~30 months). The spectral amplitude of QBO is as strong (significant) as that of annual oscillation (AO).

With a view to examining the altitude structure of QBO signal in aerosol extinction, the monthly mean zonally averaged values of τ_p (from SAGE-II) at different altitudes from 18 to 32 km in the four latitude bands are spectrum analyzed and the amplitude and phase of QBO (30 months) at different altitudes are

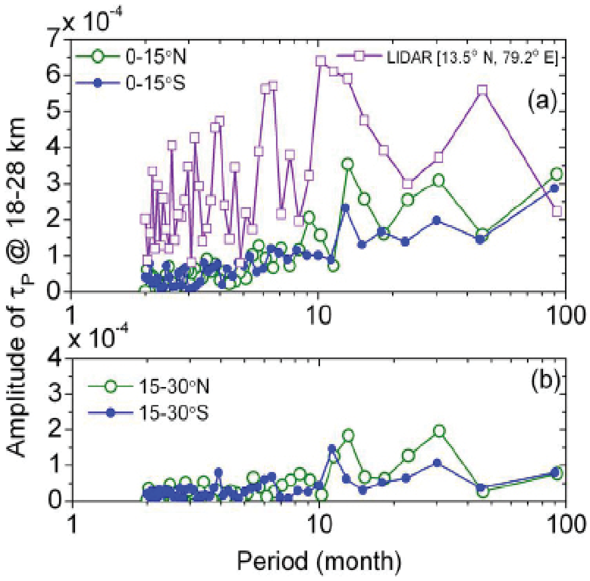

Figure 17: Amplitude spectra of τ_p in the altitude region 18-28 km, derived from the SAGE-II data for the equatorial (a) and off-equatorial regions (b) during the period 1998-2005. Amplitude spectra of τ_p obtained from lidar data at Gadanki is also shown in panel (a)

examined in Fig.18. In the equatorial region the QBO amplitude clearly shows three peaks centered around 20 km, 25 km and 30 km. The phase structure shows that the QBO around 25 km is out-of-phase with that in the upper (28-32 km) and lower regime (18-22 km). However, over the off-equatorial region, in the southern hemisphere the amplitude of QBO (in τ_p) shows a broad maximum in the altitude region 24-28 km with its peak centered around 26 km. In the northern hemisphere, it shows a peak centered around 29 km.

The cycle-to-cycle variation of the QBO (in τ_p) in the equatorial region is examined in detail by subjecting the time series of τ_p in the three altitudes 20, 25 and 30 km to wavelet analysis. This result, presented in Fig.19, shows the temporal repeatability of QBO phase structure in these three altitude regions. The

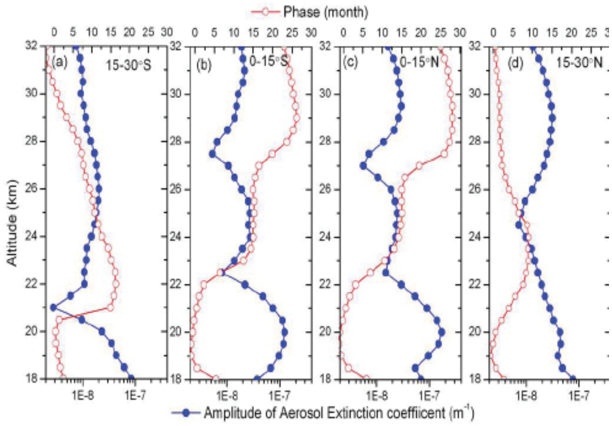

Figure 18: Altitude structure of the QBO amplitude and phase in aerosol extinction for the altitude region 18-32 km in the equatorial (0-15°N and 0-15°S) and off-equatorial regions (15-30°N and 15-30°S)

phase of QBOU matches with that of QBO in τ_p in the middle regime (25 km) where as it is in opposite phase with those in the lower (20 km) and upper (30 km) regime. Over the equatorial region, the observed features of QBO (in τ_p) in the three altitude regions is attributed to the signatures of the secondary meridional circulation (SMC) induced by the vertical shear of QBO in stratospheric zonal wind.

Gravity Wave Potential Energy and Gravity Wave Spectrum Seen by Different Satellites Techniques

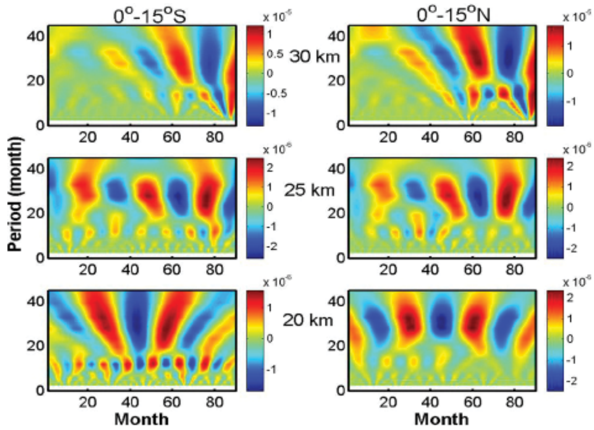

Figure 19: Wavelet analysis of mean aerosol extinction for each month at 20 km, 25 km and 30 km for the equatorial region 0-15°N and 0-15°S during the period 1998 to 2005

An investigation is made of the observational filtering effect of satellite techniques, which is the limitation of a particular technique from seeing the complete spectrum of gravity waves, using data from the limb viewing satellites, TIMED/SABER and Aura/HIRDLS with different horizontal resolutions, a radio occultation satellite COSMIC/FORMOSAT-3, and a nadir viewing satellite AQUA/AIRS. Temperature data from these four satellite payloads for the period

2006 December to 2007 November are used. Potential energy is calculated using in-house developed algorithm in the height from 20 to 40 km and averaged seasonally over the globe, i.e., for Winter (Dec-Feb), Vernal Equinox (Mar-May), Summer (Jun-Aug) and Autumnal Equinox (Sep- Nov) with respect to the Northern Hemisphere. The potential energy map obtained for SABER, HIRDLS, COSMIC and AIRS for austral winter is shown in the Fig.20 (a-d). Despite the payloads having different vertical and horizontal resolutions, their potential energy maps are strikingly similar in pattern but differing in magnitude. One of the most significant observations from these maps is the maxima at the tip of South American continent seen in potential energy values for all the satellites. During the winter corresponding to both hemispheres, gravity wave activity is very pronounced around high and polar latitudes and confined to the longitudes of -1000 to 1000, with equinoxes having minimum values. SABER has the poorest horizontal resolution of ~300 km whereas HIRDLS has a very good resolution of ~75-100 km. Both these limb viewers have good vertical resolution. So any wave that SABER captures, HIRLDS will also be able to see. But SABER has higher magnitudes than HIRDLS which can be explained on the basis of ray path of the limb view and corresponding weighting functions. As COSMIC uses radio occultation technique, the distance between consecutive profiles over the globe vary largely. But occultations over a period of time (say a few hours) will give profiles near by which will be capable of deciphering gravity waves with larger wavelength and longer periods, but not shorter wavelengths. AIRS being a nadir viewing satellite has very good horizontal resolution of ~ 45 km, but has poor

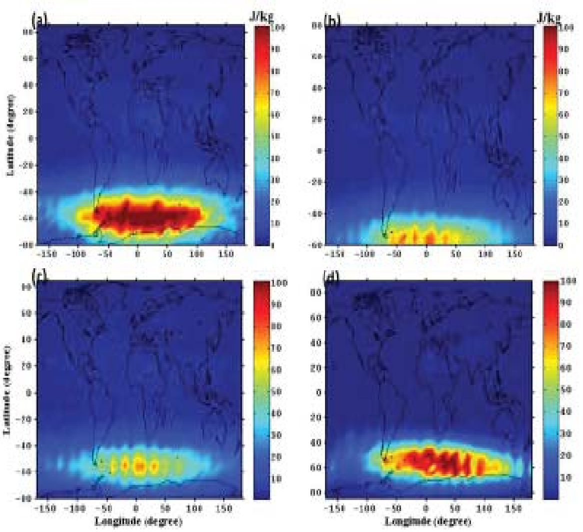

Figure 20: Global maps of gravity wave potential energies during austral winter using (a) SABER, (b) HIRDLS, (c) COSMIC and (d) AIRS satellite observations

vertical resolution which makes it impossible for it to capture waves with vertical wavelength more than 12 km. The polar highs in wave activity are attributed to the polar jets, which form a very strong source of gravity waves as well as play a role in shifting the gravity wave spectrum from lower wavelengths to higher wavelengths thereby increasing the saturation limit as well as visibility of the wave to the satellite. Poleward propagating Rossby waves break in the vicinity of tropospheric jets resulting in the generation of stratospheric Inertio-gravity waves (IGWs). Since IGWs have longer horizontal wavelengths, they can be captured by all the four satellites that we have used in this study. We have also simulated a uniform gravity wave field with known parameters over the globe and have used the sampling of these satellites to establish our conclusions.

Asynoptic spectrum estimation for satellite based planetary wave

In the backdrop of the above, it emerges that it is not possible to study the quasi 2-day wave with available satellite observations, due to resolution constraints. In a novel approach, by treating the space and time as single variable, an attempt is made to extract the quasi 2-day wave from the ascending and descending node temperature profiles of SABER around 85 km in in the 5-10°N latitudinal circle during the month of October 2006 by employing asynoptic spectrum approach. Figure 21a is the wavenumber-frequency section of temperature observations at 85 km height region, showing westward propagating wave with 2-day periodicity (frequency 0.5 day^{-1}) and zonal wavenumber 3. However the spectrum suffers from aliasing. As such, we have computed the aliasing spectrum by simulating a westward propagating quasi 2-day wave with wavenumber 3 and then sampled the same by mimicking the SABER observational pattern. Figure 21b shows the resulting aliasing spectrum, which readily reveals the presence of the simulated wave. However, there seems to be spectral leakage in the aliasing spectrum as one can note the spreading of spectral power from quasi 2-day wave to adjacent periods. In the aliasing spectrum, apart from the simulated wave (0.5, -3), there is another component at (0.6, 2), which may be an artifact due to the sampling pattern of SABER. This artifact also appears in the observed SABER spectrum shown in Fig.21a. Thus the present method for estimating the time-space asynoptic spectrum is very useful for studying the short-period planetary waves (for example quasi 2-day wave) on the global scale, which cannot be retrieved from standard spectral analysis.

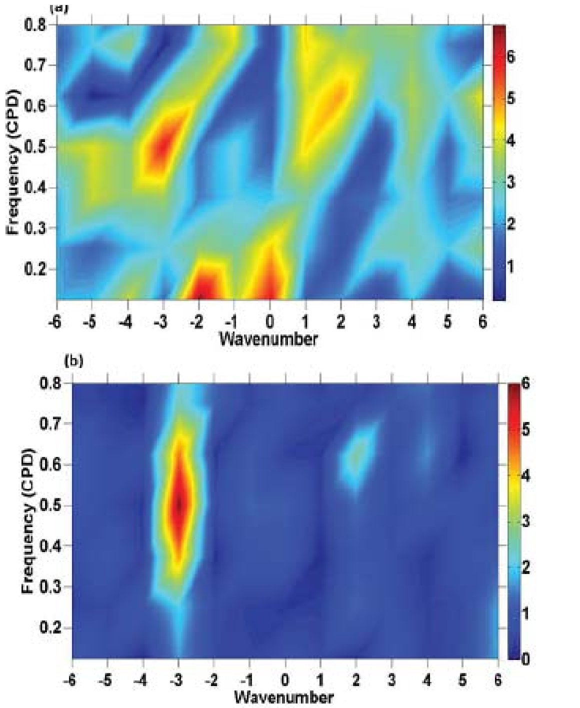

Figure 21: Frequency-wavenumber spectrum of temperature at 85 km height region over low latitude (5-10° N) estimated using TIMED/SABER observations using 15 days of observations during October 2006 (a). Aliasing spectrum for simulated westward propagating quasi 2-day wave with simulated wave (b)

4. MLT REGION STUDIES

Two-Level Wave Turbopause

The wave turbopause is defined as the mesospheric altitude, where the temperature fluctuation field indicates a substantial increase in wave amplitudes in the vertical direction and the dissipative regime ends. An analysis using 3-years (2004-2006) of SABER temperature measurements revealed that turbopause is not a single altitudinal level, but is a layer bounded by 'lower turbopause' and 'upper turbopause'. This double turbopause structure is seen at all the latitudes as shown in Fig.22 (a and b) for boreal winter and summer respectively. The lower turbopause is confined to heights below 90 km on most occasions whereas the higher turbopause shoots upto even ~110 km. Higher turbopause is seen at the winter hemisphere high latitudes. The maximum difference between the lower and higher turbopause is also seen at the winter pole and the minimum at the summer pole. Both the higher and lower turbopause follow a similar trend having maximum height at the winter pole with secondary maxima in the summer mid-latitude. The minimum values are seen at the summer pole with secondary minimum at the equator. This is expected, as more planetary and gravity wave activity is seen in the winter hemisphere. Seasonal analysis shows that

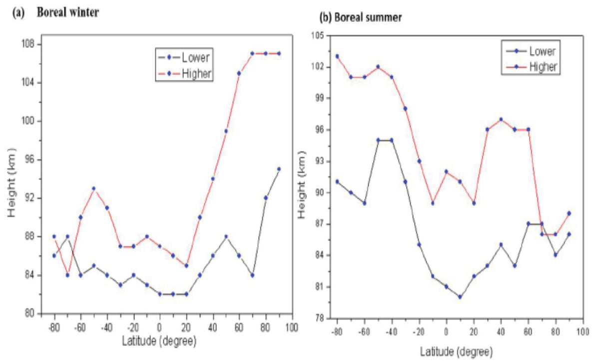

Figure 22: Latitudinal structure of two level wave turbopause heights for boreal (a) winter and (b) summer

except in summer, the turbopause is at minimum altitude at the tropics and shows rather random diurnal variations. In order to see the trend of the global wave turbopause and its relation to gravity wave activity, we have calculated the global gravity wave potential energies. The potential energy values in the MLT region are longitudinally averaged in grids of 10^0 latitude and the latitude-height section is shown in Fig. 23(a-b). The black line plotted on the potential energy map is the average turbopause height for the respective season. It is seen that the latitudinal potential energy magnitudes follow more or less a similar pattern of the turbopause height. The transition from smaller magnitudes below the turbopause to higher magnitudes above is very interesting to note. Though there is no one to one correspondence in the altitude, the pattern of transition of potential energy values is very similar to the seasonal pattern of turbopause across the latitudes. This also gives supportive evidence to the fact that shorter scale gravity waves also are controlled by the wave turbopause in their vertical propagation and characteristics over the globe.

Stratospheric and mesospheric-lower thermospheric ozone response to the abrupt changes in solar forcing

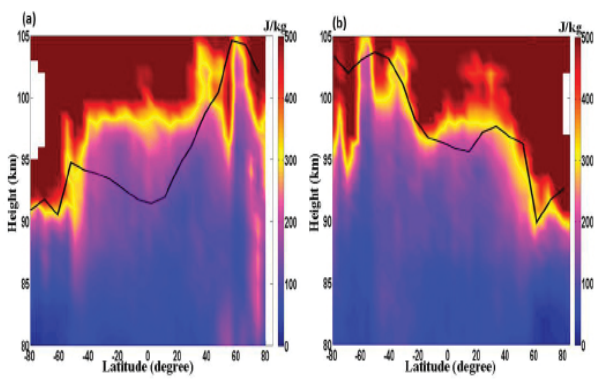

Figure 23: Latitude-Height section of gravity wave potential energies in the MLT region during boreal (a) winter and (b) summer

Altitudinal distribution of ozone in the stratosphere and MLT region during the annular solar eclipse of 15th January 2010 is studied using SABER observations over the Arabian Sea and the African region. Six locations over which ozone profiles were available close to the maximum obscuration of the Sun are analyzed to study the eclipse induced changes in the ozone Fig.24 shows the path of the annular solar eclipse overlaid by SABER ascending (blue circles) and descending (red circles) modes of observation. The three lines indicate the central (black), Northern (red) and Southern (blue) limits of the eclipse path. Keeping the eclipse path and the time of annularity in view, six observations (highlighted by an ellipse in Fig.24) over the Arabian Sea region (10°S-10°N, 45°-60°E) are chosen for further analysis as provided in table1.

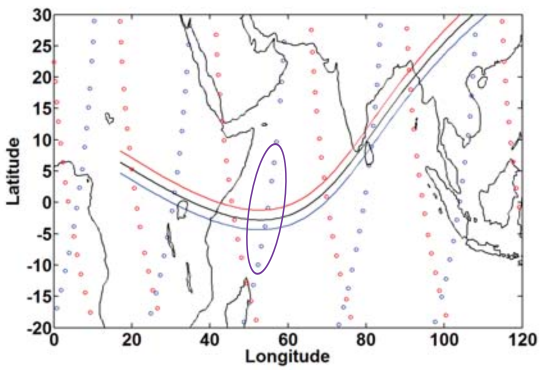

Figure 24:Path of annular solar eclipse of 15 January 2010 along with TIMED/SABER ascending (blue) and descending (red) orbits. The ellipse indicates the regions chosen for the present study

Figure 25 shows the height profiles of ozone mixing ratio over these six regions. The reference profile is constructed using the SABER observations (between 06-08 UT) during January 2010 over the study region (10°S-10°N, 5°-60°E). All the profiles shown in Fig.25 are those after the maximum obscurity of the Sun and before the end of the eclipse. In general, the profiles measured close to the maximum phase showed decrease in ozone at their peak altitudes and profiles measured slightly later showed increase in ozone. These observations are explained on the basis of balance between ozone production and loss processes. To substantiate this generalized statement, the

Table 1: Particulars of Solar eclipse over Arabian Sea region

S. No.	Latitude	Longitude	Maximum phase of eclipse (UT)	Magnitude	Time of SABER observations (UT)
1	-9.8952	52.2632	5:57:18	0.769	6:32:46
2	-6.9877	53.1803	6:01:44	0.866	6:33:05
3	-3.8093	54.0784	6:01:52	0.929	6:34:38
4	-0.8556	54.8347	6:11:04	0.909	6:34:58
5	3.3895	55.7995	6:19:36	0.803	6:36:49
6	6.3835	56.3986	6:25:02	0.732	6:37:8

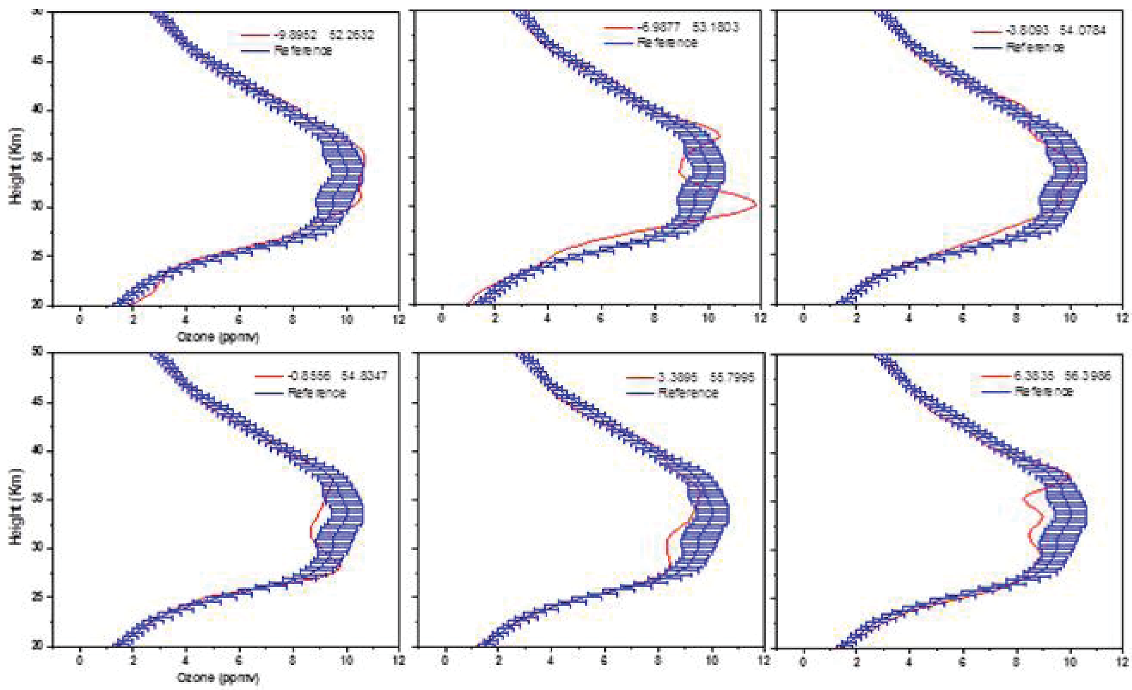

Figure 25: Height profiles of ozone observed on the eclipse day (red) over the six regions under study along with reference profiles (blue). The horizontal bars in the reference profile indicate the standard deviation

ozone profiles measured after ~ 3 hrs of maximum obscurity are also examined, which showed dramatic enhancement up to 4 ppmv in stratospheric ozone. The present study also emphasized the importance of the time of measurements of ozone with respect to the eclipse phase and their consequences. The MLT region ozone observations showed an enhancement during the solar eclipse, which is the first observational evidence. As the ozone maximum in the MLT region is predominantly in the night time owing to its longer life-time in the absence of solar radiation, the enhancement observed in the present study is attributed to reduced photodissociation of ozone. Thus it is envisaged that the present results will have important implications in understanding the ozone response to abrupt changes in solar forcing and time-scales involved in such response.

Ambipolar diffusion of meteor trails?

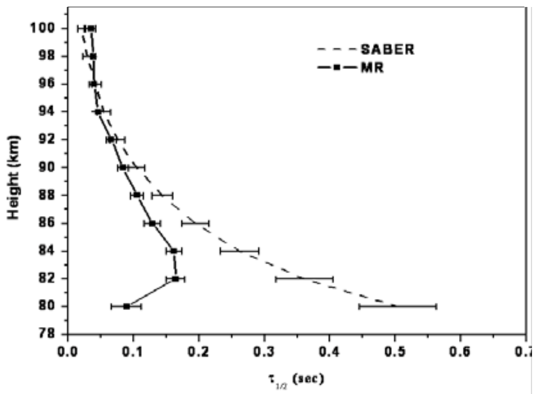

Figure 26: Height profile of half-life time of meteor trail ($\tau_{1/2}$) during the winter season of 2007 as observed by the meteor radar (MR) and estimated from SABER observations

Radar echoes from under-dense meteor trails are used to infer the temperature of the 80-100 km region of the atmosphere. In the different methods used to derive mesospheric temperature from the meteor decay times,the most important is the ambipolar diffusion of the meteor trail. So far there are no independent measurements of ambipolar diffusion coefficient to validate this assumption in the height region of 80-

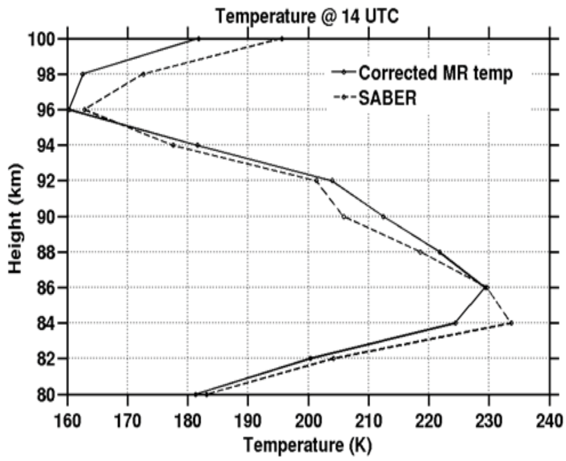

Figure 27: Meteor radar derived temperature profile (after applying the decay-time corrections) along with SABER instantaneous profile measured over Thumba

100 km. In this regard, we have estimated height profile of ambipolar diffusion coefficient (and hence the decay time) using temperature and pressure measurements by SABER. The comparison of the height profile of the meteor trail decay time as quantified by the half-time ($\tau_{1/2}$) and determined from meteor radar and SABER is shown in Fig. 26 for the winter season of 2007. The same is estimated for other seasons also. This figure clearly shows that the assumption of ambipolar diffusion is valid only in the height region of 92-100 km, and there are other processes governing the meteor decay in the 80-90 km region. The difference between the SABER and radar observed decay time profiles exhibited small day-to-day and seasonal variability. However, there is pronounced diurnal variation. As the ultimate aim of the present study is to improve the temperature retrievals from the meteor radar observations, the diurnal variation of difference profile of decay times are quantified for each season and this correction is applied for temperature retrieval. A comparison depicted in Fig.27, shows the dramatic improvement in retrieving the temperature profile from meteor decay time observations. However, the important outcome of the present study is the validation of assumption on ambipolar diffusivity of the meteor trails.

PUBLICATIONS IN REFEREED JOURNALS

1.Abhilash, S., K. Mohankumar, S. S. Das, and K. K. Kumar (2010), Vertical structure of tropical mesoscale convective systems : observations using VHF radar and cloud resolving model simulations, Meteo. Atmos. Phys., doi :10.1007/s00703-010-0087-7.

2. Das, S. S., A.K.Ghosh, K. Satheesan, A.R. Jain, and K. N. Uma (2010), Characteristics of atmospheric turbulence in terms of background atmospheric parameters inferred using MST radar at Gadanki (13.5°N, 79.2°E), Radio Sci., 45, RS4008, doi:10.1029/2009RS004256.

3. Das, S. S., K. K. Kumar, S. B. Veena, and G. Ramkumar (2010), Simultaneous observation of quasi 16-day wave in the mesospheric winds and temperature over low-latitudes with the SKiYMET radar, Radio Sci.,45, RS6014, doi:10.1029/2009RS004300.

4. Das, S. S., K. K. Kumar, and K. N. Uma (2010), MST radar investigation on inertia-gravity waves associated with tropical depression in the upper troposphere and lower stratosphere over Gadanki (13.5^{o}N, 79.2^{o}E), J. Atmos. Sol.-Terr. Phys., 72, 1184-1194, doi:10.1016/j.jastp.2010.07.016.

5. UdayBhaskar, T. V. S., D. Swain, M. Ravichandran (2010), Sonic Layer Depth variability in the Arabian Sea, Int. J. Oce. Oceano.,4, 17-28.

6. Subrahmanyam, K. V., G. Ramkumar, K. K. Kumar, D. Swain, S. Sunilkumar, S. S. Das, R. K. Choudhary, K. V. S. Namboodiri, K. N. Uma, S. B. Veena,S. R. John, and A. Babu (2011), Temperature perturbation in the troposphere-stratosphere over Trivandrum during Solar eclipse 2009/2010, Ann. Geophys., 29, 275-282, doi: 10.5194/angeo-29-275-2011.

7. John, S.R and K.K.Kumar (2011), TIMED/SABER Observations of Global Cold-Point Mesopause Variability at Diurnal and Planetary Wave Scales, J. Geophys. Res.,116, A06314, doi:10.1029/2010JA015945.

8. Kumar, K.K, K. V. Subrahmanyam and S. R. John (2011), New insights on the response of stratospheric and mesosphere-lower thermospheric ozone to abrupt changes in solar forcing, Ann. Geophys., 29, 1093-1099, doi:10.5194/angeo-29-1093-2011.

9. Kumar, K.K, D. Swain, S. R. John, and G. Ramkumar (2011), 'Simultaneous observations of SAO and QBO in winds, temperature and ozone in the tropical middle atmosphere over Thumba (8.50N, 770E)', Clim. Dyn.,doi:10.1007/s00382-010-0991-z.

10. Liu, G., T. J. Immel, S. L. England, K. K. Kumar, and G. Ramkumar (2010), Temporal modulation of the four-peaked longitudinal structure of the equatorial ionosphere by the 2 day planetary wave, J. Geophys. Res., 115, A12338, doi: 10.1029/2010JA016071.

11. Sunilkumar, S. V., K. Parameswaran, B. V. Thampi, and G. Ramkumar (2011), Variability in background stratospheric aerosols over the tropics and its association with atmospheric dynamics, J. Geophys. Res., 116, doi:10.1029/2010JD015213.

12. Uma, K. N., K.K. Kumar, and T. N. Rao (2011),VHF radar observed characteristics of convectively generated gravity waves during wet and dry spells of Indian monsoon. J. Atmos. Sol.-Terr. Phys., 73, 815-824, 2011, doi:10.1016/j.jastp.2010.07.016.

13. John, S.R., K.K. Kumar, K. V. Subrahmanyam, G. Manju, and Q. Wu (2011), Meteor radar measurements of MLT winds near the equatorial electro jet region over Thumba (8.5^{0}N, 77^{0}E): comparison with TIDI observations, Ann. Geophys., 29, 1209–1214.

14. Das, S. S., S. Sijikumar, and K. N. Uma (2011), Further investigation on stratospheric air intrusion into the troposphere during the episode of tropical cyclone: Numerical simulation and MST radar observations, Atmos. Res., 101, 928-937, doi:10.1016/j.atmosres.2011.05.023.

PUBLICATIONS IN REFEREED PROCEEDINGS

1. Das, S. S., 'VHF Radar Studies on Upper Troposphere and Lower Stratosphere (UTLS) Region During the Passage of Tropical Cyclone/Depression', Asia-Pacific Radio Science Conference-2010 held at Toyama, Japan from 22-26 September 2010.

2. Uma, K. N (2010),'VHF Radar Studies on the characteristics of Tropical Convection', Asia-Pacific Radio Science Conference-2010 held at Toyama, Japan from 22-26 September 2010.

PRESENTATIONS AT SYMPOSIA/ WORKSHOPS/ CONFERENCES

1. Babu, A., S.V. Sunilkumar, and Parameswaran, K., Latitudinal variation of Tropopause over the Indian region, Workshop on Tropical Stratosphere- Troposphere: Implications on Indian Monsoon and Climate', Indian Institute of Tropical Meteorology, Pune, 31 January- 01 February 2011.
2. Babu, V. S., and G. Ramkumar, 'Quasi-Biennial Oscillation – An evidence of relation with weather related phenomenon', National Conference on Advances in Atmospheric Remote Sensing, Weather prediction and Climate Change (ARWPCC – 2011), held at S.V. University, Tirupati, from 10- 12 March 2011.
3. Babu, V. S., G. Ramkumar, and K. V. Subrahmanyam, Study on the momentum flux of 5-6 day planetary waves in the MLT region at Trivandrum during different seasons, AS01-A008, 7th Annual General Meeting, AOGS, Hyderabad International Convention Centre, Hyderabad, July 5-9, 2010
4. Das, S. S., 'VHF Radar Studies on Upper Troposphere and Lower Stratosphere (UTLS) Region During the Passage of Tropical Cyclone/Depression', Asia-Pacific Radio Science Conference-2010 held at Toyama, Japan from 22-26 September 2010.
5. Das, S. S., K. K. Kumar, and G. Ramkumar, Aspect of the Quasi-120 Day Oscillation in Mesospheric Wind Associated with Solar Activity as Inferred from Thumba SkiYMET Radar, AS01-A010, 7th Annual General Meeting, AOGS, Hyderabad International Convention Centre, Hyderabad, July 5-9, 2010
6. John, S.R and K.K. Kumar, 'Investigations On Gravity Wave Potential Energy Seen By Different Satellites And Ground Based Techniques', AGU Chapman Conference on Atmospheric Gravity Waves and Their Effects on General Circulation and Climate, Honolulu, Hawaii, USA, 28 Feb – 04 Mar, 2011.
7. John, S.R and K.K. Kumar, 'Towards Complete Gravity Wave Spectrum in the Earth's Middle Atmosphere using Various Remote Sensing Techniques', 7th Annual General Meeting, AOGS, Hyderabad International Convention Centre, Hyderabad, July 5-9, 2010.
8. John, S.R and K.K Kumar, 'Determination of Wave Turbopause and Investigations on Possible Wave Propagation Beyond', 7th Annual General Meeting, AOGS, Hyderabad International Convention Centre, Hyderabad, July 5-9, 2010.
9. Kumar, K. K., and S. R. John, Meteor Radar Observations of Gravity Wave Drag in the MLT Region Over Thumba, AS01-A011, 7th Annual General Meeting, AOGS, Hyderabad International Convention Centre, Hyderabad, July 5-9, 2010.
10. Swain, D., K. K. Kumar, S. R. John, G. Ramkumar, K.V. Subrahmanyam, 'Investigation of Long Period Oscillations in the Equatorial Middle Atmosphere', 7th Annual General Meeting, AOGS, Hyderabad International Convention Centre, Hyderabad, July 5-9, 2010.
11. Subrahmnayam, K.V., G. Ramkumar, K.K. Kumar, S.S. Das, ,D. Swain, S.V. Kumar, Dynamical Response of the Middle Atmosphere at Trivandrum during the Solar Eclipse 2009/2010, AS14-A006, 7th Annual General Meeting, AOGS, Hyderabad International Convention Centre, Hyderabad, July 5-9, 2010.
12. Uma, K. N (2010),'VHF Radar Studies on the characteristics of Tropical convection', Asia-Pacific Radio Science Conference-2010 held at Toyama, Japan from 22-26 September 2010.
13. Uma, K.N., K. K. Kumar and T.N. Rao, VHF Radar Observed Characteristics of Convectively Generated Gravity Waves During Wet and Dry Spells of Indian Summer Monsoon, As14-A009, 7th Annual General Meeting, AOGS, Hyderabad International Convention Centre, Hyderabad, July 5-9, 2010.

INVITED TALK

1. K. Parameswaran, "Tropical Tropopause Layer Over the Indian Longitude sector and its Influence on the distribution of UTLS particulates" Stratospheric Processes And their Role in Climate (SPARC)-Local Workshop (LW), Workshop on Tropical Stratosphere-Troposphere: Implications on Indian Monsoon and Climate is being organized by Indian Institute of Tropical Meteorology, Pune, January 31 to February 1, 2011.

2. Kumar K.K and S.R. John, 'Meteor Radar Observations of Gravity Wave Drag in the MLT Region Over Thumba', 7th Annual General Meeting, AOGS, Hyderabad International Convention Centre, Hyderabad, July 5-9, 2010.

PUBLIC OUTREACH

K. N. Uma, Invited talk on, 'Easy access to education, training and science and technology: pathway to decent work for women' on International Women Day celebration at Kerala Social Service Forum (KSSF), Palakkad, Kerala, March 6, 2011.

DEPUTATION

International

1. Siddarth Shankar Das and. K. N. Uma were deputed to attend 'Asia-Pacific Radio Science Conference-2010' held at Toyama, Japan from 22-26 September 2010 for receiving "AP-RASC Young Scientist Award-2010" .
2. Sherine Rachel John deputed to AGU 'Chapman Conference on Atmospheric Gravity Waves and Their Effects on General Circulation and Climate', Honolulu, Hawaii, USA, 28 Feb – 04 Mar, 2011.

National

1. Veena Suresh Babu, and Asha Babu were deputed to'National Conference on Advances in Atmospheric Remote Sensing, Weather prediction and Climate Change (ARWPCC – 2011)', held at . S.V. University, Tirupati, from 10- 12 March 2011.
2. K.K. Kumar, K.V. Subrahmanyam,Sherine Rachel John, and Veena Suresh Babu were deputed to'7th Annual General Meeting', AOGS, Hyderabad International Convention Centre, Hyderabad, July 5-9, 2010.
3. K Parameswaran, and Asha Babu were deputed to 'Workshop on Tropical Stratosphere- Troposphere: Implications on Indian Monsoon and Climate', Indian Institute of Tropical Meteorology, Pune, 31 January- 01 February 2011.
4. Asha Babu is deputed to 'Workshop on Science and Technology Initiatives in Atmospheric Science for Engineering Staff ', National Atmospheric Research Laboratory, November 25-26, 2010.

PROJECT WORKS

M.Sc.: 2

M. Phil: 3

IONOSPHERE THERMOSPHERE MAGNETOSPHERE PHYSICS

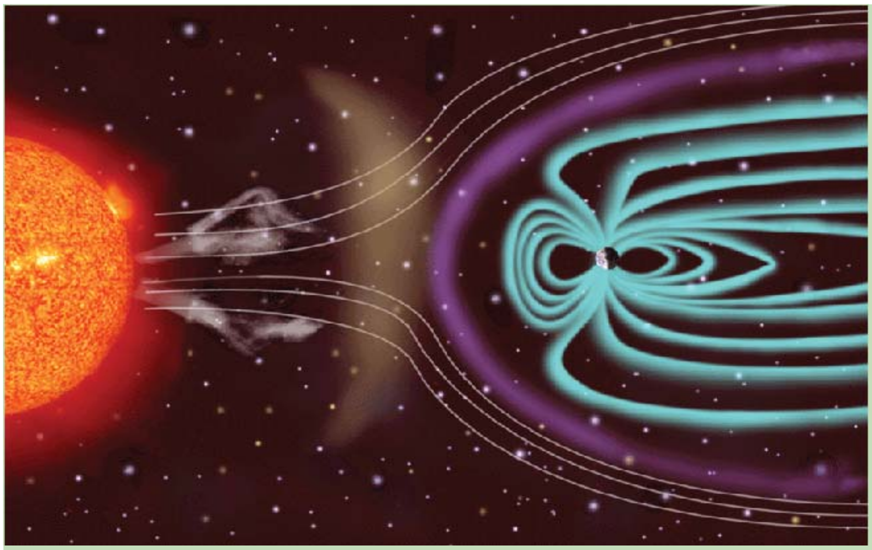

Science Faculty

Tarun Kumar Pant
Raj Kumar Choudhary
Manju G
Md. Mosarraf Hossain
*Vineeth C
Mridula N

Technical Team

Mohan Kumar S V
Sreelatha P
Pradeep Kumar P
Shajahan M
Tirtha Pratim Das
Supriya. G
Manikantan Nair
Uttam S. Purthy
Rosmy John
Johnson A J
Mohammad Nazeer M

Research Associates/ Fellows

+Smitha V Thampi
#Sreeja V
Lijo Jose
Sumod S G
Ambili K M
Madhav Haridas M K

Also Contributed

J. P. St. Maurice (ISRO ADREF visiting faculty)

**New appointment*
+For the period January-May 2011
#Post-Doctoral position in UK since Sept 2010

The aim of ITMP branch is to investigate the terrestrial upper atmosphere using (a) experiments on ground, rockets and satellites, and (b) modeling, in the context of its energetics/dynamics vis-à-vis the vertical and lateral coupling this region has with the magnetosphere above and mesosphere below it. These studies besides leading to advancement of knowledge on solar-terrestrial science, provide better input for technological applications like the GPS based navigation. Presented here are some of the important accomplishments for the year 2010-2011.

1. YOUTHSAT: PRELIMINARY RESULTS

Radio Beacon for Ionospheric Tomography (RaBIT) and Limb Viewing Hyper Spectral Imager (LiVHySI) onboard YOUTHSAT – Preliminary results

The much sought after YOUTHSAT satellite was launched successfully by the PSLV-C16 on April 20, 2010 in an ~ 818 km orbit. The Indo-Russian joint venture 'YOUTHSAT' had three scientific payloads, RaBIT (Radio Beacon for Ionospheric Tomography), and LiVHySI (Limb Viewing Hyper Spectral Imager) from ISRO and SOLRAD from Moscow State University, Russia.

RaBIT: RaBIT, a SPL-VSSC venture, is a radio beacon emitting coherent radio signal at 150 and 400 MHz frequencies. These are received using a chain of five receivers deployed along the ~76^{o}E meridian at Trivandrum, Bangalore, Hyderabad, Bhopal and Delhi. The receivers estimate the Total Electron Content (TEC) of the ionosphere through the relative phase change of the received radio signals. The TECs thus estimated near simultaneously, are used to generate a tomogram, which gives an Altitude-Latitude distribution of the ionospheric electron density. For the YOUTHSAT configuration, the tomogram covers the ionosphere from a few degrees (5-6^{o}) south of Trivandrum to about 3-4^{o} north of Delhi depending upon the satellite elevation. The RaBIT tomography network is by far the longest network existing anywhere in the world, and is unique therefore.

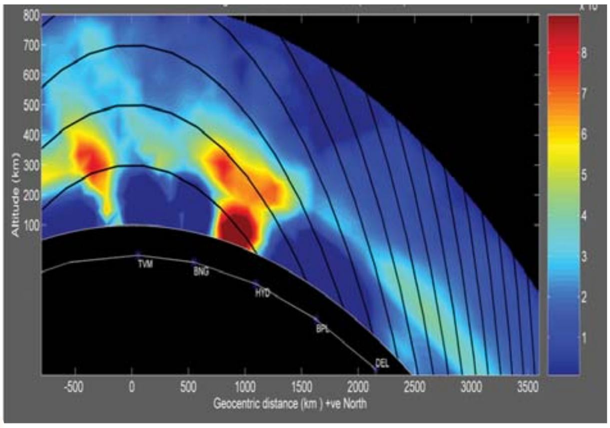

Figure 1: Altitude-latitude cross-section of the ionosphere as obtained using the RaBIT beacon signals on May 02, 2011 for the YOUTHSAT pass starting at Trivandrum at 21:43 IST. The position of RaBIT ground stations is marked in the figure. The vertical white lines represent the geomagnetic field configuration

A tomogram obtained on the night of May 2, 2011 is shown in Fig.1. It clearly reveals the presence of ionization crests (regions of enhanced electron density) around Delhi, Bangalore and south of Trivandrum at 150 and 300 km altitudes. Preliminary investigation indicates that these features are due to a Travelling Ionospheric Disturbance (TAD), which had originated over auroral regions owing to enhanced and temporally varying auroral heating. It can be unambiguously inferred from this tomogram that the wavelength of the TAD is ~ 500-700 km, which otherwise cannot be estimated through the conventional ground-based ionospheric monitoring.

LiVHySI: The LiVHySI, the second Indian payload on YOUTHSAT is an SPL-SAC endeavour. It is a wedge filter based camera having a field of view of 9^{o} x 18^{o} for imaging the atmospheric airglow emissions in the 430-950 nm wavelength range at every 1.1 nm, along the Earth's limb in the altitude region 80-600 km. The LiVHySI images the terrestrial airglow in both configurations i.e. the viewing Earth's limb along the orbit and normal to orbit. The LiVHySI is also a unique instrument, as it provides simultaneous measurements of all the atmospheric airglow emissions in the visible and near IR region

ITMP

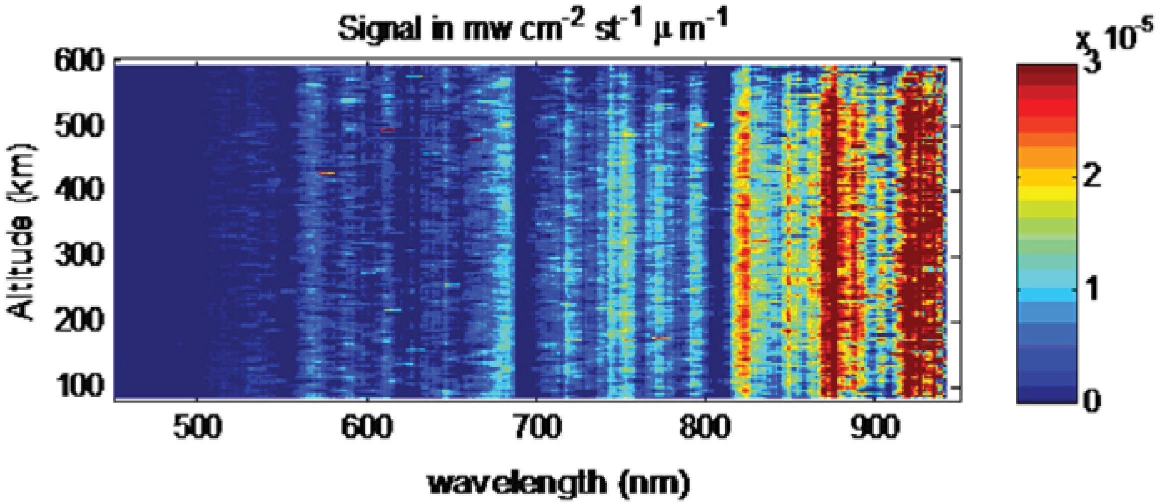

Figure 2: Typical LiVHySI image after the initial processesing. The image was taken during orbit #7

with a very high spectral resolution. Due to this hyperspectal information, the processing of the images obtained becomes non-trivial and requires significant pre-processing. The images obtained so far have clearly shown the presence of airglow emissions at 589.5, 630.0, 777.4, 830.0 and 890.0 nm which are indicative of the distribution of Sodium (Na), Atomic Oxygen (O) and Hydroxyl (OH) in the atmosphere. The information of these species is highly desired as it would lead us to the energetics and dynamics of the atmosphere at different height regions. Presented here (Fig.2) is an image obatined during LiVHySI orbit 7. It represents the hyper spectral image of Earth's limb (normal to the orbit) from a distance of about 2900 km. The image has been obtained after preprocessing that includes radiometric correction, integration time corrections, background removal, and noise removal. Presently, RaBIT and LiVHySI are performing as expected. In case of RaBIT, the Tomograms generated so far have clearly brought out (a) day and night differences in the electron density distribution, (b) evidence of the presence of the ionospheric top-side layer (c) modulations in the ionosphere due to space weather activity and (d) direct evidence of the presence of Travelling Atmospheric Disturbance (TAD). For LiVHySI, more studies are in progress.

2. STUDIES OF THERMOSPHERE AND IONOSPHERE DURING THE SOLAR ECLIPSE EVENT OF JAN 15, 2010

Local electrodynamics manifestation during the noon-time annular solar eclipse

The path of the annular solar eclipse of January 15, 2010, crossed the magnetic equator at Trivandrum, India, around local noon. A strong counter-electro-

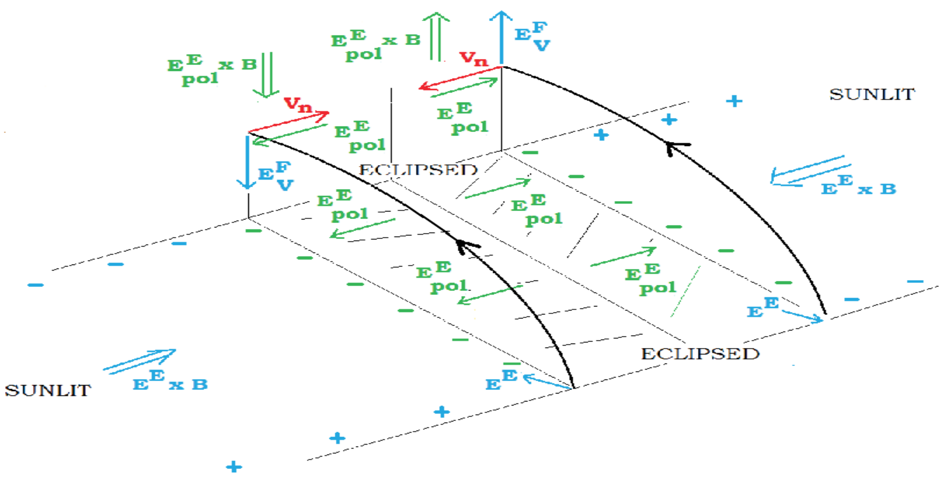

Figure 3: Electric field enhancement mechanism. East is to the right. Curved black traces: magnetic field lines. Red arrows: F region wind. Blue arrows: F region driven electric fields and their E region projections. Charges associated with this field are also shown in blue. Green arrows: E region polarization field from the electron ExB drift. Double blue arrows: E region electrons motion. Double green arrows: F region plasma motion. Zonal electric fields produced by E region polarization effects are larger than zonal fringe fields associated with the original horizontal variation of the vertical electric fields (blue fields) and fringe fields are therefore neglected

jet occurred shortly after the maximum obscuration. Moreover, as the eclipse passed overhead, the F region density peak underwent a large amplitude vertical oscillation. At the same time, there was an oscillation in the zonal electric field inferred from the Trivandrum magnetometer data. The eastward electric field that prevailed throughout the eclipse became westward after the time of maximum obscurity, reaching its largest westward value one hour before the end of the local eclipse. An explanation is offered to this based on a fast eastward moving local neutral-wind-dynamo generated by a low pressure system (LO) believed to have been triggered by the cold temperatures centered on the region of maximum obscuration. Accordingly, the eclipse had two separate impacts on the electrodynamics of the magnetic equator. The eclipse lasted for about six hours and for almost five hours, the LO that it generated produced a counter-electrojet that quickly moved eastward over the equatorial regions. Also, at the heart of the LO, the currents were interrupted by a decrease in E region conductivity, which produced electric field enhancements around the two terminators. The existence of double Pre-Reversal Enhancement (PRE) around the time of eclipse obscurity is shown in Fig.3, depicts how the electric field over the eclipse path gets modified in view of the proposed mechanism.

The impact of the January 15, 2010, annular solar eclipse on the equatorial and low latitude ionospheric density

The impact of the January 15, 2010, annular solar eclipse has been investigated using a chain of magnetometers, Total Electron Content (TEC) stations using GPS data, and the ionosonde at Trivandrum. With the help of a one-dimensional model appropriate for the region of interest, it is shown that the ionosonde data was consistent with a lower F region plasma that was moving upwards with only modest velocities in the morning hours and moving resolutely downwards in the afternoon hours (Fig.4). This means that the plasma fountain was weak in the morning hours. This motion agreed well with the local magnetometer data which revealed a weakened electrojet taking place in the morning hours while a full-blown counter-electrojet was present in the afternoon hours. It is shown that the unusual solar eclipse-induced electrodynamics resulted in a reduction in the Total Electron Content depletion not just at the magnetic equator alone but, more markedly, in the Equatorial Ionization Anomaly (EIA) zone, a further 10 degrees to the north as well. This latter point clearly shows that the eclipse led to a cut-off in the supply of plasma provided through the equatorial fountain, by altering a fundamental aspect of the equatorial electrodynamics.

3. ROCKET EXPERIMENTS TO UNDERSTAND THE IONOSPHERIC MANIFESTATIONS OF THE ANNULAR SOLAR ECLIPSE OF JAN 15, 2010

A comprehensive experimental campaign involving rocket borne in-situ measurements of various neutral and plasma parameters was undertaken during January 2010 to investigate the response of the low latitude and equatorial mesosphere thermosphere ionosphere to the solar eclipse. One important feature of this campaign was the indigenous development of experiments like the ENWi (Electron density and Neutral Wind probe) and successful rocket-borne in situ measurements of neutral wind in the lower ionosphere made using it onboard. Described here are some of the important research findings based on the ENWi data.

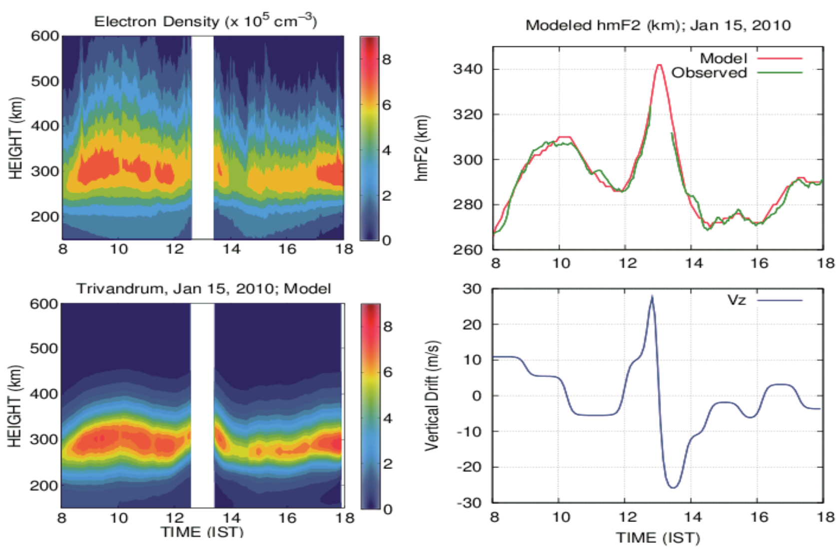

Figure 4: Top left panel: Range-time density maps deduced from the Trivandrum digisonde data on Jan 15, 2010. Bottom left panel: Range-time density maps obtained from numerical calculations where the vertical drift was adjusted as a function of time so as to have the modeled hmF2match the observed value. Top right panel: a comparison between the hmF2 that were reproduced by the calculations and those that came from the observations. Bottom right panel: Vertical drift values retrieved from the model calculations

Neutral winds in the MLT region

The vertical structures of the zonal and meridional winds in the 90-120 km region, derived using the ENWi probe on 3 rocket flights, one on the control day at 13:05 hrs and one each on the eclipse day at 13:05 and 16:00 hrs are shown in Fig.5. Time 13:05 hrs corresponds to the eclipse phase. The zonal winds on the eclipse day depicted a reversal to eastward direction in the entire altitude range above 100 km, whereas on the control day, the zonal winds are clearly westward. This eclipse induced reversal of zonal wind resulted in a reversal of the polarization electric field causing a Counter Electrojet. The meridional wind on the eclipse day is equatorward. In other words, during the progression of the eclipse there is a convergence of wind towards the eclipsed region. Associated with changes in neutral winds, the occurrence of a strong blanketing E_s layer was also observed in the ionograms. It appears that, the equatorward wind in the presence of eastward zonal wind has transported the blanketing layers generated at off equatorial regions to magnetic equatorial regions, as has been postulated earlier.

The ENWi measured zonal neutral wind in the post eclipse flight shows the presence of strong eastward wind in the entire EEJ region with increased magnitude compared to that at the peak phase. Concurrently, the meridional wind has reversed poleward.

E-region electron density

Large decrease in the electron density was observed in the E-region during the peak phase of the eclipse as revealed by ENWi measurements (Fig.6). This decrease was ascribed to the sudden cut off of the solar insolation and consequent chemical recombination. The electron density profile on the control day

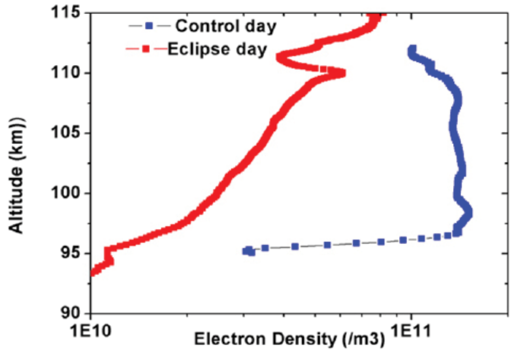

Figure 6: Electron density profiles derived from ENWi on eclipse day and the control day

matches well with the profile obtained from rocket flights over Thumba under identical conditions. The reversed electrojet signal corresponding to the blanketing Es irregularities are observed in the altitude region of negative electron density gradients above 110 km.

Eclipse effects at off-equatorial regions

In the previous section, the reversal of zonal neutral wind at magnetic equator, which is characteristic of the occurrence of a CEJ, has been presented. The occurrence of counter electrojet indicates that the ionospheric zonal electric field is either weakened or reversed. Such a weakening/reversal of the ionospheric electric field would be reflected as a weakening/inhibition of the EIA. To investigate the effect of the different parameters like weakened ionospheric electric field, eclipse induced cutoff of solar insolation and possible changes in thermospheric neutral winds at low latitudes, a study is undertaken using ionosonde data over low latitude station Gadanki and GPS TEC data over stations centered around 77° E longitude.

The time variation of the geomagnetic field at Tirunelveli on 15 January 2010 is shown (Fig.7) with

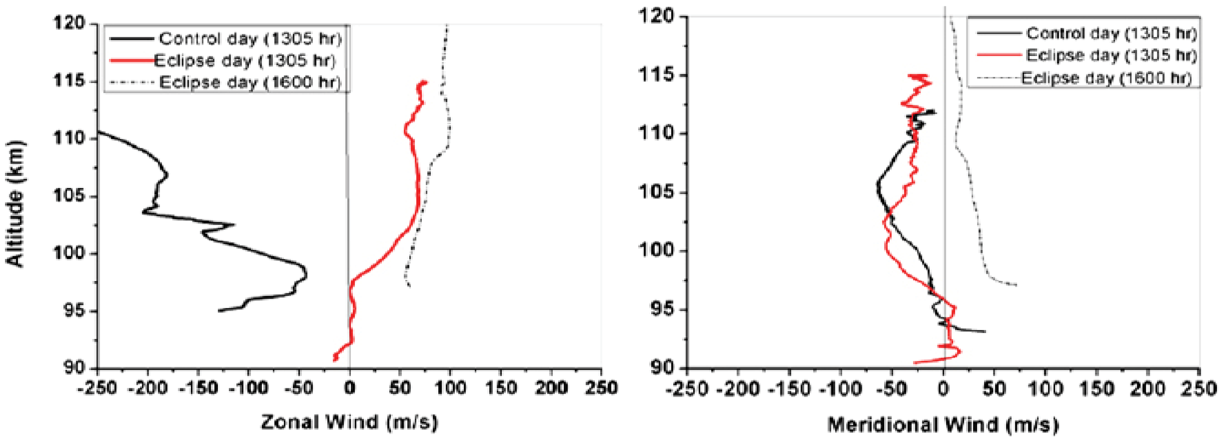

Figure 5: Neutral wind profiles from ENWi on eclipse day and control day

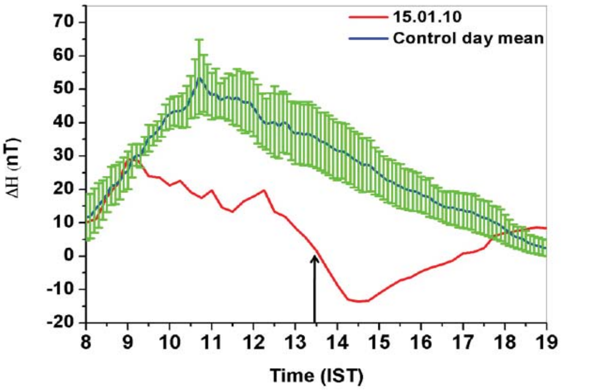

Figure 7: Time evolution of ΔH at Tirunelveli on eclipse day and a quiet day

the mean control day pattern. The control day mean pattern of ΔH shows the characteristic quiet day behavior of a gradual increase in the morning to attain a peak around noon hours followed by a steady decrease till evening hours. It is clear from the eclipse day variations that there is a gradual weakening (from 0945 hr) followed by the reversal of electric field (which is the driving force of the EIA) resulting in the counter electrojet. This implies a weakening/inhibition of the fountain effect over most part of the day.

Following two station method, used generally for estimating meridional winds at night time in the absence of production, we have estimated the daytime winds (during the solar eclipse) as the conditions are very similar to night time. The accuracy of the wind estimates, increases progressively as we approach the time of maximum obscuration. The estimated meridional wind for the period from 1200-1400 hr is shown in Fig.8. The eclipse shadow is south of the geographic equator around 1200 hrs and hence the heating up of the geographic equatorial region is continuing unabated. A poleward wind is expected in the northern hemisphere around this time and this is validated by the estimated winds also. Around 1245 hr, the shadow comes over the geographic equator and the resultant cooling occurs there. This is expected to produce an equatorward wind in both the hemispheres and the estimated winds again show the anticipated pattern. Around ~ 1345 hr, when the shadow is already north of Gadanki, the convergence in the northern hemisphere is expected to be poleward and this is borne out by the estimated winds which turn strongly poleward during this time. Such large magnitude winds can significantly contribute to the movement of ionization away from Gadanki in the post peak eclipse phase.

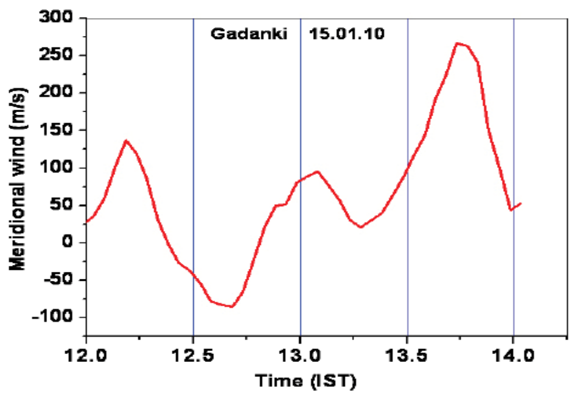

Figure 8: Temporal variation of thermospheric neutral wind close to the time of maximum obscuration on the eclipse day

Figure 9 shows the time variations of foF2 (left panel) and a new parameter called the EIA proxy parameter, on the eclipse day along with the mean control day pattern. The temporal evolution pattern on the control day mean is characteristic of the days when the ionospheric electric field is strong and attains a significantly high peak value close to noon. The high electric field on such days results in a significant noontime bite out in foF2 associated with the movement of the crest towards higher latitudes.

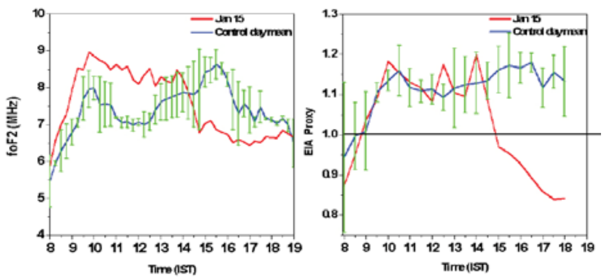

Figure 9: Temporal evolution of foF_2 (left panel) and EIA proxy (right panel) on the eclipse day viz-a-viz control day mean

On the eclipse day, the foF_2 remains more or less steady from ~1030 to ~1345 hr indicating that pumping away of the ionization from Gadanki is not taking place. The conspicuous absence of the noon time bite out in foF_2 is indicative of the fact that the crest has not moved beyond Gadanki. Also, in order to confirm that the EIA is only weakened and not fully inhibited with crest returning to Trivandrum, the time evolution of foF_2 (Gadanki)/foF_2 (TRV), referred to as EIA proxy hereafter, is examined (Fig.9, right panel). This EIA proxy parameter exceeds 1 when the EIA crest is at or beyond Gadanki. It is evident that up to 1400 hr EIA proxy is above 1, and 1430 hr onwards it is below 1.

Thus, foF_2 enhancement corresponding to an electron density increase of ~ 14% at the F_2 peak is seen over Gadanki close to the peak phase of the eclipse in comparison with the control day behavior. After the

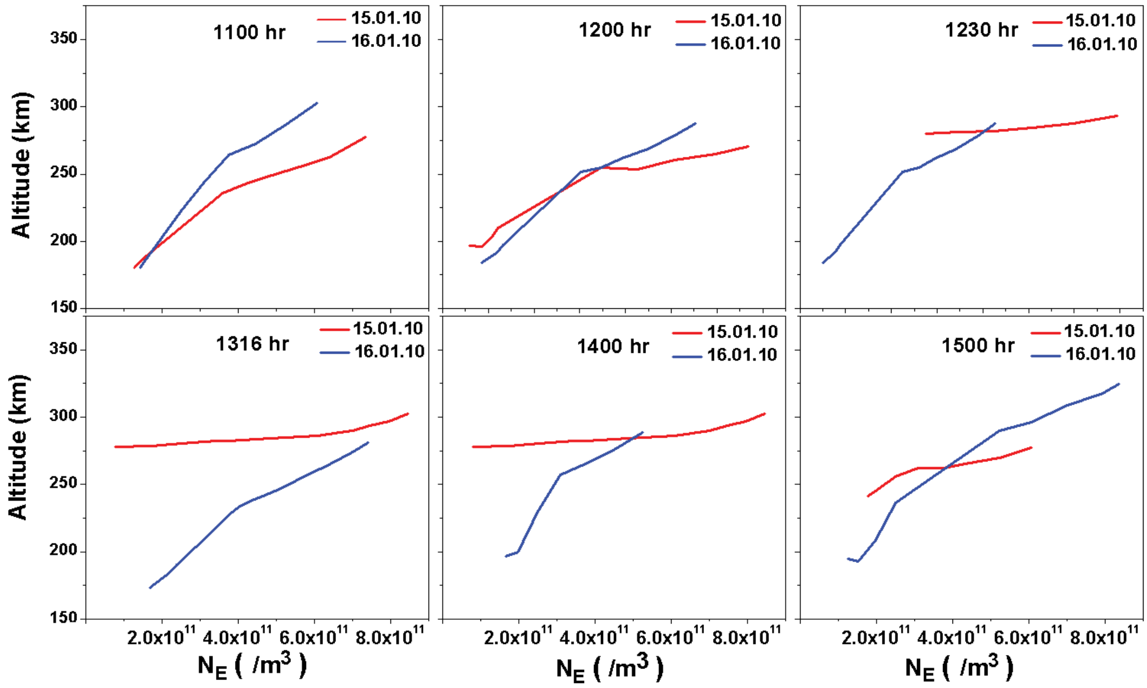

Figure 10: Electron density profile of the ionosphere during peak time of eclipse and at the same time during the control day

peak phase, the foF_2 shows a large decrease compared to the control day. The decrease in foF_2 (after maximum obscuration) is the combined effect of neutral dynamics and inhibited electrodynamics, while the higher value during the course of the eclipse is due to the effect of weakened electrodynamics.

Altitude profiles of electron density up to the F_2 peak on eclipse day and a quiet day are shown in Fig.10. It is clear from the figure that the foF_2 value is higher on the eclipse day even before the eclipse (profile of 1100 hr) as mentioned earlier. The profiles close to the eclipse peak phase (from 1200 hr) show that although the foF_2 is higher on the eclipse day, there is large reduction in electron density at altitudes below 270 km. This reduction in the lower altitude regions is attributed to the chemical recombination during the eclipse induced cut off of solar insolation. This in turn can give rise to a significant reduction in the columnar content on the eclipse day even though foF_2 is higher. In the post eclipse profiles (1400 and 1500 hrs) also, the bottom side electron densities have not recovered substantially due to the absence of significant production in the late afternoon hours.

The TEC at Bangalore (Fig.11) which is located very close to Gadanki is expected to follow similar pattern of temporal evolution as that over Gadanki. At Bangalore, the GPS TEC shows reduction with respect to control day pattern both at the peak phase and afterwards. The GPS TEC shows reduction with respect to control day pattern both at the peak phase and afterwards. The decreased TEC close to eclipse peak phase is attributed to the eclipse induced cut off of solar insolation at altitude regions below 270 km and consequent dominance of recombination, resulting in the columnar content decreasing in spite of foF_2 increase as mentioned earlier. In the post peak phase, GPS TEC behaves similar to foF_2 and shows a large reduction as a result of inhibited electrodynamics, increased poleward wind and the absence of significant recovery of ionization at lower altitudes during this time. The summary is as follows:

1. Large increase in foF_2 and simultaneous decrease in TEC are observed over low latitudes around the eclipse peak phase. The increased foF_2 is attributed to the presence of EIA crest over Gadanki as a result of weakened electrodynamics. The dominance of chem-

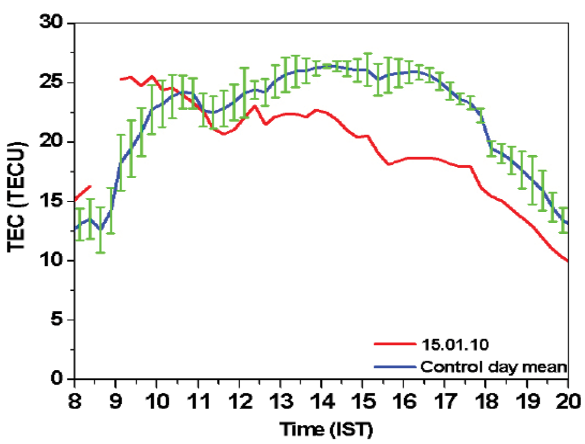

Figure 11: Time evolution of GPS TEC at Bangalore on eclipse day viz-a-viz control day mean

ical recombination at lower altitudes due to the cutting off of solar insolation and consequent reduction in electron densities leads to a significant reduction in the TEC in spite of an increase in foF_2.

2. Substantial reduction is observed in foF_2 and TEC in the post peak phase compared to mean control day pattern over low latitudes near Gadanki. This effect is attributed to the combined effects of neutral dynamics, inhibited electrodynamics and persistent depletion of lower altitude electron densities.

Estimation of zonal electric field at equatorial and low latitude region using magnetometer measurements: a new paradigm

Over the period of last 50 years, it has generally been accepted that information about zonal electric field in the equatorial and low latitude can be obtained by subtracting horizontal component of Earth's magnetic field recorded at Alibag from that at Trivandum which assumes that Trivandrum magnetic field represents the sum of contributions from the magnetosphere and E-region dynamo while field at Alibag is purely magnetospheric. However, it is postulated that Sq current could be disrupted during specific events like solar eclipse or geomagnetic storms. As such a new approach is proposed wherein we took advantage of the availability of the Sym-H index to remove global contributions from individual stations. This removed the need to use Alibag to take out the global current contributions from the equatorial magnetograms so that if something unusual was happening in the Sq current system, it would not introduce erroneous interpretations in the magnetic fluctuations induced by the equatorial electrojet. We used the 1 min sym-H index that monitors the field due to ring currents and subtracted that value from the raw data recorded at a station. The calibration for each station was checked by comparing the 2 to 3 AM recordings for the month against the symH readings obtained at the same time. In all cases a perfect straight line was obtained, which yielded the required calibration and showed that there was no random error in the magnetic field sampling and consequently no local current contribution of any significance. The local values of ΔH during the day were then calculated according to the equation:

$\Delta H = H - H_o - C \times \text{sym H}$, where the constants H_o and C were obtained by taking the slope of the raw data (H) recorded between 2 and 3 AM against the symH during that time interval. Fig.12 shows the evolution of magnetic field on the eclipse day vis-à-vis the monthly average over a number of Indian stations.

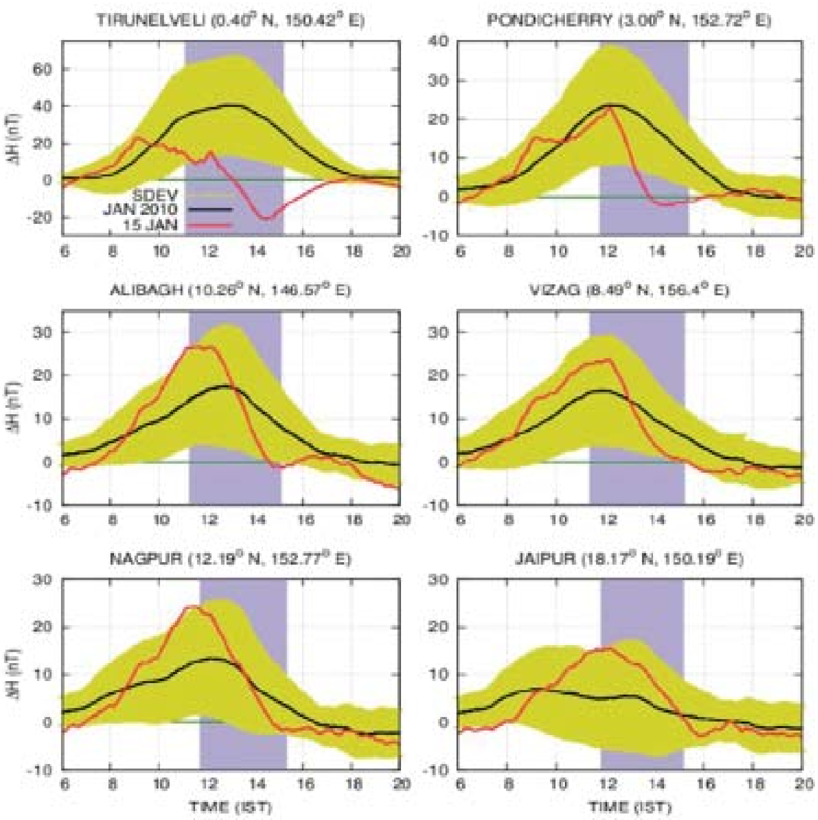

Figure 12: Monthly average of ΔH obtained using new method (black lines) and one sigma deviations from the average (yellow area) observed at six low latitude stations in India during January, 2010. Red lines: ΔH for Jan 15, 2010. The evolution of current system during the solar eclipse of Jan 15, 2010 in the Indian low latitude ionospheric region is quite evident. Highlighted blue regions indicate the duration of eclipse at each station

4. RESPONSE OF THE THERMOSPHERE AND IONOSPHERE DURING GEOMAGNETICALLY ACTIVE PERIODS

Impact of the Disturbance Dynamo on the Equatorial Ionization Anomaly

An intense disturbance dynamo was observed in the magnetic equatorial region of the Asian subcontinent on May 31, 2005. On that particular day, the ground magnetograms showed the disappearance of normal mid-day electrojet while the ionosonde data showed a substantial enhancement in the equatorial F peak density in addition to a clear reduction in the height (hmF_2) of that peak. The afternoon Total Electron Content (TEC) in the Equatorial Ionization Anomaly (EIA) was up to 2.5 times smaller than the average. In addition, a large but short-lived burst in the zonal electric field took place in mid afternoon which triggered at first a strong depletion in the equatorial TEC, but without an accompanying increase of the same in the EIA region. Furthermore, the equatorial TEC returned to its pre-depletion value after the plasma had been returned to lower altitudes. It is inferred that the zonal electric field oscillation was consistent with a disturbance dynamo of limited east-west extent, and that the meridional wind circulation countered the usual equatorial fountain effect in such a way, so as to make the plasma circulation reverse with the sign of the upward plasma drift. This contributed to a further disconnect of the equatorial plasma with the EIA regions. Fig.13a depicts a cartoon illustrating the disturbance dynamo action. Fig.13b illustrates the magnetic field variation for the said period.

The Seasonal and solar activity dependence of the threshold height (h'F)c for the triggering of Equatorial Spread F (ESF) during magnetically disturbed periods

Previously a study was conducted to delineate the threshold height (h'F)c of the base of the F layer, for the triggering of ESF irrespective of the magnitude and polarity of the meridional winds for magnetically quiet period. In the present study, the scope of this work has been extended to magnetically disturbed days, so that the disturbance induced changes if any on threshold height and its implications for ESF are brought out. For this, the ionosonde data from Trivandrum and SHAR for the summer, winter and equinox seasons for the year 2005 (low solar activity) and winter and equinox seasons for year 2002 (solar maximum) have been used. The meridional wind has been deduced for all the days using the two station method. The scatter plot of meridional wind vs the h'F for ESF and non ESF days (Fig.14), both parameters being taken just prior to or at the ESF commencement as seen in the ionograms on the ESF days and at 1900 hr for non ESF days. The scatter plot is generated for three seasons for the year 2005. Further, the non ESF days are demarcated into two categories, with one representing those days when the seed perturbation is absent and other representing those with seed perturbation in the post sunset period. For this the h'F (at 2.5 MHz) at 15 min intervals on each day during the period 1745-0600 hrs is subjected to wavelet analysis. The average amplitude of the periodicities in the range of 30-60 min during the period between 1900 and 2000 hrs is estimated as the amplitude of the seed perturbation on that day.

(a)

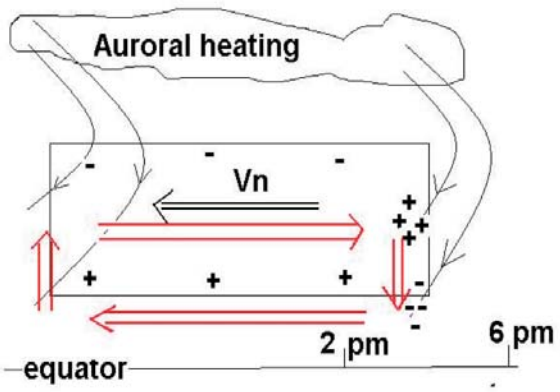

(b)

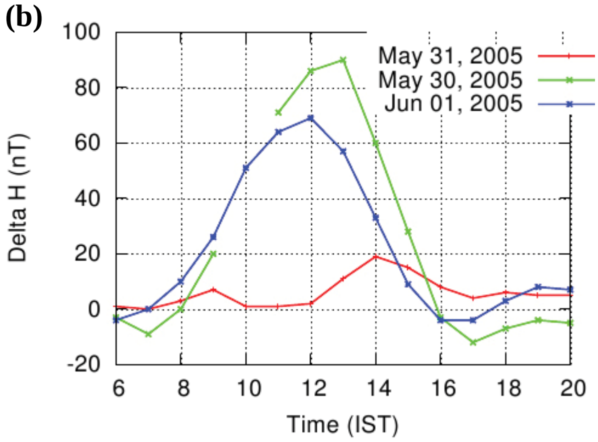

Figure 13(a): Cartoon to illustrate the origin of the zonal field reversal in mid afternoon in relation to the disturbance dynamo. Curved lines show the vertical circulation of the neutral atmosphere. Westward winds form as a consequence of the meridional Hadley cell circulation that brings down-welling air to lower latitudes. A current dynamo pushes ions towards the equator. The ions pile up at a point where the vertical component of the magnetic field becomes small. If the zonal winds end before the terminator, the Hall currents (shown by the red arrows) diverge at the end of the zonal wind stretch and depose charges in that region, as shown. (b) The EEJ induced field over equator for the period under investigation

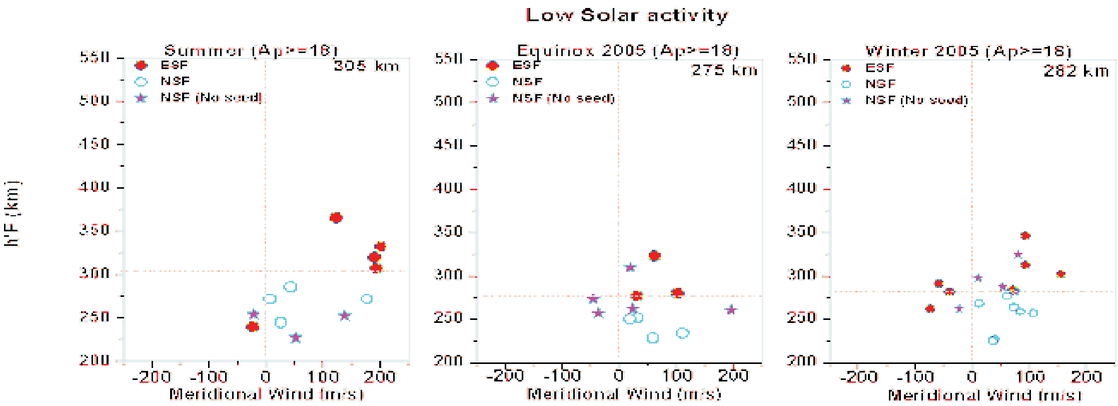

Figure 14: Scatter plot of meridional wind vs the h'F for the summer, equinox and winter seasons of 2005

The study revealed that

1) For both the solar epochs, the threshold height is higher for magnetically disturbed periods compared to quiet periods (Fig.15). This means that the neutral dynamical control over ESF occurrence becomes more important during disturbed periods than during quiet periods.

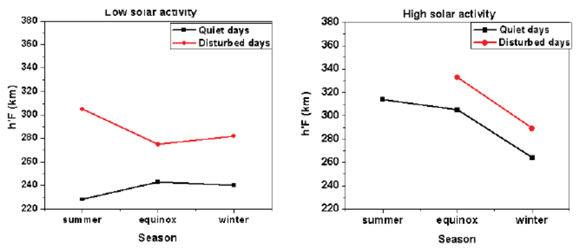

Figure 15: Seasonal variation of threshold height for magnetically quiet and disturbed period

2) Similar to the behaviour during magnetically quiet period, during disturbed period also the threshold height increases with solar activity. It seems that the temperature related effects on scale height which is the suggested causative mechanism for increased scale height in summer and equinox of high solar activity during quiet days is equally effective in producing similar effects during disturbed periods.

3) For low solar activity, the disturbed period threshold height is highest in summer with lower and comparable values in equinox and winter.

4) For high solar activity, the disturbed period threshold height is much higher for equinox than for winter. The summer threshold height could not be determined due to lack of sufficient data.

Evidence for the effect of prompt penetration electric field on equatorial thermosphere ionosphere system under different IMF conditions

Two space weather events, one on March 31, 2006 and the other on April 09, 2006, were investigated to illustrate the impact of prompt penetration electric field in the equatorial upper atmosphere through variability in the daytime thermospheric 630.0 nm dayglow emission intensity. Observations of the thermospheric dayglow (O^1D 630.0 nm) intensity revealed significant modulation during these events, concurrent with the changes in the interplanetary conditions and ensuing prompt penetration.

On March 31, 2006, the IMF Bz showed a northward

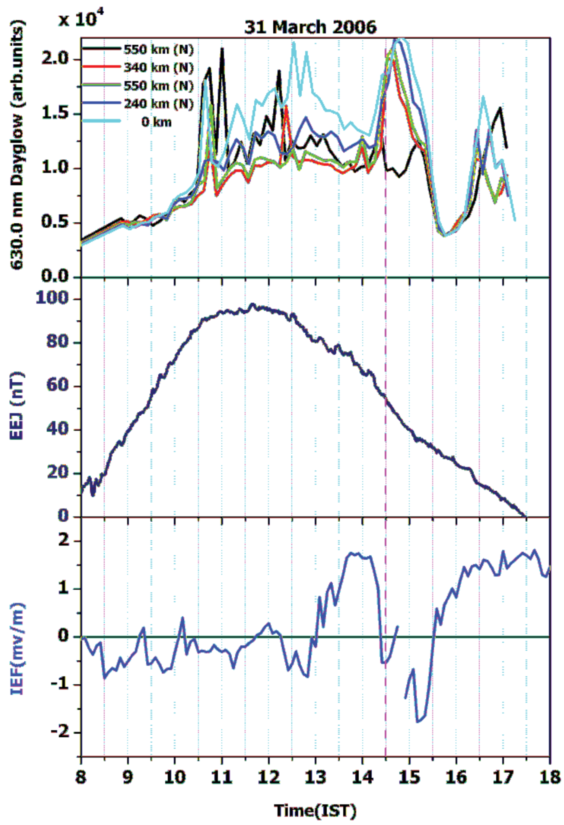

Figure 16: The bottom panel shows the large variations in the interplanetary dawn-dusk electric field (IEF on 31 March, 2006). The simultaneous changes that occurred in the thermospheric dayglow intensity measured at different elevations in the meridional direction, N representing north, are shown in the top panel. The prompt responses of EEJ are marked in the middle panel. The dotted magenta line denotes the simultaneity of the event

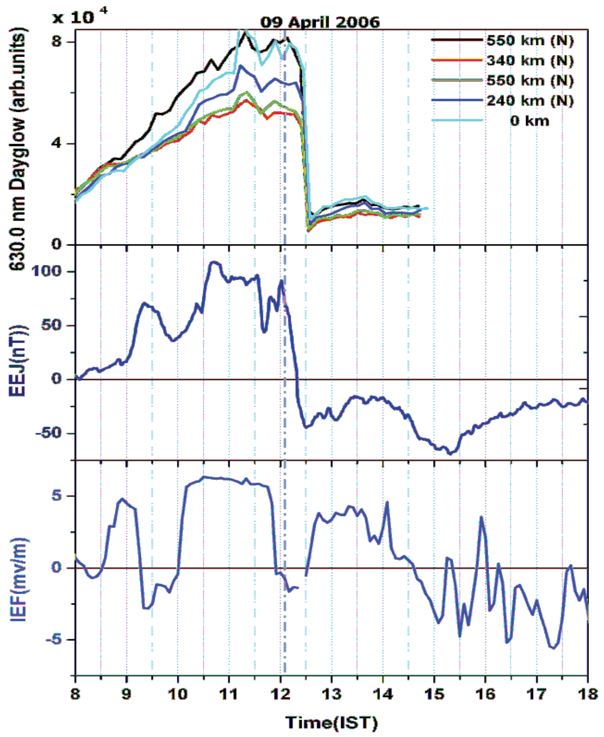

Figure 17: Same as Figure 16, but for 09 April, 2006

turning at ~ 14:30 IST with a susequent southward turning at ~15:30 IST (not shown here). The interplanetary electric field (IEF) turned eastward at ~13:00 IST followed by a westward excursion at ~ 14:30 IST and recovering at ~15:30IST. These changes in the IEF manifested in the 630.0 nm dayglow emission intensity, as enhancement at ~14:30 followed by a sudden depletion at ~ 15:30 IST which lasted for about half an hour (Fig.16). Interestingly, the dayglow intensity regained immediately afterward reaching values similar to that around noon. The near simultaneity of these IMF/IEF changes and the alterations in the thermospheric dayglow intensity indicates the presence of prompt penetration electric field (Fig.16).

During the space weather event of April 2006, the magnetospheric ring current developed significantly with the ring current index Sym-H reaching a minimum of ~100 nT on April 09, 2006. Interestingly, the interplanetary magnetic field IMF Bz turned northward at ~ 12:00 IST and at the same time, IMF By turned eastward and remained near + 10 nT for the rest of the day (not shown here). The resulting interplanetary dawn-dusk electric field (IEF) turned westward at ~ 12:00 IST manifesting as a strong prompt westward field over the equatorial ionosphere. A sharp decrease was observed in the dayglow emission intensity over and around Trivandrum, which continued up to 12:30 IST (Fig.17). The ionograms showed an abrupt decrease in F2 peak height (hmF_2) accompanying these changes (not shown). The presence of high altitude F3 layer was also noticed during the morning hours.

These events are comprehensively studied using the TEC measurements from both GPS and CRABEX. This study brought out the important aspect of the coupling of equatorial thermosphere and ionosphere in context of the sun-earth interaction during active space weather.

Response of equatorial thermosphere ionosphere system during the solar flare events of January, 2005

The period of January 2005 was unique as a number of solar flare events took place within a span of few days. The thermospheric responses to these were investigated using the O(1D) 630.0 nm dayglow emission intensity measurements over and around Trivandrum. In this context, we present here two striking solar flare events, one being slow flare event on January 17 where the growth of X-ray flux took about 2.5 hours, and the other a spontaneous one on January 19. The thermospheric 630.0 nm dayglow measured during these two days is shown in Fig.18, along with the enhancement of the X-ray (1-8 Å) fluxes measured by GOES-10 (Geo-stationary Operational Environmental Satellite). We also considered the EUV fluxes (not shown here) as measured simultaneously by the Solar EUV Monitor (SEM) onboard Solar Hemispheric Observatory (SOHO). Due to the insufficient (data breaks) nature of the TEC data over Trivandrum, the variation of GPS vertical total electron content (VTEC) as measured over Bangalore, a station just outside the equatorial region was also studied. The VTEC is depicted along with the dayglow variability in the top panels of Fig.18. As can be seen from the figure, during both the events the ionosphere appears to be responding to the solar flares almost instantaneously and shows that the VTEC increases by about 3-4 TEC units. This sudden enhancement is believed to be due to the increase in photoelectrons due to a sudden increase in the solar EUV flux associated with these flare events. However, despite the enhanced flare induced photo-dissociation and photo-ionization, the relative enhancement in the dayglow intensity is found to be less.

As can be seen, the dayglow enhancement in response to the solar X ray fluxes is found to be quite different for these two cases.

Interestingly, the dayglow intensity enhancement on January 19 was found to be larger than that on January 17 while the X-ray flux being lesser. However,

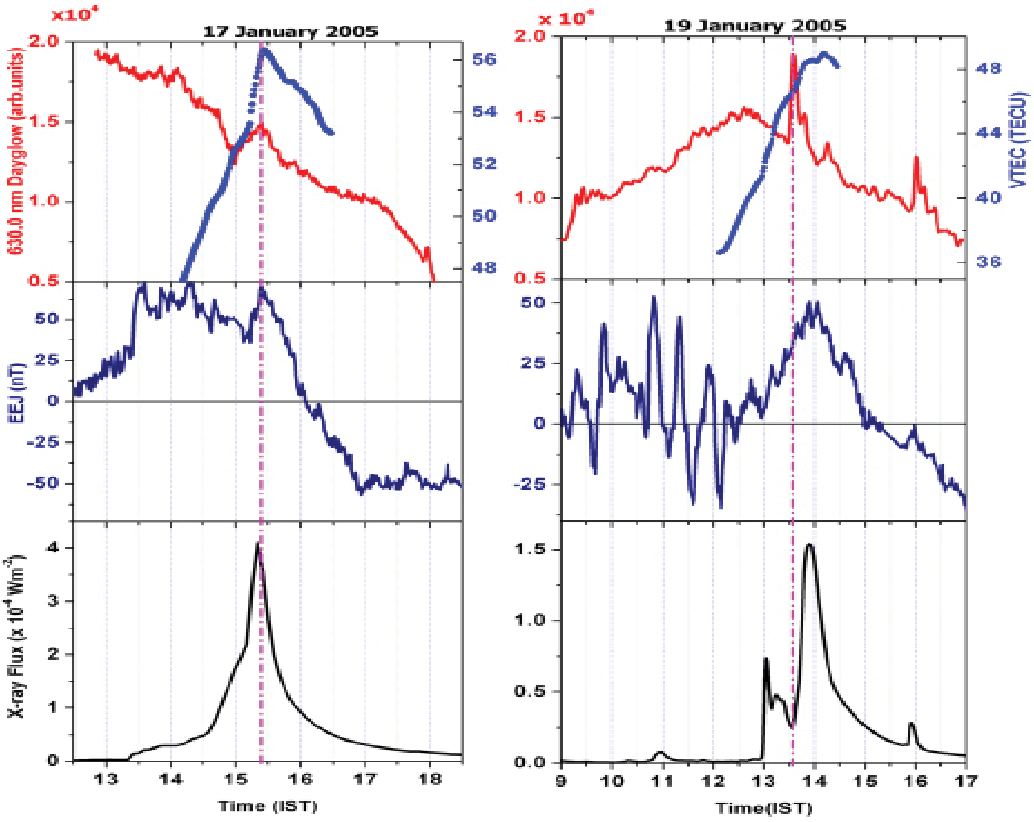

Figure 18: The prompt response of X class solar flare in the EEJ , TEC and neutral 630.0 nm dayglow over Trivandrum during 17 (left) and 19 January (right) 2005. The dotted-dashed vertical lines in the figures indicate the time when dayglow intensity exhibited the maximum change during the flare

the ionospheric response as seen in terms of VTEC has been proportional to the flux. On the whole, it can be said that while the ionospheric response appears to be proportional to the X-ray flux during the flare, the thermospheric response, as manifested in the thermospheric dayglow intensity, is not. These changes in the thermosphere and the ionosphere have been investigated in detail in view of the storm time dynamics of the equatorial thermosphere-ionosphere system.

5. INVESTIGATION OF EQUATORIAL COUNTER ELECTROJET

Equatorial Counter Electrojet - Evidence for Association with Meteoric Activity

First direct observational evidence for the role of meteoric activity in the generation of the equatorial Counter Electrojets (CEJ) is presented. The investigation has been carried out using two years (2006 and 2007) of data from Proton Precession Magne-

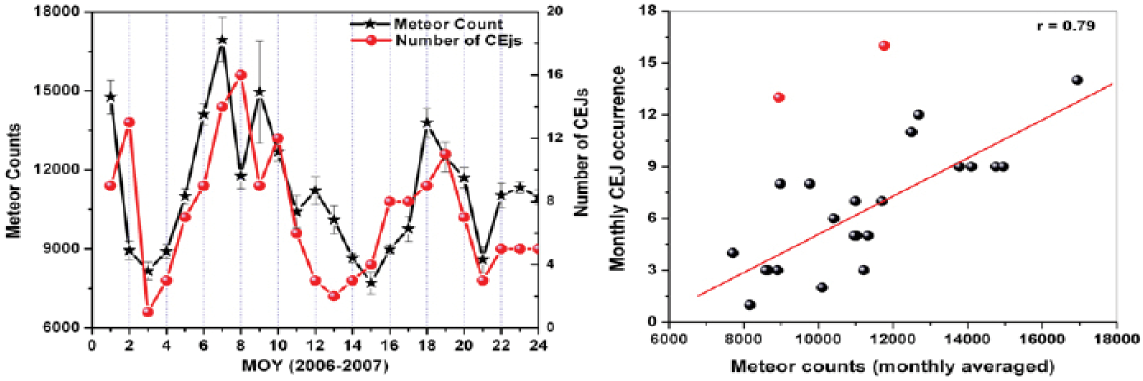

Figure 19: The monthly averaged meteor counts and the monthly occurrence rate of CEJ (partial and full after noon CEJ's) for the years 2006 and 2007 (right panel). The correlation between monthly averaged meteor counts and the monthly occurrence of CEJ for the years 2006 and 2007 (left panel)

tometer and Meteor Wind Radar over Trivandrum. It has been found that the occurrence of afternoon CEJ events during any given month is proportional to the average meteor counts over the location [shown in Fig.19 (left panel)]. Fig.19 (right panel) shows the correlation between monthly averaged meteor counts and the monthly occurrence of CEJ. They show good correlation with a correlation coefficient of 0.79. The two red points correspond to cases when the correlation between the meteoric activity and the occurrence of CEJ due to the geomagnetic disturbance prevailing during the time. This study gives the first observational evidence for the effect of meteoric dust in the generation of CEJ.

Variability in Daytime Mesopause Temperature and Winds

This study discusses variation of the daytime zonal wind and OH temperature estimated using meteor radar and MWDPM respectively at upper mesospheric altitudes during the afternoon Equatorial Counter Electrojet (CEJ) events over Trivandrum. The CEJ events are identified by taking the difference between the surface magnetic field measurements of Trivandrum and Alibag, as has been traditionally done. As can be seen from Fig.20, associated with the CEJ events there occurs: (i) an eastward acceleration in the zonal wind at 98 km altitude, and (ii) a clear-cut cooling in the mesopause, the magnitude of which is proportional to the extent of the magnetic field reversal. These results are discussed in terms of the role played by the upward propagating gravity waves, neutral winds and the changes in the mesospheric chemistry.

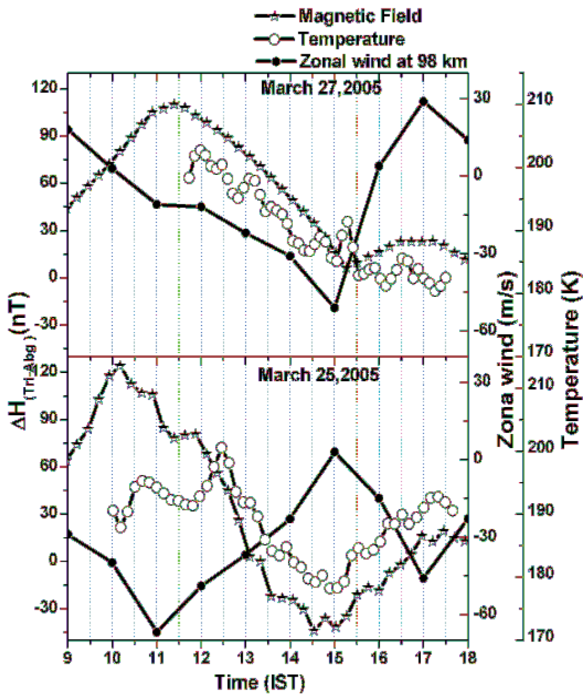

Figure 20: Temporal variation of EEJ strength (DHTRV - DH ABG), mesopause temperature and zonal wind at 98 km for March 25 and 27, 2005

6. INVESTIGATION OF EQUATORIAL SPREAD-F

Planetary Waves Influence on the Occurrence time of ESF

An experimental evidence of Planetary Waves (PWs) modulating the day-to-day occurrence time of the Equatorial Spread F (ESF) during the winter months of the northern hemispheric Sudden Stratospheric Warming (SSW) events is reported. The investigation has been carried out using the data from the digital Ionosonde and Proton Precession Magnetometer located at Trivandrum. The analysis has been performed on three years of data, which include two SSW years and a non-SSW year. Results showed that the occurrence time of the ESF is modulated by a PW of quasi 16-day periodicity during the winter months of the SSW years, when the PW exhibit an enhancement in its amplitude (Fig.21). It has been shown earlier

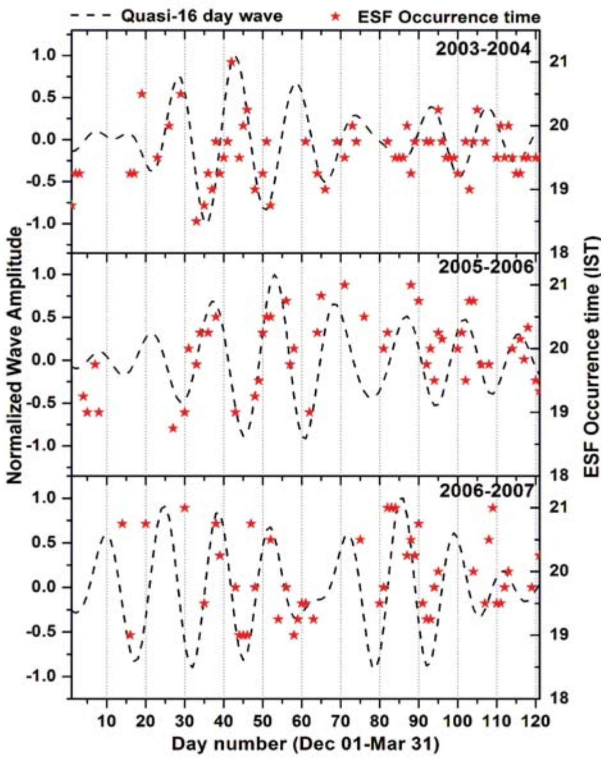

Figure 21: Day-to-day variation of time of occurrence of ESF for the considered period represented by the star. The dotted line represents the normalized quasi 16 day wave in ESF occurrence time, which is taken as the 'reference wave'. The modulation in ESF start time almost in agreement with the wave is seen clearly in this figure

that the quasi 16-day wave is dominant in the equatorial atmosphere-ionosphere region mostly during the northern hemisphere winter. In this context, the above mentioned modulation in the ESF time appears to be a consistent ionospheric feature. It is suggested that the PWs propagated to ionospheric altitudes from the lower atmosphere region through modified electrodynamics. However, it can also be conjectured that the electrodynamics gets modified on account of the wave propagation itself. Though the exact mechanism is yet to be explored, the results presented in this study are very important since the ESF is believed to be highly un-predictable in its occurrence.

Large-Scale Wave Structure and their relation to Equatorial Spread F

Extensive observations of the ESF have shown that there are occasions when the growth-rate of the primary generation mechanism, i.e. the Rayleigh-Taylor (RT) instability, is inadequate to amplify the thermal fluctuations of the F-region plasma to the observed amplitudes of ESF irregularities. In such cases, an initial perturbation is necessary for the 'seeding' of the instability mechanism. The digital ionosonde (Digisonde, DPS-4D) at Trivandrum has been used to infer the presence of Large-Scale Wave structure (LSWS), which is believed to be one of such pre-requisites for the generation of ESF. These waves manifest themselves in the ionograms as 'satellite' traces and multi-reflected echoes (MREs). This aspect of the correlation between the presence of LSWS and the ESF occurrence is being scientifically pursued across the globe and the present study is the first of its kind from the Indian sector. Fig.22 (a) shows the digisonde observations before an ESF event (onset at 14:16 UT, not illustrated). The corresponding Doppler skymap is shown in the bottom panel (Fig.22b). The skymap, in geomagnetic coordinates, shows the locations of the F-region reflection points for frequencies between 4 and 5 MHz from within a cone of 30° around zenith. The ionogram shows the presence of a 'satellite' trace or 'oblique' echo in the 2F and 3F traces. The satellite trace is seen to be coming from the eastern direction. The skymap (bottom panel) also shows significant number of 'sources' from the off-vertical. These oblique echoes are the signatures of the LSWS.

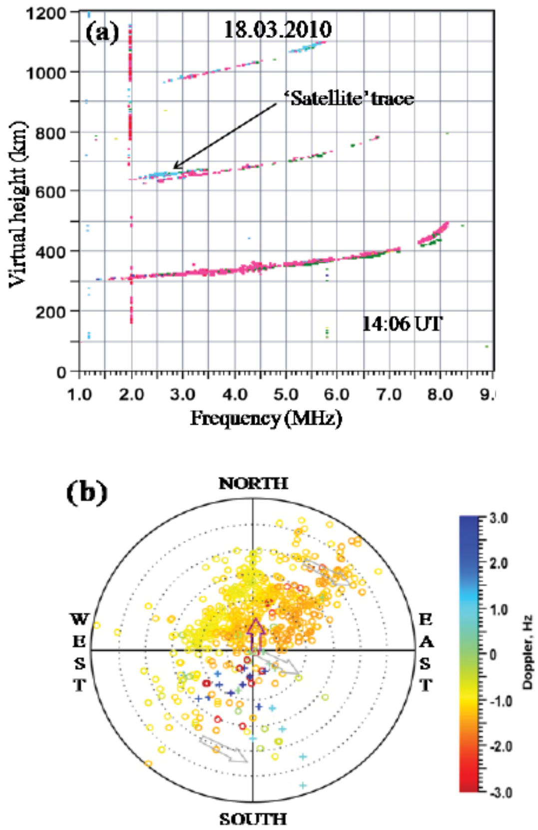

Figure 22: (a) Ionogram showing the 'satellite' trace about 10 minutes before the onset of ESF indicating the presence of wave. The X-axis is the frequency, in linear scale and the Y-axis shows the virtual height. (b) The Doppler skymap showing the echos coming from the North-East direction. The observation is on 18/03/2010

7. DAYGLOW VARIABILITY IN UPPER MESOSPHERE AND THERMOSPHERE

Trends in the temporal evolution of daytime 630.0 nm airglow emissions over Trivandrum in context of equatorial ionspheric/thermospheric variability

It is well recognized that the three major processes responsible for producing the daytime 630.0 nm airglow are the photo electron impact of O, photo dissociation of O_2 and dissociative recombination (DR) of O_2^+ ions. The DR is known to contribute significantly to the dayglow at the low latitudes, and the observed dayglow variability is successfully explained in view of the evolution of Equatorial Ionization Anomaly (EIA). Nonetheless, over the dip equator, the spatio-temporal variability of the dayglow emission intensity appears to be significantly different from that over low latitudes. Our analysis reveals that the observed variability in the dayglow 630.0 nm emission cannot be explained based only on the evolution of EIA, as over the equator the F-region plasma shows both vertical and meridional drifts during daytime. The observed trends in the temporal evolution 630.0 nm dayglow exhibits significant day-to-day variability in conjunction with the behavior of Equatorial electrojet (EEJ). Presented in Fig.23 are three representative

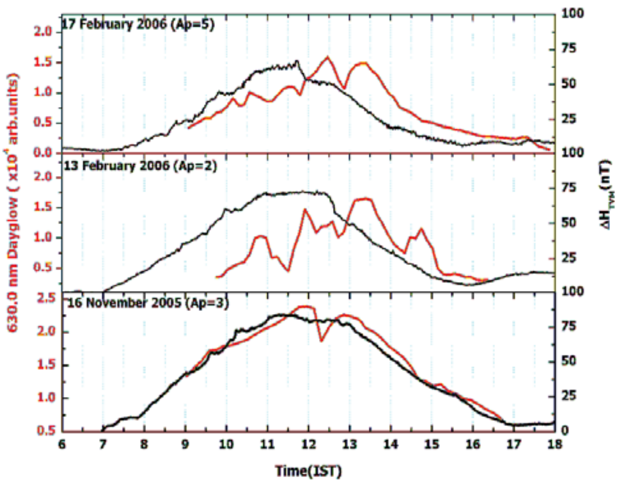

Figure 23: Examples for three cases, where the trends in the both dayglow and EEJ shows good correlation (bottom), do not exhibit any correlation (middle) and shows a correlation with a time delay of ~1 hr (top)

cases, where (1) the trends in the both dayglow and EEJ show good correlation (bottom panel), (2) do not exhibit any correlation (middle) and (3) show positive correlation with a time delay of one hour (top). The cases where good correlation is observed, with and without time-delays, the dayglow variability appears to be controlled by the prevailing electric field and consequent vertical plasma drift redistributing the electron density over and around the equator. However, cases where no direct correlations are observed, the observed dayglow variability are ascribed to non-local dynamical forcing. On the whole, a plausible explanation is explored in the context of the Equatorial plasma drifts and anomaly generation using various ionospheric/thermospheric measurements (ionosonde, TEC) in detail.

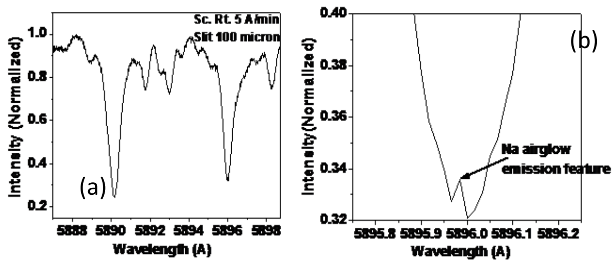

Figure 24: (a) Solar Fraunhofer D lines (5890 and 5896 Å) on a clear day measured with the spectrometer, (b) Zoomed in D1 line (5896 Å) showing the Na airglow emission

Daytime Sodium Airglow Emission Measurements over Trivandrum using a Scanning Monochromator: First Results

In a significant, first time, advancement, a technique based on a 1-meter scanning monochromator for ground based measurements of daytime sodium (Na) airglow at 5896 Å has been developed in-house and demonstrated. Fig.24a shows the solar Fraunhofer D lines measured by the spectrometer. The zoomed in D1 line (Fig.24b) shows the Na airglow emission feature. To study the Na airglow intensity variability, within a day and from day-to-day, simultaneous measurement of OH airglow has been carried out using the Multi-wavelength dayglow photometer. Fig.25a-d show the comparisons of normalized intensities of Na and OH emissions on four different days. For Fig.25a, b and d maximum cross-correlations obtained are respectively 0.97, 0.87 and 0.78 with zero time lag. Obviously the Na and OH emissions variability on these 3 days show excellent correlations without any noticeable time delay.

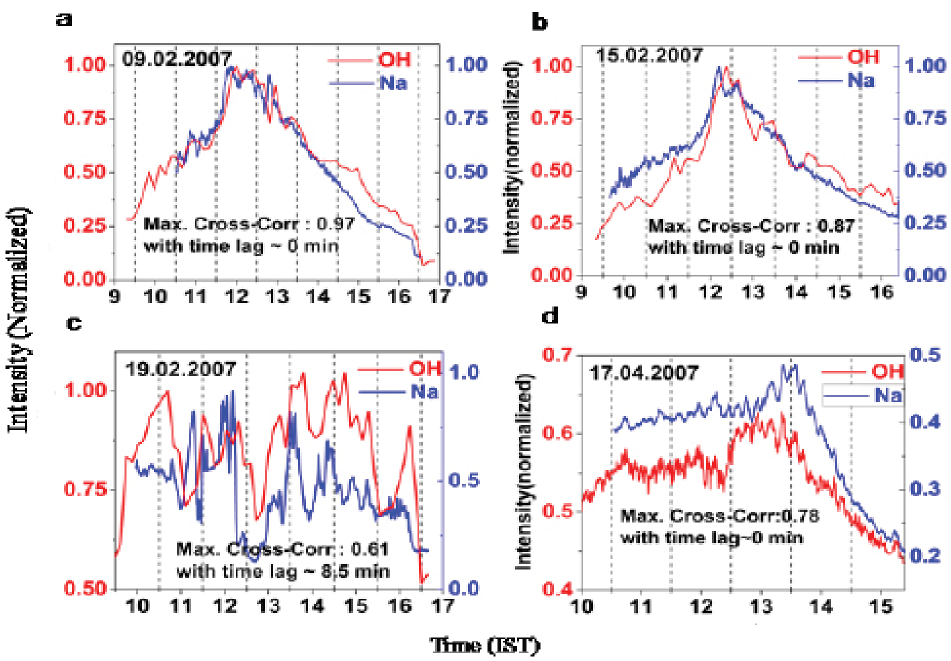

Figure 25: (a)-(d) Comparative plot of the temporal variabilities of the Na and OH emissions on 4 days during February, 2007

However, the maximum cross-correlation obtained for Fig.25c is 0.61 with a time lag ~ 8.5 minutes. For daytime Na airglow emissions, it is well-known that resonant excitation plays the dominant role. On the other hand, daytime OH emissions owe only to the photo-chemical excitations.

To investigate the reason behind similar variability, the Chapman chemical scheme for excitation of Na atoms and the chemical excitation mechanism for daytime OH airglow have been considered. It is obvious from the respective chemical schemes that O and O_3 play similar role in the excitations of both the airglows. As both the airglows originate from the same altitude region (90 km), the effect of dynamical activity (waves) is expected to be same for both the emissions. Hence, similar variability in these emissions is believed to be due to the similar role played by the [O] and O_3 (in their photo-chemical excitations) and the dynamics occurring at the same altitude region. The wavelet analysis of these emission intensities reveals the presence of gravity waves of periodicity ~1.5 hour as seen in Fig.26.

This shows that the gravity waves play significant role in producing the short-scale oscillations in these emissions.

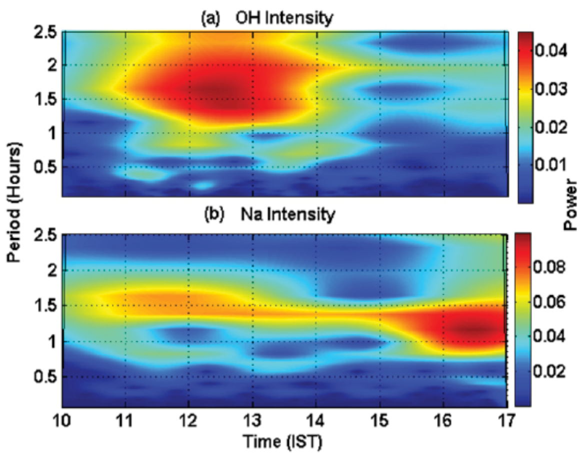

Figure 26: Wavelet periodograms of (a) OH Intensity and (b) Na Intensity, on February 19, 2007

Spatial Heterodyne Spectrometer development for imaging airglow

Interference spectrometers, such as Fabry-Perots and Michelsons, offer significant advantages over conventional grating spectrometers for the study of faint spatially extended sources, such as (1) throughput, typically 200 times larger than grating spectrometers; (2) compact size, especially at high resolution; and (3) relative ease of attaining high resolution. The Spatial Heterodyne Spectrometer (SHS) offers all the above advantages and also offers relaxed flatness tolerances ~ 20-50 times compared to that of a Fabry-Perot and does not require complex scanning mechanism like Michelson based Fourier transform spectrometer. Besides SHS does not require precision imaging to achieve diffraction-limited spectroscopic performance and defects can largely be removed in data processing. Consequently, SHS is emerging as an important tool in study of planetary atmospheres. Keeping this in mind, the development of a SHS on a table top for ground based measurements of faint airglow emissions at wavelengths 5577, 5890, 5896, 6300, and 6364 Å, which originate from different altitude regions of earth's atmosphere has been undertaken.

Figure 27: Table-top set for the SHS in optical aeronomy laboratory

The SHS has been set up with a pair of identical blazed gratings (1800 grooves/mm, ruled area ~ 56 × 56 mm^2, blaze wavelength at 6300 Å nm) mounted in precision rotation stages, a non-polarizing cube beam splitter and a pixelink CCD (1392 × 1040 pixels, 6.45 × 6.45 μm^2) as the detector. Preliminary alignment is carried out using a He--Ne laser and near zero path difference is obtained between the two arms (Fig.27). Critical adjustment is made using a Ne spectral lamp (6304.8 Å line emission) to tune the system at Littrow configuration for observation of 6300 Å airglow emissions. To do this, light from the Ne lamp is filtered using a narrowband interference filter (6303 Å, FWHM 11 Å) and allowed to go through the system with the gratings rotated to the angle ~ 34°. Fig.28 (a), (b) and (c) show fringe patterns during the initial

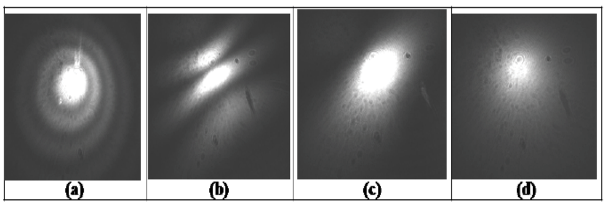

Figure 28: The fringe patterns during the initial alignment. The system tuned to Littrow configuration produce interferogram of zero spatial frequency, as shown in panel (d)

ITMP

alignment. For observation of 6300 Å airglow emissions, the system tuned to Littrow configuration produce interferrogram of zero spatial frequency, which is shown in Fig.28d. The SHS is now ready for field test for having high resolution (~ 0.05 Å) measurement of the 6300 Å airglow emission and also for further improvement with the ultimate goal to make it in the form of a payload for satellite based studies of the aeronomy of planetary atmospheres.

RO investigations of planetary ionospheres and atmospheres

In view of the potential of R.O. techniques for investigating the characteristics of planetary atmospheres and ionospheres and also in the back drop of the effects using the Chandrayaan-I data, a proposal ROX (Radio Occultation eXperiment) has been prepared for the forthcoming 2013 Mars mission and has now been short listed. The experiment envisages the use of coherent S and X band transponders for the orbiter for RO retrievals. In addition, two experimental developments are being initiated with a futuristic outlook for possible Martian exploration (period 2016/2018). These are the top side summary of Martian ionosphere and the spatial heterodyne spectroscopy of Martian Thermosphere.

PUBLICATIONS IN REFEREED JOURNALS

1. Vineeth, C, T. K. Pant, K. K. Kumar and S. G. Sumod, “The Tropical Connection to the Polar Stratospheric Sudden Warming through Quasi 16-day wave”, Ann. Geophys., 28, 2007–2013, 2010.

2. Vineeth, C, T. K. Pant, S. Gurubaran, M. M. Hossain and R. Sridharan, “A comparison of Optically measured Daytime Mesopause Temperatures over the Tropics during the Solar Maximum and Minimum Periods, Earth, Planet Space, 62, 647–653, 2010.

3. Sreeja, V., S. Ravindran and T. K. Pant, “Features of the F3 layer Occurrence over the Equatorial Location of Trivandrum”, Ann. Geophys., 28, 1741-1747, 2010.

4. Hossain, M. M, T. K. Pant, C. Vineeth, S. G. Sumod and R. Sridharan, “Daytime Sodium Airglow Emission Measurements over Trivandrum using a Scanning Monochromator: First Results”, Ann. Geophys., 28, 2071–2077, 2010.

5. Sharma, K., R. S. Dabas, S. K. Sarkar, R. M. Das, S. Ravindran, and A. K. Gwal, Anomalous enhancement of ionospheric F2 layer critical frequency and total electron content over low latitudes before three recent major earthquakes in China, J. Geophys. Res., 115, A11313, doi:10.1029/2009JA014842, 2010.

6. Mathew, T. J, S. R. P. Nayar, S. Ravindran and T. K. Pant, Characteristics of the equatorial F-region vertical plasma drift observed during post-sunset and pre-sunrise hours, Adv. Space Res., 46, 618–625, 2010.

7. Pant, T. K., C. Vineeth, S. G. Sumod and L. Jose, “Evidence for the Lowering of the Centroid of Daytime Thermospheric O (1D) 630.0 nm emission over the Magnetic Equator:- First results” Adv. Space Res., 47, 729–735, doi:10.1016/j.asr.2010.08.011, 2011.

8. Vineeth, C, T. K. Pant and R. Sridharan, “Daytime Mesopause Energetics over a Tropical Station, Trivandrum (8.5oN, 77oE):- An Investigation using the Multiwavelength Dayglow Photometry”, J. Geophys. Res., 116, A01304, doi: 10.1029/2010JA015633, 2011.

9. Vineeth, C, T. K. Pant, S. G. Sumod, K. K. Kumar, S. Gurubaran, R. Sridharan, “Planetary Wave-tidal interactions over equatorial MLT region and their possible implications for the Equatorial Electrojet”, J. Geophys. Res., 116, A01314, doi: 10.1029/2010JA015895, 2011.

10. Sreeja, V, T. K. Pant and L. Jose and S. Ravindran, “Long Duration Westward Electric Field Penetration to the Dayside Equatorial Ionosphere during the Main Phase of the Geomagnetic Storm on 22 July 2009”, J. Geophys. Res., 116, A03303, doi: 10.1029/2010JA016013, 2011.

11. St.-Maurice, J. P, K. M. Ambili, and R. K. Choudhary, “Local electrodynamics of a solar eclipse at the magnetic equator in the early afternoon hours”, Geophys. Res. Lett., 38, L104, doi:1029/2010GL046085, 2011.

12. Bagiya,M.S., K.N.Iyer, H.P.Joshi, S.V.Thampi, T.Tsugawa, S.Ravindran, R.Sridharan and B.M.Pathan. “Low-latitude ionospheric thermospheric response to storm time electrodynamical coupling between high and low latitudes” J.Geophys.Res., 116, A01303, doi:10.1029/2010JA015845, 2011.

13. Manju, G, V. Sreeja, S. Ravindran and S. V. Thampi, “Towards Prediction of L band scintillations in the Equatorial Ionization Anomaly (EIA) Region”, J. Geophys. Res., 116, A02307, 8 PP., 2011, doi: 10.1029/2010JA015893 (AGU Editor’s choice AGU: Space weather).

14. Balan, N, M. Yamamoto , V. Sreeja, I. S. Batista, K. Lynn, M. A. Abdu, S. Ravindran, T. Kikuchi, Y. Otsuka, K. Shiokawa , S. Alex, “A statistical study of the response of dayside equatorial F2 layer to the main phase of intense geomagnetic storms”, J. Geophys. Res., 116, A03323, doi: 10.1029/2010JA016001, 2011.

15. Jose, L, S. Ravindran, C. Vineeth, T. K. Pant and S. Alex, Investigation of the Response time of the Equatorial Ionosphere in context of the Equatorial Electrojet and Equatorial Ionisation Anomaly, Ann. Geophys., 29, 1267-1275, 2011.

16. Sumod, S. G, T. K. Pant, C. Vineeth, M. M. Hossain and M. Antonita, “Response of Tropical Mesopause to the longest Annular Solar Eclipse of this millennium”, J. Geophys. Res., 116, A06317, doi: 10.1029/2011 2010JA016326, 2011.

17. Sumod, S. G, T. K. Pant, C. Vineeth and M. M. Hossain “A new insight into the vertical neutral-ion coupling between the mesopause and ionosphere F region”, Ann. Geophys., 29, 421–426, 2011.

18. Mridula, N, G. Manju., T. K. Pant, S. Ravindran, L. Jose and S. Alex, ”On the significant impact of the moderate geomagnetic storm of March 2008 on the Equatorial Ionization Anomaly region over Indian longitudes”, J. Geophys. Res., 116, A07312, doi:10.1029/2011JA016615, 2011.

PRESENTATIONS IN SYMPOSIA/WORKSHOPS/ CONFERENCES

International

1. Manju, G, P. Sreelatha, S. Ravindran, R. John, N. Naik, S. Thampi, P. Pradeep Kumar, S. V. Mohan Kumar and R. Sridharan, A new Ionospheric Probe for insitu measurements of neutral wind and electron density, AOGS, July 2010, Hyderabad, India.

2. Ravidran, S, N. Mridula, R. Sridharan, R. S. Dabas, A. D Sarma, R. Sarma, G. Manju and T. K. Pant, Spatio-temporal variability of the equatorial and low latitude Ionosphere-Results from the Indian Ionospheric tomography experiment, AOGS, July 2010, Hyderabad, India.

3. Sreeja, V , T. K. Pant, C. V. Devasia, L. Paxton, Response of the Equatorial and Low Latitude Ionosphere Thermosphere System to the Space Weather events During the Declining Phase of the Solar Cycle 23, AOGS, July 2010, Hyderabad, India.

4. Patra, A. K, L. Joshi, P. C. Peddapati, T. K. Pant, New Aspects of F Region Plasma Irregularities Revealed by the Gadanki Radar, AOGS, July 2010, Hyderabad, India.

National

1. Sumod, S. G, T. K. Pant, C. Vineeth, M. M. Hossain, Response of Tropical Mesopause to the longest Annular Solar Eclipse of this millennium, National Workshop on Solar Eclipse, Trivandrum, India, 2011.

2. Jose, L, T. K. Pant, C. Vineeth and Sumod, S. G, Electron Density variation during the Annular solar Eclipse: An investigation using the Modern Digisonde, National Workshop on Solar Eclipse, Trivandrum, India, 2011.

3. Hossain, M. M, T. K. Pant, C. Vineeth and S. G. Sumod, Spatial Heterodyne Spectrometer Development for imaging Airglow emissions", International Conference on contemporary Trends in Optics and Opto-electronics, XXXV Symposium of Optical Society of India, India, January 2011.

4. Hossain, M. M, C. Shakher, and T. K. Pant, Convective flow field visualization and temperature measurement therein using digital holography, International Conference on contemporary Trends in Optics and Opto-electronics, XXXV Symposium of Optical Society of India, India, January 2011.

INVITED TALKS /LECTURES

R. K. Choudhary

1. "A Study on the respective role of Kelvin-Helmholtz Instabilities and Gravity waves in the generation of Quasi-Periodic echoes at Gadanki", AOGS10, Hyderabad, India, July, 2010.

2. "Global Positioning System satellites (GPS) and civil aviation" International Seminar on Space Science and Technology, N.S.S. Hindu College, Changanacherry, October 12, 2010.

3. "Modeling of Ionospheric structures using TEC data", Brainstorming on Space and Climate, PRL, Ahmed-abad, April 27-28, 2011.

Tarun Kumar Pant

4. "The Polar Sudden Stratospheric Warming (SSW) and Its Possible Manifestations in the EquatorialMeso-sphere-thermosphere-ionosphere", AOGS10, Hyderabad, India, July, 2010.

5. "Investigation of the Mesopause Energetics and Its Possible Implications on the Mesosphere-lower Thermo-sphere –ionosphere (MLTI) Processes", AOGS10, Hyderabad, India, July, 2010.

ACADEMIC PROJECTS

Internship for M. Sc. Physics: 5

PLANETARY SCIENCE BRANCH

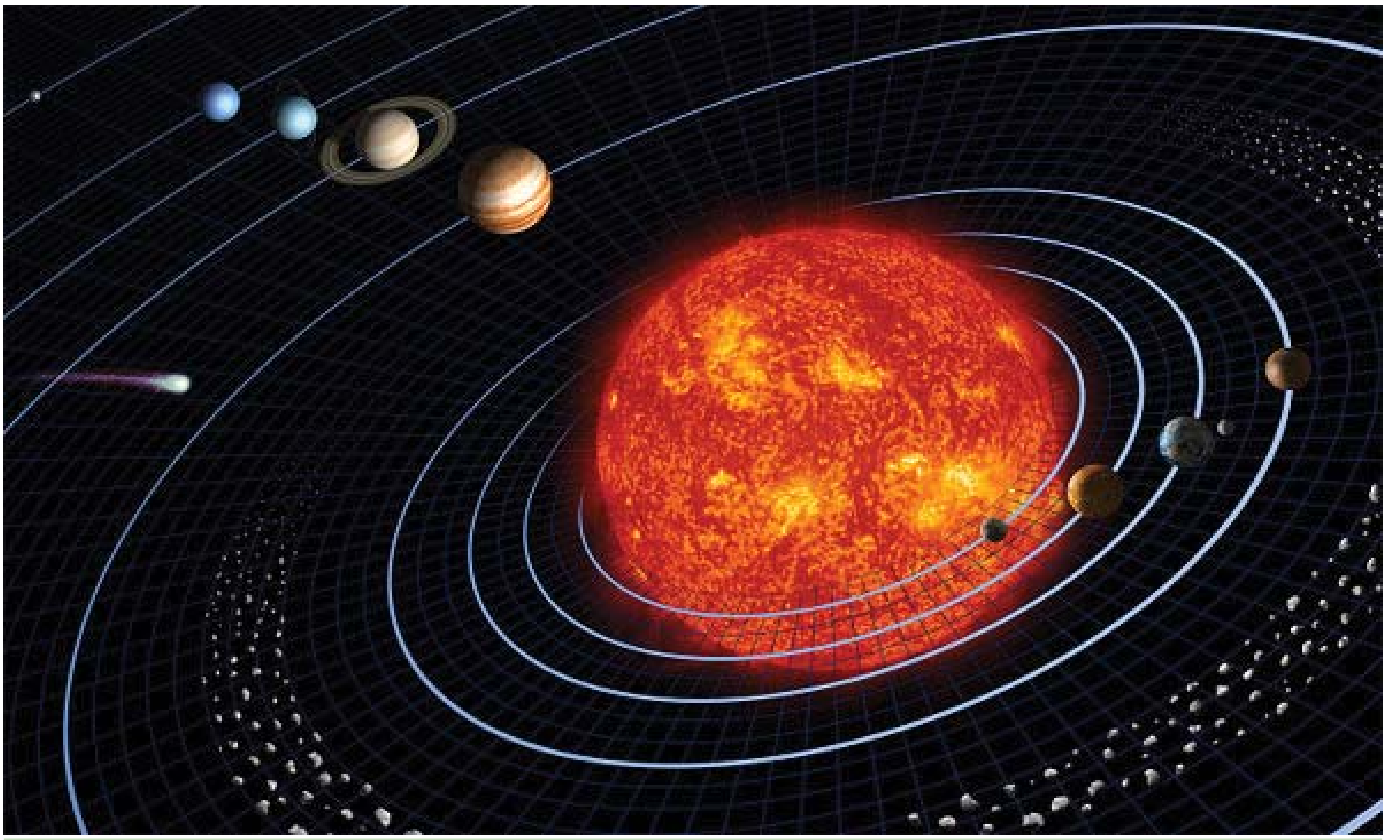

Science Faculty

Anil Bhardwaj
Satheesh Thampi R
Vipin Kumar Yadav
Dhanya M B
Gogulapati Supriya

Technical Team

Mohankumar S V
Sreelatha P
Pradeepkumar P
Tirtha Pratim Das
Neha Naik
Rosmy John

Research Fellows

Sonal Kumar Jain
Susarla Raghuram
Abhinaw Alok

The academic pursuit of Planetary Science Branch (PSB) encompasses the study of the processes initiated due to the interaction of solar radiation with planetary bodies, including planets, comets, and planetary satellites. It includes experimental investigation of planetary environment, including in-house development of instruments, and theoretical modeling of the processes. The activities of PSB are linked to ISRO's planetary missions – starting with the first mission Chandrayaan-1, continuing on to Chandrayaan-2, and looking ahead to Mars-2013 and future missions.

1. SARA EXPERIMENT ONBOARD CHANDRAYAAN-1: SCIENCE RESULTS

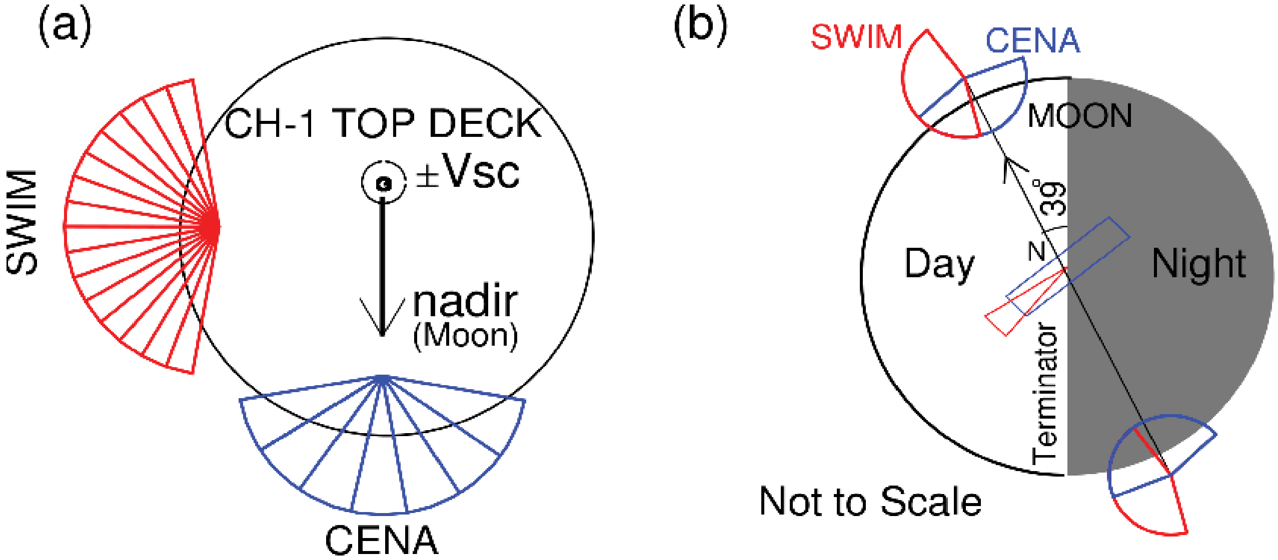

Figure 1: (a) The mounting and Field of View (FoV) of CENA and SWIM on Chandrayaan-1. The arrow shows the direction of nadir and the direction of spacecraft velocity vector. CENA has a FoV of 7° x 160° which is divided into 7 angular pixels, the position of the extreme view directions are shown in the figure by numbers 0 and 6. SWIM has a FoV of ~ 7°x 160°, with 16 angular pixels, the position of the extreme view directions are shown in the figure by numbers 0 and 15. (b) The FoV of SWIM and CENA along with the orbital motion of Chandrayaan-1 on 6 February 2009, where the orbital plane was at an angle of ~ 39° with the day-night terminator

The Sub-keV Atom Reflecting Analyzer (SARA) experiment onboard the orbiter of Chandrayaan-1, an international collaborative effort, that produced several new results on Moon and the lunar-solar wind interactions, consisted of 2 sensors: CENA (Chandrayaan-1 Energetic Neutrals Analyzer) and SWIM (Solar Wind Monitor) mounted as shown in Fig. 1a. Both the sensors have fan-shaped FoV and were mounted on the top deck enabling nadir viewing with their FoVs in the same plane. The SWIM mounting was such that the centre view direction of SWIM is almost 90° to that of CENA. Due to this mounting, as shown in Fig. 1b, a few view directions of SWIM looked at the Moon surface, and this has enabled the following interesting investigations (not originally contemplated with the SARA).

a. Global Influence of Lunar Crustal Fields on the Solar Wind Flow

Although, the Moon lacks a strong global magnetic field, it has regions of crustal magnetization called "magnetic anomalies", which interact with the solar wind. The SWIM has observed reflected protons from these magnetic anomalies, mainly in the lunar surface-looking and horizon-looking pixels (Fig.2).

From the map of the reflected proton fluxes over the lunar far-side (Fig.3), it is found that proton reflection is a global feature of the solar wind interaction with the Moon and that a maximum reflection efficiency of ~50% is seen at the strongest magnetic anomalies (Fig.3).

On an average, over the anomaly regions, ~ 15% reflection is observed (Fig. 4). Averaged over the whole far-side hemisphere, the total reflection is ~ 2%. These observations suggest that magnetic anomalies act in a coherent way, so as to create a weak magnetosphere-like obstacle, globally affecting the solar wind flow (though in much reduced way compared to that on Earth). The proton reflection reduces the implantation rate of hydrogen on to the lunar surface and may affect space weathering of the surface, especially at the magnetic anomaly regions.

b. Statistical Analysis of Solar Wind Protons in Near-Lunar Plasma Wake

As the solar wind flows past the Moon, a cavity is formed behind it. Solar wind ions and electrons, driven by the pressure gradient penetrate in to this cavity. As the thermal velocity of solar wind ions are less (~ 50 km s^{-1}) compared to the bulk velocity of solar wind (~ 350 km s^{-1} on an average), entry of solar wind ions in to the cavity would not occur close to the Moon. This cavity, which is devoid of any ions and which gets closed at larger distance downstream, is called lunar plasma wake and it is slightly tilted (maximum ~ 6°) from the optical shadow of Moon due to the aberration of solar wind. However, SWIM has made a surprising observation of protons close to

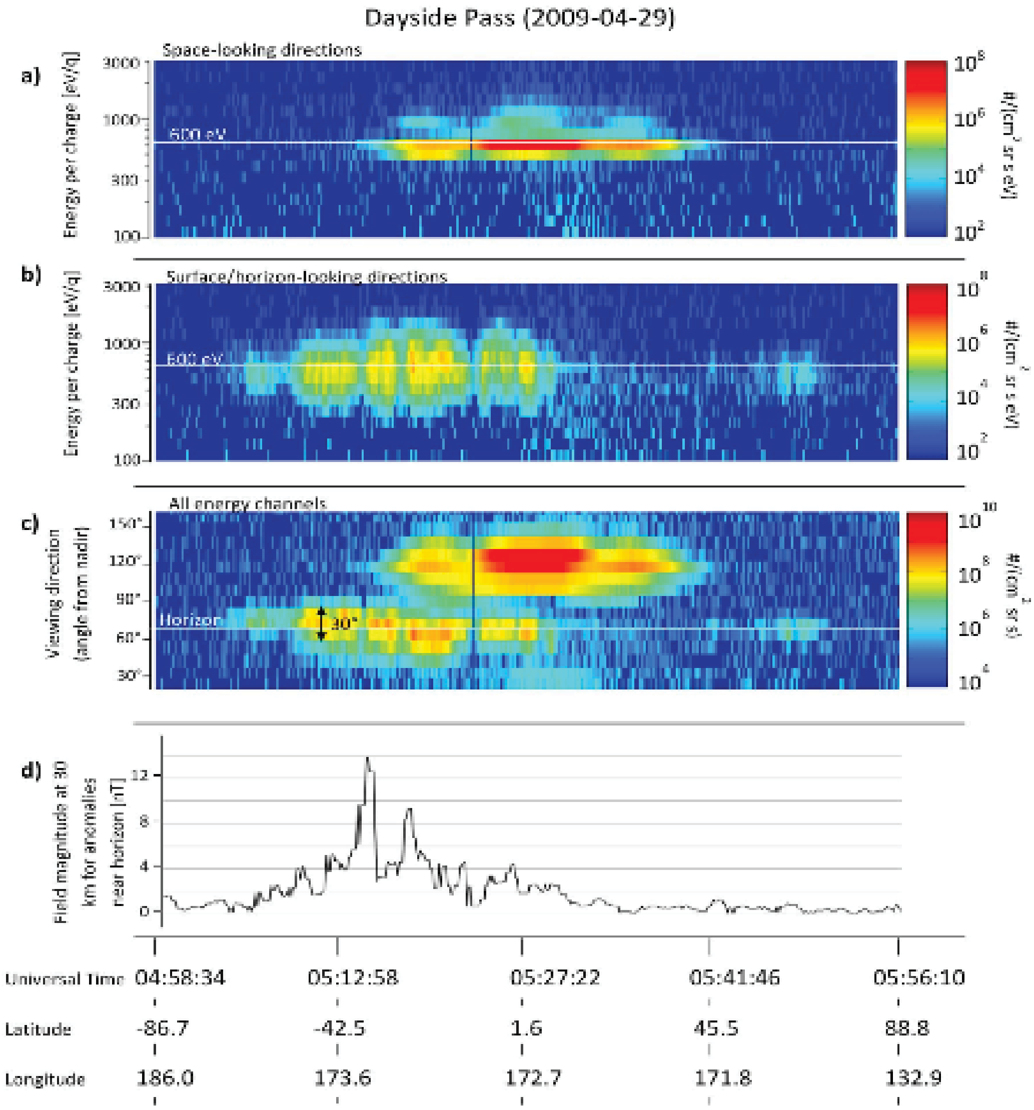

Figure 2: Dayside pass of Chandrayaan-1 between 04:58 and 05:57 UT on 29 April 2009, over the Imbrium antipode magnetic anomalies. The energy distribution of the differential flux observed by SWIM/SARA, summed over (a) five space-pointing directions (104° – 142° from nadir) and (b) five surface-pointing directions (44°– 80° from nadir). (c) The direction distributions in angle from nadir, of the differential flux, integrated over the 100 eV – 3 keV energy range. (d) For reference, the strength of magnetic anomalies near the horizon. The strength is given in field magnitude at 30 km altitude, in model by Purucker [2008], from Lunar Prospector data. Time and selenographical coordinates are also shown

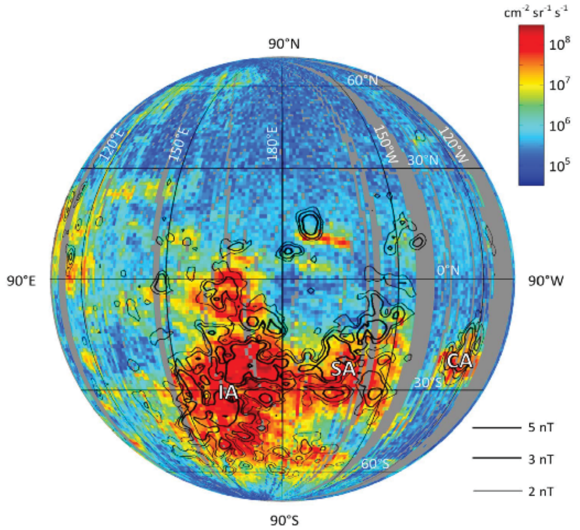

Figure 3: The map of deflected solar wind protons in the 200 eV – 1.7 keV energy range from SWIM/SARA observations. The peak differential flux of protons is traced linearly to the surface of the Moon and binned to a 1° × 1° resolution. Black contours show modeled 2 nT, 3 nT and 5 nT magnetic field strength at 30 km altitude. The large anomaly cluster at the Imbrium Antipode (IA) , as well as the Serenitatis Antipode (SA), Crisium Antipode (CA) and several smaller magnetic anomalies are clearly seen. The figure is drawn showing far-side of Moon as viewed from space

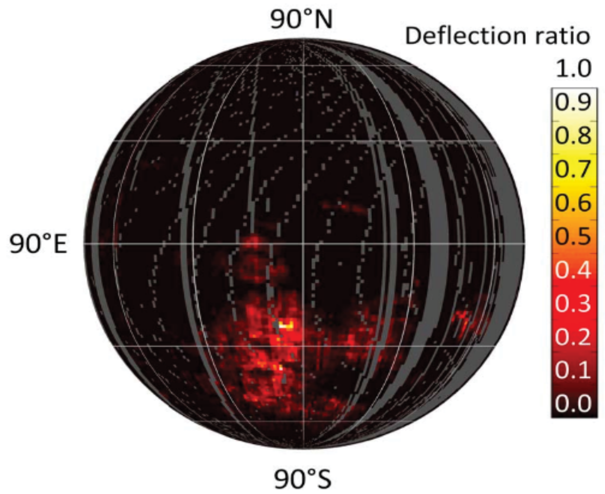

Figure 4: Map of the ratio between out-flowing proton flux calculated from SWIM data and inflowing proton flux calculated from WIND satellite data

the lunar surface (~ 100 km from Moon surface) and even deep inside the lunar plasma wake in almost all orbits. As the solar wind is a magnetized plasma, the entry of solar wind ion to plasma wake is governed by the orientation of the interplanetary magnetic field (IMF). Of the 4 possible mechanisms suggested for ion entry to the near wake, 3 favor ion entry in a direction perpendicular to IMF and one favors entry of ions parallel to IMF. As these mechanisms were proposed on the basis of case studies with a fixed IMF orientation, a statistical analysis is required to understand the dominant entry mechanism and whether the mechanisms vary when we move from near the wake boundary to the deep wake.

Entire SWIM data from the 100 km orbits were considered for the analysis after excluding the orbits when Moon was inside the Earth's bowshock and magnetotail regions. A map of total number of observations by SWIM binned into 100 x 100 km grids projected in the YZ-plane of aberrated lunar-centered solar ecliptic (LSE) coordinates sytem is shown in Fig.5.

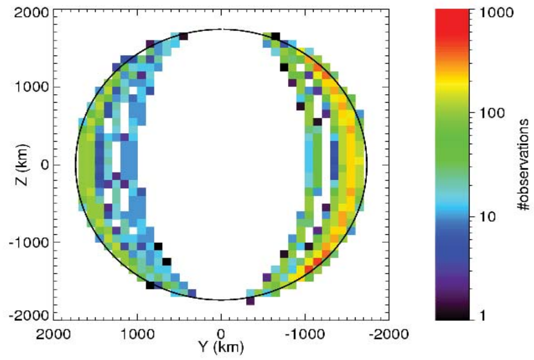

Figure 5: Map of number of observations by SWIM in the lunar plasma wake, when Chandrayaan-1 was in 100 km orbit. The map is in aberrated LSE co-ordinate system projected along -x, i.e., in the yz plane of LSE as viewed from behind (nightside) the Moon. The circle represents the projected surface of Moon. LSE co-ordinate system has its origin located at the centre of the Moon, with x axis pointing toward the Sun, z axis is towards ecliptic north pole, and y axis completes the right-hand co-ordinate system.

The counts obtained in each grid are converted in to the differential flux (cm^{-2} s^{-1} sr^{-1}) and the map of the average differential flux is shown in Figure 6(a). The differential flux of protons appears to be symmetric between the dawn side ($-Y_{LSE}$) and dusk side ($+Y_{LSE}$) of the Moon. To remove the influence of the variation in the upstream solar wind flux on the observed flux of wake ions, we have normalized the observed ion flux in the wake by the upstream solar wind flux taken from ACE (Advanced Composition Explorer) satellite after time shifting the ACE data to account for the solar wind propagation time. The resulting map is shown in Fig. 6b.

It revealed that the normalized differential flux (Fig. 6b) also is symmetric between dawn side and dusk side of the Moon, implying a symmetric (with respect to dawn and dask) filling of the near-lunar wake. This suggests that in the near-lunar wake the ion expands into the wake independent of IMF orientation (i.e., magneto-sonic expansion rather than the sonic expansion).

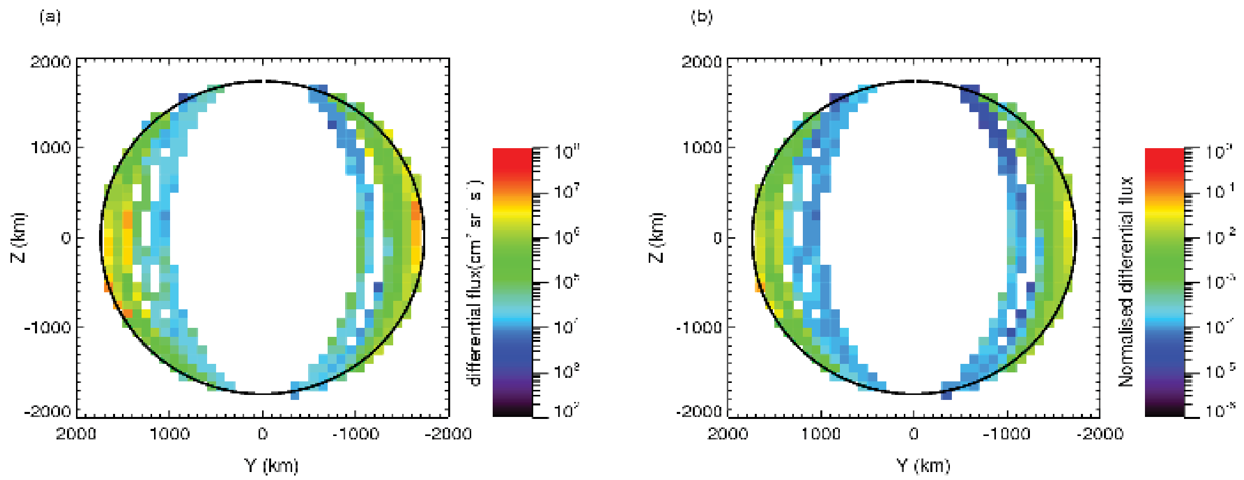

Figure 6: Map of the differential flux observed by SWIM in the lunar plasma wake of the Moon (left panel). The map with observed differential flux of wake ions normalized to the upstream solar wind flux (from ACE), in aberrated LSE frame (right panel)

c. Search for Backscattered Neutral He from the Moon

An investigation to search for backscattered neutral He atom from lunar surface has been conducted by combining the CENA and SWIM data. The orbits, when Moon was in the undisturbed solar wind, were chosen. The amount of backscattered He from lunar surface depends on the amount of He (in the form of He^{++}) in the impinging solar wind. The measure of incident He^{++}/H^{+} ratio in solar wind is obtained from the SWIM measurements. This ratio is found to agree well with the ACE satellite measurement at L1 point after accounting for the solar wind propagation time between L1 point and Moon. The search for the signature of backscattered neutral He in the CENA data involves the analysis of mass spectra of neutral atoms. Due to the lower mass resolution of CENA, the mass peak of neutral He is expected to lie with that in the tail of the mass peak of neutral H atom. A non-negative least square solver to fit hydrogen and helium peak in the neutral mass spectra was applied. The amplitudes of the two fitted peaks were compared to determine the ratio of He to H, which should correlate with that obtained from the SWIM. The results did not show a good correlation between these two, implying that the fraction of backscattered helium from lunar surface could be much lower than that of hydrogen.

2. DELIVERY OF ARCHIVED SARA SCIENCE DATA TO ISSDC

Archival of the SARA scientific data in Planetary Data System (PDS) format, separately for CENA and SWIM along with their respective housekeeping data and auxiliary data for each orbit in separate files, has been done by SPL-ESA-IRF team. The SARA data has been archived in the Planetary Data System (PDS) format, (adopted by ISRO for the archival of Chandrayan-I data), separating for CENA and SWIM along with the respective house-keeping and auxiliary data for each orbit of Chandrayan-I in separate file. The Experimenter to Archive Interface Control Document (EAICD), (a key document describing the

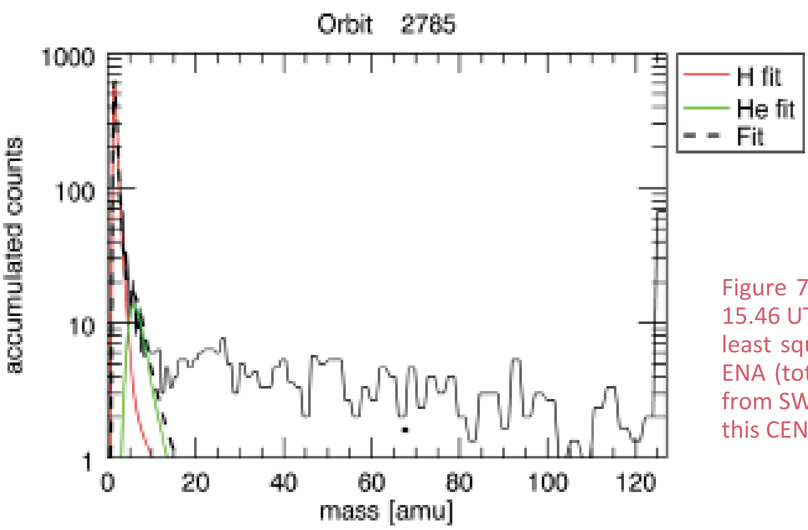

Figure 7: A sample spectrum of CENA obtained at 15.46 UT on 28 June 2009 showing the non-negative least square solver fit for H and He along with the ENA (total) fit. The He/H abundance ratio obtained from SWIM does not match with that obtained from this CENA spectrum fit

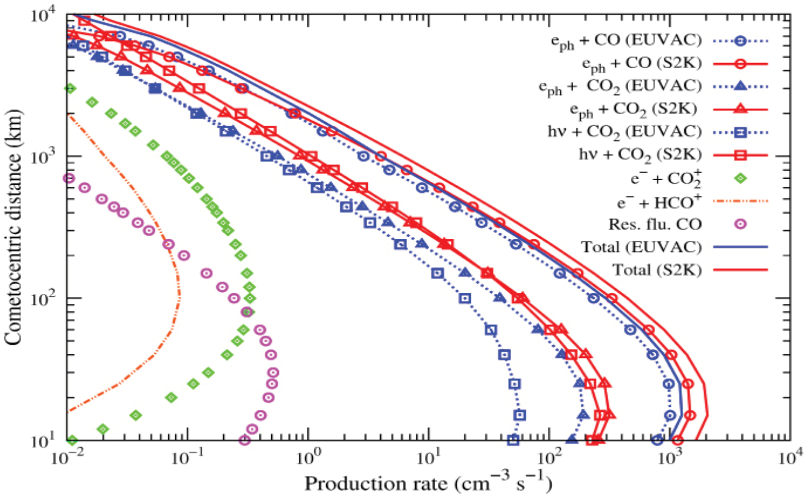

Figure 8: Radial profiles of various production mechanisms of CO($a^3\Pi$) in comet 1P/Halley on 13 March 1986 for relative abundance of 4% CO_2 and 7% CO. The calculated profiles for dissociative recombination of CO_2^+ and HCO+, and resonance fluorescence of CO are shown for EUVAC solar flux only. Res. flu. = resonance fluorescence of CO molecule. e_{ph} = Photoelectron, hv = Solar photon, and e^- = thermal electron

SARA data products, their generation, naming convention, organization and content within a data product directory, information about the quality flag, time stamping, and other aspects) was prepared by SPL, while the Generic Data Processor (GDP) (the pipeline for the archival of the data sets) was configured at the ESA. The 'PDS dataset structure' was generated and checked for compatibility in series before approval. These archived data sets were subsequently validated by the SARA team for its scientific content and were delivered to Indian Space Science Data Centre (ISSDC) on 15 June 2011 for release of SARA data to public.

3. MODELING STUDIES

Production of CO Cameron Band Emission in Comet 1P/Halley

On comet 1P/Halley the Cameron (1-0) band ($a^3\Pi$–$X^1\Sigma$) has been observed by International Ultraviolet Explorer (IUE) on several days in March 1986 around the Giotto encounter period. A coupled chemistry-emission model has been developed to assess the importance of various production (Fig. 8) and loss mechanisms of CO($a^3\Pi$) and to calculate the intensity of Cameron band emission on different days of IUE observation. Two different solar EUV flux models, (EUVAC and SOLAR2000) and different relative abundances of CO and CO_2, were used to evaluate the role of photon and photoelectron in producing CO molecule in $a^3\Pi$ state in the cometary coma. The production rates obtained using SOLAR2000 solar flux models were higher than from that of EUVAC model (Fig.8); the photodissociation of CO_2 is larger by a factor of 2.5, while photoelectron impact excitation is larger by a factor of ~ 1.5. It is found that in comet 1P/Halley, 60-70% of the total intensity of the Cameron band emission is contributed by electron impact excitation of CO and CO_2, while the contribution from photodissociative excitation of CO_2 is small (20-30%) (Fig.9). Thus, in comets where CO and CO_2 relative abundances are comparable, the Cameron band emission is largely governed by electron impact excitation of CO and not by the photodissociative excitation of

Figure 9: The integrated brightness profiles as a function of projected distance from nucleus for different production processes of the Cameron band, using EUVAC solar flux model and relative contribution of 4% CO_2 and 7% CO. The calculated total brightness profile for SOLAR2000 model solar flux is also shown

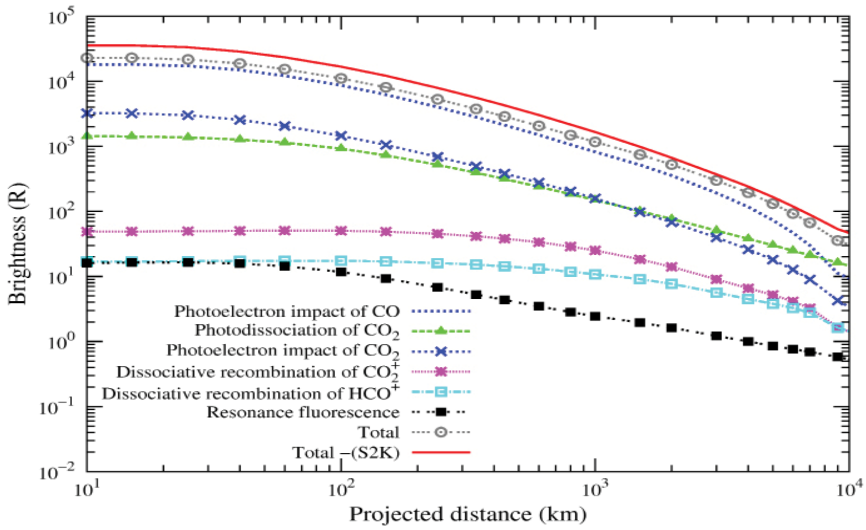

CO_2 as has been assumed earlier. Since electron impact excitation is the major production mechanism, the Cameron emission can be used to derive photoelectron density in the inner coma rather than the CO_2 abundance.

N_2 Vegard-Kaplan Band Emissions in Martian Dayglow

Recently, for the first time, N_2 Vegard-Kaplan band ($A^3\Sigma^+_u - X^1\Sigma^+_g$) emissions have been observed in the Martian dayglow by the SPICAM Ultraviolet Spectrograph aboard Mars Express mission. We have developed a model to explain the production of N_2 Vegard-Kaplan bands on Mars. The steady state photoelectron fluxes and volume excitation rates have been calculated using the Analytical Yield Spectra (AYS) technique. Since inter-state cascading is important for triplet states of N_2, the population of any given level of N_2 triplet states is calculated under statistical equilibrium considering direct excitation, cascading, and quenching effects. Relative population of all vibrational levels of each triplet state is calculated in the model (Fig.10).

Line of sight intensities and height-integrated overhead intensities have been calculated for Vegard-Kaplan (VK), First Positive ($B^3\Pi_g$ - $A^3\Sigma^+_u$), Second Positive ($C^3\Pi_u$ - $B^3\Pi_g$), and Wu-Benesch ($W^3\Delta_u$ - $B^3\Pi_g$) bands of N_2. Our calculations suggest that a reduction in the N_2 density by a factor of 3 in the Mars Thermospheric General Circulation Model is required to obtain agreement between calculated limb profiles of VK (0-6) and SPICAM observation (Fig.11). Calculations are carried out to asses the impact of model parameters, viz., electron impact cross sections, solar EUV flux, and model atmosphere, on the emission intensities. Constraining the N_2/CO_2 ratio by SPICAM observations, we suggest the N_2/CO_2 ratios to be in the range 1.1 to 1.4% at 120 km, 1.8 to 3.2% at 140 km, and 4 to 7% at 170 km. During high solar activity the overhead intensity of N_2 VK band emissions would be ~ 2.5 times higher than that during low solar activity.

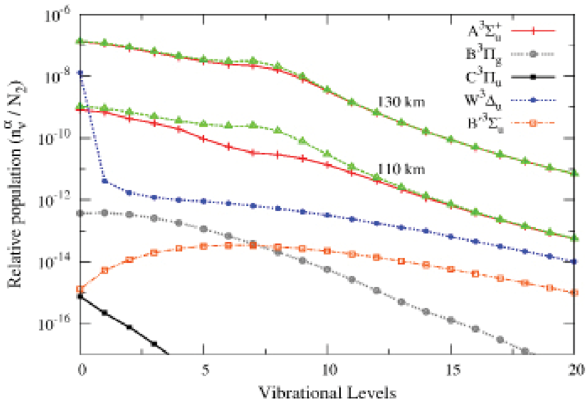

Figure 10: The relative populations of vibrational levels of different triplet states of N_2 with respect to the N_2 density at 130 km. Dashed line with triangle shows the relative vibrational populations of A state at 110 and 130 km, respectively, without considering the quenching

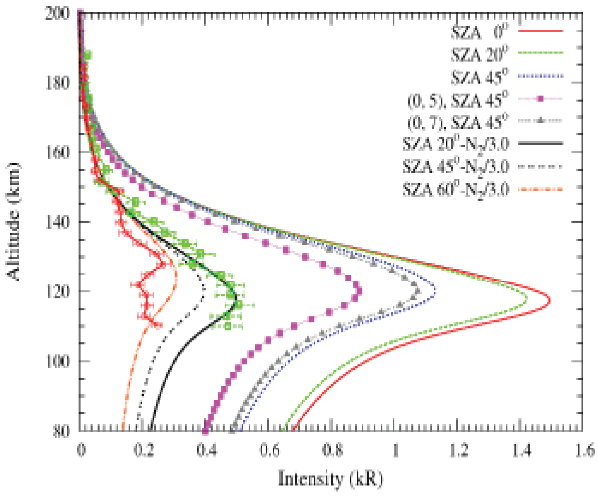

Figure 11: Calculated limb intensity of the N_2 VK (0, 6) band at different solar zenith angles and for the VK (0, 5) and (0, 7) at SZA = 45°. Lines with symbols (open squares, SZA = 8°–30°; open circles, SZA = 36° – 64°) represent the averaged observed value of the VK (0, 6) band for solar longitude (Ls) between 100° and 171° taken from Leblanc et al. [2007]. The calculated intensities, when the N_2 density is reduced by a factor of 3, are also shown, which show a better match with the SPICAM/Mars Express observation

N_2 Triplet States Vibrational Populations and Band Emissions in Dayglow of Venus

A model for N_2 triplet states band emissions in the Venusian dayglow has been developed for low and high solar activity conditions. Steady state photoelectron fluxes and volume excitation rates for N_2 triplet states have been calculated using the Analytical Yield Spectra (AYS) technique. Model calculated photoelectron flux is found to be in good agreement with Pioneer Venus Orbiter-observed electron flux (Fig.12).

Since inter-state cascading is important for triplet states of N_2, the populations of different levels of N_2 triplet states are calculated under statistical equilibrium considering direct electron impact excitation, and cascading and quenching effects. Densities of all vibrational levels of each triplet state are calculated in the model. Height-integrated overhead intensities of N_2 triplet band emissions are calculated, the values for Vegard-Kaplan ($A^3\Sigma_u^+$ - $X^1\Sigma_g^+$), First Positive ($B^3\Pi_g$ - $A^3\Sigma_u^+$), Second Positive ($C^3\Pi_u$ - $B^3\Pi_g$), and Wu-Benesch ($W^3\Delta_u$ - $B^3\Pi_g$) bands of N_2, are 1.9 (3.2), 3 (6), 0.4 (0.8), and 0.5 (1.1) kR, respectively, for so-

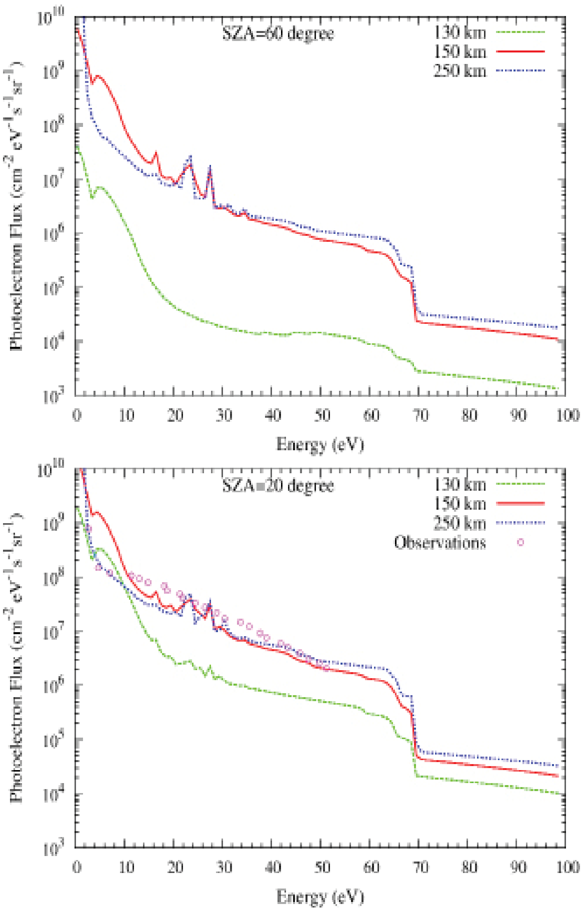

Figure 12: Model calculated photoelectron flux for low (upper panel) and high (bottom panel) solar activity conditions at 130, 150, and 250 km. Symbols in bottom panel represent the Pioneer Venus Orbiter-observed values averaged over 206–296 km and 8°–35° SZA, taken from Spenner et al. (1997)

lar minimum (maximum) conditions. The intensities of the three strong Vegard-Kaplan bands (0, 5), (0, 6), and (0, 7) are 94 (160), 120 (204), and 114 (194) R, respectively, for solar minimum (maximum) condition. Limb profiles are presented for VK (0, 5) and (0, 6) bands (Fig.13). Calculated intensities on Venus are about a factor 10 higher than those on Mars. The present study provides a motivation for a search of N2 triplet band emissions in the dayglow of Venus with the SPICAV instrument on the Venus Express mission.

4. INSTRUMENTATION

a. CHACE-2 Payload for the Chandrayaan-2 mission

The CHACE-2 (Chandra's Atmospheric Composition Explorer-2) experiment is one among the five payloads selected to fly aboard the Chandrayaan-2 orbiter mission and draws its heritage from CHACE-1. However, CHACE-2 would work in different modes

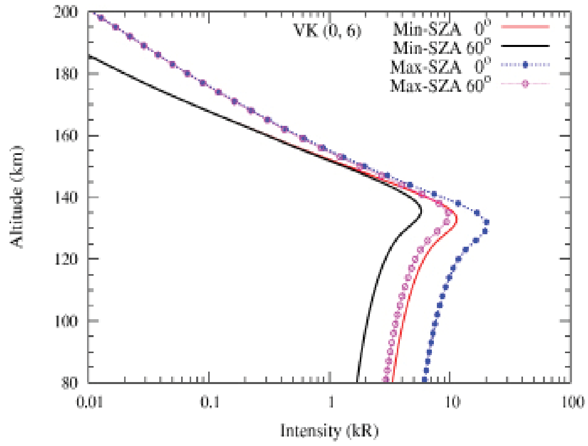

Figure 13: Calculated limb intensity of VK (0, 6) band for low (min.) and high (max.) solar activity conditions, at SZA of 0° and 60°

of observations, over the mission lifetime of more than 1 year and would monitor the global variation of the lunar neutral composition as well as its short and long term variations.

Unlike the CHACE-1, which was a short (44 minutes) duration impactor-borne experiment in the sunlit side of the Moon, the CHACE-2 will be onboard the orbiter in a polar orbit of 200 km altitude and will analyze the lunar neutral atmosphere continuously during the lunar days and nights. While CHACE-1 had the mass range of 1-100 amu, the CHACE-2 covers a mass range of 1-300 amu. The CHACE-1 experiment has observed total pressure of 10^{-7} Torr in the dayside side of moon, while the total pressure in the nightside of the Moon was 10^{-12} Torr near the lunar surface as measured by the Apollo mission.

In order to ensure that the CHACE-2 functions optimally at the diverse pressure levels two broad modes of operation are envisaged, viz. the mass sweep mode and the trend mode. In the mass sweep mode, the entire mass range of 1-300 amu will be scanned by the instrument within a pre-defined time (depends on the scan rate). On the other hand, in the trend mode, a maximum number of eight pre-selected species can be simultaneously tracked and their temporal evolution can be studied with a good sampling frequency, and hence at high spatial resolution. In the CHACE-1 experiment only the mass sweep mode was exercised. The development of CHACE-2 is in progress (see under ATD).

b. New Initiatives and Facilities

LEIMA: Developmental activity of Low Energy Ion Mass Analyser (LEIMA) is in progress with the improved version of the instrument. The ion optics simulations to optimize the energy, mass and angular resolutions are underway. In parallel, engineering drawing of LEIMA using CAD and the process for fabrication is also in progress. Two chevron-type Micro channel Plates (MCP) along with power supplies, have been procured and being testing.

PLEX: Preliminary design of the PLasma Energy eXplorer (PLEX) using cylindrical geometry is in progress. Presently the extensive simulations are underway using SIMION to optimise the energy and angular resolutions as well as the field of view of the instrument. This instrument is being proposed for the Mars 2013 mission.

Plasma Wave Detectors: All planetary bodies having an ionosphere are capable of sustaining electromagnetic and electrostatic waves. Few of earlier missions to Mars, have performed experiments in this regard and have reported low frequency oscillations (in kHz range). Plasma wave studies provide valuable information on solar wind-planet interaction, the generation of planetary radio emissions, understanding the magnetosphere physics, the energy distribution in plasma, etc. To achieve this scientific objective, it is proposed to develop spherical Langmuir probe to characterize the plasma in the ionosphere, electric dipole probe to detect the wave electric field and magnetic loop probes to the measure the wave magnetic fields. The developed instruments shall be tested on a sounding rocket before freezing the final flight model design.

High Vacuum chamber: For testing, characterization and calibration of in-house developed planetary payloads, a custom designed 1-metre class Space Simulation Chamber is being setup at SPL as part of PSB activities. The chamber can attain the ultimate vacuum of 1×10^{-7} m bar within 4 hours. The high vacuum chamber is cylindrical in shape with torrispherical dished ends with one end weld closed. The other end will have torrispherical dished door with dolley mounted mechanism having a working platform fixed inside the door. Suitable job mounting table with manual three-axis movement with linear manipulators along X, Y, Z axis and rotation about perpendicular axis over the platform has been designed and included in the facility. The fabrication of the chamber is in progress and it will be installed and commissioned at SPL shortly. A high-level committee is constantly reviewing the progress.

Ion Source: Another major facility required for the testing and calibration of space borne plasma analysers is the Ion Source. Presently we have procured a low energy ion source (30 eV- 1 keV with narrow energy spread) (model LiIon50). The source is compatible with a variety of gases, including reactive gases such as O. The primary electron current is subject to ionization enhancement processes, which allow up to 30 mA beam current to be generated at 100 eV.

"STOP-PRESS"

Keeping ISRO's Mars and future planetary missioins, with the earliest opportunity in November-December 2013, SPL has made a series of science proposals for exploring the Mars from the surface to the exosphere and beyond. In this, the PSB has proposed the following experiments and out of these MENCA and PLEX have been short listed for possible inclusion in the 2013 Mars mission.

1) Martian Exosphere Neutral Composition Analyzer (MENCA).

2) PLasma Energy eXperiment for Mars (PLEX)

3) Plasma Wave Detection Experiments for Mars mission.

4) Charge-Exchange X-rays from Martian exosphere, to study Martian exosphere and loss of its atmosphere.

BOOKS EDITED/PUBLISHED

Anil Bhardwaj, Editor-in-Chief, Advances in Geosciences, Volume 25, World Scientific Publication, Singapore, 2011.

PUBLICATIONS IN REFEREED JOURNALS

1. Y. Futaana, S. Barabash, M. Wieser, M. Holmström, A. Bhardwaj, M. B. Dhanya, R. Sridharan, P. Wurz, A. Schaufelberger, K. Asamura, "Protons in the Lunar Wake Observed by the SARA Instrument on Board Chandrayaan-1", Journal of Geophysical Research, 115, A10248, pp1-9, doi:10.1029/2010JA015264, 2010.

2. Sridharan R., Ahmed S.M., Tirtha Pratim Das, Sreelatha P., Pradeepkumar P., Naik Neha, Gogulapati Supriya. “The Sunlit Lunar Atmosphere: a Comprehensive Study by CHACE on the Moon Impact Probe of Chandrayaan-1”, Planetary and Space Science, 58, 1567-1577, doi:10.1016/j.pss.2010.07.027, 2010.

3. Anil Bhardwaj and Susarla Raghuram, “Model for Cameron band emission in comets: A case for EPOXI mission target comet 103P/Hartley 2”, Monthly Notices of the Royal Astronomical Society, 412, L25-L29, doi:10.1111/j.1745-3933.2010.00998.x, 2011.

4. Charles Lue, Yoshifumi Futaana, Stas Barabash, Martin Wieser, Mats Holmstrom, Anil Bhardwaj, M. B. Dhanya, Peter Wurz, “Strong influence of lunar crustal fields on the solar wind flow”, Geophysical Research Letters, 38, L03202, pp1-5, doi:10.1029/2010GL046215, 2011.

5. Sonal Kumar Jain and Anil Bhardwaj, “Model calculation of N2 Vegard-Kaplan band emissions in Martian Dayglow”, Journal of Geophysical Research, Vol. 116, E07005, doi:10.1029/2010JE003778, 2011.

6. Anil Bhardwaj and Sonal Kumar Jain, “Calculation of N_2 triplet states vibrational populations and band emissions in Venusian Dayglow”, Icarus, doi:10.1016/j/icarus.2011.05.026, 2011

PUBLICATIONS IN REFEREED PROCEEDINGS

1. Tirtha Pratim Das , Prasanna Mahavarkar, Gogulapati Supriya, Satheesh Thampi, P. Sreelatha, P. Pradeepkumar, Neha Naik, S V Mohankumar and Anil Bhardwaj, “Accurate Estimation of the Total Pressure using a Mass Spectrometer below the X-ray limit”, Proc. International Conference on Innovative Science and Engineering Technology (ICISET 2011), ISBN 978-81-906377-5-6, Vol. 1, page 76, 2011.

2. Tirtha Pratim Das, Gogulapati Supriya, Prasanna Mahavarkar, Neha Naik, P. Sreelatha, P. Pradeepkumar, S V Mohankumar, Anil Bhardwaj and R. Sridharan; “Study on the Water Vapor Desorption Rate from Space-Borne Mass Spectrometers under Simulated Deep Space Vacuum”; Proc. International Conference on Innovative Science and Engineering Technology (ICISET 2011), ISBN 978-81-906377-5-6, Vol. 1, page 430, 2011.

PRESENTATIONS IN SYMPOSIA/WORKSHOPS/CONFERENCES

International

1. Susarla Raghuram and Anil Bhardwaj, Model of Cameron Band Emission in Comet P/Hartley 2, Seventh AOGS Annual Meeting, Hyderabad, India, July 5-9, 2010.

2. H. Misawa, F. Tsuchiya, A. Bhardwaj, K. Imai, T. Kondo, and A. Morioka, Variation features of Jupiter’s synchrotron radiation, Seventh AOGS Annual Meeting, Hyderabad, India, July 5-9, 2010.

3. M. B. Dhanya, Anil Bhardwaj, R. Sridharan, Stas Barabash, Martin Wieser, Yoshifumi Futaana, Mats Holmström, Peter Wurz, Audrey Schaufelberger and Kazushi Asamura, A New Look at the Lunar-Solar Wind Interaction: An overview on Results from the SARA Experiment aboard Chandrayaan-1, Seventh AOGS Annual Meeting, Hyderabad, India, July 5-9, 2010.

4. Sonal Kumar Jain and Anil Bhardwaj, Model for ultraviolet dayglow emissions on Mars, Seventh AOGS Annual Meeting, Hyderabad, India, July 5-9, 2010.

5. C. M. Lisse, A. Bhardwaj, K. Dennerl, S. J. Wolk, D. J. Christian, S. J. Wolk, D. Bodewits, T.H. Zurbuchen, Solar System X-rays from Plasma Processes, Seventh AOGS Annual Meeting, Hyderabad, India, July 5-9, 2010.

6. R. Sridharan, S. M. Ahmed, Tirtha Pratim Das, P. Sreelatha, P. Pradeepkumar, Neha Naik, Gogulapati Supriya, and Anil Bhardwaj, First Dayside Lunar Atmosphere Measurements: Results from Chandra’s Altitudinal Composition Explorer (CHACE) aboard MIP/Chandrayaan-1 Seventh AOGS Annual Meeting, Hyderabad, India, July 5-9, 2010.

7. Anil Bhardwaj, Chandrayaan-1: India’s First Mission to the Moon, 38th COSPAR Scientific Assembly, Bremen, Germany, 18-25 July, 2010.

8. Anil Bhardwaj, Electron Impact Processes in Cometary Coma: Implications for Cometary Missions, 38th COSPAR Scientific Assembly, Bremen, Germany, 18-25 July, 2010.

9. Martin Wieser, Stas Barabash, Yoshifumi Futaana, Mats Holmström, Anil Bhardwaj, R. Sridharan, M.B. Dhanya, Audrey Schaufelberger, Peter Wurz, and Kazushi Asamura, Energetic neutral atom imaging of the moon: Observation of a mini-magnetosphere above a lunar magnetic anomaly, 38th COSPAR Scientific Assembly, Bremen, Germany, 18-25 July, 2010.

10. Yoshifumi Futaana, Stas Barabash, Martin Wieser, Mats Holmström, Anil Bhardwaj, M. B. Dhanya, R. Sridharan, P. Wurz, A. Schaufelberger, K. Asamura, Plasma expansion into the lunar wake: Observation of protons by the SARA/SWIM sensor onboard Chandrayaan-1, 38th COSPAR Scientific Assembly, Bremen, Germany, 18-25 July, 2010.

11. Anil Bhardwaj, Chandrayaan-1: Indian First Mission to the Moon, International Symposium of the Science and Utilization of the Moon (SUM2010), Research Institute for Science and Engineering, Waseda University, Tokyo, Japan, 7–9 September, 2010.

12. Tirtha Pratim Das, Gogulapati Supriya, Prasanna Mahavarkar, Neha Naik, P. Sreelatha, P. Pradeepkumar, S V Mohankumar, Anil Bhardwaj and R. Sridharan, Study on the Water Vapor Desorption Rate from Space-Borne Mass Spectrometers under Simulated Deep Space Vacuum, International Conference on Innovative Science and Engineering Technology (ICISET-11), Rajkot, 8-9 April, 2011.

13. Tirtha Pratim Das , Prasanna Mahavarkar, Gogulapati Supriya, Satheesh Thampi, P. Sreelatha, P. Pradeepkumar, Neha Naik, S V Mohankumar and Anil Bhardwaj, “Accurate Estimation of the Total Pressure using a Mass Spectrometer below the X-ray limit”, International Conference on Innovative Science and Engineering Technology (ICISET-11), Rajkot, 8-9 April, 2011.

National

14. R. Satheesh Thampi, Low Energy Ion Mass Analyser (LEIMA), Brainstorming Session on Mars Science and Exploration, Physical Research Laboratory, Ahmedabad March 24-25, 2011.

15. Vipin K. Yadav, X-ray experiments using shadow masks for space application in Intermediate energy range, Young Astronomers Meet (YAM-2010), Physical Research Laboratory, Ahmedabad, September 3-5, 2010.

16. Vipin K. Yadav, Planetary Magnetic Field and Plasma Wave detection experiments onboard Indian Orbiter Mission, Mars Mission Brain Storming Session, Physical Research Laboratory, Ahmedabad, March 24–25, 2011.

Project Reports

1. Anil Bhardwaj, Tirtha Pratim Das, P. Sreelatha and P. Pradeepkumar; CHACE-2 Project Report, SPL-CHACE-2-PR-1, 2010.
2. Tirtha Pratim Das, G. Supriya, P. Sreelatha, P. Pradeepkumar; CHACE-2: Information for the Reliability and Quality Assurance (R&QA) Team, SPL-TN-CHACE-2-3, 2011.
3. Tirtha Pratim Das and G. Supriya; Preliminary Inputs for Designing the Chassis of CHACE-2, SPL-TN-CHACE-2-1, 2011.
4. Tirtha Pratim Das, et al., Characterization Experiments on CHACE-2 Engineering Model, SPL-CHACE-2-PR-2, 2011.
5. M. B. Dhanya, Santa Martinez, Harold Metselaar, Martin Wieser, Futaana Yoshifumi, Anil Bhardwaj, Stas Barabash, Detlef Koschny, SARA Experimenter to Archive team Interface Control Document, CH1-SARA-EAICD-V1.0, 2011.

DISTINGUISHED LECTURES AND INVITED TALKS

Anil Bhardwaj

1. Key Note Lecture “Indian Lunar Mission Chandrayaan-1”, at 16th National Seminar on Physics and Technology of Sensors, February 11, 2011, Department of Physics, Lucknow University, Lucknow.
2. Distinguish Lecture on “Planetary Sciences”, Liquid Propulsion System Centre (LPSC), Mahindragiri, Tamilnadu, October 4, 2010.

3. “Chandrayaan-1: India’s First Mission to the Moon”, 38th COSPAR Scientific Assembly, Bremen, Germany, 18-25 July, 2010.
4. “Electron Impact Processes in Cometary Coma: Implications for Cometary Missions”, 38th COSPAR Scientific Assembly, Bremen, Germany, 18-25 July, 2010.
5. “Indian First Mission to the Moon: Chandrayaan-1”, International Symposium of the Science and Utilization of the Moon (SUM2010), Research Institute for Science and Engineering, Waseda University, Tokyo, Japan, 7–9 September, 2010.
6. “Solar System and the Chandrayann-1 Mission”, National Seminar on “Advances in Science, Emerging Technologies and Societal Development (ASETS-2011)”, Bodhananda Research Foundation for Management & Leadership Studies, KSCSTE, Trivandrum, Jan. 15, 2011.
7. “Mars Atmosphere: Present Understanding, Brainstorming Session on Mars Science and Exploration, Physical Research Laboratory, Ahmedabad, March 24-25, 2011.
8. “Solar System X-ray Emissions”, International Workshop on Planetary Atmospheres, Physical Research Laboratory, Ahmedabad, July 12-13, 2010.
9. “Solar System and the Chandrayaan-1 Mission”, Colloquium at Sardar Patel University, Vallabh Vidyanagar, Gujarat, Jan. 6, 2011.
10. “Mars Atmosphere: Present Knowledge and Questions”, 11th PLANEX Workshop, Ahmedabad, Jan.5, 2011.

Vipin K. Yadav

1. “Imaging of X-ray radiation emitted from Astrophysical plasma sources using Shadow Masks”, 25th National Symposium on Plasma Science & Technology (PLASMA-2010), Institute of Advanced Study in Science & Technology, Guwahati, December 8-11, 2010.

PUBLIC OUTREACH LECTURES

Anil Bhardwaj

1. “Chandrayaan-1: Indian Lunar Mission”, Public Outreach Lecture of AOGS-2010, St. Andrews High School Bowenpally, Hyderabad, July 9, 2010.
2. “Chandrayaan-1 Mission, INSPIRE program, NIIST, Trivandrum, Sept. 23, 2010.
3. “Planetary and Space Sciences”, delivered at Teachers’ Workshop as a part of Space Week Celebrations at VSSC, Trivandrum, October 5, 2010.
4. “Indian Moon Mission Chandrayaan-1”, National College, Trivandrum, December 3, 2010.
5. “India’s First Lunar Mission Chandrayaan-1”, INSPIRE Winter Science Camp, National Institute of Technology, Calicut, December 20, 2010.
6. “Chandrayaan-1: Indian Mission to Moon”, Scientific Awareness Programme as part of the National Science Day, Equatorial Geophysical Research Laboratory (IIG’s Regional Centre at Tirunelveli), Tirunelvei, Tamil Nadu, 26 February 2011.
7. “Solar system Mysteries”, DST-INSPIRE Internship Program, KIIT University, Bhubaneswar, Orissa, March 14, 2011.
8. “Indian Lunar Mission Chandrayaan-1”, INSPIRE Summer camp, Krishi Vigyan Kendra, Banasthali University, May 12, 2011.
9. “Indian Lunar Mission Chandrayaan-1”, INSPIRE Program, MITS School of Biotechnology, Bhubaneswar, Orissa, June 9, 2011.

M. B. Dhanya

1. Talk on “Super Moon” at All India Radio, Trivandrum, on 18 March 2011.
2. Telephonic Talk on “Super Moon” at Club FM 94.3, on 18 March 2011.

HINDI PRESENTATIONS

1. Anil Bhardwaj, Invited talk on Chandrayaan-1 Mission at the Inter-centre Technical Hindi seminar, LPSC Valiamala, Sept 22-23, 2010.

2. T.P. Das, Gogulapati Supriya, P. Sreelatha, P. Pradeepkumar, Neha Naik, R. Sridharan, “Exploration of Moon by CHACE”, Inter-centre Technical Hindi seminar, LPSC Valiamala, Sept 22-23, 2010.

3. Sonal Kumar Jain, Susarla Raghuram, and Anil Bhardwaj, “Mars and Comet mission”, Inter-centre Technical Hindi seminar, LPSC Valiamala, Sept 22-23, 2010.

4. M. B. Dhanya, Anil Bhardwaj, S. V. Mohankumar, and R. Sridharan. “Study of interaction between lunar surface and Solar wind by SARA on board Chandrayaan-1”, Inter-centre Technical Hindi seminar, LPSC Valiamala, Sept 22-23, 2010.

CONVENING OF SCIENTIFIC SESSIONS

Anil Bhardwaj

1. Co-Convener, Session PS02 “Plasma processes in the solar system”, AOGS 7th Annual Meeting, Hyderabad, India, July 5-9, 2010.

2. Co-Convener, Session PS11 “Science and Exploration of the Moon”, AOGS 7th Annual Meeting, Hyderabad, India, July 5-9, 2010.

3. Member, Scientific Organizing Committee, International Symposium on Planetary Science, Tohoku University, Sendai, Japan, March 8-11, 2011.

4. Member, Scientific Organizing Committee, 12 Years of Science with Chandra, Meeting in a Meeting with the American Astronomical Society, Boson, USA, 23-25 May, 2011.

DEPUTATION TO CONFERENCE/WORKSHOP/INSTITUTE/SCHOOL

International

1. Anil Bhardwaj, 38th COSPAR Scientific Assembly, Bremen, Germany, 18-25 July, 2010.

2. Anil Bhardwaj, International Symposium of the Science and Utilization of the Moon (SUM2010), Research Institute for Science and Engineering, Waseda University, Tokyo, Japan, 7–9 September, 2010.

National

1. Anil Bhardwaj, M. B. Dhanya, Sonal Kumar Jain, Susarla Raghuram, Seventh AOGS Annual Meeting, Hyderabad, India, July 5-9, 2010.

2. Anil Bhardwaj, Gogulapati Supriya, Sonal K. Jain, Susarla Raghuram, International Workshop on Planetary Atmospheres, PRL, Ahmedabad, July 12-13, 2010.

3. M. B. Dhanya, Gogulapati Supriya, Sonal Kumar Jain, Susarla Raghuram, Anil Bhardwaj, Inter-Centre Technical Hindi Seminar, LPSC, Sept. 22-23, 2010.

4. R. Satheesh Thampi, Matlab-Simulink training, HRDD, VSSC, October 10-11, 2010.

5. R. Satheesh Thampi, Data analysis of Chandrayaan-1 imaging payloads - HySI and TMC, PRL & SAC, Ahmedabad, Nov. 28-30, 2010.

6. Gogulapati Supriya, R. Satheesh Thampi, M. B. Dhanya, Familiarization in Scientific Ballooning, TIFR High-Altitude Balloon Facility, Dec. 13-15, 2010.

7. Anil Bhardwaj and Abhinaw Alok, 11th PLANEX Workshop on “Exploration of Mars and Moon”, Ahmedabad, Jan.3-7, 2011.

8. Vipin K Yadav, R. Satheesh Thampi, M. B. Dhanya, G. Supriya, Anil Bhardwaj, National Workshop: Results on Solar Eclipse (NaWRoSE), January 27-28, 2011.

9. Anil Bhardwaj, Satheesh Thampi, Vipin K Yadav, Brainstorming Session on Mars Science and Exploration,

Physical Research Laboratory, Ahmedabad, March 24-25, 2011.

10. Gogulapati Supriya, International Conference on Innovative Science and Engineering Technology (ICI-SET-11), Rajkot, 8-9 April, 2011.

11. Vipin K Yadav, Gogulapati Supriya, R. Satheesh Thampi, One day in-house skill development training Programme on "Vacuum techniques–Generation and Measurement of Vacuum", HRDD, VSSC, May 20, 2011.

ACADEMIC PROJECTS

Project/Thesis Supervision

INSA Summer Research Fellowship	2
M. Sc.	2

ATMOSPHERE TECHNOLOGY DIVISION

Engineers

Mohankumar S V
Sreelatha P
Pradeep Kumar P
Tirtha Pratim Das
Shajahan M
Dinakar Prasad Vajja
Neha Naik
Manikantan Nair N

Technical Assistants/ Tradesman

Pramod P P
Mohammed Nazeer M
Rosmy John
Lali P T
Anumod P G
Ajeeshkumar P S
Satheeshkumar B
Johnson A J
Asoka Kumar G S
Uttam S Purty

ARFI & ICARB

AEROSOL RADIATIVE FORCING OVER INDIA
INTEGRATED CAMPAIGN FOR AEROSOLS, GASES AND RADIATION BUDGET

Project Team

Krishnamoorthy K
Suresh Babu S
Mukunda Gogoi
*Sreekanth V
†Vijayakumar S Nair
Sobhan Kumar K
Dinkar Prasad Vajja
Pramod P P
Ajeesh kumar P S
Santosh Kumar Pandey
#Beegum Naseema
Jai Prakash Chaubey
Arun Kumar V H
Manoj M R

Also contributed

Mannil Mohan
Prijith S S

*Relieved from SPL w.e.f. *Mar 2011 & #Dec 2010*
†Has been at ICTP, Italy and joined very recently

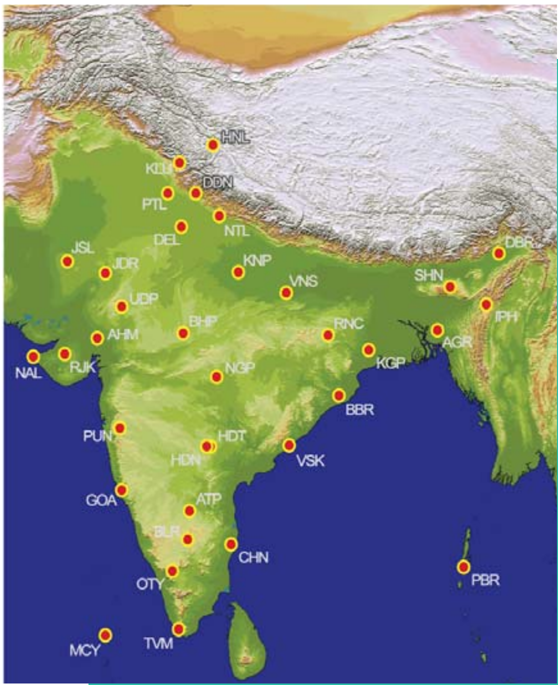

Figure 1: The current constitution of the ARFINET. Data on multiple aerosol parameters are available from all these stations in the ARFI database

Aerosol Radiative Forcing over India (ARFI) and Integrated Campaign for Aerosol gases and Radiation Budget (ICARB) are the two projects of ISRO-GBP, implemented by SPL and aiming at evolving accurate regional aerosol characterization, incorporating the heterogeneities in space, time, and spectral domains, for estimating the Aerosol Radiative Forcing over India and to assess the impacts on regional and global climate. It uses the national network (ARFINET) of aerosol observatories (35 observatories are now operational, Fig.1), and integrated, multi-platform approach involving aircraft, ship and satellites. With a view to quantifying the climate implications of the atmospheric warming by elevated aerosol layers especially the Black Carbon (BC), a focused experiment RAWEX (Regional Aerosol Warming Experiment) has been formulated under ARFI, which would bring in a synergy of measurements and modeling. The details of accomplishments during the review period are given below.

1. DO BC LAYERS BUILD 'THEIR OWN HOMES' UP IN THE ATMOSPHERE?

The high altitude balloon measurements of the vertical profiles of the mass concentration of aerosol black carbon (BC) concurrently with the atmospheric thermodynamics, under the Regional Aerosol warming Experiment (RAWEX) of ARFI during March 2010, have, for the first time provided experimental evidence and quantification of the effects of BC absorption on the stability of the atmosphere.

The photograph of the balloon with the payload just after the launch, the flight path and the mean altitude distribution of BC are shown respectively in the left, middle and right panels of Fig.2. The BC profile shows several very interesting and surprising features.

- A nearly steady level of BC in the lower atmosphere, up to an altitude of ~2 km above ground, above which it gradually increased superposed with weak fluctuations.
- A sharp thin layer (P1) of very high BC concentrations in the altitude region ~ 4.5 km
- Above this, BC remained moderate to low, superposed with several weaker and narrower peaks, before coming down to very low values at ~ 6 km and remaining so until ~ 8 km.
- A second layer (P2) of enhanced BC is indicated above 8 km; however this peak is not fully resolved as the Aethalometer was commanded off because of the very low flow rate.

The possible role of atmospheric thermodynamics in the formation of multiple layers of BC is examined in Fig.3, where the vertical profiles of wind speed, wind direction and potential temperature, all derived from the concurrent measurements on-board the balloon are shown in the first two panels from the left. The wind direction remained steady northerly-northeasterly up to 5.5 km, more than 1 km above P1 (the first and strongest layer), while the speed did not reveal rapid changes; being between 4 to 7 ms^{-1}. Thus there was no drastic change in the airmass type and advection strength. This was also confirmed by airmass back trajectory analysis. From 5.6 to 6.4 km, though the wind drastically shifted to westerly and remained so up to 9 km and above, BC concentration did not reveal any impact; it remained very low until 8 km again suggesting no long range transport. Between 8 and 8.5 km BC increased significantly to reach a peak at 8.3 km. Interestingly, the wind speed sharply increased above 8 km, from ~ 6 ms^{-1} to very high values of ~ 15 to 20 ms^{-1}, associated probably with the tropi-

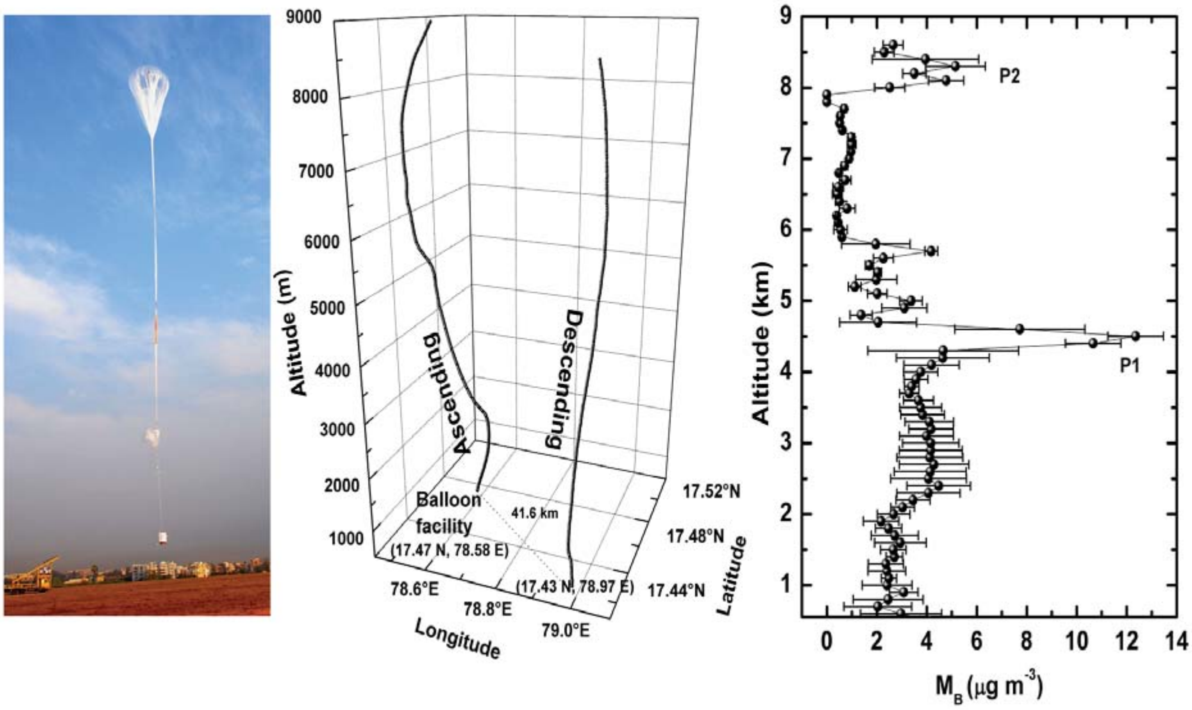

Figure 2: The photograph of the balloon with the payload just after the launch (left panel), the flight trajectory (middle panel) and the mean altitude distribution of BC (right panel)

cal westerly jet stream and this might have led to confinement of BC at this level leading to the high BC. The altitude distribution of θ (potential temperature) showed an adiabatic condition and the prevalence of convective turbulence up to 1 km, above which θ increased with altitude showing a convectively stable sub-adiabatic atmosphere up to ~ 2 km. Above 2 km, θ remained steady with altitude again, showing a convectively unstable region extending up to ~ 4 km. In this region, the wind speeds were also higher (~ 7 ms^{-1}) and directed from north-easterly region. Above 4.7 km, θ showed a sharp inversion and changed back to sub-adiabatic, stable condition that extended up to 7 km. It is quite possible that this strong inversion might be responsible for confining BC at 4.5 km leading to the sharp peak (P1). It is, however, also possible that this strong inversion has resulted from a local warming caused by enhanced absorption (of solar radiation) by the strong layer P1 in BC.

To examine this further, in the third panel of Fig.3, we have shown the vertical profile of mean ambient temperature (T, from concurrent measurements on-

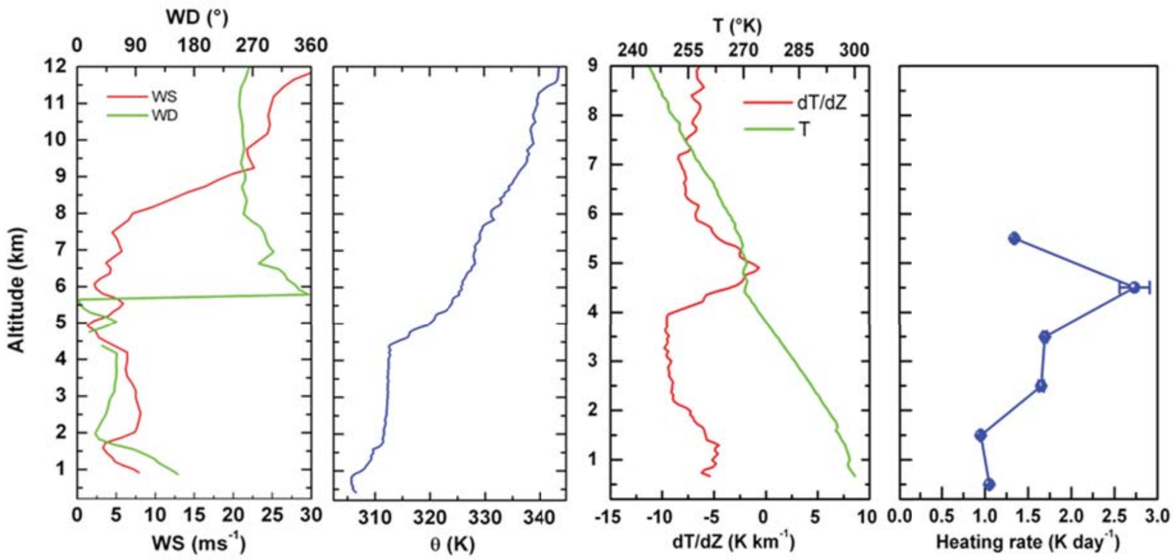

Figure 3: The vertical profiles of wind speed, wind direction (extreme left panel); potential temperature (second panel, ambient temperature (measured) and lapse rate (estimated) (third panel), and the calculated aerosol heating rate profile (extreme right panel)

ARFI

board balloon) and the environmental lapse rate (dT/dz) derived from it. To our surprise, a sharp decrease in the environmental lapse rate (ELR) from ~ 9 K km^{-1} in the region below 3 km to reach values as low as ~ 0.8 K km^{-1} at 4.5 km at P1 is seen. The ELR then gradually recovered to near normal values at higher altitudes before started falling again around the second peak at 8 km to ~ 6 K km^{-1} . These sharp changes in ELR results from the absorption of radiation by the BC layers. To confirm this further, we estimated the heating rate profile using the altitude distribution of BC and the vertical profile of extinction coefficient from the CALIPSO satellite data which had an over pass over the region on the day of BC profiling. The vertical profile of percentage contribution of BC extinction to the CALIPSO derived layer extinction showed large variability; with values ranging from 10 - 80 % and most of the high values were above 3 km. The layer extinction and the contribution of BC to the layer extinction are incorporated into the urban aerosol model and the corresponding profile of single scattering albedo (ω) is estimated. The diurnally averaged values of the net short wave radiation absorbed in each layer and the resulting heating rates are estimated and are shown in the extreme right panel of Fig.3. It reveals very large heating (~ 2.8 K day^{-1}) at ~ 4.5 km, thereby confirming earlier inferences.

Thus, the elevated BC layers in free troposphere absorbed solar radiation leading to warming of the local ambient, which increased the atmospheric stability (decreased the lapse rate). The stable layer, thus created, is conducive for maintaining the BC layer longer, without dissipation (by inhibiting turbulent mixing) and thus increases its lifetime leading to further enhanced absorption. Thus raises an interesting question: Do BC layers build 'their own homes' up in the atmosphere? To examine this more flights are being conducted.

Though the aerosol heating at higher levels could not be estimated (due to non-availability of satellite data), it is pertinent to note that the warming at P2 would be much higher (as the air is thinner). These are the altitudes where thin cirrus clouds form over the tropics and the strong warming would significantly influence these clouds.

2. AEROSOL SCATTERING PROFILES ABOVE MABL OVER BAY OF BENGAL: RESULTS FROM W_ICARB AIR SEGMENT

During the (Winter) Integrated Campaign for Aerosols gases and Radiation Budget (W_ICARB), airborne measurements of total and hemispheric backscatter coefficients (σ_{scat} and β_{scat}) were made over

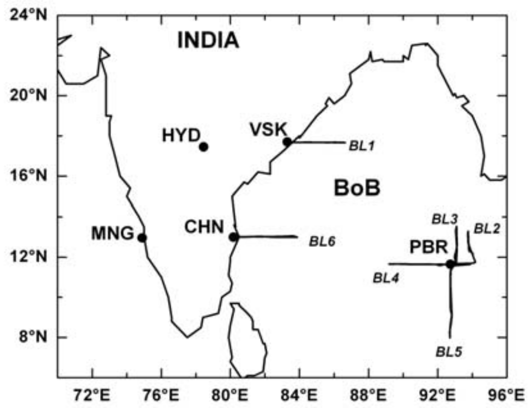

Figure 4: Ground projection of the aircraft flight track during W_ICARB aircraft sorties along with the base stations overlaid on the Indian subcontinent map

several regions of coastal India and for the first time over eastern BoB (Fig.4) using a three wavelength integrating nephelometer. The measurements include high resolution multi-level (ML) sorties for altitude profiles and bi-level (BL) sorties for spatial gradients within and above the Marine Atmospheric Boundary Layer (MABL) over BoB. These profiles are investigated aided by the vertical structure of the atmospheric stability, derived from concurrent GPS aided radiosonde ascents. The vertical profile off Visakhapatnam (VSK) is shown in Fig.5 as a typical example. The σ_{tsc} showed a nearly steady or weakly increasing trend up to ~ 1.5 km above ground indicating a spatially homogenous well mixed region, after which the scattering coefficient dropped off rapidly. The vertical structure of potential temperature revealed a convectively well-mixed region upto ~ 1.5 km, where σ_{tsc} remained nearly steady. The decrease above was quite rapid off the Indian mainland, while it was more gradual in the eastern BoB. The scattering AOD in the region 0 – 3000 m altitude was ~ 0.22 (off-VSK) and 0.14 (off-PBR) which respectively accounted for nearly 45% of the columnar AOD off VSK (& north-western BoB) and 60% off PBR (eastern BoB), suggesting that most of the aerosols were confined to the lower troposphere, particularly over PBR, during winter, in contrast to that of pre-monsoon season, revealed in earlier ICARB.

Investigation on the horizontal gradients (Fig.6) revealed that the scattering coefficients over northern BoB were 3 to 4 times higher compared to that of central BoB; within and above the MABL. However, over the eastern BoB, due north and south of PBR, within and above MABL, a significant gradient in σ_{tsc} has been observed, with σ_{tsc} decreasing from south to north with large vertical gradient especially due south of PBR. This is attributed to increased abun-

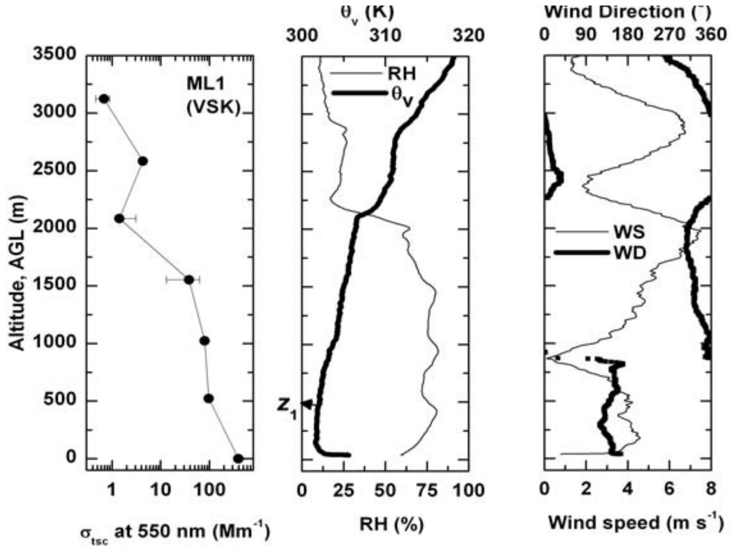

Figure 5: Vertical profiles of total scattering coefficient (left panel); virtual potential temperature (θ_v, thick solid line in the middle panel), relative humidity (RH, thin solid line in the middle panel); wind direction (WD, thick solid line in the right panel), wind speed (WS, thin solid line in the right panel) over VSK. z1 denotes the vertical extent of the well-mixed region

dance of sea-salt aerosols, produced in-situ by the strong winds that prevailed there, as revealed by the QickScat data. Over the central BoB, eastward gradients in total scattering coefficient (σ_{tsc}), Angstrom wavelength exponent (α) and aerosol back scatter ratio (b) within and above MABL, suggested increasing abundance in aerosols with increasing dominance of accumulation mode (increasing continental influence) towards east; indicative of aerosols being carried over to the study region by the synoptic easterly airmass from the East Asian regions.

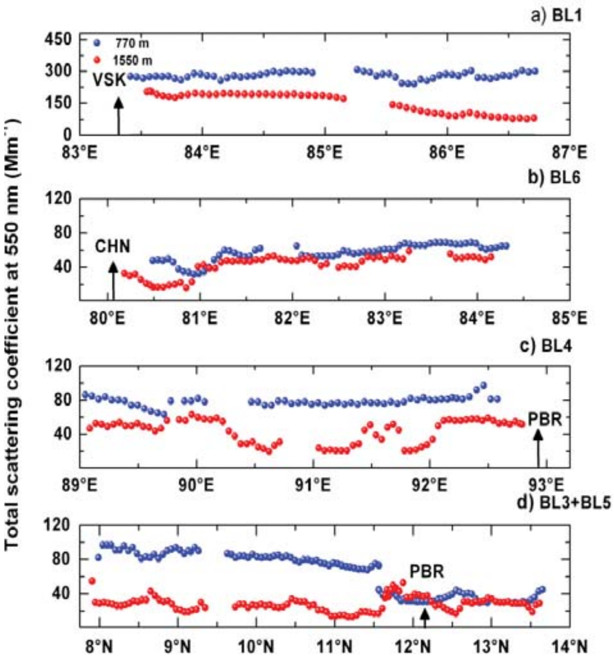

Figure 6: Longitudinal/latitudinal variation of total scattering coefficient during bi-level sorties a) off-VSK (BL1, first panel), b) off-CHN (BL6, second panel), c) off-PBR (westwards, BL4, third panel), d) off-PBR (north-south, BL3+BL5, fourth panel). The arrows indicate the corresponding base station longitude/latitude

3. SPATIAL DISTRIBUTION AND VERTICAL STRUCTURE OF MABL AEROSOLS OVER BAY OF BENGAL DURING WINTER: RESULTS FROM W_ICARB OCEAN SEGMENT

The tropical marine atmosphere is different in several respects from those of extra-tropical regions; being characterized by several layers such as surface layer, mixed layer, transition layer, cloud layer, and trade wind inversion. The dynamical process in the MABL would in-turn affect the vertical distribution of aerosols which in turn would have a role in scattering phase function. With a view to examine these, the altitude variation of aerosol number-size distribution (NSD) has been investigated for the first time using an optical particle counter attached to a tethered blimp onboard ORV Sagar Kanya, over five different locations (Fig.7) over the Bay of Bengal (BoB) and Eastern Arabian Sea off Trivandrum during the W_ICARB.

From the vertical profiles of the measured number size distributions, the following physical parameters were estimated as a function of altitudes: (i) number density of the submicron (accumulation mode, N_{ACC}) and coarse mode (N_{COA}) aerosols (ii) effective radius (iii) mode radius and standard deviation. The vertical profiles of effective radius, mode radius and standard deviation are shown in Fig.8.

The significant observations are:

1. The highest concentration of accumulation and coarse mode particles occurred over northern BoB, at the surface and in the MABL, followed by Eastern BoB and Eastern Arabian Sea. The least concentration was seen in the north eastern BoB.

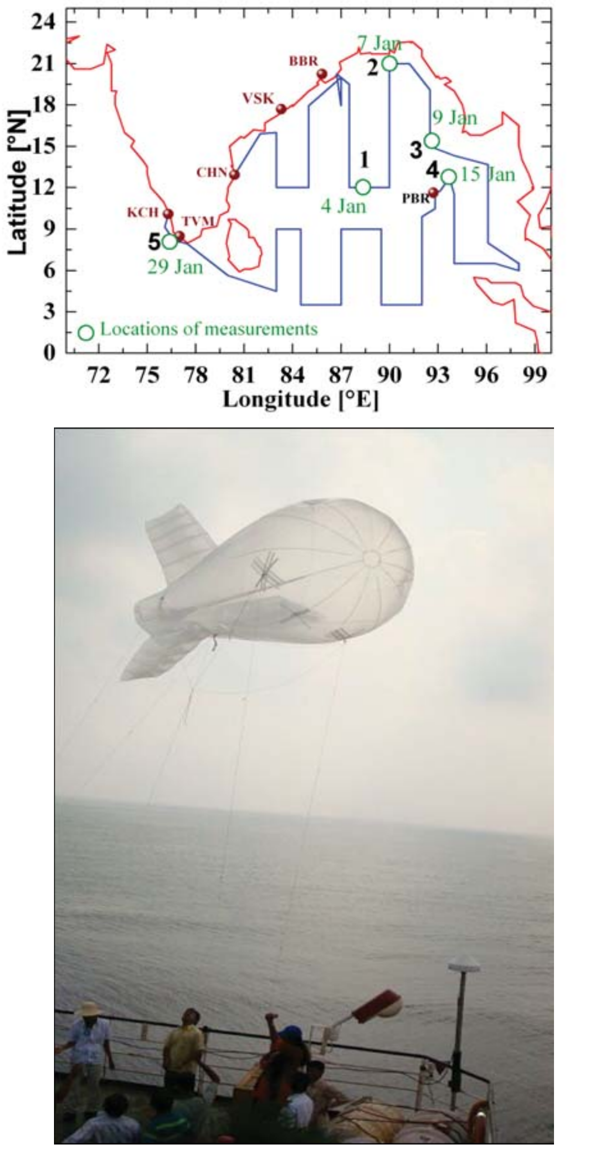

Figure 7: The ship track during W-ICARB. The locations from where the tethered balloon experiment were made are shown with hollow circles (top panel). Hoisting of tethered balloon onboard Sagar Kanya during W-ICARB (bottom panel)

2. All the profiles, except that over the Arabian Sea, showed a rapid decreases in N_{COA}, R_{eff} and r_{m2} from the surface to 50 m altitude emphasizing the ocean surface as the major source of coarse mode aerosols. The rather narrow width of the coarse mode suggests that the major contribution comes from a single source (sea spray).

3. The coarse mode particles had the lowest mode radius and widest distribution over the eastern Arabian Sea, close to peninsular India suggesting multiple sources impacting the coarse mode, probably sea salt and advected dust.

4. The accumulation mode distribution remained nearly the same throughout the oceanic region, showing larger spatial homogeneity.

5. Eventhough r_{m2} and R_{eff} remained rather steady within the MABL at each location, their values differed from location to location. Northeastern BoB had the highest R_{eff}, mainly because of the very large depletion in accumulation mode (submicron) aerosol concentration over this region.

This poses serious concern on the suitability of near surface measurements for the climate impact assessment of aerosols especially when significant amount of aerosols are present above the surface.

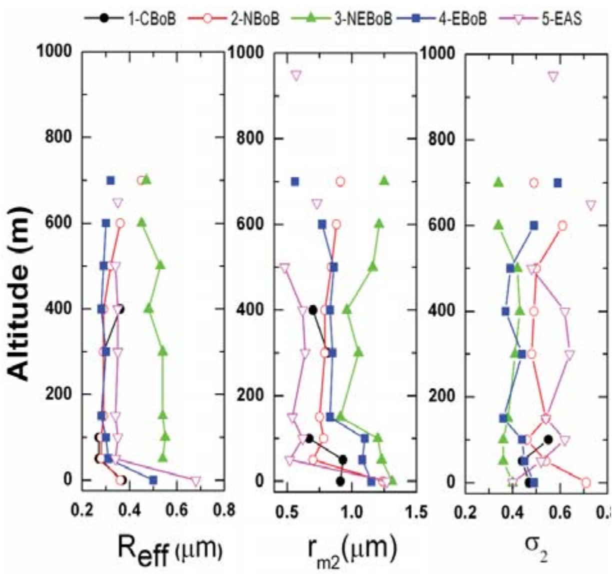

Figure 8: Altitude distribution of effective radius, mode radius and standard deviation in MABL over Bay of Bengal

4. SOUTHERN BAY OF BENGAL: MORE ANTHROPOGENICALLY IMPACTED? RESULTS FROM ICARB

Of the oceanic regions adjoining the Indian landmass, the BoB is more anthopogenically impacted than AS and Indian Ocean; despite a proper quantification is still at large. Performing a closure study for the first time, synchronizing the extensive measurements of optical, physical and chemical properties of BoB aerosols during ICARB, the horizontal and vertical gradients in the fractional contribution of anthropogenic aerosols to the composite system and the direct radiative forcing (anthropogenic aerosol forcing) over BoB has been delineated and quantified.

As the first step of the closure study, the consistency and inter-comparibility of the various measurements were established. The total mass concentration as measured by the QCM averaged over the measurement duration of the high volume sampler (HVS) (in the left panel of Fig.9) showed a good agreement, indicating that both the instruments (QCM and HVS) sampled similar airmass and the coarse spatio-tempo-

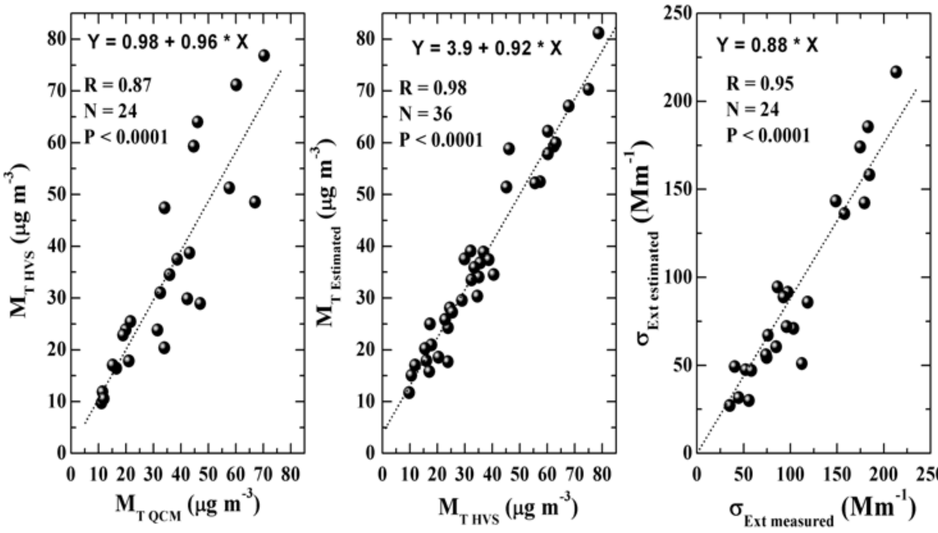

Figure 9: Inter-comparison of aerosol parameters measured and estimated during ICARB. (i) daily mean total mass concentration (M_T) measured using Quartz Crystal Microbalance (QCM) and High Volume Sampler (HVS), (ii) Total mass concentration measured using HVS (M_{T_HVS}) and estimated (M_{T_est}) from the measured weights of aerosol species, (iii) Extinction coefficients measured (σ_{est_mes}) and estimated (σ_{ext_est}) from the chemical characterization

ral resolution of the HVS measurements (compared to QCM) did not lead to any significant bias in the inferences of the composition. As the next step, the chemically resolved information from the gravimetric analysis of HVS sample have been used to estimate the composite aerosol mass concentration using chemical parameterization equation and this was compared against the actual measurement by the HVS in the middle panel of Fig.9. It indicates that the chemical parameterization of BoB aerosols from the measured species accounted for more than 90% of the composite aerosol mass concentration. This facilitated estimation of the extinction coefficient of aerosols from chemistry and this is compared with the extinction coefficient obtained from measurements (scattering and absorption coefficients) onboard in the right panel of Fig.9. It shows again a very good association with a correlation coefficient of 0.95 and slope of 0.88, indicating the consistency between the optical properties of BoB aerosols estimated from the chemical speciation and those from direct measurements.

Now the association of surface aerosol properties with columnar properties over northern and southern BoB, were made in the scatter plot of AOD at 500 nm against the composite accumulation mass concentration (M_A) in Fig.10. The ordinate intercept represents the AOD above the mixed layer and the regression slope indicates the rate of change of AOD with M_A. It is interesting to note that there exists a fairly high value of AOD (0.2 at 500 nm) above the boundary layer in the northern BoB, while over the southern BoB the values are as low as ~ 0.09. Consequently the association of AOD with surface aerosol mass concentration is much stronger over the southern BoB. These observations also indicate the presence of strong elevated aerosol layer over the northern BoB, (which also has been confirmed by independent aircraft measurements).

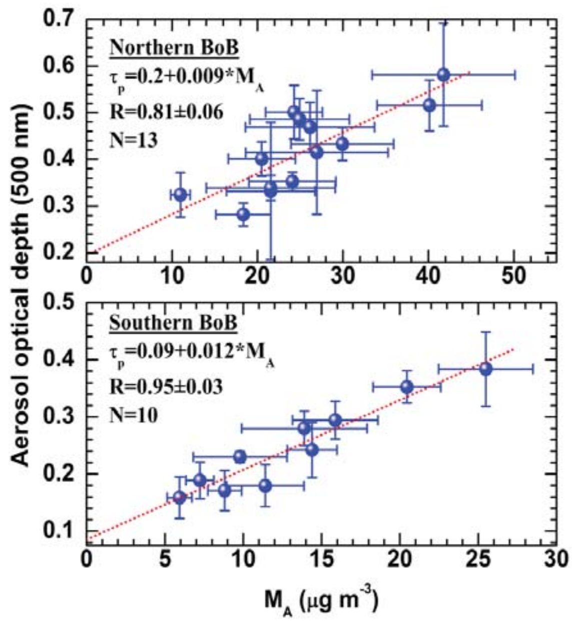

Figure 10: Scatter diagram of daily mean M_A and AOD at 500 nm over northern (Top panel) and southern (middle panel) BoB

The regional variation of the anthropogenic fractions of composite aerosol mass concentration and extinction coefficients (with in the MABL) and columnar AOD are shown respectively in panels from top to bottom of Fig.11 for the northern (north of 15°N), central (10 - 15°N) and southern (below 10°N) BoB. In the same figures are also shown the regional variation of the total (natural + anthropogenic) mass concentration, extinction and AOD. While the total mass concentration decreased from north to south, the fractional contribution of anthropogenic aerosols increased from north to south. In other words, Northern BoB, which is believed to be under the strong impact of anthropogenic sources from the Indo Gangetic Plain, had the highest fraction of natural aerosols, where as the Southern BoB, which is far removed and believed to be less impacted by the Indo-Gangetic

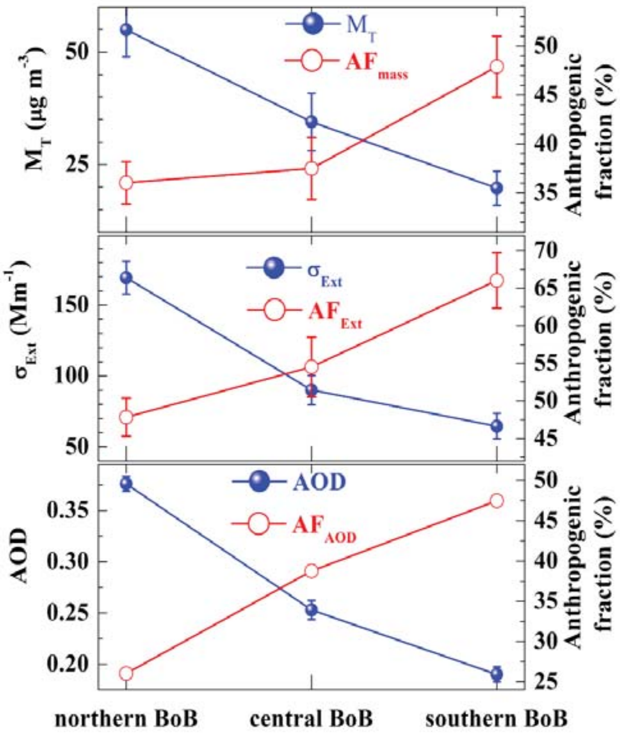

Figure 11: Spatial variations of aerosol mass loading (M_T), extinction coefficient (σ_{ext}) and AOD are shown respectively from top to bottom panels. Anthropogenic fractions (%) of M_T, σ_{ext} and AOD over Northern BoB, CBoB and Southern BoB were shown in corresponding panels on the right abscissa

Plain and East Asian effects had the highest anthropogenic fraction. Similar results are seen in extinction and AOD also. Most interestingly and importantly, the spatial variations of total and anthropogenic fractions are quite opposite in nature.

The composite aerosol forcing (ARF_C), anthropogenic aerosol forcing (the anthropogenic component of ARF_C) and ARF_{A_MABL} (fraction of anthropogenic component in the MABL to the total anthropogenic component) over the northern, central and southern BoB are estimated and shown in Fig.12. One of the major outcomes of the study is that, despite the large spatial heterogeneity in AOD and other aerosol parameters over the BoB, the anthropogenic aerosol forcing remained near-steady with a mean value of -3.5 Wm^{-2}. While anthropogenic aerosol forcing accounted for ~ 33% of radiative forcing due to composite aerosols over Northern BoB, its share increased to as high as 57% over the Southern BoB. Most interestingly while the radiative forcing due to composite aerosols decreased steeply from Northern BoB to Southern BoB, its anthropogenic counter-part (ARF_A) increased from north to south. It is also important to note that the contributions of the anthropogenic aerosols in the MABL (ARF_{A_MABL}) to ARF_A decreased steadily from north to south. The anthropogenic aerosols in the MABL contributed to as much as 74% to the columnar ARF_A in Northern BoB, its contribution dropped to ~40% over central BoB and to 37% over Southern BoB, indicating significant abundance of fine, anthropogenic aerosols in the higher levels of the atmosphere over the Southern BoB. Here it is to be borne in mind that the exclusion of carbonaceous aerosols from anthropogenic component will lead to an under/overestimation of anthropogenic radiative forcing depending on the relative dominance of BC in carbonaceous aerosols. However, delineating the anthropogenic fraction of carbonaceous aerosols, especially when strong sources of biomass and fossil fuel burning coexist, as is the case with Asian regions, is a challenging issue.

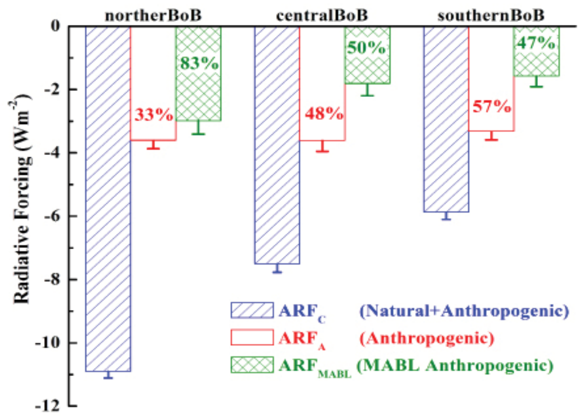

Figure 12: Composite aerosol radiative forcing (ARF_C), anthropogenic radiative forcing (ARF_A) and anthropogenic aerosol radiative forcing of boundary-layer aerosols (ARF_{A_MABL}) over the northern, central, and southern BoB. The percentage contribution of ARF_A to ARF_C and ARF_{A_MABL} to ARF_A are also shown in the respective panels. It is important to note that the contributions of the anthropogenic aerosols in the MABL (ARF_{A_MABL}) to ARF_A decreased steadily from north to south indicating significant abundance of fine, anthropogenic aerosols in the higher levels of the atmosphere over the Southern BoB

5. MULTI-YEAR AEROSOL CHARACTERISTICS AND SHORTWAVE RADIATIVE FORCING FROM NORTH-EASTERN INDIA: RESULTS FROM ARFI

Viewed in the context of unique geographical features, discrete climate and colossal natural resources, the northeastern region of India urges special attention for studying the climatic impact of atmospheric aerosols. Accordingly, the multi-year data from the ARFI network observatory at Dibrugarh (since October 2001) have been used to characterize the aerosols near the surface and in the vertical column and to assess the impact on shortwave radiative forcing.

The annual variations of total (M_t) and accumulation (M_a) aerosol mass concentrations and the accumulation fraction $A_f = M_a/M_t$ are shown in the top panel of Fig.13. It shows

1. Both the M_t and M_a depict very similar annual variations with a broad annual peak from December till February and low during June-July; with a peak to trough ratio of ~ 3.

2. The annual high of M_t was 75.6 ± 17.7 μg m^{-3} in February and low 24.8 ± 6.5 μg m^{-3} in June.

3. Accumulation mode aerosols contributed more than 50% to the total aerosol mass concentration throughout the year; being highest during Dec-Feb (mean A_f ~ 0.87 ± 0.03) and lowest (A_f ~ 0.54 ± 0.01) in July.

The annual variation of monthly mean BC mass concentrations and AOD are shown in the middle and bottom panels of Fig.13. The BC mass concentrations show the highest value ~ 18.7 ± 2.5 μg m^{-3} in January and lowest (~ 1.1 ± 0.05 μg m^{-3}) in June, while AOD peaks in the month of March (~ 0.69 ± 0.13), de-

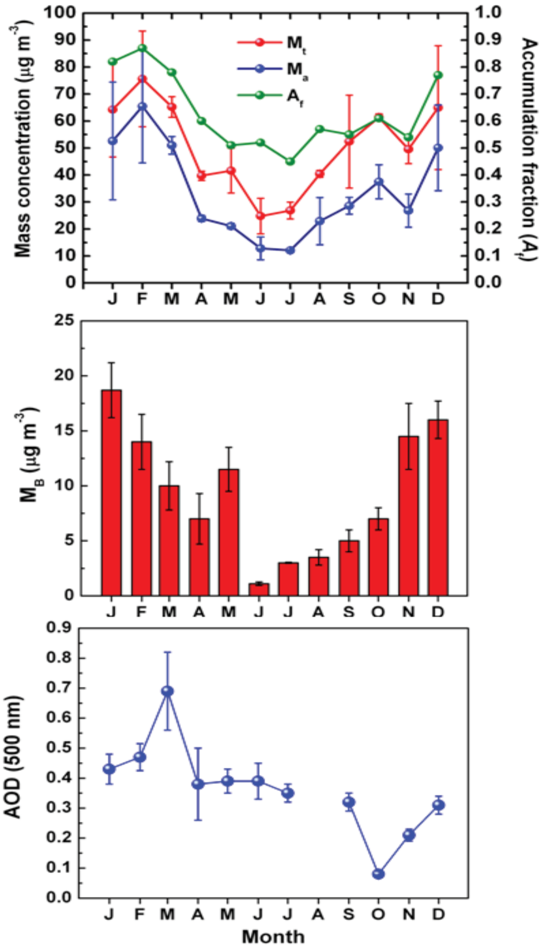

Figure 13: Annual variation of monthly mean (a) top panel: total (M_t), submicron (M_a) aerosol mass concentrations and Accumulation aerosol mass fraction (A_f); (b) middle panel: BC mass concentration (M_B, μg m^{-3}); and (c) bottom panel: columnar AOD at 500 nm

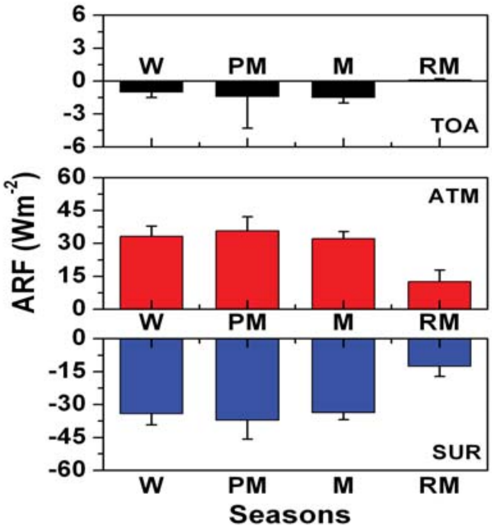

Figure 14: Seasonal mean aerosol radiative forcing at (a) top of the atmosphere (TOA), (b) atmosphere (ATM), and (c) surface (SUR). The vertical lines through the points represent the standard error of the mean

creases subsequently gradually to the lowest value in October (~ 0.08 ± 0.01) with a weak secondary peak in September. These annual variations are attributed mainly to the contrasting synoptic meteorological conditions prevailing at Dibrugarh.

Using the observed values of AOD and BC mass fraction (M_B/M_t) and the estimated values of aerosol single scattering albedo, and phase functions, the shortwave aerosol radiative forcing (ARF) for clear sky conditions are estimated for winter (W), pre-monsoon (PM), monsoon (M) and ret-monsoon (RM) season. The seasonal mean values of ARF, (in Fig.14) clearly indicate that even though the absolute magnitude of forcing at TOA is very small (~ 1.0 Wm^{-2}), significant cooling of < -35 Wm^{-2} at the surface with an atmospheric warming as high as 32 to 35 Wm^{-2} are observed during winter, pre-monsoon and monsoon seasons, when AOD values went up to ~ 0.69 at 500 nm. Compared to this, the magnitudes of the atmospheric warming is quite low (< 15 Wm^{-2}) during the ret-monsoon season, when AOD values are as low as ~ 0.08.

6. THE OPTICAL AND PHYSICAL PROPERTIES OF ANTARCTIC AEROSOLS: RESULTS OF POLAR RESEARCH FROM ARFI

Antarctica, being separated from the other populated continental masses, is one of the most pristine location on the Earth, to examine the natural and background aerosols. Also the change in the snow albedo due to deposit of aerosols (especially BC) has assumed large climatic significance. In view of the above a polar research program has been initiated under ARFI jointly

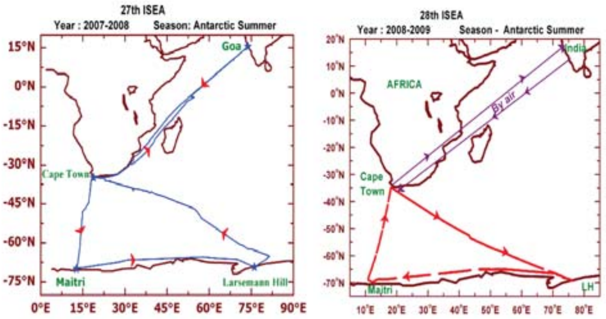

Figure15: Cruise route of 27th and 28th Indian Scientific Expeditions to Antarctica and two Antarctica locations

with National centre for Antarctic and Oceanic Research (NCAOR), Goa. Extensive aerosol measurements were made during the 27th and 28th Indian Scientific Expedition to Antarctica (ISEA). The cruise track and the measurement locations in Antarctica are shown in Fig.15.

The measurements of spectral aerosol optical depth (AOD) and size segregated and total mass concentrations (M_T) were made from two coastal locations in the Eastern Antarctica, Maitri (70ºS, 12ºE, 123 m MSL) and Larsemann Hills Island (LH; 69ºS, 77ºE, 48 m MSL locationa for the third Indian Antarctic station). The temporal variation of AOD at 500 nm (Fig.16) shows significant day to day variations. The comparable values for the AOD at 500 nm over Maitri (mean $\tau \sim 0.034 \pm 0.005$) and LH (mean $\tau \sim 0.032 \pm 0.006$) indicates the good spatial homogeneity in the columnar aerosol properties over the coastal Antarctica. The mean spectral variation of AOD is shown in Fig.17 for three distinct regions. The Angstrom exponent α showed accumulation mode dominance at Maitri ($\alpha \sim 1.2 \pm 0.3$) and coarse mode dominance at

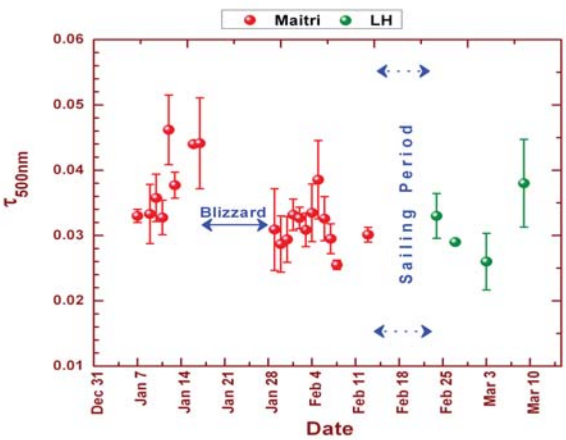

Figure 16: Daily average AOD at Maitri and LH during 27th ISEA, where the red circles represent Maitri observation and blue circles those measured over LH. The vertical lines passing through the circles represent the respective standard deviations

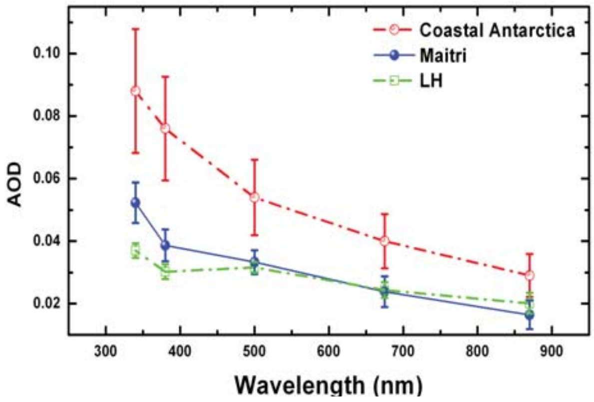

Figure 17: Spectral variation of AOD over oceanic region adjacent to the Antarctic coast and over the Indian stations at Maitri and Larsemann Hills

LH (0.7 ± 0.2). On the other hand, mass concentration (M_T) of ambient aerosols showed relatively high values ($M_T \sim 8.25 \pm 2.87\ \mu g\ m^{-3}$) at Maitri in comparison to LH ($M_T \sim 6.03 \pm 1.33\ \mu g\ m^{-3}$).

Effect of Blizzard

Snowfalls during blizzards are quite efficient sinks of aerosols. At Maitri, a long blizzard event (20th January to 28th January 2008) occurred during the study period. The impact of this on the measured and derived aerosol properties are shown in Fig.18, which reveals a sudden drop in the columnar AODs and α after the event. The mean AOD value remained low for a week and was comparable to the values at LH showing that the snow scavenging has cleaned the

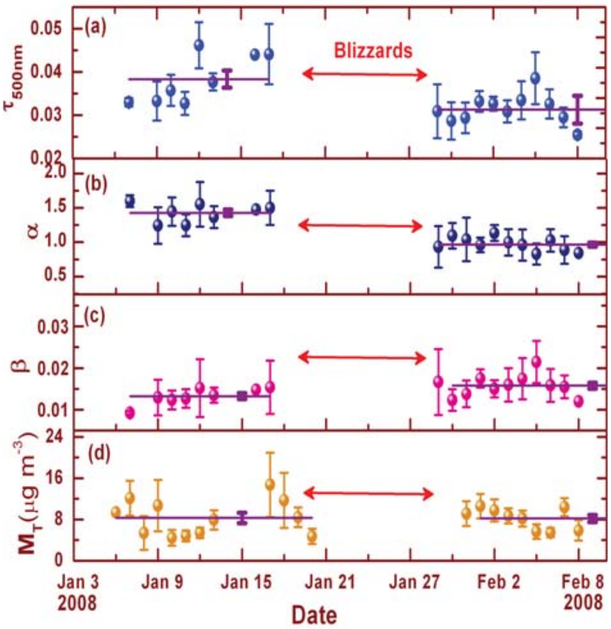

Figure 18: AOD, α, β and MT in four panels respectively from the top to bottom. Points are the daily mean values, the vertical bars through them are the standard deviation and the horizontal lines represent the mean value of the parameter before and after the blizzard

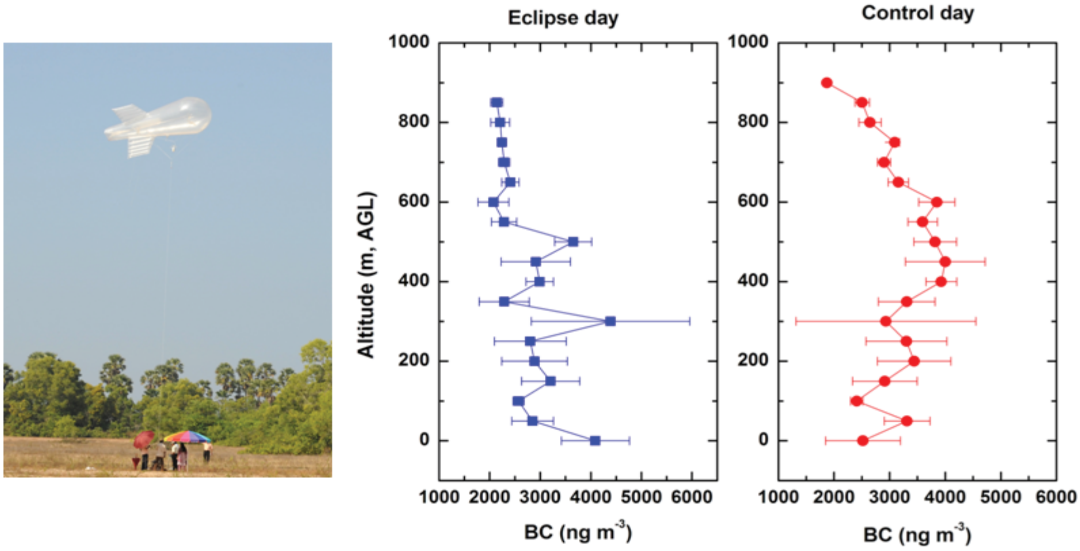

Figure 19: Photograph showing the hoisting of the tethered balloon. Micro-aethalometer is seen tied to the belly strings (left panel); Vertical profiles of BC mass concentrations (M_B), on the eclipse (middle panel) and control (right panel) days

environment over Maitri significantly, particularly at higher levels. Examining the other parameters, it is interesting to note that, there was a significant decrease in α, indicating wet removal of the accumulation aerosols.

7. PERTURBATIONS IN THE VERTICAL PROFILES OF AEROSOL BC IN THE ABL DURING THE ANNULAR SOLAR ECLIPSE

The effect of annular solar eclipse on the altitude profiles of aerosol black carbon (BC) in the atmospheric boundary layer (ABL) over Trivandrum and its association with the changes in the ABL are investigated from the concurrent measurements of the parameters using a microaethalometer and meteorological sensors attached to a tethered balloon and GPS based Pisharoty sondes. A photograph of the experimental setup is shown in Fig.19 (left panel) while the deduced BC profiles are shown in the middle (eclipse day) and right (control day) panels.

The profiles, in general, depicted similar features up to an altitude of ~ 200 m on both the days, above which they differed conspicuously with profiles on eclipse day showing increasingly lower concentration at higher altitudes. Examination of the profiles of the meteorological parameters showed that the altitude of maximum convection has fallen rapidly during the eclipse period compared to that on control day indicating a reduced vertical mixing and shallow convection on eclipse day. Comparison of diurnal variations of BC at the surface level showed that the rate of decrease in BC during daytime on the eclipse day was smaller than that on the control day due to the reduced convection, shallow ABL and consequent reduction in the ventilation coefficient (Fig.20). Moreover the time of the nocturnal increase has advanced by ~ 1:30 hr on the eclipse day, occurring at around 19:30 IST in contrast to all the other days of January 2010, where this increase usually occurs well after 20:30 IST. This is attributed to the weak sea-breeze penetration on the eclipse day, which led to an early onset of the land breeze.

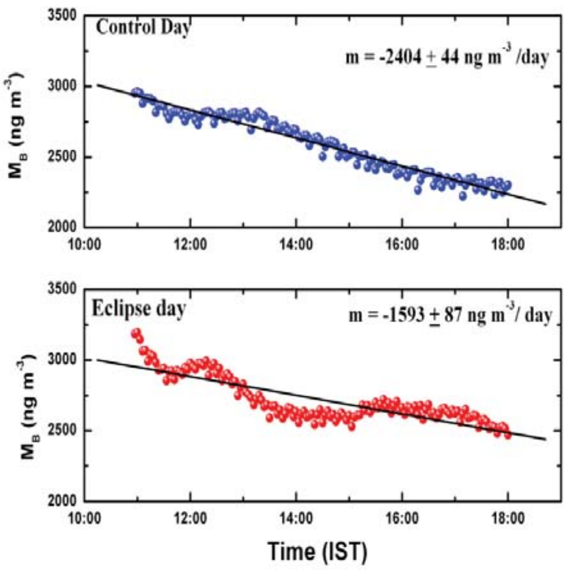

Figure 20: Temporal variation of BC mass concentration during daytime on eclipse day and control day. The rate decrease in M_B during daytime on eclipse day is much less compared to that on control day

8. ARABIAN SEA-AN AEROSOL SOURCE REGION DURING PRE-MONSOON?

Aerosol system over the Arabian Sea during pre-monsoon (March-April) is highly heterogeneous because of the contributions from locally generated marine aerosols and transported particles from the surrounding land masses, which is strongly governed by the three dimensional wind field and the associated wind parameters such as convergence and vorticity. A quantitative analysis of aerosol loading as well as the flow of aerosols across the Arabian Sea in the pre-monsoon season of years 2003-2009 have been made using AOD at 550 nm and mass concentration data from MODIS (Terra and Aqua), aerosol extinction coefficient profiles from CALIPSO, and reanalysis winds from NCEP-NCAR, considering the aerosol transport in terms of horizontal aerosol mass flux (HAMF).

The study domain over the Arabian Sea and its four boundaries (northern, eastern, western and southern) are shown in Fig.21. HAMFs across the four boundaries were computed using the MODIS aerosol data and NCEP winds for the lower (1000 and 925 hPa) and the upper (850 to 400 hPa) atmospheric levels separately. For this, a regression was first established between the MODIS measured column integrated aerosol mass concentration (M, expressed in μg/cm^2) and the AOD (τ) over the study domain . Then M was distributed vertically according to the aerosol extinction profile observed by CALIPSO.

The mean pre-monsoon AOD over the study domain, illustrated in Fig.22a displays a decreasing trend from 2003 to 2006, then jumps to a maximum in 2007 and stays around there till 2009; however the variation in

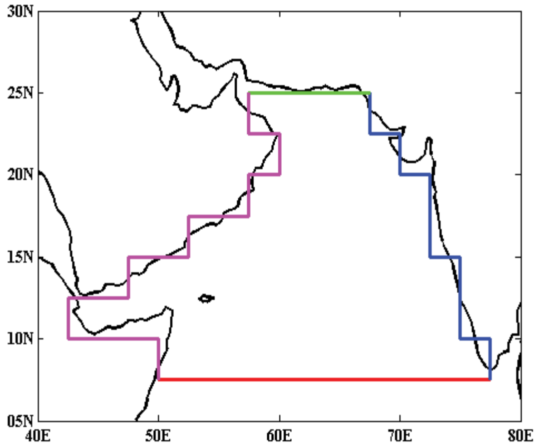

Figure 21: The study domain over the Arabian Sea with its northern, eastern, western and southern boundaries indicated by green, blue, magenta and red colours

aerosol loading remained within ~18% . Fig.22(b) to 22(e) show the lower and upper HAMFs across the northern, eastern, western and southern boundaries respectively, with the positive (negative) value indicating the flow into (out of) the study domain. At the lower level, the aerosol flow was outward through all the four boundaries (except in the case of the northern boundary in the years 2003, 2004 and 2005 when the flow was inward). In the upper level, aerosol flow was into the Arabian Sea across the northern and eastern boundaries [Fig.22(b) and 22(c)] in all the years while it was outward through the southern boundary [Fig.22(e)] and through the western boundary except in the years 2006, 2008 and 2009 (Fig.22d).

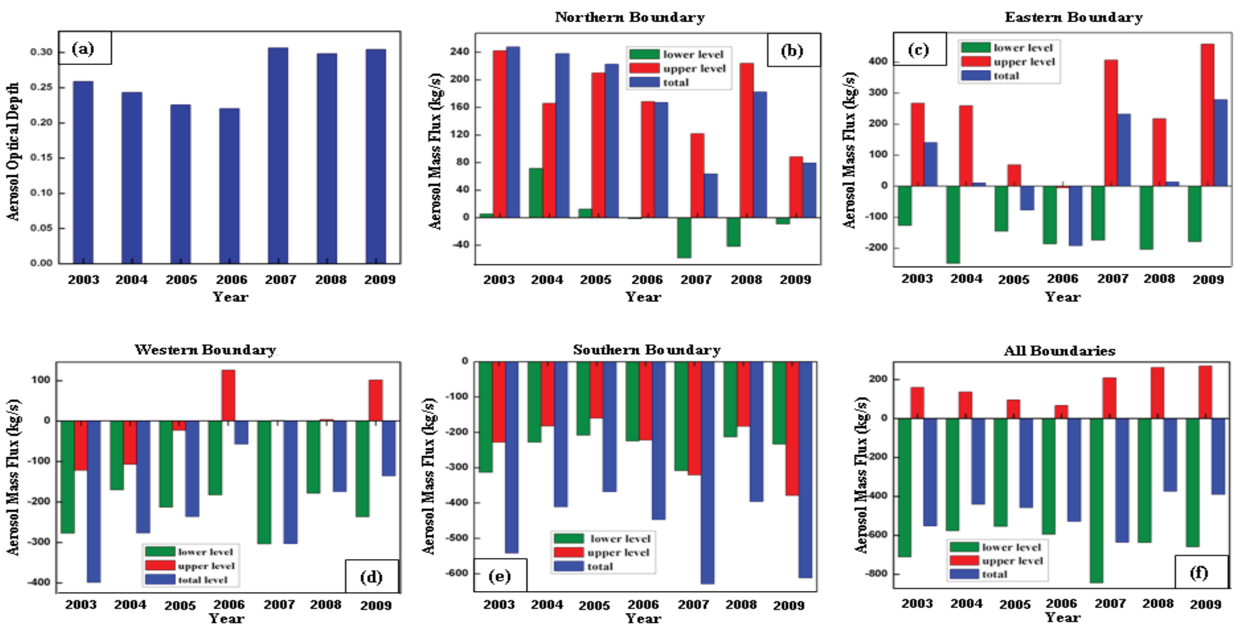

Figure 22: Mean aerosol optical depth over the study domain (a), HAMF at lower and higher levels and the resultant flux across different boundaries (b to e) and the net flux across all the boundaries together (f) during pre-monsoon for the years 2003-2009

Fig.22(f) shows that the resultant flow was inward in the upper level in all the years but it was far exceeded by the net outward flow in the lower level making the total resultant aerosol flux from the study domain, outwards. This suggests that the Arabian Sea is a significant source of aerosols during the pre-monsoon season. This inference was further examined through the estimation of the source strength of aerosol generation over the study domain using of the aerosol flux continuity equation.

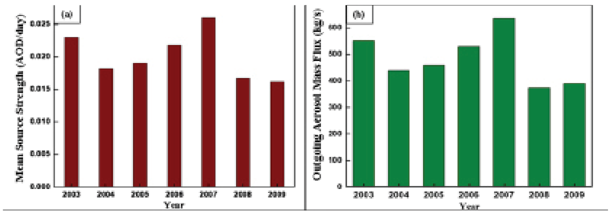

Figure 23: The mean aerosol source strength over the study domain (a) and the total resultant outward aerosol flux across the boundaries (b) for the years 2003-2009

The MODIS AOD, with vertical distribution adjusted according to the CALIPSO profiles, and the reanalysis horizontal winds from NCEP over the study domain were introduced into the continuity equation and the mean aerosol source strength was computed for the pre-monsoon season. This along with the total resultant outward aerosol flux across the boundaries of the study domain, estimated earlier, is illustrated in Fig.23(a) and 23(b) respectively. The striking similarity between the two further confirms that the Arabian Sea is a prominent source of aerosols during the pre-monsoon season.

9. ARFI DATA CENTRE

One of the major objectives of the ARFI is to collate, quality check, archive and (restricted) disseminate the data from the ARFINET for research, policy and societal applications. In this context an ARFI data center is being evolved. This has been an R&D activity, requiring lot of iterations to evolve a common and comprehensive, at the same time user-friendly, archival system. Accordingly a classified and catalogued database has been generated. It is currently being experimented in VSSC/SPL intranet and after required fine-tuning and security enabling, the basic products will be available in public domain through a password controlled restricted access and eventually would be linked to ISRO's Geoportal. With a view to effectively disseminate scientific information that has been generated through the sustained efforts of more than two decades, this domain will also have a well-collated section containing the scientific accomplishments.

Figure 24: The ARFI homepage in the website under development

10. NEW INITIATIVES

a. RAWEX-GVAX A joint Indo-US experiment

Taking cue from ICARB, a new experiment, RAWEX (Regional Aerosol Warming Experiment), has initiated in 2010 under ARFI. At the same time US-DOE (United States – Department of Energy) has proposed and approved a new experiment, Ganges Valley Aerosol Experiment (GVAX) as a joint Indo-US collaborative experiment. In view of the overlapping scientific interests in the two experiments, the joint RAWEX-GVAX experiment has been approved for implementation by Chairman, ISRO during 2011-12. As part of this experiment, ground based and air borne measurements of aerosol and cloud properties would be made from the Indo-Gangetic plain and balloon borne measurements are planned from Hyderabad, Nagpur and Udaipur in addition to the regular measurements from the ARFI Network. The intensive field phase of the experiment will be during February – April, 2012.

b. Arctic Expedition

While, under ARFI, the southern ocean and Antarctic region have been explored for a few years in the past jointly with NCAOR,Goa, the Arctic remained uninvestigated, despite the importance of Polar aerosol characterization. As such, taking advantage of the opportunity provided by the NCAOR, a collaborative program has been undertaken to explore the Arctic region. As a first step, extensive measurements of aerosol properties were made from the Norwegian Arctic region (Ny-Alesund, 79°N, 12°E) during the 4th Indian Arctic Expedition (July - August, 2010). The experimental set up was made at Gruvenbadet in Ny Alesund which is free from the local anthropogenic activities and away from the Himadri (Indian station) station at Ny Alesund (Fig.25). This activity is being followed up with more expeditions in 2011. During winter months, the strong pressure gradient push air northward and aerosols are transported into Arctic from mid-latitude sources where as the summer provides a more pristine conditions to characterize the global background aerosol conditions.

Figure 25: Experimental set up at Arctic

PUBLICATIONS IN REFERRED JOURNALS

1. Suresh Babu, S., Sreekanth, V., Nair, V.S., Satheesh, S.K., Krishna Moorthy, K. Vertical profile of aerosol single scattering albedo over west coast of India during W_ICARB, Journal of Atmospheric and Solar-Terrestrial Physics, 72 (11-12), pp. 876-882, 2010.

2. Krishna Moorthy. K., S. N. Beegum, S. Suresh Babu, A. Smirnov, S. R. John, K. R. Kumar, K. Narasimhulu, C. B. S. Dutt, and V. S. Nair, "Optical and physical characteristics of Bay of Bengal aerosols during W_ICARB: Spatial and vertical heterogeneities in the marine atmospheric boundary layer and in the vertical column Journal of Geophysical Research., 115, D24213, doi: 10.1029/2010JD014094, 2010.

3. Vijay Kumar S Nair, S. K. Satheesh, K. Krishna Moorthy, S. Suresh Babu, Prabha R. Nair, and S. K. George , "Surprising observation of large anthropogenic aerosol fraction over the 'near pristine' southern Bay of Bengal: Climate implications", Journal of Geophysical Research., 115, D21201, doi:10.1029/2010JD013954,2010.

4. Pathak, B., Kalita, G., Bhuyan, K., Bhuyan, P.K., Moorthy, K.K. Aerosol temporal characteristics and its impact on shortwave radiative forcing at a location in the Northeast of India, Journal of Geophysical Research, 115 (19), art. no. D19204, 2010.

5. Suresh Babu, S., Krishna Moorthy, K., Satheesh, S.K. Latitudinal gradient in aerosol properties over the Indian and Southern Oceans during the austral summer, Current Science, 99 (10), pp. 1384-1389, 2010.

6. Satheesh, S. K., V. Vinoj and K. Krishna Moorthy, Assessment of aerosol radiative impact over oceanic regions adjacent to Indian sub-continent using multi-satellite analysis, Advances in Meteorology, doi:10.1155/2010/139186, 2010.

7. Sobhan Kumar Kompalli, S. Suresh Babu and K. Krishna Moorthy, "Inter-comparison of Aerosol Optical Depth from the Multi Wavelength Solar Radiometer with other radiometric measurements" Ind. Jour. of Radio and Space Phy., Vol.39, pp 364-371, December 2010.

8. Kaskaoutis, D.G., Kalapureddy, M.C.R., Krishna Moorthy, K., Devara, P.C.S., Nastos, P.T., Kosmopoulos, P.G., Kambezidis, H.D. Heterogeneity in pre-monsoon aerosol types over the Arabian Sea deduced from ship-borne measurements of spectral AODs, Atmospheric Chemistry and Physics 10 (10), pp. 4893-4908, 2010

9. Satheesh, S.K., Vinoj, V., Krishna Moorthy, K. Radiative effects of aerosols at an urban location in southern India: Observations versus model, Atmospheric Environment, 44 (39), pp. 5295-5304, 2010.

10. Jai Prakash Chaubey, K. Krishna Moorthy, S. Suresh Babu, and Vijayakumar S. Nair, "The optical and physical properties of atmospheric aerosols over the Indian Antarctic stations during southern hemispheric summer of the International Polar Year 2007–2008", Annales Geophysicae, 29, 1–13, doi:10.5194/angeo-29-1-2011,2011.

11. Mukunda M. Gogoi, Binita Pathak,K. Krishna Moorthy, Pradip K. Bhuyan, S. Suresh Babu, Kalyan Bhuyan and Gayatri Kalita, "Multi-year investigations of near surface and columnar aerosols over Dibrugarh, northeastern location of India: Heterogeneity in source impacts", Atmospheric Environment, 45,1714-1724, doi:10.1016/j.atmosenv.2010.12.056,2011.

12. Balakrishnaiah, G., Kumar, K.R., B. S. K. Reddy, K. R. Gopal, R.R. Reddy, L.S.S. Reddy, Y. N. Ahammed, K. Narasimhulu, K. Krishna Moorthy, S. Suresh Babu, Analysis of optical properties of atmospheric aerosols inferred from spectral AODs and Ångström wavelength exponent, Atmospheric Environment, 45, 1275-1285,doi:10.1016/j.atmosenv.2010.12.002,2011.

13. Kumar, K.R.,. Narasimhulu, G. Balakrishnaiah, B. Suresh Kumar Reddy,Rama Gopal, R.R. Reddy, S.K. Satheesh, K. Krishna Moorthy and S. Suresh Babu, "Characterization of aerosol black carbon over a tropical semi-arid region of Anantapur, India", Atmospheric Research., 100, 12-27, doi:10.1016 / j.atmosres.2010.12.009,2011.

14. Suresh Babu, S., Sreekanth, V., K. Krishna Moorthy, Mohan,Mannil, N.V.P. Kirankumar, D. Bala Subrahamanyam, Mukunda M. Gogoi, Sobhan Kumar Kompalli, Naseema Beegum, Jai Prakash Chaubey,

V.H.Arun Kumar, Ravi K Manchanda, “Vertical profiles of aerosol black carbon in the atmospheric boundary layer over a tropical coastal station: Perturbations during an annular solar eclipse, Atmospheric Research., 99,471-478, doi: 10.1016/ j.atmosres. 2010.11.019, 2011.

15. Menon, H.B., Sangekar, N., Lotliker, A., K. Krishna Moorthy, Vethamony, P. Aerosol optical thickness and spatial variability along coastal and offshore waters of the eastern Arabian Sea, ICES Journal of Marine Science, 68 (4), pp. 745-750, 2011.

16. Kumar, K.R.,, K. Narasimhulu, G. Balakrishnaiah, B. Suresh Kumar Reddy, K. Rama Gopal, R.R. Reddy, L.S.S. Reddy, K. Krishna Moorthy, S. Suresh Babu, C.B.S. Dutt, “Spatial heterogeneities in aerosol properties over Bay of Bengal inferred from ship-borne and MODIS observations during ICARB-W cruise campaign: Implications to radiative forcing”, Atmospheric Environment.,45,404-412, doi:10.1016 / j.atmosenv.2010.10.004, 2011.

17. Sinha, P.R., R.K. Manchanda,, J.V. Subbarao, U.C. Dumka, S. Sreenivasan, S. Suresh Babu, K. Krishna Moorthy, “Spatial distribution and vertical structure of the MABL aerosols over Bay of Bengal during winter: Results from W-ICARB experiment”, Journal of Atmospheric and Solar-Terrestrial Physics,73,430–438, doi:10.1016/j.jastp.2010.10.011,2011.

18. Suresh Babu, S., K. Krishna Moorthy, R. K. Manchanda, P. R. Sinha, S. K. Satheesh, D. P. Vajja, S. Srinivasan, and V. H. Arun Kumar, “Free tropospheric black carbon aerosol measurements using high altitude balloon: Do BC layers build “their own homes” up in the atmosphere?”, Geophysical Research Letters, 38, L08803, doi:10.1029/2011GL046654,2011.

PUBLICATIONS IN REFERRED PROCEEDINGS

International

1. S Suresh Babu, Jai Prakash Chaubey and K Krishna Moorthy, Aerosol properties over coastal Antarctica during Southern hemispheric summer: Scavenging by snow and possible climate implications, Proceedings of Science and geopolitics of Arctic and Antarctic (SaGGA). 252-254, 2010.

2. Mukunda M Gogoi, K Krishna Moorthy, S Suresh Babu, Jai Prakash Chaubey, V Sreekanth, Sobhan Kumar Kompalli and Tushar P Prabhu, “Columnar aerosol extinction characteristics: Measurements from a free-tropospheric observatory in western-Himalayas”, International Conference of Solar Radiation and Aerosol (ICSRA -2011), April 14-15, 2011 organized by Institute of Engineering, Tribhuvan University, Khatmandu, Nepal. Page no. 22.

3. Sobhan Kumar Kompalli, V Sreekanth, Jai Prakash Chaubey, Mukunda M Gogoi, S Suresh Babu, Tushar P Prabhu and K Krishna Moorthy, “Aerosol number size distribution measurements at Hanle, a free tropospheric high-altitude site in Western Himalayas”, International Conference of Solar Radiation and Aerosol (ICSRA -2011), April 14-15, 2011 organized by Institute of Engineering, Tribhuvan University, Khatmandu, Nepal. Page no.37.

4. Jai Prakash Chaubey, S Suresh Babu, Mukunda M Gogoi, Sobhan Kumar Kompalli, V. Sreekanth, K. Krishna Moorthy and Tushar P Prabhu, “Black Carbon aerosol over a high altitude (~ 4.52 km) station in western Indian Himalayas International Conference of Solar Radiation and Aerosol (ICSRA -2011), April 14-15, 2011 organized by Institute of Engineering, Tribhuvan University, Khatmandu, Nepal., Page no.15.

PRESENTATIONS

1. V. S. Nair, K. K. Moorthy, S. S. Babu, S. K. Satheesh, and P. R. Nair, Aerosol Radiative forcing over Bay of Bengal: Anthropogenic versus Natural, International AOGS conference at Hyderabad, July, 2010

2. S. N. Beegum , K. K. Moorthy , S. S. Babu, Aerosol Microphysics and Source Characteristics over Port Blair, International AOGS conference at Hyderabad, July, 2010

3. R. K. Manchanda, P. R. Sinha, S. Suresh Babu and K. Krishna Moorthy, Aerosol Dynamics over Bay of Bengal, International AOGS conference at Hyderabad, July, 2010
4. M. M. Gogoi, S. Suresh Babu, V. S. Nair and K. K. Moorthy, Spatial Distribution of Aerosol Single Scattering Albedo Over Bay-Of-Bengal Inferred from Concurrent Shipboard Measurements, International AOGS conference at Hyderabad, July, 2010
5. V. Sreekanth, K. K. Moorthy, S. K. Satheesh and S. Suresh Babu, Vertical and horizontal structure in the aerosol scattering properties over Bay of Bengal during winter: Role of East Asian advection and prevailing meteorology, International AOGS conference at Hyderabad, July, 2010.
6. S. Suresh Babu, V. Sreekanth, K. K. Moorthy, and S. K. Satheesh, Seasonal contrast in the vertical structure of aerosol black carbon over Indian region and its implications: Results from ICARB, International AOGS conference at Hyderabad, July, 2010

INVITED TALKS /LECTURES

K. Krishna Moorthy

Aerosol Radiative Forcing and Impacts for Indian region : ISRO initiatives, UNEP sponsored ABC science team meeting, 23-24, March 2011, Kathmandu.

Invited Plenary lecture on 'South Asian aerosols- facts and issues', International AOGS conference at Hyderabad, July, 2010

Invited talk on 'ARFI: The aerosol project of ISRO & ARFINET: The ISRO aerosol network' NCAP meeting of MOEF, 30 August 2010.

Invited talk on 'Aerosol Forcing over Oceanic regions adjoining India: New insights from ICARB' dmsp symposium, Goa, 19-21, October, 2010

S. Suresh Babu

Talk on 'Black Carbon over India' in the International symposium on "Black Carbon: Current research and policy perspectives", Lucy Cavendish College, Cambridge, 21-22 October 2010, through video conference from IISc, Bangalore.

Talk on 'Balloon borne Atmospheric Sciences' in the 3-day National Familiarization Workshop on Scientific Ballooning at Balloon Facility of TIFR, Hyderabad, 13-15, December, 2010.

Talk on 'Regional Aerosol Warming Experiment – a new initiative of ISRO' , in the break out session on GVAX 'Atmospheric System Research Program Science Team Meeting' at San Antonio, Texas, USA, March 28 – April 1, 2011.

CONVENING SCIENTIFIC SESSIONS

- S. Suresh Babu, Co- convener, session on 'Asian Aerosols and Climate: The known and unknown' in the International AOGS conference at Hyderabad, 2010
- S. Suresh Babu, Chaired three sessions in the International AOGS conference at Hyderabad, 2010

DEPUTATIONS TO CONFERENCES/WORKSHOPS/INSTITUTE/SCHOOL

1. K. Krishna Moorthy, UNEP sponsored ABC science team meeting, 23-24, March 2011, Kathmandu.
2. S. Suresh Babu, 'Atmospheric System Research Program Science Team Meeting' at San Antonio, Texas, USA, March 28 – April 1, 2011
3. Sobhan Kumar Kompalli, "Indo-US Conference-cum-Workshop on Air Quality and Climate Research" during 14-24 March, 2011" at Administrative Staff College, Hyderabad.

4. Jai Prakash Chaubey, International Conference of Solar Radiation and Aerosol (ICSRA -2011), April 14-15, 2011 organized by Institute of Engineering, Tribhuvan University, Khatmandu, Nepal.

5. Jai Prakash Chaubey, 4th Indian Arctic Expedition during July-August 2010.

6. Sobhan Kumar Kompalli, “3 day familiarization workshop on scientific ballooning” at National balloon Facility, 13-15 December 2010, Tata Institute of Fundamental Research, Hyderabad.

ACADEMIC PROJECTS

Internship for M. Sc. Physics: 2

Summer projects of National Science Academies: 2

ABLN&C

Atmospheric Boundary Layer Network and Characterization

Project Team

#Mannil Mohan
##Rajeev K
Bala Subrahamanyam D
Kiran Kumar N V P
Siji Kumar S
Sandhya K Nair
Santosh Muralidharan
*Denny P Allapattu
Lali P T
Marina Aloysius
Prijith S S
Anurose T J
Neethu Purushothaman

#Superannuated on 31 May, 2011
##Since June 2011
**NCAOR, Goa*

1. ATMOSPHERIC BOUNDARY LAYER NETWORK AND CHARACTERIZATION (ABLN&C)

Atmospheric Boundary Layer Network and Characterization (ABLN&C) is one of the projects of ISRO-GBP, being implemented through SPL and aimed at the investigation of the boundary-layer processes through systematic experimental campaigns over land and ocean, and through numerical simulations. During the review period, 3 new stations have been chosen for the expansion of the network out of them one station has been added to the existing network. The network is maintained with the help of inter-departmental and university collaboration.

Tropical Indian Ocean campaign

With a view to investigating the ocean-atmosphere interaction processes in the Marine Atmospheric Boundary Layer (MABL) over the Tropical Indian Ocean during northern hemispheric summer monsoon season (July-August 2010) intense observations were made onboard Oceanic Research Vessel Sagar Kanya (ORV-SK), during its 274th expedition named as Tropical Indian Ocean (TIO) Cruise, as a joint venture with NCAOR, Goa. The TIO cruise had a latitudinal coverage from 10°N to 18°S (Fig. 1). The expedition had basically three components. 1) Vertical profiling of MABL using balloon borne Pisharoty sondes, 2) surface layer meteorological measurements using Automatic Weather Station and 3) manual observations of meteorological parameters through hand held instruments. The cruise also included two time series measurements for a period of 24 hours; with one station in the Northern hemisphere (8°N, 76°E) hereafter referred as TS1 (marked in the figure) adjacent to Trivandrum and the other station in the Southern hemisphere (18°S, 68°E) hereafter referred as TS2 (marked in the figure) during which a total of 12 Pisharoty sondes (6 each) were launched for studying the diurnal variability of the MABL and upper atmosphere. The aim was to investigate the North-South contrast in the MABL characteristics and the lower atmosphere during the main phase of the monsoon. The data have been used for the following investigations.

1) Turbulence and Inertia-Gravity Wave Generation by Tropical Easterly Jet

The time series measurements at TS1 conducted on 11 July 2010 comprised of balloon ascents at 0600,

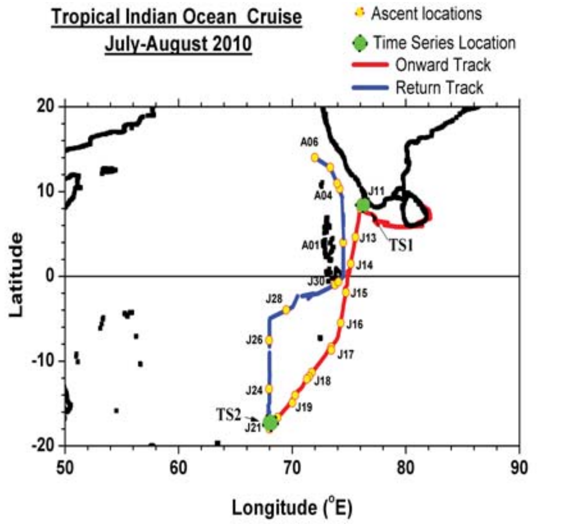

Figure 1: Cruise track of SK-274 during TIO. The approximate position of the ship on various Julian days is marked on the cruise track. Prefix J and A are used with the dates for July and August 2010, respectively. TS1 and TS2 indicate the location where time series measurements were conducted

1230, 1800, 2000, and 2400 local time and surface measurements. These data are used to investigate the characteristics and dynamics of the Tropical Easterly Jet (TEJ) core. It was observed that the jet core lies around tropopause (16.6 km), and had a peak easterly wind around 60 ms^{-1}. Maximum wind shear (0.08 s^{-1}) in TEJ occurred near 18 km. Richardson number profiles (not shown) frequently decreased below the critical value R_{ic} (= 0.25) in the jet stream indicating instability. This can lead to intense clear air turbulence (CAT). Two important parameters for quantifying this turbulence, namely the turbulent kinetic energy dissipation rate (ε) and eddy diffusion coefficient (K), have been estimated through Thorpe length (L_T) method.

Figure 2a-c show the time-altitude distribution of L_T, log(K) and log(ε). Fig.2a shows a region of comparatively higher magnitude of L_T above 10 km; the upper boundary of which coincided with the tropopause. This shows a layer of high turbulence in comparison with rest of troposphere and lower stratosphere. Mean and maximum magnitude of L_T in this band has been 85 m and 250 m respectively. Similar to L_T, magnitude of K (Fig.2b) also was higher in the upper troposphere (between 10 and 16.5 km) with K > 10 m^{2}s^{-1} indicating enhanced turbulence. In this layer, the mean value of K was 8 m^{2}s^{-1} with a maximum of 24 m^{2}s^{-1}. Here, the enhancement of the wind shear around tropopause reduced Ri to the critical value required to trigger the Kelvin Helmoltz Instability (KHI). The subsequent breaking of the KH waves might have resulted in the

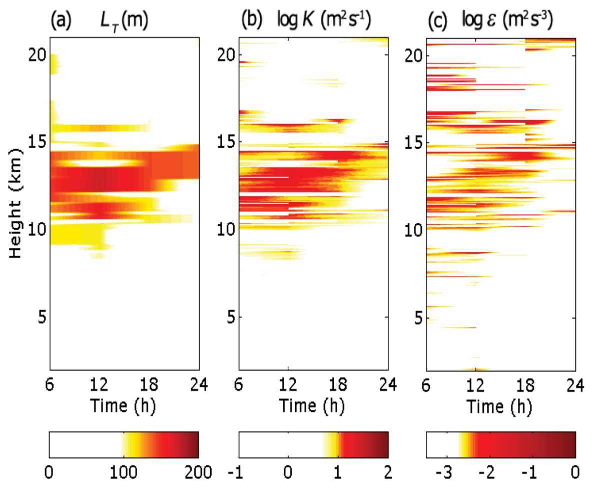

Figure 2: Time altitude distribution of LT, K and ε

enhanced turbulence. Fig.2c shows higher magnitude of above 10 km. Unlike L_T and K, the magnitude of ε shows higher values above 16 km. This could be due to the increase in static stability above 16 km.

Fig.4 shows the typical examples of the quasi-monochromatic gravity waves in the middle and upper troposphere (MUT) and lower stratosphere (LS) observed at 1230 local time. The quasi-monochromatic wave components [u′, v′, T′] are derived by harmonic fitting to the fluctuation components. Unlike the velocity fluctuations, the temperature fluctuations are normalized by the background temperature (T'/T_o). Hodographs of horizontal disturbances are also shown at the extreme right panels. The vertical wavelengths in the LS and MUT regions are calculated to be 3.3 km and 4.2 km respectively. The zonal (meridional) amplitudes at LS and MUT are about 1.5(3.3) m s^{-1} and 1.3 (2.1) m s^{-1} respectively. The amplitude of T'/T_o has been observed to be about 1.4% in LS and 0.5% in MUT region. As the Gravity Wave (GW) energy propagates vertically away from the source region, from the figure 3d it can be seen that in the LS region, the disturbance wind vector rotates in clockwise direction (GW energy propagates upward) and in the MUT, rotation is in anti clockwise direction (GW energy propagates downward) thereby identifying the wave source to be in the tropopause region, which is the TEJ.

Vertical profiles of thermodynamic parameters

To investigate the differences in the ABL in the regions of high convective activity (TS1) and subsidence dominated southern region (TS2), thermodynamic parameters such as virtual potential temperature (θ_V), equivalent potential temperature (θ_e), saturation equivalent potential temperature (θ_{es}) and specific humidity (q) obtained from Pisharoty sonde ascents at TS1 and TS2 were analyzed. Figure 4a-d show typical daytime convective boundary layer profiles of q, θ_V, θ_e and θ_{es} corresponding to 1230 local time for the two stations. The magnitudes of q are higher at TS1 (10-16 g kg^{-1}) compared to TS2 conducted at 18°S (6-11g kg^{-1}). However, q becomes almost negligible (< 4 g kg^{-1}) over 18°S station in the higher altitudes (> 3 km) indicating the presence of relatively dry environment which can be attributed to descending limb of the Hadley cell over that latitude. The vertical and meridional winds from ECMWF data for the period indicated the presence of descending limb of Hadley

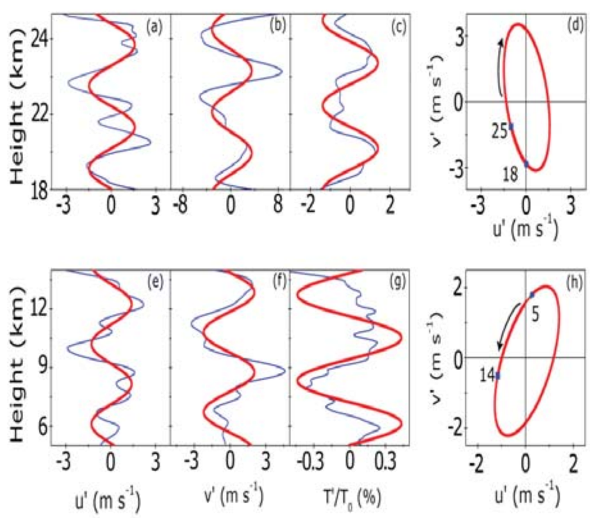

Figure 3: Gravity wave components and hodograph (1230 local time) for (a-d) lower stratosphere, (e-h) middle and upper troposphere. The red lines are derived monochromatic waves and blue lines are fluctuation components

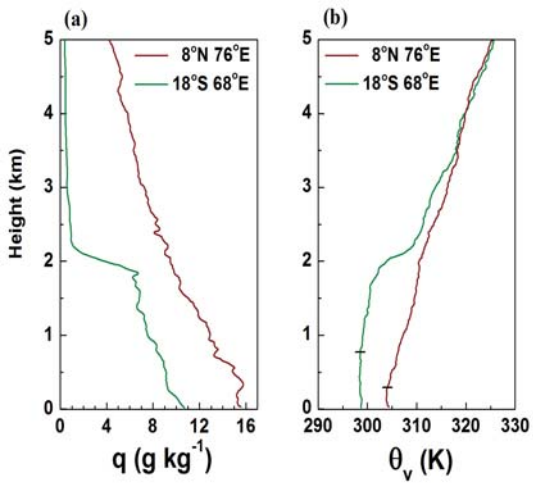

Figure 4: Typical vertical profiles of (a) q at TS1 (8°N, 76°E) and TS2 (8°N, 76°E) stations (b) θv at TS1 and TS2 stations. (c) θe & θes at TS1 station (d) θe & θes at TS2 station. Horizontal bars in θv profiles denote the observed Mixed Layer Height

cell. Large values of q (> 4 gkg^{-1}) at about 5 km observed over 8°N can be attributed to enhanced convection. This was also supported by very low values of the vertical profiles of a parameter δθ (difference between θ_{es} and θ_e) at TS1. The trade wind inversion (at 2 km) can be identified by a maximum in θ_e and minimum in θ_{es}. All these lead to the inference that 8°N region has been more convective compared to 18°S. The ABL structure changed dramatically between 8°N and 18°S stations. Mixed Layer Height (MLH) magnitudes inferred from θ_V and q profiles were about 800 m at TS2, while it was just 300 m at TS1. The high value of MLH at TS2 is mainly attributed to the strong surface heating (SST-AT of about 1.6°C) and high winds of about 11 ms^{-1} at 18°S as compared to TS1 where the SST-AT and winds were 0.8°C and 5 ms^{-1}, respectively.

DATA ARCHIVAL

As part of the data policy, a data archival system is being worked out for ABLN&C. At present the data obtained from the network stations are archived in DVDs in the standard format. A better archival system would be evolved shortly.

ATMOSPHERE TECHNOLOGY DIVISION

Engineers

Mohankumar S V
Sreelatha P
Pradeep Kumar P
Tirtha Pratim Das
Shajahan M
Dinakar Prasad Vajja
Neha Naik
Manikantan Nair N

Technical Assistants/ Tradesman

Pramod P P
Mohammed Nazeer M
Rosmy John
Lali P T
Anumod P G
Ajeeshkumar P S
Satheeshkumar B
Johnson A J
Asoka Kumar G S
Uttam S Purty

Atmosphere Technology Division (ATD) is responsible for the design and development of new experiments, techniques and payloads as well as augmentation, support and maintenance of ongoing activities of SPL. The Space Borne Instrumentation Section of ATD focuses on the design and development of payloads and their ground checkout systems. The activities of ATD during the reporting year are detailed below.

1. YOUTHSAT ACTIVITIES

The Youthsat, launched on April 20, 2011, carried two scientific experiments of SPL; Radio Beacon for Ionospheric Tomography (RaBIT) and Limb Viewing HYper Spectral Imager (LiVHYSI). The ATD co-ordinated the development of RaBIT with RFAFD of VSSC and established a Payload Operation Centre (POC) at SPL. Ground stations were setup at Trivandrum, Bangalore, Hyderabad, Bhopal and New Delhi for reception of RaBIT data, which were tested and qualified with the payload. All the five stations locked onto the RaBIT signal, with enough overlap between the stations.

RaBIT estimates the total electron content (TEC) along the satellite-receiver ray path. The ground stations are equipped with coherent receivers capable of receiving the VHF and UHF signals at 150 and 400 MHz based on a Two Line Element (TLE) file and gives the TEC and scintillation index in standard file format. A supervisory program has been developed in Python language to meet the RaBIT file management requirements as per the ISSPC, following the schematic Fig. 1.

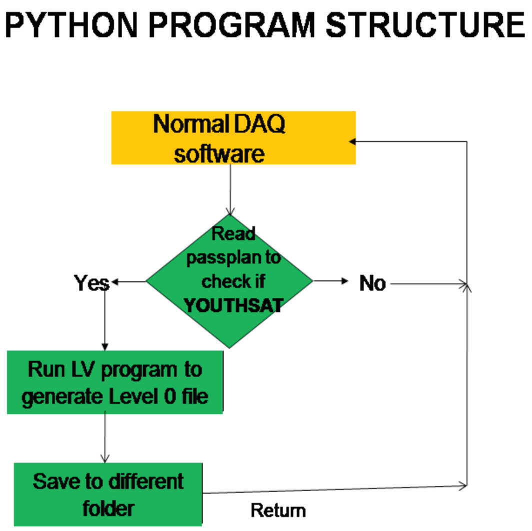

Figure 1: Python program structure

Another software has been developed in LabVIEW for generation of the Level-0 data file and an information file which is also integrated into the modified program in Python. These files are then sent to ISSDC via sftp.

This Level-0 data provided to generate the ionospheric tomogram products (Level-1). The Level-0 and Level-1 data are also accessible to SPL (POC), for further scientific analysis. A typical tomographic product from RaBIT is shown in Fig. 2.

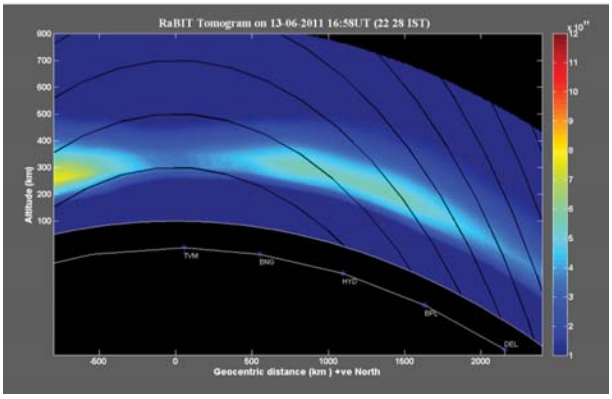

Figure 2: A typical tomogram products, generated using RaBIT data of 13 June 2011

2. POC FOR YOUTHSAT PAYLOADS AT SPL

A Payload Operations Centre (POC), setup at SPL and having internet connectivity to ISSDC and the ground stations, regularly communicates with ISSDC for exchange of data from RaBIT and LiVHYSI. It is planned to extend the chain of ground receiver stations by including three more stations almost along the same meridian, viz.,Thanjavur, Nagpur and Nainital (Fig.3), to improve the spatial extent and resolution of the tomograms.

Figure 3: Indian Network of Beacon Receivers

3. DEVELOPMENT OF THE CHACE-2 FOR CHANDRAYAAN-2 MISSION

The CHACE-2 (Chandra's Atmospheric Composition Explorer-2) is one of the payloads selected for Chandrayaan-2 orbiter. Drawing heritage from its predecessor CHACE-1, CHACE-2, a quadrupole mass spectrometer based instrument, would analyze the lunar neutral atmosphere in the mass range of 1-300 amu at 200 km lunar altitude. The CHACE-2 will monitor the global variation of the lunar neutral composition as well as its short and long term variations.

The salient features of the CHACE-2 are:

a. Extended mission duration

b. Multiple modes of operation, amenable to be telecommanded

c. Extended mass range (1-300 amu)

d. Enroute operation of the instrument to acquire the background spectra.

The CHACE-2 instrument would be mounted along the ram direction. The background spectra will be subtracted to eliminate any effect of the outgassing species. In order to conserve the onboard power, CHACE 2 will be switched ON in time-sharing basis.

In order to evaluate the instrument transfer function and its behaviour under ultra high vacuum condition, a set of characterization experiments have been performed. Electrical characterization of the CHACE-2 Engineering Model (EM) (Fig.4)has been carried out to study the current drawn by the instrument at different phases of its operation and the stability thereof. These results will be used for power budgeting and to fix the DC/DC Converter specifications as well as to characterize the surge currents.

With a view to characterizing the mass spectrometer and to arrive at the optimum values of the detector bias voltage (EMV – Electron Multiplier Voltage), the scan rate (in mass sweep mode) and dwell time (in trend mode), the following characterization experiments have been conducted.

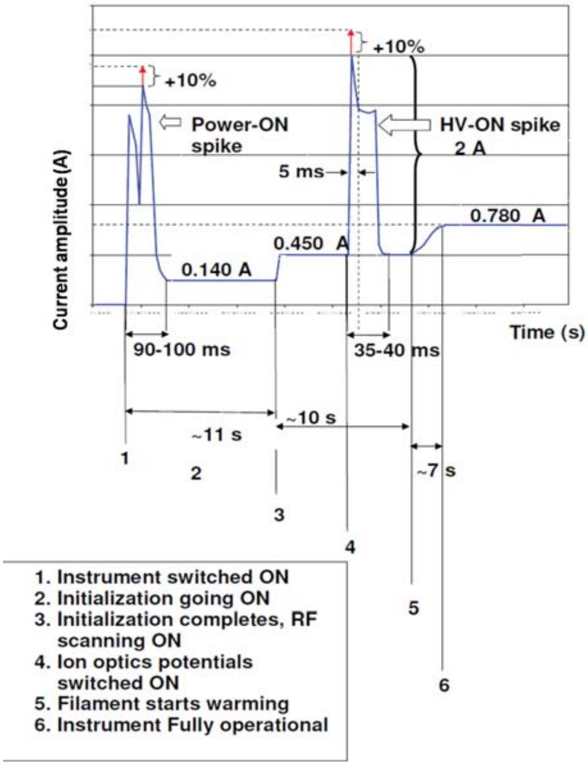

Figure 4: The current drawn by CHACE-2 EM during its power ON sequence as well as under steady state of operation. The current values have an uncertainty of 10 percent

Operating range of the Electron Multiplier Voltage (EMV) and scanning rate

Experiments have been performed to choose the optimum range of operation of the Electron Multiplier Voltage, (EMV) of the Channel Electron Multiplier (CEM) detector for maximization of the Signal-to-Noise Ratio (SNR). The signal strength increases rapidly with EMV for relatively low voltages (~ 1.2 kV) and tend to saturate at higher voltages. However as the detector noise keeps on increasing, the SNR vs EMV curve becomes bell-shaped (Fig.5).

The mass scanning time of CHACE-2 is defined as the time to completely acquire a spectrum from 1 to 300 amu. Although slower scan rate reduces the mass-spectral noise (Fig. 6), the spatial resolution of

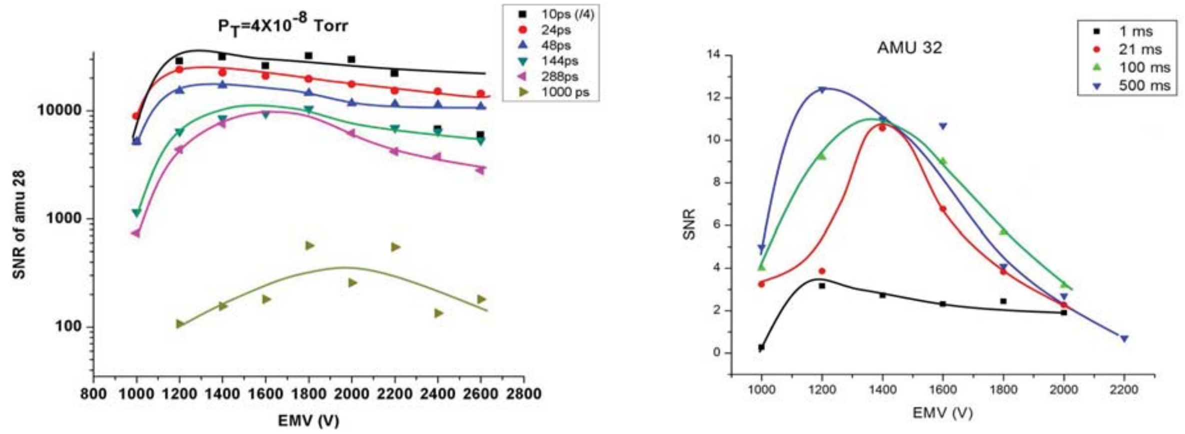

Figure 5: (Left): Results obtained in mass sweep mode. The scan rate is varied to get the family of curves. (Right): Results obtained in the trend mode. The dwell time (comparable with the scan time in the mass sweep mode) is varied to get the family of curves.

the sampling of the lunar atmosphere will be poor at the slower scanning rates. Hence, a trade off was called for between the mass-spectral noise and the spatial resolution.

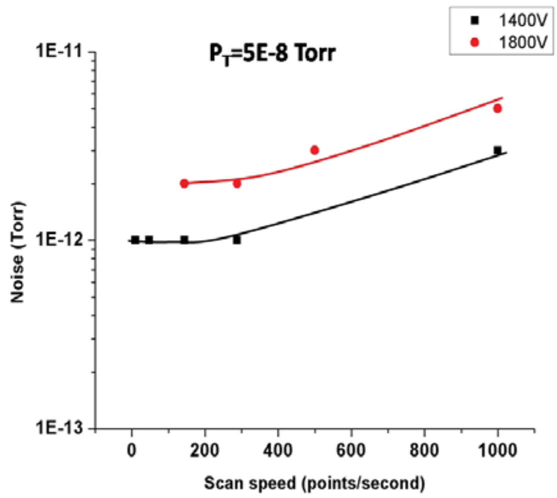

Figure 6: Variation of the mass spectral noise with scan speed at different multiplier voltages. Very slow scan rates do not reduce the mass spectral noise to an appreciable extent, but degrade the spatial resolution of the science data

b. Water vapour desorption rate under UHV

Quantitative interpretation of the science data from neutral mass spectrometers for atmospheric hydration requires estimation of the adsorbed water vapor. As the prolonged exposure of the instrument to the deep space environment accelerates the water vapor desorption, there is a need to characterize the dehydration profile. The Engineering Model of CHACE-2 has been exposed to ultra high vacuum conditions and the water vapor desorption from the instrument has been studied. It is found that about four weeks of continuous exposure to deep space vacuum is enough for the instrument to desorb most of the adsorbed water vapor (Fig.7).

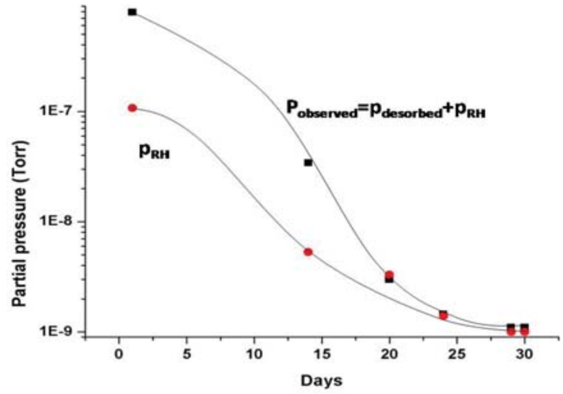

Figure 7: Variation of the observed hydration level (combined partial pressures of water and hydroxyl) and the theoretically computed hydration level (p_{RH}) in the absence of any desorption from the instrument with the number of days of pumping. The two curves merge as time progresses because of the continuous decontamination process in vacuum

c. Transient Response in Ultra High Vacuum

Unlike the CHACE-1, the CHACE-2 would be switched ON at multiple occasions en-route Moon in order to acquire a set of reference spectra. Also, during the operational phase in the stabilized lunar orbit, the CHACE-2 will have to be switched ON, each time for a per-determined duration, in between switch OFF periods in order to conserve the on-board power. This calls for experiments to characterize the transient behaviour of the mass spectrometer. As such, a few House Keeping (HK) parameters related to the emission circuit of the ionizer, have been monitored. The filament voltage is adjusted in a close-loop configuration to maintain the stability of the emission current. During the transient phase, the filament voltage rises gradually and ultimately attains a steady value depending on the total pressure (Fig. 8); the settling time being longer lower pressures. In the lunar ambience, it is expected that the settling time of the emission system will be approximately 30 minutes. Thus, CHACE-2 should be operated for a minimum period of 1 hour on each switching ON in order to acquire adequate number of background spectra after the instrument gets stabilized.

The effects of the variation of the different parameters of the CHACE-2 (EM), viz. the scan rate, Electron Multiplier Voltage (EMV), dwell time, focus voltage (FV), etc. on its performance have been studied. Based on the above characterization experiment, the following ranges of parameters have been selected for CHACE-2.

- *Electron Multiplier Voltage EMV*:

  1200 V to 1800 V for mass sweep mode

  1100 V to 1600 V for trend mode

- *Scan Rate*:

  10 points /second to 288 points/second

- *Focus Voltage*: -20 V

As part of the initial functional tests, a detailed timing analysis has been performed on the EM, to help finalize the optimum scanning and communication parameters. Besides, experiments were conducted to characterize the ratings of space qualified capacitors. In order to finalize the rating of the DC-DC converter, measurements of the surge current spikes have been made.

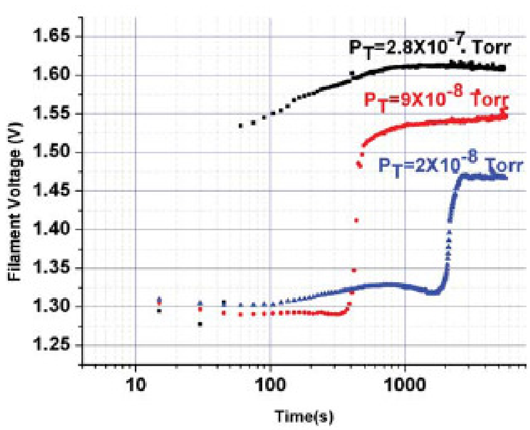

Figure 8: Variation of the filament voltage with time. It is observed that the filament voltage and hence the emission current take more time for stabilization at lower pressures

The Conceptual design of CHACE Integrated System Management Unit (CISMU) and the Onboard System for CHACE Operation and Telecommand (OSCOT) are completed. OSCOT (Fig. 9) is a FPGA based system with onboard RAM and EEPROM memory, IEEE1553 interface, RS232C interface and LVDS interface. It controls the operation of the Mass Spectrometer, acquires the data and transfers it to the solidstate data recorder onboard the Chandrayaan-2 and processes and executes the telecommand from the ground. It is also envisaged to reload the onboard program from ground if required.

A LabVIEW based checkout software (schematically shown in Fig. 10) to provide online data acquisition, analysis, plotting and archiving has been developed for the stand-alone tests planned for the payload during its developmental stages. The new software integrates the functions of data analysis, archiving and plotting programs.

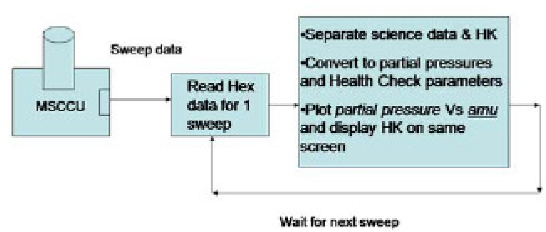

Figure 10: CHACE – 2 Online Software

A technique has been innovated to estimate the night side pressure of the moon with good accuracy where the conventional Bayard-Alpert ionization gauge, built-in within CHACE-2, is not expected to work because of the X-ray limit. Below the X-ray limit, estimating the total pressure by summing the mass-spectral peaks requires prior knowledge of normalization constant that makes the sum-over-peaks equal to the total pressure. However, the normalization constant itself varies with the total pressure for higher detector voltage, required to detect tenuous particle concentrations.

It is found that this uncertainty can corrupt the estimate by an error of ~ 70-80%. An iterative algorithm has been developed to reduce the magnitude of this problem, and has been verified with experimental data. It is found that it could estimate the total pressure with error less than 5 %.

4. HF RADAR

The activities related to HF radar involves (a) maintaining the present radar operational for immediate scientific needs and (b) develop a new digital receiver and data acquisition system. The details are given below.

Development of a new digital receiver and data acquisition system

The block diagram of the state of the art Digital Receiver being developed is shown in Fig. 11. Designed on the principle of FPGA based hardware, developed usinig VHDL, the system comprises of four modules: Signal Generation and Down Conversion block, Timing and control signals generation, Signal Processing and Memory Card interfacing for data storage & Graphical User Interface(GUI).

Signal Generation (DDS) and Down Conversion (DDC) module constitutes the front end of the digital HF radar receiver. Virtex-6 FPGA board is used for the generation of pulsed 18 MHz Sine wave, 1 MHz Sine and 1 MHz Cosine signals for transmission and down conversions respectively. Digital Signal Synthesizer consists of Look Up Tables (LUT) (which stores trigonometric values), Address generation and decoding unit (for generating the signal wave of the desired frequency) and a Combinational circuit (which controls the mode of generation). The Digital Down Conversion block forms the heart of the new digital hybrid which does the operation of the down conversion and down sampling to retrieve the signal of interest I (in phase) and Q (in quadrature) at required data rate and bandwidth. It is characterized by Digital multipliers (for mixing the signal to the base band), Filter chain (for decimating and filtering the signal) and a Gain block (to adjust the gain of the signal). The Revised Architecture eliminates the mixer block by taking the advantage of the ADC under sampling technique. Timing and Control Signals Generation block is responsible for controlling the whole module by the generation of control signals. Controller and Clock manager distributes the clock for different blocks derived from the master clock for maintaining coherency. The Signal Processing block consists of a 'run time' reconfigurable FFT processor which is to be later integrated into H.F Radar module. The design has been implemented using the following architecture comprising of a series of FIFO's (First in First Out), ROM's (for storing twiddle factors). The data from the Radar after processing has to be stored

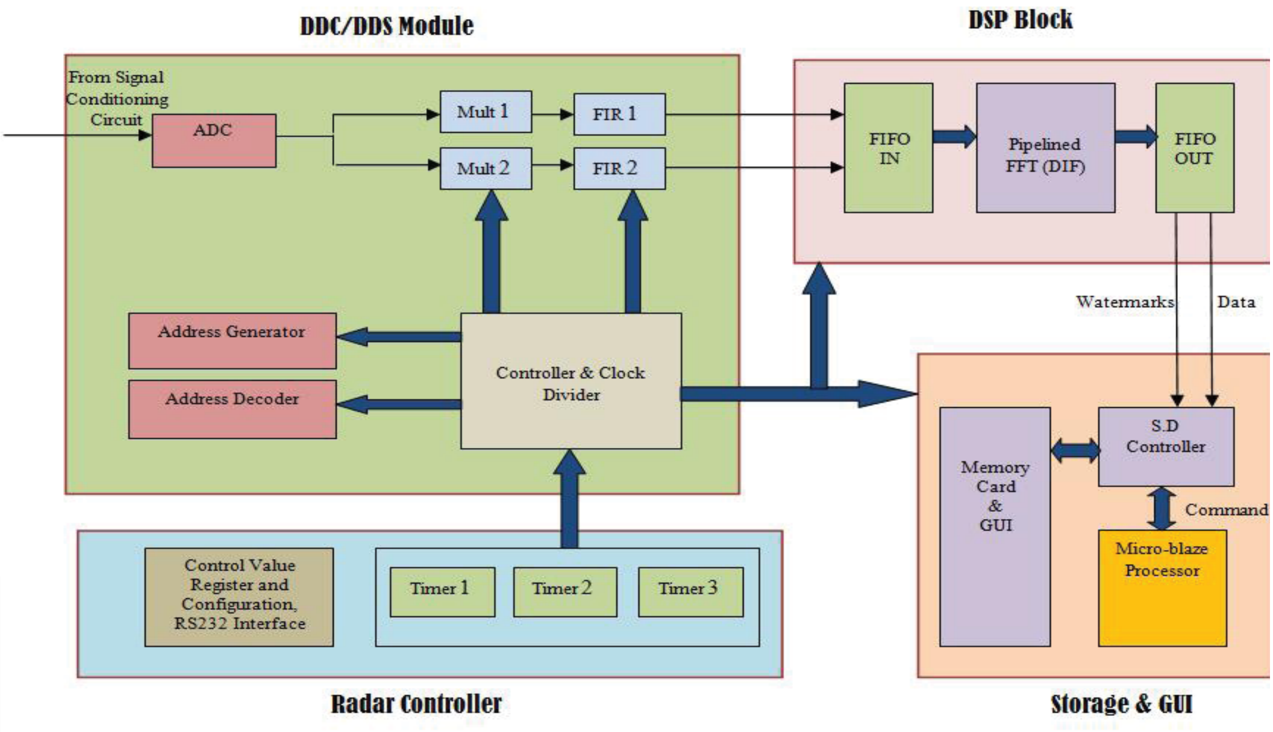

Figure 11: Generalized Top Level Architecture of the HF Radar Digital Receiver

for future reference. For that, SD Card is being used which is of capacity 32GB (SDHC). The host controller resides in Virtex-6. Software simulation and code modules are in the advanced stages. The required hardware platform is being procured.

Maintenance of present radar system

Every effort has been taken to maintain the existing system operational. The nuvistor based front end amplifier of the receiver had to be replaced by solid

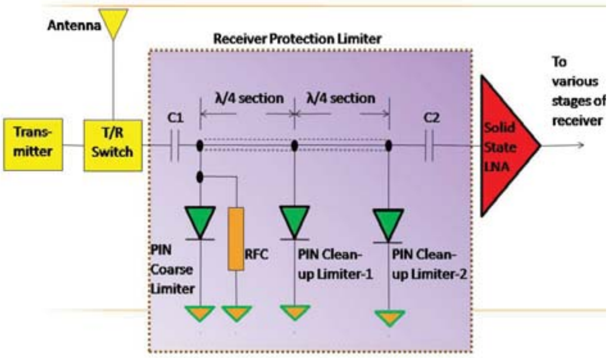

Figure 12: Receiver Protection Limiter for HF Radar

state module. A receiver protection limiter (Fig. 12) was designed, developed, tested and implemented in the system for improved isolation from the high power transmitter. The personal computer used in the system has been replaced after a breakdown. After a short break, the radar is back in operation. A sample spectrum output is shown in Fig.13.

5. PARTIAL REFLECTION RADAR

The 2.5 MHz Partial Reflection radar has been indigenously built in SPL and commissioned in April 2004. This high-power, pulsed, coherent radar has been operated since then for investigating the atmospheric drift velocities in the study of mesosphere –lower thermosphere (MLT - 65 to 95 km) region and has been complimenting/supplementing the balloon/rocket flights and Meteor wind radar data in the MLT region, until 2008.

With the change of the PC hardware and operating system with time and also due to several modifications the system underwent led to a cascading effect with respect to the digital data interface and associated software and the radar became non-operational, despite several attempts. In view of the importance the radar system for MLT region studies, it has been decided to outsource the development, supply and installation of digital radar controller, receiver and data acquisition system based on state of the art PC platform and OS, to a competent agency. Detailed specifications for the Digital receiver and Data Acquisition system have been generated based on that of the existing PR radar.

6. IONOSONDE

The Digisonde Portable Sounder (DPS-4) was maintained operational throughout the year in TERLS. The necessary civil electrical and AC support for en-

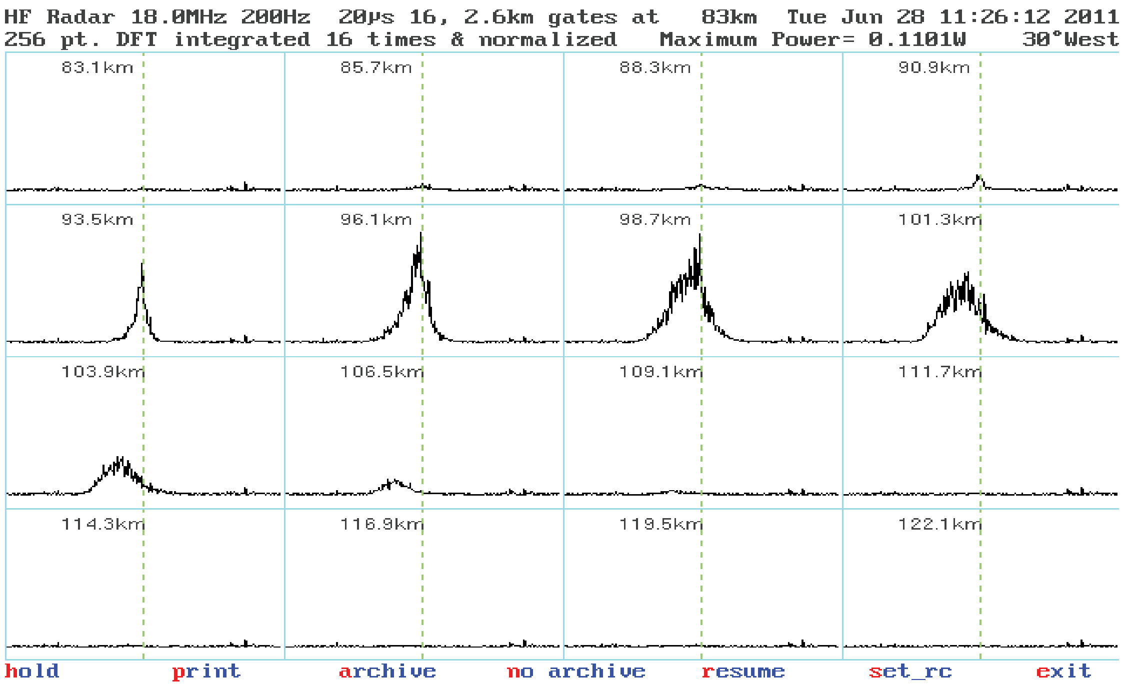

Figure 13: Sample spectrum from HF Radar

ATD

suring continuous operation of the equipment were provided. The data has been archived on DVDs for future use. Recently (in May), the Digisonde was severely affected probably by lightning resulting in a breakdown. The system has been brought back to normal operating condition.

7. TECHNICAL DEVELOPMENTS FOR ARFI PROJECT

ARFI project of ISRO-GBP is aimed at establishing a network of aerosol observatories over Indian main land for the complete characterization of atmospheric aerosols for the estimation of aerosol radiative forcing. Technical development and support to the ARFI-NET is an important activity of ATD. The following were accomplished during the report period.

New stand-alone Control and Data Acquisition System for MWR

The in-house built MWR (Multi-Wavelength solar Radiometer), which measures AOD at 10 wavelengths remains the backbone instrument for the network of aerosol observatories (ARFINET) under ISRO-GBP over nearly 3 decades. In order to ensure long-term operation and data continuity and to reduce dependancy on the rapidaly changing PC technology and operating system, a microcontroller-based stand-alone control and data acquisition system has been designed, developed and successfully field tested. The system would replace the existing PC-based control and data acquisition system, which makes use of ISA addon cards and DOS/ Windows 98 operating system. The new unit (Fig. 14) can normally operate in stand-alone mode and optionally interface with a PC when and where available. The salient additional features of the stand-alone system are

• PC independent operation, control and data storage in memory card

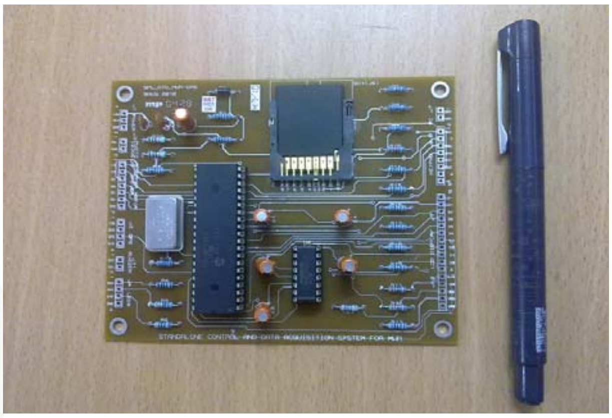

Figure 14: Stand-alone Control and Data Acquisition Card of MWR

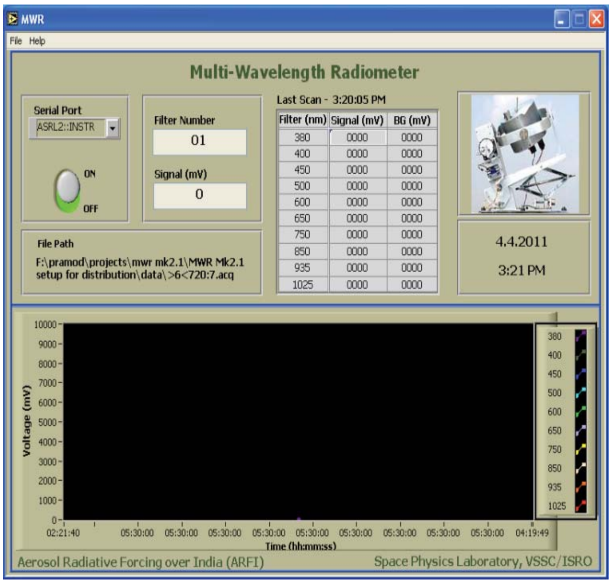

Figure 15: Lab VIEW based GUI Program of MWR

• Customized keypad for menu options

• GPS based time information for improving the accuracy of derived products

• 20x4 LCD for online data display

• Digital data output in RS-232 format

• Disabling Sun tracking automatically after 7 pm if the instrument is left unattended

• Compact microcontroller-based unipolar stepper motor driver

A Lab VIEW based GUI program has been developed to log online raw data from the stand-alone system to PC for further analysis. This program has the following features

• display online data in graphical and tabular formats (Fig.15)

• convert raw data to legacy '.ACQ' and '.DAT' file formats

• download bulk data from the stand-alone system.

A science based cloud screening and editing softwarre is beiing developed and could be added to the present system.

ARFINET observatories: New and Augmented

As part of ARFI network expansion, MWR, were installed/refurbished at Ooty (Tamilnadu Agricultural University), Bangalore IISc, Hyderabad (NRSC), Dibrugarh (Dibrugarh University), Shillong (NESAC) and Nagpur RRSC. A net radiation sensor was installed at Anantapur (Sri Krishnadevaraya University) and Nagpur.

Solar Power Station for aerosol observatory, Hanle

A high altitude aerosol observatory was established at Hanle (4500 m above mean sea level) in Trans-Himalayas under ARFI project. The observatory consists of scientific instruments MWR, Aethalometer, Net radiation sensor and SMPS. It has provided continuous data on aerosols for this region for the first time, over a long period. At present, power to these instruments is taken temporarily from the solar power station of telescope observatory of IIA. A 2KW solar power system was procured based on load requirement, Sun-hours per day, size of the battery bank and size of the solar array. The system is sufficient for providing power to the aerosol observatory. The procured system has been installed and tested at SPL lab (Fig. 16) and is ready to be installed at Hanle station. Power backup of the system can be increased by adding more number of solar PV (Photo-Voltaic) modules.

Figure 16: Deployment of Solar PV modules of 2 KW Solar Power System

High Altitude Balloon borne Experiment (RAWEX-01, RAWEX-02,02B)

As a part of ARFI_RAWEX, the in-house developed balloon payload experiment using commercial Aethalometer has been successfully conducted twice from National Balloon Facility, TIFR, Hyderabad on 8th January 2011 and 27th April 2011. BC (Black Carbon) measurements were made up to 10.5 km altitude.

The payload (Fig. 17) is a modified version of ground-based Aethalometer along with an in-house developed data acquisition, telemetry and command interface unit for switching on and off the instrument at desired pressure levels (Fig. 18), control unit and a GPS Receiver. Ground-based Aethalometer has been modified to work at higher altitudes. Its internal air pump was replaced with three external dc air pumps for achieving high flow rate. An air chamber has been designed for cascading the external pumps.

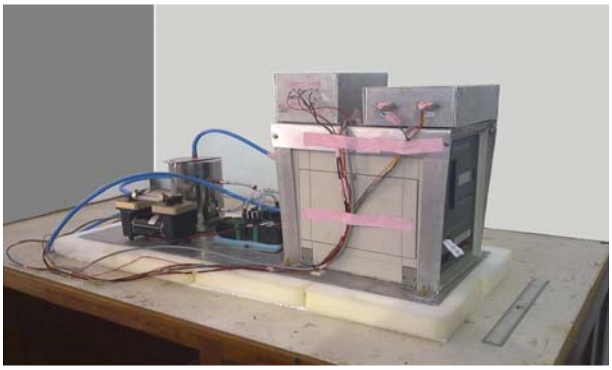

Figure 17: Integrated Payload for RAWEX Balloon Flight

The results from the first flight (27th March 2010) are published in the prestigious international journal,

Geophysical Research Letters, of American Geophysical Union.

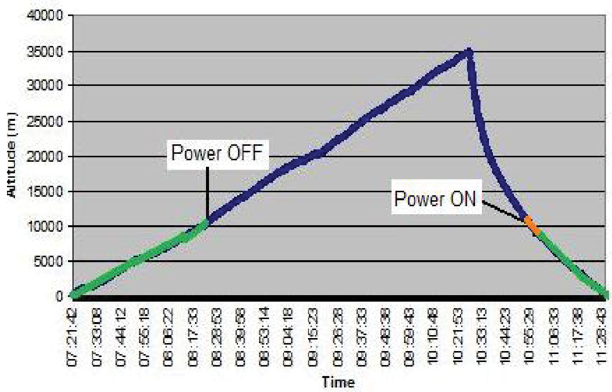

Figure 18: Trajectory of RAWEX Balloon flight

8. EXPERIMENTS FOR BOUNDARY LAYER STUDIES

ATD provides support for the operation of various ground experiments for boundary layer studies. These include Disdrometer (RD-80), Automatic Weather Station, Ultra Sonic Anemometer and Doppler SODAR etc., The antenna shield of indigenously developed SODAR was renovated with foam lining. ATD has extended support for the regular launching of GPS Sonde from this station on a weekly basis. Data from Disdrometer and Automatic weather station have been archived regularly. ATD has participated in the Monsoon Boundary Layer Experiment campaign and RONAC (Research on organization of atmospheric convection) experiments.

Onboard Data Storage and Retrieval System for the Tethersonde

This is an augmentation of the existing Tethersonde, by incorporating a microcontroller based data acquisition and SD memory card storage system to the onboard circuit, without affecting its normal operation and telemetry. This not only provides a redundancy to data, but also ensures uninterrupted data collection even during telemetry breaks. Apart from this onboard segment, there is also a ground segment that retrieves the stored data from the SD memory card to PC and converts them in to physical units in the same fashion, as done by the dedicated ground receiver of the tethersonde (Fig. 19). The results obtained by the dedicated receiver and the new system were compared and verified. Thus this system provides a total redundancy to the tethersonde data, eliminating data loss due to telemetry problems.

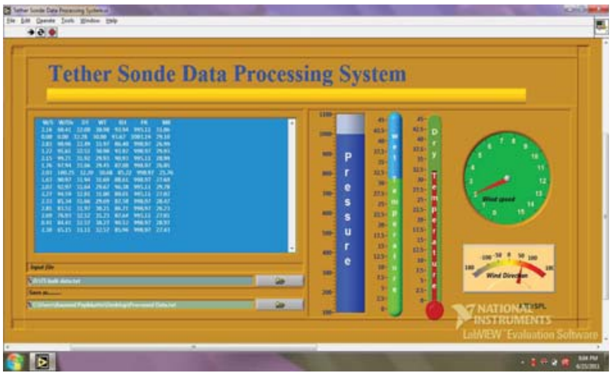

Figure 19: Tethersonde Data processing and display system

9. MECHANICAL ENGINEERING WORKS

Design, draughting and fabrication has been carried out for various ongoing projects of SPL These include: design and generation of part drawings for day and night air glow photometer, chassis for CCD camera and monochromater autoscanning system for optical aeronomy, chassis for RaBIT transmitter simulator, mount for 14 inch telescope for Raman Lidar with tilt and leveling, mount for Pyronometer and Pyrgeometer, optical fiber and lens mount (Teflon make), housing for automatic weather station, CAD design for chassis for Control and DAS of MWR etc.

10. SPL INTERNET WEBSITE DEVELOPMENT

The hardware architecture of SPL website has been finalised in consultation with COM division of VSSC. The servers and workstations for hosting the site are being procured. Broad specifications have been finalized for development of website by outsourcing.

11. TECHNICAL SUPPORT

ATD had maintained Intranet LAN in SPL for scientific data transfer, email, personal Information system and COWAA applications and Internet nodes for publication survey, submission and web browsing applications. The Intranet network in TERLS area has been extended to Aeronomy and MPL buildings. Connectivity has been upgraded to Optical fibre for building T-68 (ATS) of SPL.

12. ONGOING ACTIVITIES- AUGMENTATION/ REFURBISHMENT

Space Borne Instrumentation Laboratory

A temperature test chamber for environmental testing of scientific payloads, a table top model climatic test chamber has been initiated. ESD safe wrist straps, soldering rework station, illuminated magnifier etc have been procured for flight level soldering of components. For RF system testing, a distortion analyzer and noise source have been procured.

Data Acquisition System for Raman Lidar

A Raman Lidar is being developed inhouse as an add-on channel to the existing Micro Pulse Lidar. This receiver channel will have the full system for reception of return input light at Raman shifted wavelength along with a Data Acquisition system built around NI PCI 6602 card which has 32 bit 80MHz counters. This system is designed to count the photons received by the PMT of the Raman lidar receiver in multi bins corresponding to the height range of the signals. A LabView based GUI program is being developed for the data acquisition and online plotting.

All Time Photometer for Air Glow measurements

The design of mechanical system of a computer controlled all time Photometer has been completed and the fabrication drawings are being prepared.

Design and Development of ARFINET Data Disseminator System

Currently, there are 37 aerosol observatories operational under ARFINET. Each observatory consists of several scientific instruments. The instrumental data are received now by email mostly with delays leading to backlogs. With a view to avoid this and ensue timely data transmission to SPL, a fully automatic data disseminator system is being developed. This microcontroller based system would collect data from upto eight instruments through its serial interfaces and forward them automatically at set regular interval to the data center. The system developed will enable collection and sending of data over Public Switched Telephone Network (PSTN) modem.

GSM based Data Transfer System

GSM (Global System for Mobile Communications) based data transfer system is being developed for transferring data wirelessly from one location to another location any where in India. The system uses SMS (Short Message Service) of mobile communication system for data transfer. The GSM system is planned to be used for transferring RAWEX payload data in real time during flight from National balloon Facility, TIFR, Hyderabad to SPL, VSSC, Trivandrum.

Short-range Wireless Communication System

Short-range low power wireless communication system is being developed for data communication between out door field instrument and indoor PC. Line of sight range of the system is 500 m. This would be deployed at different locations such as Hanle.

Data Display System

A wall mounted large format Data display is being developed by using high brightness and low power dot matrix LEDs. This is used for conveniently displaying scientific data of various instruments for better viewing.

Development of IR-MWR

Development of IR-MWR (Infra Red -Multi Wavelength Radiometer) has been initiated. This will include the 1100, 1200, 1250, 1300, 1550, 1600, and 1650 nm bands.

TECHNICAL REPORTS

1. Design and Development of Payload, Telemetry and Telecommand Interface for the High Altitude Balloon borne measurements of Aerosol Black Carbon under RAWEX: SPL-TR-01-2011
2. Stand-alone Data Acquisition System for QCM Impactor: SPL-TR-02-2011
3. Compact Unipolar Stepper Motor Driver for Multi Wavelength solar Radiometer (MWR): SPL-TR-03-2011

PROJECT REPORTS

1. Anil Bhardwaj, Tirtha Pratim Das, P. Sreelatha and P. Pradeepkumar ; CHACE-2 project report (SPL-CHACE-2-PR-1)
2. Tirtha Pratim Das, G. Supriya, P. Sreelatha, P. Pradeepkumar; CHACE-2: Information for the Reliability and Quality Assurance (R&QA) Team, SPL-TN-CHACE-2-3, 2011.
3. Tirtha Pratim Das and G. Supriya; Preliminary Inputs for Designing the Chassis of CHACE-2, SPL-TN-CHACE-2-1, 2011.
4. Tirtha Pratim Das, et al., Characterization Experiments on CHACE-2 Engineering Model, SPL-CHACE-2-PR-2, 2011.

A total of 12 technical innovations have been submitted for inclusion in the ISRO's catalogue of innovations.

INTERNAL REPORTS

1. Tirtha Pratim Das; Planetary Exploration Using Rover (Lecture note for 11th PLANEX workshop)
2. Preliminary design document for EACE and ENWi payloads (SPL:TR:TSE-09-2009)
3. Circuit Design document for ENWi payload (SPL:TR:TSE-10-2009)
4. Timing analysis of EACE payloads for TSE-2010 (SPL:TR:TSE-12-2009)
5. Augmentation of coherent beacon ground receiver for YOUTHSAT data reception (TBR)

TEST REPORTS

1. Test plan document for Coherent Radio Beacon Receiver for RaBIT payload.
2. Test results of Coherent Radio Beacon Receiver for RaBIT payload.
3. GATE test document for ENWi payload: TSE-2010

DEPUTATIONS TO CONFERENCES/WORKSHOPS/INSTITUTE/SCHOOL

Sreelatha P - International Beacon Symposium, Barcelona, Spain from June 07-11, 2010

PUBLICATIONS IN REVIEWED PROCEEDINGS

1. Tirtha Pratim Das , Prasanna Mahavarkar, Gogulapati Supriya, Satheesh Thampi, P. Sreelatha, P. Pradeepkumar, Neha Naik, S V Mohankumar and Anil Bhardwaj; "Accurate Estimation of the Total Pressure using a Mass Spectrometer below the X-ray limit" ; Proc. International Conference on Innovative Science and Engineering Technology (ICISET 2011), ISBN 978-81-906377-5-6, Vol 1 , page 76, 2011

2. Tirtha Pratim Das, Gogulapati Supriya, Prasanna Mahavarkar, Neha Naik, P. Sreelatha, P. Pradeepkumar, S V Mohankumar, Anil Bhardwaj and R. Sridharan; "Study on the Water Vapor Desorption Rate from Space-Borne Mass Spectrometers under Simulated Deep Space Vacuum"; Proc. International Conference on Innovative Science and Engineering Technology (ICISET 2011), ISBN 978-81-906377-5-6, Vol 1 , page 430, 2011

PRESENTATIONS IN SYMPOSIA/WORKSHOPS/CONFERENCES

- Sreelatha P, Sudha Ravindran, Rosmy John and Sridharan R, Development of coherent beacon receiver system for the Indian CRABEX stations, IBSS, June 2010, Barcelona, Spain.

- Manju G., Sreelatha P., Sudha Ravindran, Rosmy John, Neha Naik, Satheesh Thampi, Pradeepkumar P, S. V. Mohan Kumar and R. Sridharan, A new Ionospheric Probe for insitu measurements of neutral wind and electron density, AOGS, July 2010, Hyderabad, India.

Pradeepkumar P., Sreelatha P., Dinakar Prasad Vajja, S.V. Mohankumar, Anumod P.G. and Neha Naik, Embedded Controller Unit for Earth's Atmospheric Composition Explorer (EACE) payload onboard rockets flown during Sooryagrahan 2010 campaign, 27th & 28th January 2011, NaWRoSE-2011 (National Workshop on Results of Solar Eclipse –2011).

Sreelatha P, Rosmy John, Manju G, Neha Naik, Pradeepkumar P, Mohankumar S V & R Sridharan, Development of Electron density and Neutral Wind (ENWi) probe payload during Sooryagrahan 2010, 27th & 28th January 2011, NaWRoSE-2011 (National Workshop on Results of Solar Eclipse –2011).

Neha Naik, Sreelatha P, Pradeepkumar P, Dinakar Prasad Vajja, Anumod PG, Rosmy John and S. V. Mohankumar, 'Prabhav' – The checkout software for EACE payload data conversion and plotting, 27th & 28th January 2011, NaWRoSE-2011 (National Workshop on Results of Solar Eclipse –2011).

Tirtha Pratim Das, R Sridharan, S M Ahmed, P Sreelatha, Pradeepkumar P, Neha Naik, Gokulapati Supriya, CHACE: In search of the lunar atmosphere, NWASS-23-24 November, 2010.

Tirtha Pratim Das, In Situ Study of the Martian Upper Atmosphere using Neutral Mass Spectrometer, Brainstorming Session on the Exploration of Mars, Physical Research Laboratory, Ahmedabad, 24-24 March 2011.

INVITED TALKS /LECTURES

Pradeepkumar P.

World Space Week lectures at 12 schools in Kozhikode district during 5 to 7 October 2010 covering 3726 students, 240 teachers and 23 PTA members.

Tirtha Pratim Das

Discovery of water on Moon; Organized by Amateur Astronomers Organization, Kerala (AASTRO Kerala), 07th October, 2010

Discovery of Water on Moon : Its scientific and Technological Significances; Organized by the Department of Applied Physics, University of Calcutta, 24th November, 2010

The Night we smelt the Moon ; Organized by Kalpana Chawla Centre for Space and Nano Sciences, Calcutta and South Point High School, Calcutta; 25th November, 2010

CHACE : In Search of the Lunar Atmosphere; National Workshop on Atmospheric and Space Sciences, S.K. Mitra Centre for Research in Space Environment, University of Calcutta, 23rd November-24th November, 2010

Planetary Exploration using Rovers; Organized PLANEX, PRL, Ahmedabad, 05th January, 2011

CONVENING OF SCIENTIFIC SESSION

Tirtha Pratim Das; Planetary Exploration using Rovers; 11th PLANEX Workshop on "Exploration of Mars and Moon" , Physical Research Laboratory, Ahmedabad, January 3-7, 2011

AWARDS

Tirtha Pratim Das; Best Paper Award for the innovation of a technique to estimate very low pressures (less than the X ray limit of the ionization gauges) prevailing at tenuous planetary atmospheres by in situ measurements from an orbiter platform. The award was conferred at the International Conference on Innovative Science and Engineering Technology (ICISET 2011), held at VVP Engineering College, Gujarat Technological University, Rajkot, Gujarat, between 08th and 09th April, 2011.

TRAININGS UNDERGONE

- Tirtha Pratim Das : 3 Day workshop on Scientific Ballooning at National Balloon Facility (NBF), TIFR, Hyderabad
- Tirtha Pratim Das : Training on Vacuum Technology : In-house training organized by HRDD, VSSC
- Neha Naik, 'Training program on embedded systems', HRDD, VSSC, 28th September and 25th October 2010.

ACADEMIC PROJECTS

M.Tech. 2

B.Tech 30